CURRENT-INDUCED VIBRATION IN MULTI-TUBE MARINE RISER

G. RZENTKOWSKI, M.Eng.

CURRENT-INDUCED VIBRATION IN MULTI-TUBE MARINE RISER

by

©G. Rzentkowski, M.Eng.

A thesis submitted to the School of Graduate Studies in partial fulfillment of the requirements for the degree of Doctor of Philosophy

Faculty of Engineering & Applied Science
Memorial University of Newfoundland
St. John's, Newfoundland
Canada

July, 1990

To My Mother,

Czesława Rzentkowska (1928-1985)

Acknowledgements

First and foremost, sincere gratitude is expressed to my supervisor, Dr. J.H. Lever, for his guidance and encouragement during the work on this thesis. Thank you Jim. I wish also to extend my deep appreciation to the other members of the supervisory committee, Dr. R.E. Baddour and Dr. M.J. Hinchey, for their constructive suggestions and persistent interest in this work.

I take this opportunity to thank my wife, Magda, for her understanding and continued support, especially important during the stressful final period. This acknowledgement would be incomplete if I did not mention my two little sons, Bartek and Phillip, without their loving attention this study could have been finished in a shorter time frame. Also, I wish to thank my father and parents-in-law for their silent support from across the miles.

In closing, I wish to express my gratitude to the Natural Sciences and Engineering Council of Canada for the financial support in the form of research grants and to the Canada Employment and Immigration Centre for the unemployment assistance which allowed me to complete this study.

To anyone else, who contributed to this work - thank you.

Abstract

This study looks at the non-linear behaviour of cylinder arrays subjected to fluid cross-flow. The emphasis is on the hysteresis phenomena, associated with fluidelastic excitation, which prove essential in the stability analysis in a low mass-damping parameter range typical for multi-tube marine risers. Since an array generates a high level of turbulence, this forcing mechanism is also included. The present work represents a significant departure from previous studies where attention was primarily focused on linearized fluid mechanics.

A detailed experimental program, conducted in an attempt to reduce the number of degrees-of-freedom needed to model post-stable behaviour of a fully flexible cylinder array, provides a clear explanation for the underlying excitation mechanism. It shows that the fluid-damping force, associated with the transverse-to-flow motion of a single flexible cylinder, can induce hysteresis-type post-stable behaviour. That is, the underlying fluidelastic mechanism requires only one degree-of-freedom to operate. With this observation as a guide, a theoretical model is formulated. The proposed model is a modified time-domain version of an earlier linearized steady-state formulation for fluidelastic instability, developed by Lever and Weaver, which is based on one-dimensional flow and a phase lag between cylinder motion and flow adjustment. First, the fluidelastic equation of motion is solved analytically to third order using the first approximation method of Kryloff and Bogoliuboff. The effect of turbulence is examined *via* superposition of both excitation mechanisms (the random field of turbulence is represented by a flat power spectrum). Next, a fully non-linear solution is found using a direct numerical integration of the equation of motion. The essential features of the stability behaviour are discussed with the aid of bifurcation theory by analogy with corresponding static systems.

The fluidelastic analysis predicts a stable limit cycle which becomes unstable as the mass-damping parameter is increased. Physical arguments, however, suggest

that an opposite behaviour should occur, pointing to a weakness in the model formulated here. A significant improvement, leading also to prediction of hysteresis effects, is derived from an assumption that the phase lag is governed by cylinder motion and decreases with increasing oscillatory amplitude. The combined analysis shows that the fluidelastic stability boundary, when characterized by an unstable bifurcation, may be reduced by turbulence (the rate of reduction is directly proportional to turbulence strength and inversely proportional to unstable limit cycle). For a stable bifurcation, the fluidelastic stability boundary is virtually unaffected and the effect of turbulence is only apparent (interpretation of response curves).

Contents

List of Figures

List of Tables

List of Symbols

a	- limit cycle amplitude
$a(t)$	- time-dependent limit cycle amplitude
$\dot{a}(t)$	- rate of change of limit cycle amplitude
$a(s,t)$	- streamtube area perturbation function
$\vec{a}$	- particular solution vector
c_d, c_o, c_n	- damping coefficients: drag-dependent, structural and net
d	- cylinder diameter
f, f_o	- frequency of cylinder vibration: flow-velocity-dependent and natural (in quiescent air)
f_x, f_y	- frequency of cylinder vibration: streamwise and transverse-to-flow
$f(s)$	- area perturbation decaying function
$f(y,\dot{y})$	- non-linear function of cylinder displacement and velocity
$\vec{f}(\vec{x})$	- function of solution vector
h	- flow resistance coefficient
i	- streamtube identification index
k_0, k_n	- stiffness coefficients: structural and net.
l_0	- cylinder length
l, l'	- relevant fluid inertia length: at state of equilibrium and at limit cycle
m, m_o	- cylinder mass: per unit length and effective

$\bar{m} \equiv \frac{m}{\rho d^2}$	- mass parameter
$\bar{m}\delta \equiv \frac{m\delta}{\rho d^2}$	- mass-damping parameter
$\bar{m}\delta_0$, $\bar{m}\delta_{fe}$, $\bar{m}\delta_n$	- mass-damping parameters: structural, fluidelastic and net
n	- solution index
$p(s,t)$	- unsteady fluid pressure perturbation
s	- position coordinate along streamtube
s_0	- distance along streamtube to inlet
t	- time
t_0	- initial time
$u(s,t)$	- unsteady flow velocity perturbation
v	- static deflection
$\vec{w}$	- transformed solution vector
$\dot{\vec{w}}$	- transformed time derivative of solution vector
x	- streamwise cylinder position coordinate
$\vec{x}$	- solution vector
$\vec{x}_0$	- initial solution vector
$\dot{\vec{x}}$	- time derivative of solution vector
y, $\dot{y}$, $\ddot{y}$	- transverse-to-flow cylinder coordinates: position, velocity and acceleration
A	- peak amplitude
A_0	- steady streamtube area at inlet of unit cell
A_n	- n-peak amplitude
A_{RMS}	- mid-span RMS amplitude
$A(s,t)$	- unsteady streamtube area
$\bar{A}_n$	- average n-peak ampitude
$\bar{A}(s)$	- steady streamtube area

B, B_0	- positive constant
B_1, B_2	- quasi-steady force coefficient
C	- positive constant
C_0	- intersection point of decay envelope with response axis
C_D, C_L	- force coefficients: drag- and lift-dependent
C_r	- dimensional random excitation coefficient
C_r', C_r''	- nondimensional random excitation coefficients
D	- non-linear operator
D_E	- equivalent length of flow attachment
E	- amplitude of harmonic excitation
$F(y, \dot{y})$	- non-linear function of cylinder displacement and velocity
F_{St}	- stochastic force
F_{max}	- Nyquist frequency
F_E, F_T	- fluid force: fluidelastic and turbulence
J	- joint acceptance
K, K_1, K_2, K_3, K_4	- quasi-static force coefficient
N	- number of cycles
P	- array pitch
P_S	- static load
P_{SC}	- critical static load
P_0	- steady fluid pressure at inlet of unit cell
$P(s,t)$	- unsteady fluid pressure
$S_U \equiv \frac{fd}{U}$	- Strouhal number
$S(f)$	- power spectral density of turbulence force field per unit length
T	- transverse pitch of array
T_{max}	- maximum simulation time (from Nyquist criterion)

T_{sim}	- total simulation time
T_n	- period of oscillation
$T(Y)$	- average return period
U	- flow velocity
U_0	- steady flow velocity at inlet of unit cell
$U_r \equiv \frac{U_0}{\omega l}$	- reduced flow velocity
U_C, U_I, U_H, U_P, U_U	- flow velocities: critical, initial, hysteresis, pitch and upstream
$U_{Pr} \equiv \frac{U_P}{f_0 d}$	- reduced pitch velocity
$U(s,t)$	- unsteady flow velocity
$\bar{U}_U$	- mean upstream flow velocity
$\bar{U}(s)$	- steady flow velocity
Y, Y_{max}	- peak displacements: random and maximum
Y_0	- amplitude of initial harmonic disturbance
α	- area perturbation decaying constant
α_0	- angle defining array pattern
β	- time lag reduction constant
γ	- frequency of harmonic excitation
δ	- logarithmic decrement of damping
δ_0, δ_{fe}, δ_n	- logarithmic decrement of damping: in quiescent air, fluidelastic and net
$\bar{\delta}$	- limit of motion space
ϵ	- imperfection parameter
$\bar{\epsilon}$	- limit of initial perturbation
ζ	- damping ratio
ζ_x, ζ_y	- damping ratio: streamwise and transverse-to-flow

η_1, η_2	- non-linear parameters
λ	- variable of characteristic equation for linear oscillator
μ	- small positive constant
μ_1	- non-linear parameter
ρ	- fluid density
σ	- standard deviation
$\tau(s)$	- time lag between cylinder motion and flow adjustement
τ_0	- time lag at inlet of unit cell ($s = -s_0$)
ϕ	- eigenfunction at mid-span
ω, ω_0	- angular frequency of oscillation: flow-velocity-dependent and natural (in quiescent air)
$\omega(a)$	- angular frequency of oscillation at limit cycle
Δ	- discriminate of characteristic equation
Δt	- time increment
ΔU	- velocity increment
ΔU_{min}	- minimum velocity increment
ΔY	- initial harmonic disturbance inrement
$\Theta(t)$	- total phase of cylinder motion at limit cycle
Λ	- control parameter
Λ_C, Λ_H	- control parameters: critical and hysteresis
Λ'_C	- critical control parameter reduced by turbulence
$\Phi(t)$	- phase of cylinder motion at limit cycle

Chapter 1

Introduction

In a world faced with an energy supply problem, especially a tremendous demand for the mobile energy provided by hydrocarbons, the sea bottom attracts much attention. Offshore hydrocarbons are associated primarily with the continental margins which contain 99 % of the ocean's potentially recoverable resources. It has been estimated that 65 % of these hydrocarbons will be discovered at water depths below 200 m (continental shelf), 30 % at 200 to 2500 m (continental slope) and only 5 % at greater water depths (continental rise and oceanic basin), [1]. Consequently, the industry is at present developing the technology for exploration and production on the continental shelves and slopes. Technical difficulties in design of offshore structures are considerable because of the need for operation in increasing depths and ever more hostile environmental conditions, especially near the East Coast of Canada and in the North Sea.

The offshore activities are presently carried out with a large variety of mobile and fixed structures. The mobile structures, mainly used in the exploration phase, include submersible and jackup platforms, and floating units (semisubmersible, ship, barge) to increase drilling capability and to provide greater mobility. Once a commercially attractive hydrocarbon field has been discovered, the production phase starts primarily with the use of fixed platforms. These include pile-founded framed structures (made of welded tubular members) and heavy gravity structures suitable

for activities in extremely severe conditions, and also compliant guyed tower platforms and tension leg platforms for application in greater depths. However, due to the diminishing number and size of hydrocarbon discoveries, the trend in offshore developments is very much towards floating production units combined with mobile subsea systems. In a subsea system, the wellheads and associated equipment are mounted on a seafloor template or frame. The maximum operational depth is about 1500 m.

1.1 Marine riser

The interest in floating production facilities has led to the development of complex multi-tube riser systems, an important link between the floating structure and the subsea system. The production riser, schematically shown in Figure 1.1, has to be flexible in order to resist the hydrodynamic load. It consists of a cluster of pipes: typically, an export riser and a number of flowline and auxiliary risers interconnected along their length by spacers (spreader bars) suspended in a main structural system on a number of cables (the distance between the spacers is designed to meet operational requirements for installation and maintenance). The deep-water riser is additionally provided with buoyancy devices to reduce tensile stresses. The flowline risers convey the crude oil from the wells to the production facility on the surface. The export riser conducts the processed crude to the pipeline on the ocean floor. The auxiliary risers, used for various purposes, include gas lift pipes and maintenance pipes for guiding tools. Typically, the cross-sectional configuration of this multi-tube riser systems has a form of a circular array (a central export pipe is surrounded by one or two arrays of smaller satellite pipes), a linear array or, mainly in connection with tension leg platform, a dense rectangular array (highly regular square or staggered, appearing solid when viewed from any direction other than along a row or column).

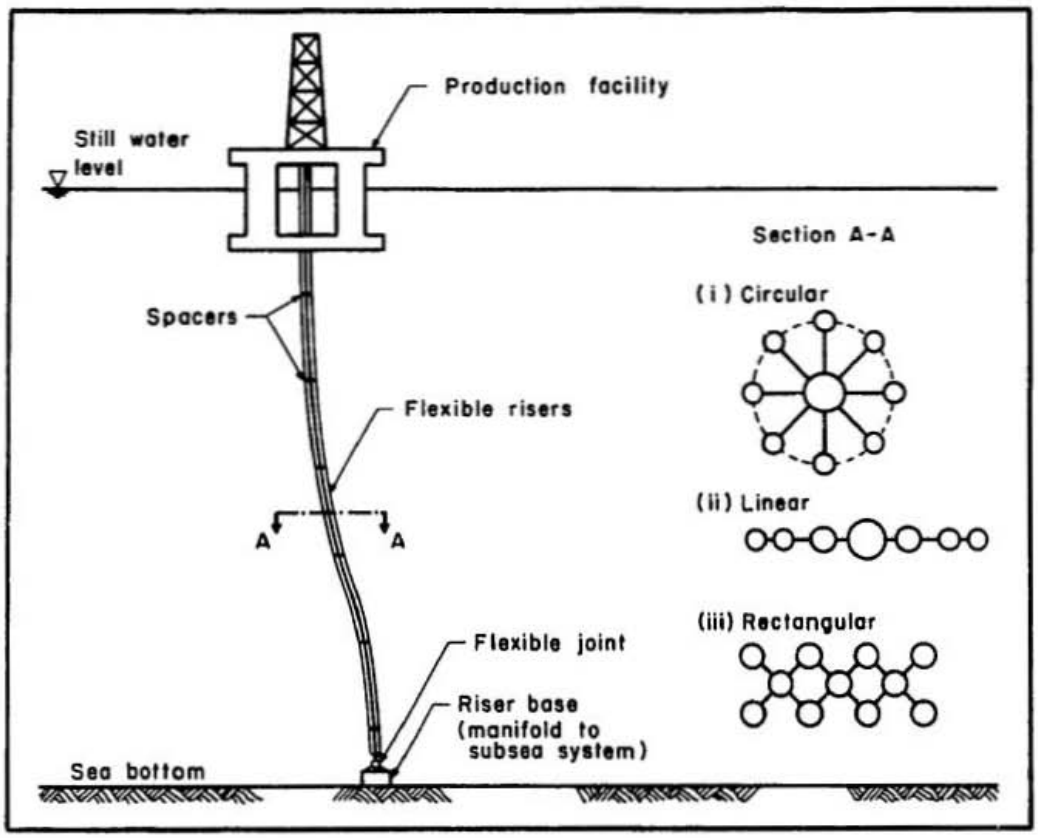

Figure 1.1: Schematical representation of multi-tube production riser.

The production riser, extending over large depths, is exposed to a variety of hydrodynamic loads (see Figure 1.2). In the upper stratum of the sea, these loads are caused by waves, surface currents (mainly wind-driven and tidal) and movements of the production platform. In the lower stratum, the loads are reduced to current forces resulting from large scale oceanographic circulations and movements of heavy density water masses. As a result, an intimate knowledge of the wave, current and wind climate in the vicinity of the offshore platform is necessary for the riser analysis. Based on these data the hydrodynamic loads may be determined in the following basic steps:

- formulating the mathematical description, either deterministic or stochastic, of the water particle kinematics in the absence of the structure (selecting a

suitable wave theory or a wave spectrum)

- computing the hydrodynamic loading from the fluid motion using Morison's equation (a combination of acceleration and drag forces in the upper part of the riser, and drag forces only in the lower part) and based on a rigid prism representation for the marine riser
- formulating an adequate model of interaction between the motion of the fluid and the flexibly mounted pipes (hydroelastic oscillations).

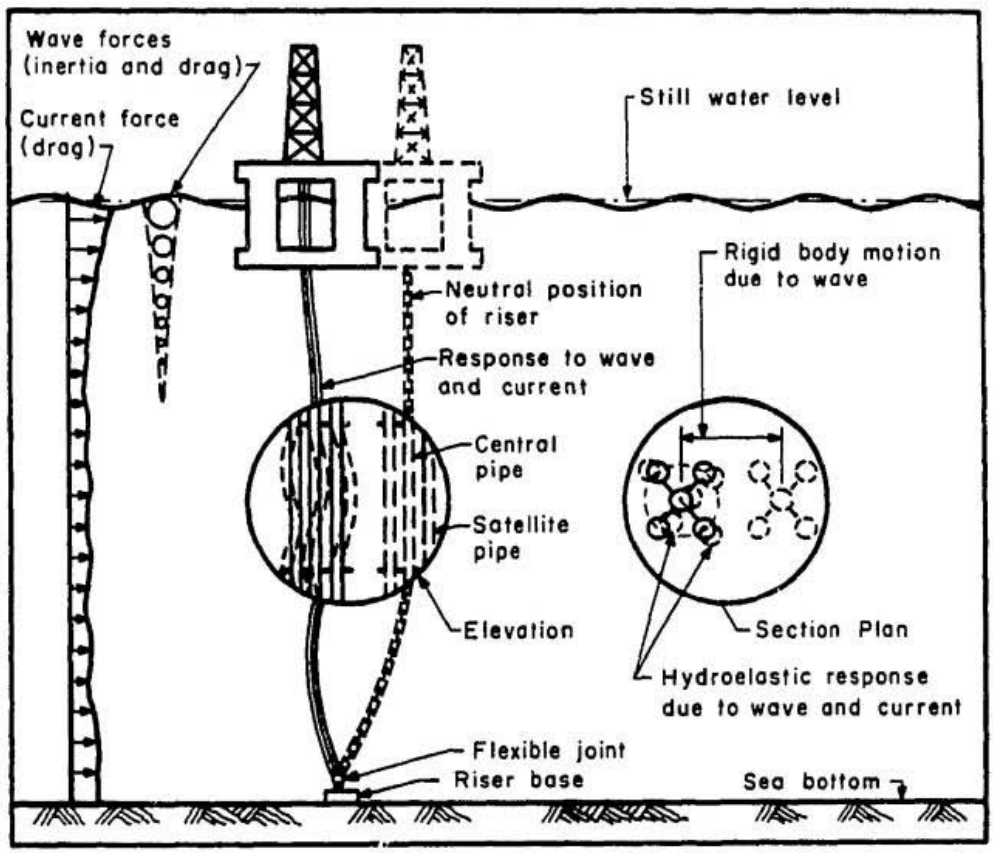

Figure 1.2: Multi-tube production riser exposed to environmental load.

The production riser is structurally a cluster of slender members with a very small moment of inertia. Thus, the riser is very sensitive to these loads which may cause the large amplitude oscillations of two types (see Figure 1.2):

- rigid pipe motion; oscillations in a combined longitudinal, transverse and rotational motion with the period close to the period of wave cyclic load
- relative motion between the individual pipes; superharmonic oscillation, superimposed on a rigid pipe motion and amplified by the hydroelastic excitation mechanisms

1.2 Problem formulation

The production riser, which has an expected lifetime of several decades, must be carefully designed in order to preserve its integrity. An operational failure may reduce or even curtail production and, more importantly, may foul the environment. As a consequence, an intimate understanding of the production riser response to the environmental loads is necessary. Over the years a large amount of experience has been collected. However, hydroelastic oscillations, arising in dense arrays of pipes, were typically disregarded in common offshore platform design practice (a rigid prism model was *a priori* assumed). Recently, they have started to attract attention recognized already as a major problem affecting the operation of a variety of heat exchangers and overhead transmission lines. Hydroelastic oscillations may cause catastrophic damage of risers (e.g. splitting at mid-span) in a very short period of time as a result of pipe-to-pipe clashing. Alternatively, mechanical failure may occur due to fatigue and fretting wear at the supports (spacers), after several years of service, resulting from smaller amplitude oscillations which are always present.

Both types of oscillations, and the effect of their mutual interaction, are of interest in the present study. However, only current-induced forces are analysed since it is unlikely that excessive vibration develops in the wave active zone during each half period. Also, the wave zone is typically a small percentage of the total riser length. By the direct analogy to heat exchanger tube bundle, the multi-tube riser is considered in the form of an infinite rectangular pipe cluster (Figure 1.3 defines the various

array patterns; normal square, rotated square, normal triangle and parallel triangle). This allows the present study to be based on extensive research conducted in recent years in the field of power generation (this research has successfully attempted to identify and to develop a better understanding of the excitation mechanisms in pipe arrays subjected to the fluid cross-flow).

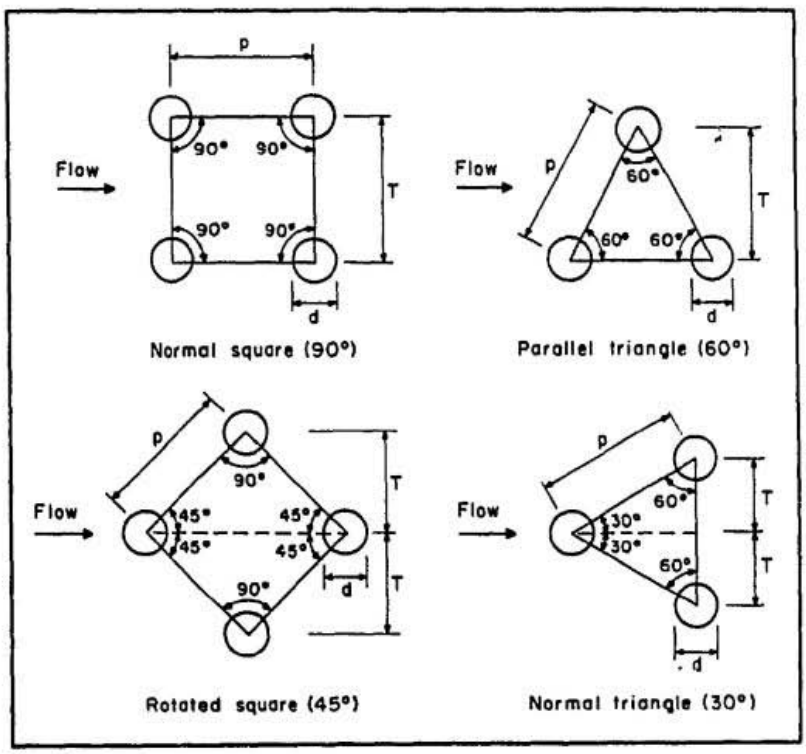

Figure 1.3: Standard pipe array patterns.

While some uncertainties still exist, it is generally accepted that hydroelastic oscillations in water flow are excited by turbulence buffeting, Strouhal periodicity (vortex shedding) and fluidelastic instability. Figure 1.4 shows schematically the vibration of a pipe array (the production riser) which may be caused by these excitation mechanisms (note that hysteresis loop results from non-linear effects of fluidelastic instability).

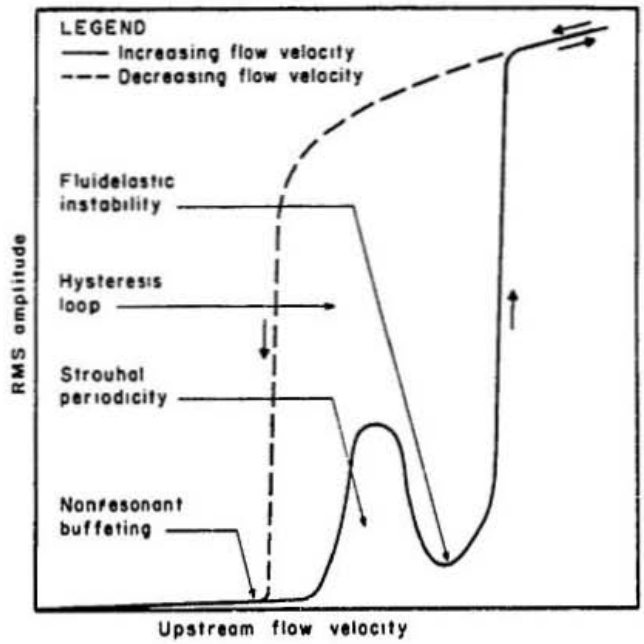

Figure 1.4: Hydroelastic oscillations of pipe array in fluid cross-flow.

Turbulence buffeting is due to the random pressure fluctuations existing in upstream flow (especially important in the wave/current active zone) and also generated by an array itself. The excitation is normally broad-band and the pipe response is that of randomly forced oscillations with a small amplitude related to the 1-2 power of flow velocity. These vibrations are capable of producing pipe failure in the form of fretting wear at the supports and this may occur only after several years of service. Since the production riser has a longer amortization period, turbulence buffeting cannot be neglected in design consideration.

Strouhal periodicity is a periodic excitation mechanism existing in pipe arrays which is similar to conventional vortex shedding, e.g. there is a constant Strouhal number associated with it. However, while the source of the periodicity is generally accepted to be boundary layer separation due to a free-shear layer instability, there is normally insufficient spacing between pipes in an array to permit a conventional vortex street to form. Oscillations are excited when the frequency of flow periodicity

coincides with the one of natural frequencies of pipe. In this case, the pipe response is essentially that of a narrow banded linear system at resonance. Thus, Strouhal periodicity can cause very large amplitude vibrations and short term damage, especially in the upstream pipe rows, unless the bundle is tuned to operate out of the critical frequency range by suitable pretensioning.

Fluidelastic instability is not associated with flow periodicity but rather with the motion of the pipe which, at sufficiently high flow velocity, couples with the flow such that energy is transferred to the pipe, amplifying its motion. The mechanism of fluidelastic instability, *de facto* strongly non-linear, is neither fully recognized nor understood. One explanation gaining general acceptance is that this violent self-excited phenomenon is due to a phase lag, resulting from fluid inertia, between cylinder motion and flow adjustment. Large amplitude vibrations, induced by fluidelastic instability, have the greatest potential for catastrophic damage of the production riser. The flow velocity at which the pipe cluster becomes unstable is called the critical flow velocity. This cannot be exceeded under any circumstance in real environmental conditions. In principle, the essential design requirement is to predict this critical flow velocity.

Two of these mechanisms are the focus of present research; fluidelastic instability, as a most severe problem, and turbulence buffeting which is always present and can interact with other mechanisms.

1.2.1 Research objective

While substantial progress has been made in understanding fluidelastic instability, the most reliable tools used in its prediction are still empirical. Moreover, the basic practical question still remains unanswered. Namely, what is the critical flow velocity from an operational point of view? Fluidelastic instability, as a strongly non-linear phenomenon, can lead to hysteresis-type behaviour of a pipe cluster: a rapid

response jump to unstable oscillations, at the critical flow velocity, which persist even for significant reduction in flow velocity below its critical value. Interestingly, unstable osillations may be excited by a sufficiently large disturbance within the hysteresis region. Therefore, in our opinion the critical hysteresis velocity, the lower limit of this region, is the practical stability boundary for a pipe cluster. With this rationale behind, the present study focuses on non-linear phenomena due to fluidelastic instability and attempts to answer some fundamental questions:

- What is the mechanism causing the hysteresis-type, post-stable behaviour of a pipe cluster?
- What is the role of neighbouring pipes motion and array geometry in inducing this behaviour?
- What is the role of other excitation mechanisms in triggering the instability?

This work differs in several aspects from previous studies where attention was primarily focused on linear effects. It is hoped that it will lead to a more quantitative guidance in marine riser design against current-induced hydroelastic vibration.

1.2.2 Research scope

A theoretical, non-linear model for flow-induced vibration in pipe arrays is developed including the combined effects of fluidelastic instability and turbulence buffeting. An earlier steady-state theoretical model for fluidelastic instability in heat exchanger tube bundles is adopted, modified and then extended to include random turbulence and non-linear fluidelastic forcing terms. Array stability is examined using catastrophe theory and a numerical time-domain simulation.

In an attempt to verify the proposed model, an experimental research program with pipe arrays in air-flow was undertaken and a comparison was done with the extensive experimental data previously reported on flow-induced vibration.

Chapter 2

Previous work

Most of the work on hydroelastic behaviour of marine riser has concentrated on vortex shedding, since large amplitude oscillations, often described in the open literature (as in Reference [2,3], for example), were exclusively associated with this excitation mechanism. Collapse of slender circular members in steady current, [4], and fatigue failure in waves, [5], attributed to vortex shedding, are known to have occurred. Although oscillations of the single-pipe riser are presently well analysed (e.g. wake oscillator model, statistical model and numerical procedure based on discrete vortex, [6,7]), the flow interference effects in the multi-tube riser are neither fully recognized nor understood.

Experiments on the tandem configuration of pipes showed that the drag and lift forces are functions of pipe separation and their orientation with respect to the flow, [8]. However, all the vortex shedding phenomena, characteristic for single pipe, modified by flow interference at small gap (especially important for cylinder in a lee of upstream cylinder), can also occur, [9,10]. For multiple pipe systems, the situation is more complex since the wake interference arises from more than one pipe. Therefore, a number of Strouhal numbers may be detected, dependent on array configuration and flow orientation, as a recent experimental study on a five-pipe cluster suggested, [11]. The dominant response occurred at the lowest Strouhal number, $Su = 0.20$, which is typical for vortex shedding from a single pipe in the

flow regime of interest. Interestingly, for some flow orientations, large amplitude oscillations persisted even for flow velocities well above critical (thus, outside the "lock-in" region). Another work, on many multi-tube riser configurations, showed that the "lock-in" amplitude of transverse oscillations may be 3-4 times higher from that for the single pipe, [12]. In view of these experimental studies, [11,12], it can be suggested that the multi-tube riser may suffer also from another excitation mechanism, which is obscured by vortex shedding and can be easily mistaken for it, especially in the complex ocean environment.

Therefore, it would seem appropriate to reexamine multi-tube riser vibration problems in the light of the experience in power generation technology, where much progress has been made since the time when it was believed that vortex shedding was the only excitation that could cause large amplitude vibrations. Substantial literature, which has appeared on various aspects of flow-induced vibration, is summarized in several informative reviews and design guidelines (as in References [13-17], for example). Experimental studies on pipe arrays in water flow indicate that both phenomena, fluidelastic instability and vortex shedding, were (for some array configurations) very difficult to separate, [11,18-20]. Characteristic of fluidelastic instability, especially in water flow, is its ability to display hysteresis-type behaviour, [21-23]. Therefore, fluidelastic instability can be excited by vortex shedding since both mechanisms nearly coincide, leading to considerable confusion in their interpretation even under controlled laboratory conditions. In fact, failures routinely attributed to vortex shedding were mainly caused by fluidelastic instability, [24,25]. Additional confusion may result from turbulence buffeting since the observed periodicity in the flow may be associated with the dominant frequency of turbulence, [26]. It happened that two different hypotheses, turbulence buffeting and vortex shedding, were used to describe and predict the same resonance mechanism, [24,26].

2.1 Fluidelastic instability

2.1.1 Heat exchanger: an infinite array in water and gas flows

Analytical models

The large amplitude whirling motions, characteristic of fluidelastic instability, were first observed by Roberts in the 1960s. His analytical model, [27], was based on the existence of bistable jets which he observed experimentally in the separated flow behind a single row of cylinders. The predicted stability boundary and limit cycle oscillations correlated well with his own experimental data. It is worth noting that this non-linear model predicted the hysteresis-type post-stable vibration which was observed experimentally 20 years later. Since the existence of the jet-switching mechanism was considered to be limited and the model was not extended to deal with multi-row arrays, this work was unfortunately largely ignored.

Since the first analytical approach by Roberts to understand and predict the mechanism underlying fluidelastic instability, several models have been proposed. Most widely used is the semi empirical quasi-static model for a single row of cylinders originally developed by Connors, [28], in the early 1970s. Connors found that the fluidelastic instability mechanism is position dependent, and that for certain patterns of intercylinder displacements, energy may be extracted from the flow. The stability curve, found by Connors, is expressed by a simple relation between two nondimensional parameters, the reduced flow velocity, $\frac{U}{fd}$, and the cylinder mass-damping parameter, $\frac{m\delta}{\rho d^2}$:

$$\frac{U}{fd} = K(\frac{m\delta}{\rho d^2})^{0.5} \tag{2.1}$$

where the proportionality constant for his cylinder row was found empirically to be, K=9.9. This equation gained general acceptance due to its simplicity and close agreement with experimental data. However, this model only recognized and did

not explain the mechanism of fluidelastic instability. All of the underlying fluid mechanics was absorbed into the empirical factor, K.

In the mid 1970s, Blevins, [29,30], turned the analysis, in a more formal mathematical way, to multi-row arrays for which he retained the form of equation (2.1). The proportionality constant, K, was obtained based on the fluid force coefficients measured for each type of array. In an attempt to bring some insight into this constant, Blevins extended the analysis to the quasi-steady flow theory including the forces associated with fluid drag: (i) the jet-switch force, [30], and (ii) the flow-velocity dependent damping force, [7]. For the sake of simplicity, the fluid force coefficients were replaced with equivalent approximate analytical expressions which were functions of the array pitch ratio, $\frac{P}{d}$ (see Figure 1.3).

Ever since then, many efforts have been made to empirically determine the value of K and to modify existing semi-empirical models. Careful experiments resulted in various refinements of equation (2.1), such as separating the two dimensionless parameters, δ and $\frac{m}{\rho d^2}$, and adjusting the exponents on each. For example, the stability equation proposed by Weaver and El-Kashlan, [31], takes the form:

$$\frac{U}{f_o d} = K_1 (\frac{m}{\rho d^2})^{0.29} \delta^{0.21} \tag{2.2}$$

while Paidoussis, [32], suggested the formula:

$$\frac{U}{f_o d} = K_2 (\frac{m}{\rho d^2})^{0.4} \delta^{0.4} (\frac{P}{d} - 1)^{0.5} \tag{2.3}$$

where the constants, K_1 and K_2, were obtained experimentally. The parameter, $\frac{P}{d}$, defines the array pitch ratio similarly as in the Blevins' model, [7].

Chen initiated a different line of development from that which was based on the Connors' quasi-static hypothesis. He first proposed a semi-empirical dynamic model based on the cylinder-to-cylinder interaction mechanism, [33,34]. In this study, Chen formulated expressions for coupled unsteady fluid force coefficients (inertial, damping and stiffness). Tanaka and Takahara, [35], pursued this development

and obtained a very good agreement between their own experimental and theoretical stability results which were generated using measured unsteady displacement-, velocity- and acceleration-dependent fluid force coefficients. However, this analysis, which required measurement to be made over the entire range of upstream flow velocity, U, was from a practical point of view both lengthy and costly.

The outcome of the various research efforts was only partially successful in serving as design guidelines. All of these models had to be restricted to the analysis of systems sufficiently similar (array pattern and pitch) to those for which the empirical force coefficients had been obtained. Furthermore, these semi-empirical studies offered little insight into the understanding of the fluidelastic instability phenomenon. Therefore, in the 1980s, research attention was once again focused on the fluid mechanics of the problem, leading to a new series of studies.

An extension of the quasi-static theories was a quasi-steady model, based on the mechanism responsible for damping-induced galloping of iced transmission lines, developed by Price and Paidoussis, [36]. This model, requiring less empirical input in the form of fluid-dynamic stiffness terms measured quasi-statically, was formulated for double row arrays. An attempt was made to generalize the stability expression to account for most array geometries. A modified form of the stability equation was then derived:

$$\frac{U}{fd} = B_1(\frac{P}{d} - 1)^{1.7}[1 + (1 + B_2\frac{m\delta}{\rho d^2})^{0.5}] \tag{2.4}$$

where the constants, B_1 and B_2, were obtained from quasi-static force coefficients. Thus, they depended on array geometry. This work was further refined and modified by incorporating phase-lag cylinder motion and motion-induced fluid forces, [37,38], and by prescribing a specific inter-cylinder modal pattern, [39]. These refinements allowed the authors to study the behaviour of a single flexible cylinder in the middle of a rigid array and the behaviour of a fully flexible array, respectively. In general, the comparison of the analytical results with the available experimental data was found

to be reasonable. In a very recent work, Price and Valerio, [40], extended the quasi-steady theory to account for non-linear fluid forces. This analysis was restricted to a single flexible cylinder constrained to move in the transverse-to-flow direction only. The resulting non-linear equations were solved using the first approximation method of Kryloff and Bogoliuboff. This model predicted stable limit cycle oscillations in a whole range of the mass-damping parameter. The rate of increase of predicted amplitudes with flow velocity was, however, much greater than that experimentally observed.

Chen continued the development of his unsteady model, following the work of Tanaka and Takahara, [35]. In this remarkable study, [41,42], the author undertook an analytical formulation of unsteady fluid forces. Unfortunately, some of those forces, strongly dependent on array geometry, could not be obtained in the theoretical way. Using quantities measured by Tanaka and Takahara, [35], Chen found excellent agreement with existing stability data. It is worth noting that he first recognized two different mechanisms responsible for fluidelastic instability; a damping-controlled (single degree-of-freedom velocity mechanism) which is predominant in a lower range of the mass-damping parameter, typical for liquid and gas flows, and a stiffness-controlled (Connors/Blevins instability, multi degree-of-freedom displacement mechanism) which is predominant in a higher range of the mass-damping parameter, that is in gas flows.

In the first attempt to account for non-linear unsteady fluid forces, Gasteiger, [43], formulated a semi-empirical model for a single flexible cylinder in an otherwise rigid array. The damping and stiffness coefficients were modelled as a sum of first and third order terms in both the x- and y-directions, including cross-coupling effects. The author obtained these coefficients from decay curves, recorded in quiescent fluid and in fluid flow, based on an equivalent linearization technique. Since this study required separate measurements at each flow velocity and for each array geometry,

it was limited to the first row of cylinders. Interestingly, for a square array, the model predicted the existence of both stable and unstable limit cycles at low values of the mass-damping parameter. In a recent study, Andjelic *et al.*, [44], proposed numerical procedure to recognize the fluid force coefficients in Gasteiger's non-linear equation. The authors adopted a numerical code for solving the non-linear differential equations of oscillatory systems. In this way, the stability boundary and the post-stable cylinder mid-point motion could be calculated, for various sets of the fluid force coefficients, and then compared with experimental results. This numerical procedure was further modified by Ducci, [45], using centre manifold theory. This complex analysis allowed the author to compute the unknown fluid force coefficients directly from experimental data; the net damping as a function of flow velocity.

At the opposite extreme from these largely empirical models are the analytical models based either on a steady-state solution or a potential flow theory. Lever and Weaver, [46], recognized fluidelastic instability as a unique mechanism resulting from a phase lag between cylinder motion and flow redistribution. Their theoretical model was based on some experimental observations which led to reasonable simplifying assumptions. The fluid mechanics was modelled using the one-dimensional unsteady Bernoulli equation. They considered the transverse-to-flow harmonic motion of just one cylinder surrounded by rigid neighbours. This theoretical model was further developed by the authors to include the effects of streamwise dynamic and static instability, [47,48]. In spite of the simplicity of the model, the agreement between analytical prediction and experimental data was remarkable, especially for parallel triangle and rotated square arrays. These predictions correlated very well with the precise predictions of Chen, [41,42], and Tanaka *et al.*, [35], without the need for experimentally obtained fluid force coefficients. However, in contrast to remaining theories, the stability condition was a linear function between reduced flow velocity and mass-damping parameter for high values of these parameters. In follow up

studies, the original model of Lever and Weaver, [46], was further extended and modified. Yetisir and Weaver, [49], used curvelinear coordinates for the flow and two degree-of-freedom for the cylinder, while Lever and Rzentkowski included a random field of turbulence to examine linear response curves, [50].

Another interesting group of theoretical models is based on the potential flow formulation. First studies - presented by Balsa, [52], and Chen, [34] - although helpful in understanding the underlying fluid mechanics, found very limited applications due to their poor analytical predictions. Therefore, this formulation was again carefully rederived by Paidoussis *et al.*, [51], to explore the capabilities and limitations of the potential flow theory for flow-induced vibration in cylinder arrays. This modified study also incorporated a phase lag between cylinder displacement and the resulting fluid force, following the work by Lever and Weaver, [46]. Although the authors found better agreement between analytical prediction and experimental data, the formulation of the stability problem in terms of ideal flow theory must be considered as rather unsuccessful.

Summa summarum; extensive research on fluidelastic instability in cylinder arrays, concerning power generation technology, has resulted in a variety of theoretical models which can be categorized in two different ways: (i) according to the applied fluid mechanics (quasi-static, quasi-steady, unsteady) and (ii) according to practical application (semi-empirical, analytical).

The quasi-static models, [28-32], are based on the assumption that the fluid forces depend on the static cylinder deviation from its reference configuration. All the models, developed so far, are combinations of analytical solutions and experimental data. The resulting fluidelastic instability is the fluid-stiffness controlled mechanism.

The quasi-steady models, [7,36-40], also need quasi-static measurements of fluid forces which are then assumed to additionally depend on cylinder motion. The

cylinder velocity is assumed to be constant at any given instant of time. The vector addition of the cylinder velocity and the flow velocity yields an angle of attack effect which changes with tube motion. The resulting fluidelastic instability is the fluid-stiffness and fluid-damping controlled mechanism.

The unsteady models, [27,33-35,41-43,46-52], are based on experimental data and empirical correlations which express fluid forces as a function of cylinder displacement, velocity, and acceleration. The general expressions for fluid force are non-linear. However, the fluid mechanics are linearized in most studies to permit suitable analytical solutions. The resulting fluidelastic instability, as for quasi-steady flow theory, is generally the fluid-stiffness and fluid-damping controlled mechanism (except the single-degree of freedom models, [46-50]).

The semi-empirical models require experimental input in the form of fully unsteady, [27,33-35,40-43], or steady time-averaged data, [7,28-32,36-39]. It follows that practical application is strongly limited by dependence on the measurement and its quality.

The analytical models, [34,46-52], require very little or no empirical input and, with improvement, may have the greatest potential to serve as design guidelines. Unfortunately, this research, except for the models based on the original theory of Lever and Weaver, [46-50], has not been very successful.

Hysteresis effects

While many models for fluidelastic instability have been proposed, most are based on linearized fluid mechanics (except Reference [27,40,43]). Thus, the response of the modelled cylinder array becomes infinite at the point of instability unless non-linear structural mechanics are included. However, in real experimental situations, the system response at this point may be controlled by non-linear fluidelastic effects, as recent experimental studies suggest.

In an investigation into the post-stable behaviour of a parallel triangular array, Lever and Rzentkowski, [53], found that a single flexible cylinder, which was positioned in the fourth row of an otherwise rigid array, experienced a gradual transition from stable to unstable oscillations as flow velocity was increased beyond its critical value, while a fully flexible array experienced a rapid response jump. In the latter case, the unstable oscillations persisted for small reduction in flow velocity below critical. The width of the observed hysteresis region was 5-23 % of the critical flow velocity, U_C, decreasing with increasing damping. Hara, [21], reported qualitatively similar results for single cylinder rows in water cross-flow. He observed relatively broad hysteresis (30 % U_C) at low values of the mass-damping parameter which disappeared at high values. Chen and Jendrzejczyk, [22], also examined a tube row in water cross-flow, but with only three flexible cylinders. The reported width of the hysteresis region was 30 % U_C, identical as that found by Hara at low values of the mass-damping parameter.

Andjelic and Popp, [54], observed phenomenologically different behaviour; the hysteresis of a single flexible cylinder. In this case, the cylinder was located in the second row in a normal triangular array and the width of the hysteresis region was 20 % U_C. More extensive experimental studies of this array were reported in another work by Andjelic, [55]. The author found, in agreement with References [21,53], that the hysteresis effect becomes less pronounced, following an increase in the mass-damping parameter.

Hysteresis behaviour has also been observed to occur in fairly realistic heat exchanger test rigs by Godon, [56], who investigated 1.33-1.42 normal triangular arrays, and by Halle *et al.*, [23], who investigated 15 cylinder-in-shell configurations in four standard patterns. Godon reported hysteresis regions of 3-39 % of the critical flow rate, while Halle *et al.* reported regions of 12-49 % of the critical dynamic head (U^2).

Interestingly, it has been found experimentally that instability in a cylinder array may be excited by a sufficiently large disturbance whenever the system is operating within the hysteresis region. Chen and Jendrzejczyk, [22], first performed such excitation studies on a 1.75 pitch ratio cylinder row. The authors called the state defined by the lower limit of the hysteresis region the "excited instability" and the state defined by the higher limit the "intrinsic instability". In a more comprehensive study, performed on a 1.375 pitch ratio triangular array, Lever and Rzentkowski, [53], found that only a fully flexible array can display the hysteresis behaviour. The instability was excited by two types of transient disturbance; cylinder displacement and flow velocity.

The existence of hysteresis effects in cylinder rows was first analytically recognized by Roberts, [27]. However, the author did not explore in detail the phenomenon, probably, due to the lack of experimental evidence supporting it. Therefore, the recent works by Price and Valerio, [40], and Gasteiger, [43], are the only attempts to analytically describe the post-stable behaviour of pipe arrays due to fluidelastic excitation. Both of these models are semi-empirical. The first requires the measured variations of the lift and drag coefficients as the cylinder is displaced in the transverse-to-flow direction, while the second is based on an experimental identification technique for the unsteady fluid force coefficients (see also Reference [44,45]). Thus, these models are strongly dependent on the measured data and their quality.

2.1.2 Marine riser: a finite array in water flow

To the author's knowledge, fluidelastic instability of a multi-tube riser, subjected to a steady current, was first observed and explicitly recognized by Moe and Overvik, [57]. A rigid pipe cluster (relative motion between the pipes was not allowed) underwent a violent self-excited oscillations, predominantly in the transverse to the flow

direction, which resulted from negative damping (velocity mechanism). This study suggested that an instability excited on one of the members can trigger an unstable mode of the multi-tube system.

Fluidelastic instability in a steady current was also observed by Panicker and Yancey, [58], in model studies of Mobil's deepwater production riser which consisted of a linear array of flexible flow lines. In this case, the pipes violently oscillated in pairs of two in modes perpendicular to each other (phenomenon often referred as galloping). The observed vibration modes and critical velocities for instability proved that the underlying excitation mechanism is fluidelastic instability and not vortex shedding. In an attempt to study this phenomenon, Ottesen Hansen and Panicker, [59], adopted the Blevins' model (for a densely spaced infinite linear array of pipes with pitch to diameter ratio, $\frac{P}{d} < 1.7$), [7], in which the flow velocity was assumed to be uniformly distributed between pipes. Since this assumption cannot be valid for a system with large spacing to diameter ratio (typically, $2 < \frac{P}{d} < 4$ for this riser type), the authors defined empirically the flow velocity distribution function and modelled the flow field between pipes using the two-dimensional steady Bernoulli equation. In this way, the spacing parameter, $\frac{P}{d}$, enters into the stability conditions. The inner solution of the problem ($\frac{P}{d} < 1.7$), the modified Blevins' formula, takes the form:

$$\frac{U}{fd} = K_3(\frac{m\delta}{\rho d^2})^{0.5}[2(\frac{P}{d})^{-6} - (\frac{P}{d})^{-5}]^{-0.25} \tag{2.5}$$

while the outer solution ($\frac{P}{d}$>4) is:

$$\frac{U}{fd} = K_4(\frac{m\delta}{\rho d^2})^{0.5}(\frac{P}{d})^{0.5} \tag{2.6}$$

where the coefficients, K_3 and K_4, are stability constants (K_4 is inversely proportional to the steady drag coefficient, C_D). The authors found very good agreement with experimental data of Ishigai *at al.*, [60], for the outer solution, and that of Blevins, [7], for the inner solution.

Fluidelastic instability in steady flow was also observed in the recent laboratory tests on the model of the Buchan production riser (five-pipe circular cluster) performed in a wind tunnel by Paidoussis *et al.*, [61] and in a water tunnel by Price *et al.*, [11]. In these tests, all pipes were rigidly mounted, except the monitored one. Interestingly, unstable oscillations of individual pipes were first excited by vortex shedding but, unlike this excitation phenomenon, they persisted for all flow velocities above the critical value. This proved that, in addition to vortex shedding, fluidelastic instability had been occurring. The observed critical flow velocities were equivalent to current velocities of the order of 1 $\frac{m}{sec}$ (2 *knots*) or less which are very common, especially, in costal regions.

Also, interesting to note is the analytical study presented by Ottesen Hansen *et al*, [62], although it is beyond the scope of this research. The authors examined the occurrence of fluidelastic instability in waves of a rectangular array of risers used in connection with tension leg platforms. The hydrodynamic load, arising from the wake interaction between the pipes, was approximated by the quasi-steady model for instability of twin power conductors in strong winds, [63]. They identified both types of instability (that is the instability of a rigid pipe array and the wake galloping of the spans between spacers of the downstream pipe) either as unstable oscillations excited only in one half period of a wave or a continuous growth of vibration from half period to half period. The authors reduced this analysis to individual pairs of pipes with spacers, assuming that instability of any one of the pairs is sufficient to cause instability of the total system. They found that fluidelastic instability depends primarily on the Keulegan-Carpenter number, the pipe spacing and the ratio between water depth and wave length. However, the size of the unstable region was very limited, indicating that instability in current is a far more severe problem.

2.2 Turbulence buffeting

The nature of turbulence-induced vibration or buffeting in cylinder arrays and its relation to Strouhal periodicity was also first recognized in the field of power generation. All of the early studies, before the 1960s, considered "vortex shedding" to be the main mechanism causing vibration. However, in 1964, Owen, [26], identified the periodic excitation mechanism as two separate phenomena. He suggested that the relatively broad band turbulence is operative at all flow velocities but its peak broadens and shifts to higher frequencies when the flow velocity increases. Thus, turbulence can also cause resonance, at a specific flow rate, similar to vortex shedding. This study, however, was rejected by Chen in an experimental work on vortex shedding, [24]. It started a period of confusion in which two different hypotheses gained acceptance for the same excitation mechanism. Worth noting is the fact that Owen and Chen predictions were in reasonably close agreement.

Whatever the true mechanism underlying flow periodicity in cylinder arrays was, it was necessary to develop design guidelines to prevent cylinder failures. Two resonance models, essentially the same, have been proposed for a lightly damped linear system subjected to random excitation. Thus, these models eliminated the influence of an off-resonant Strouhal peak in the turbulence spectrum on cylinder response.

The first model, developed by Pettigrew and Gorman, [64], gave a remarkably simple formula for predicting the mid-span RMS amplitude, A_{RMS}, of cylinder response:

$$A_{RMS} = \frac{S^{0.5}(f)}{(4\pi^5 f^3 m^2 \zeta)^{0.5}} \tag{2.7}$$

where the power spectral density of the random force field per unit length, $S(f)$, was assumed, based on experimental evidence, to be proportional to the flow dynamic

head. That is:

$$S^{0.5}(f) = \frac{1}{2} C_r(f) \rho d U^2 \tag{2.8}$$

with the effective random excitation coefficient, $C_r(f)$, obtained experimentally for various cylinder array geometries. The random force field was assumed to be homogenous and fully correlated along the cylinder length.

The second, equally simple, response design expression was developed by Blevins *et al.*, [65], in the form:

$$A_{RMS} = \frac{S^{0.5}(f) J \phi}{(64\pi^3 f^3 \zeta)^{0.5}} \tag{2.9}$$

where the joint acceptance, J, would be equal to one if the force field was perfectly correlated. The power spectral density function, $S(f)$, was proposed in a similar form to equation (2.7), except for the nondimensionalizing factor, $\frac{U}{d}$, that is:

$$[S(f)\frac{U}{d}]^{0.5} = \frac{1}{2} C_L \rho d U^2 \tag{2.10}$$

where the lift coefficient, C_L, replaced the random excitation coefficient, $C_r(f)$.

The agreement between both methods is remarkably close, considering that Pettigrew and Gorman obtained their excitation coefficient from experiments in water flow, showing U^2 dependence for RMS cylinder response, while Blevins *et al.* obtained their coefficient from experiments in air flow, showing $U^{1.5}$ dependence. Unfortunately, a later experimental study, aimed at a more precise prediction of the turbulence response in terms of flow velocity, showed higher discrepancy. The Pettigrew and Gorman model was supported by the Sandifer and Bailey experiments, [66], performed in water flow with parallel triangular array, suggesting that the cylinder turbulence response varies proportionately with U^2. These results were contradicted by Taylor *et al.*, [67], who showed $U^{1.5}$ dependence, very similar to Blevins theoretical prediction, for a cylinder in a single row. Price *et al.*, [68], found that the response amplitude varied approximately linearly with flow velocity for a single flexible cylinder in a rotated square array. A follow up study by these au-

thors, [69], using the same array but with smaller pitch ratio, indicated $U^{1.4}$ and $U^{2.2}$ dependence for a flexible cylinder in the second and fifth row, respectively. It can be concluded, based on these experimental observations, that the cylinder turbulence response is approximately bracketed by U and $U^{2.2}$. It is difficult to explain this significant experimental discrepancy, except to say that the turbulent cylinder response is dependent on both the array geometry and the cylinder position, and may be dependent on Reynolds number (flow velocity).

As a design guideline, the approach proposed by Pettigrew and Gorman, [64], has the advantage of being simpler. Dimensional inconsistency can be eliminated by introducing the power spectral density function of the random force field, $S(f)$, in the form proposed by Blevins, equation (2.10), as outlined in the theoretical study on turbulence buffeting by Lever and Rzentkowski, [50].

2.3 Fluidelastic instability and turbulence buffeting interaction

Extensive research on fluidelastic instability and turbulence buffeting in cylinder arrays, subjected to fluid cross-flow, has also attempted to identify the interaction effect between both excitation mechanisms. This has been a subject of major experimental controversy, particularly in the practical estimation of stability boundary. All of the early studies, [70-72], showed that turbulence may increase or decrease the critical flow velocity for fluidelastic instability, depending on turbulence characteristics which was stimulated by generators upstream of the tested arrays. To resolve this dilemma, Price *et al.*, [68,69], recently performed a detailed experimental investigation and found that the presence of turbulence generators has little or no effect on the onset of fluidelastic instability. The authors concluded that the interstitial flow characteristics, beyond the first few rows, are governed by the array itself, independent of upstream conditions. Evidently, this significantly hinders experimental

investigations of the problem. Thus, to the author's knowledge, no experimental evidence exists regarding the actual coupling (true interaction mechanism) between turbulence and fluidelastic instability in cylinder arrays and an alternative method of stimulating turbulence characteristics within an array is needed.

The apparent influence of turbulence on fluidelastic instability (interpretation of response curves) was examined theoretically by Lever and Rzentkowski, [50]. Since their study was based on a linearized analysis, the two mechanisms superimpose and the actual effect of the interaction is suppressed. Nevertheless, it showed that increasing turbulence reduced the apparent stability boundary based on amplitude response curves; the size of the reduction depended on the practical threshold definition used. This, to a certain extent, explains the contradictory results from early experimental studies of this problem, [70-72].

Chapter 3

Fundamental concept of marine riser stability

The concept of dynamic stability is extremely important in wide variety of engineering applications. Unfortunately, in the majority of practical cases, there is no universal definition which can globally described the stability of the system at hand. The state of motion is rather complex and it may be stable in one respect and unstable in another. Therefore, the question of instability should be investigated from various points of view. However, the system under consideration and not its practical applications must dictate the choice of definition. Consequently, recognizing the nature of the system is the most important step to adopt the appropriate definition of stability.

Therefore, this chapter first defines the marine riser as a physical system and then discusses various aspects of its stability using the standard definitions of Lyapunov.

3.1 Marine riser as a physical system

The multi-tube production riser, exposed to environmental load, is shown schematically in Figure 1.2. As pointed out in the Introduction, two types of oscillations may be observed: (i) a rigid body motion due to wave cyclic load and (ii) relative motions between the pipes in a cluster due to hydroelastic excitation (turbulence buffeting, Strouhal periodicity and fluidelastic instability). However, it is very in-

structive at this point to consider some classifications based strictly on the theory of vibration. Depending on the source of excitation and its physical properties, the riser response may be categorized as:

- forced stochastic
- periodic: forced and self-excited
- self-excited: decoupled and coupled.

The marine riser "rigid body" response due to wave load, depending on its representation, would be either stochastic or periodic (no self-excited "rigid body" oscillations). Relative pipe motions would be stochastic, periodic and self-excited. Turbulence buffeting would give rise to a forced stochastic response. Strouhal periodicity would represent a periodic process, either self-excited (inside the "lock-in" region) or forced (otherwise). Fluidelastic instability would generate self-excited oscillations, either decoupled (a rigid cluster - single degree-of-freedom representation) or coupled (a flexible cluster - multi degree-of-freedom representation) when relative pipe motions affect the flow characteristics. All of these oscillations cannot exist in their pure form, since the riser response is very complex due to the interaction of different excitation mechanisms. Thus, the nature of this system may be exactly represented only by a complex self-excited oscillator subjected to periodic and stochastic disturbances. Thus, in a more general context, the marine riser must be considered as a non-conservative and non-autonomous system. Non-conservative; since the riser may have an unlimited energy source in the form of fluid cross-flow (thus, the fluid force are not derivable as a gradient of a total energy function). Non-autonomous; since the riser response is directly time dependent due to waves and turbulence. Moreover, the marine riser subjected to fluid flow, as a self-excited oscillator, represents a non-linear system. Therefore, the stability definition must consider the non-linear effects - the existence of limit cycle oscillations.

3.2 Fundamental concept of stability

A unified view of the stability of motion may be given by Lyapunov's definitions, [73], which stipulate that a state is stable whenever in the motion, following a sufficiently small initial disturbance, in terms of initial displacements and velocities, the displacements and velocities remain as small as desired for all positive time (e.g. when a system is disturbed from an equilibrium state, transient oscillations decay with time). Since this concept of stability is very important for subsequent development of present work, it will be treated in detail based mainly on the Lyapunov's definitions presented by Andjelic, [55].

3.2.1 Lyapunov's definitions

Consider a non-autonomous system described by a set of first order differential equations, derivable in the solution space. This set of equations may be expressed in vector notation as:

$$\dot{\vec{x}} = \vec{f}(\vec{x}, t) \tag{3.1}$$

where $\vec{x} = (x_1, x_2, ..., x_n)^T$, $\vec{f} = (f_1, f_2, ..., f_n)^T$ and $\dot{\vec{x}} \stackrel{\text{def}}{=} \frac{d\vec{x}}{dt}$. The initial conditions and the characteristic solutions are given by $\vec{x_0} = \vec{x}(\vec{x_0}, t_0; t_0)$ and $\vec{x} = \vec{x}(\vec{x_0}, t_0; t)$, respectively.

<u>Definition 3.1:</u>

The particular solution $\vec{x}(\vec{a}, t_0; t)$ is <u>stable</u> if it is possible to find a positive $\bar{\delta}(\bar{\epsilon}, t_0)$ for any sufficiently small $\bar{\epsilon}>0$ such that

$$| \vec{x_0} - \vec{a} | < \bar{\delta}(\bar{\epsilon}, t_0) \Rightarrow | \vec{x}(\vec{x_0}, t_0; t) - \vec{x}(\vec{a}, t_0; t) | < \bar{\epsilon} \tag{3.2}$$

for all positive time, $t \geq t_0$. Otherwise the particular solution $\vec{x}(\vec{a}, t_0; t)$ is <u>unstable</u>. The particular solution $\vec{x}(\vec{a}, t_0; t)$ is said to be <u>asymptotically stable</u> if it is stable

and, in addition, one has:

$$\lim_{t\to\infty} \mid \vec{x}(\vec{x_0}, t_0; t) - \vec{x}(\vec{a}, t_0; t) \mid = 0. \tag{3.3}$$

Figure 3.1 displays graphically Lyapunov's concept of stability; $\vec{x}(\vec{x_0}, t_0; t)$ is the perturbed motion and $\vec{x}(\vec{a}, t_0; t)$ is the equilibrium state of the motion whose stability is being investigated. The motion space consists of the phase plain $(\vec{x}, \dot{\vec{x}})$ and time, t, as the independent coordinate.

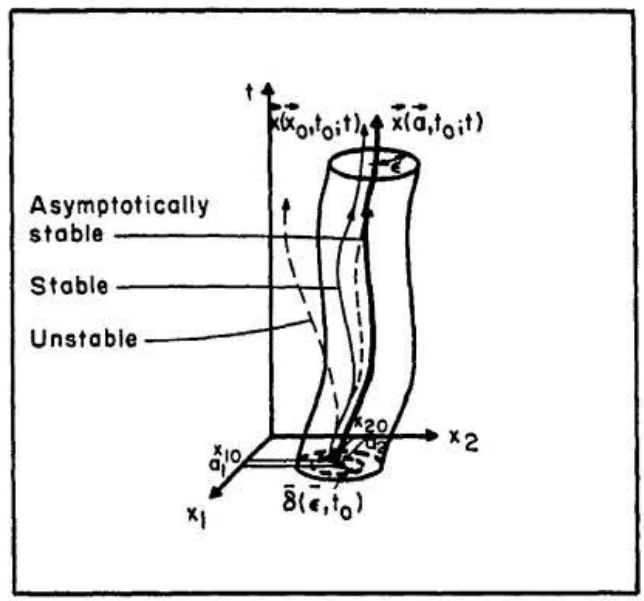

Figure 3.1: Solution vector in motion-domain.

If the particular solution is stable or asymptotically stable, the equilibrium state, without loss of generality, may be taken to be trivial. Referring to Definition 3.1, this assumption requires a transformation of coordinates in the following form:

$$\vec{w} = \vec{x} - \vec{x}(\vec{a}, t_0; t). \tag{3.4}$$

Thus, the differential equation (3.1) becomes:

$$\dot{\vec{w}} = \vec{g}(\vec{w}, t). \tag{3.5}$$

The trivial equilibrium solution of this equation, $\vec{w} = \vec{0}$ (that is, $\vec{g}(\vec{0}, t) = \vec{0}$) is now equivalent to the particular solution of equation (3.1), $\vec{x}(\vec{a}, t_0; t)$. Figure 3.2 defines the concept of stability of a non-atonomous system in transformed coordinates.

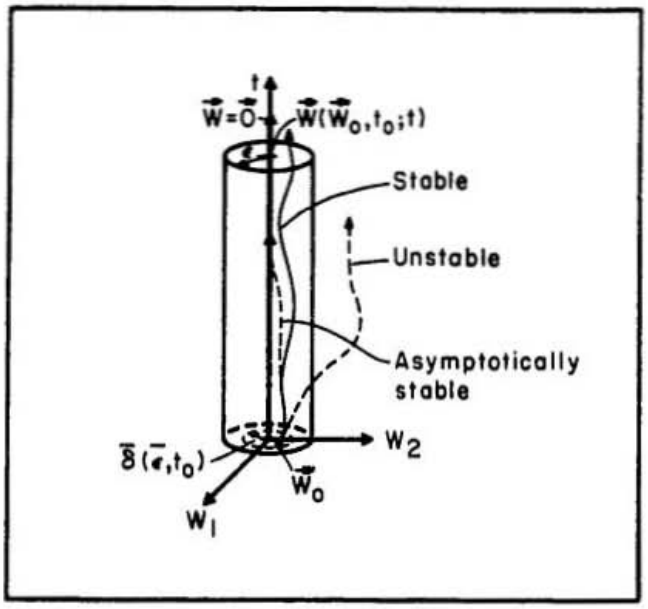

Figure 3.2: Solution vector in transformed motion-domain.

Definition 3.2:

The trivial equilibrium state, $\vec{w}(\vec{w}_0, t_0, t) = \vec{0}$, is stable, if at any time, t_0, it is possible to find a positive $\bar{\delta}(\bar{\epsilon}, t_0)$ for any sufficiently small $\bar{\epsilon}>0$ such that following the initial disturbance, $\vec{w}_0 = \vec{w}(\vec{w}_0, t_0; t_0)$,

$$| \vec{w}_0 | < \bar{\delta}(\bar{\epsilon}, t_0) \tag{3.6}$$

only one perturbed state of motion exists, $\vec{w}(\vec{w}_0, t_0; t)$, and the inequality:

$$| \vec{w}(\vec{w}_0, t_0; t) | < \bar{\epsilon} \tag{3.7}$$

is satisfied for all positive time, $t \geq t_0$. Otherwise the state, $\vec{w}(\vec{w}_0, t_0; t)$, is unstable. The state, $\vec{w}(\vec{w}_0, t_0; t)$, is said to be asymptotically stable if it is stable and, in addition, one has:

$$\lim_{t \to \infty} | \vec{w}(\vec{w}_0, t_0; t) | = 0. \tag{3.8}$$

In other words, the equilibrium state represented by the origin of the motion space, $\vec{w}(\vec{w_0}, t_0, t) = \vec{0}$, is stable if the pertubed state of motion, $\vec{w}(\vec{w_0}, t_0; t)$, remains within a cylinder of arbitrarily small radius, $\bar{\epsilon}$, provided that, following the initial disturbance, the vector $\vec{w_0} = \vec{w}(\vec{w_0}, t_0; t_0)$ is within a circle of sufficiently small radius, $\bar{\delta}(\bar{\epsilon}, t_0)$.

3.2.2 Non-linear effects

It is inferred from equation (3.1) that Lyapunov's definition of stability can be applied to linear and non-linear systems, although, in the latter case, it is related to local properties. This section outlines the resulting limitations, considering a particularly simple non-linear oscillator, whose equation of motion is given by:

$$\ddot{x} + c_n\dot{x} + k_n x + D(x^2 + \dot{x}^2)\dot{x} = F_{St}(t) \tag{3.9}$$

where x is the displacement and c_n and k_n denote the net damping and stiffness coefficients, respectively. These coefficients can, in general, be expressed as a function of the control parameter, Λ, which contains positive (structural) and negative (e.g. flow-induced) contributions. D is a non-linear operator (e.g. flow-induced, as the control parameter) and $F_{St}(t)$ represents stochastic forcing.

Autonomous system

First, consider an autonomous self-excited oscillator, [74]. In this system, the independent variable t does not enter explicitly, thus $F_{St}(t) = 0$ (its state of motion can be represented on a phase plane). When $D = 0$, the system becomes a damped linear oscillator with a characteristic equation given by:

$$\lambda^2 + c_n\lambda + k_n = 0. \tag{3.10}$$

Oscillatory motion exists only if the discriminant of the characteristic equation is negative, $\Delta < 0$. This condition yields a complex conjugate pair of roots which

define the state of motion on the phase plane; either a stable focus, neutral centre or unstable focus if the pair acquire, respectively, either a negative, zero or positive real part. Consequently, depending on the control parameter, Λ (e.g. flow velocity), which governs local properties, the system is either asymptotically stable ($\Lambda < \Lambda_C$), stable ($\Lambda = \Lambda_C$) or unstable ($\Lambda > \Lambda_C$), as shown in Figure 3.3a (solid and dashed lines denote stable and unstable equilibrium states, respectively). Since only one state of motion exists on the phase plane for a given Λ, Definition 3.2 may be considered as a global definition of dynamic stability.

When $D \neq 0$, the stability analysis must consider a dynamic bifurcation problem. It can be shown, [74], that the bifurcation formula for equation (3.9) is given by:

$$Da^3 + c_n a = 0 \tag{3.11}$$

where a is an oscillation amplitude. In this case, the response curve (defined by a and Λ) has two branches: $a = 0$ (trivial equilibrium state) and $a^2 = -\frac{c_n}{D}$ (limit cycle). These branches intersect each other at a point of bifurcation, $c_n = 0$ ($\Lambda = \Lambda_C$); stable for $D > 0$ and unstable for $D < 0$. The bifurcations are of the Hopf-type since they are symmetric and dynamic.

The stable bifurcation shows up on the phase plane as a stable focus for $\Lambda < \Lambda_C$ and as an unstable focus and a stable limit cycle for $\Lambda > \Lambda_C$ (see Figure 3.3(b)). Thus, the system is asymptotically stable and stable, respectively. Although in the latter case the stability may be only locally defined, since the size of an unstable domain increases with Λ from zero at Λ_C. It follows that this system is globally stable only if is asymptotically stable, $\Lambda < \Lambda_C$. At this point, it is very instructive to introduce the concept of degree of stability by defining the size of perturbation needed to trigger instability, [76]. Evidently, the degree of stability is infinite for $\Lambda < \Lambda_C$ for both linear and non-linear systems. Therefore, the linearized stability analysis may only quantitatively differ from the non-linear one.

The unstable bifurcation is characterized on the phase plane by a stable focus

and an unstable limit cycle for $\Lambda < \Lambda_C$, and by an unstable focus for $\Lambda > \Lambda_C$ (see Figure 3.3(c)). Thus, the system is globally unstable, although may be considered as locally stable for $\Lambda < \Lambda_C$ due to the existence of a stable domain which decreases with Λ to zero at Λ_C. It follows that this system has only a finite degree of stability in this region and this becomes infinite if the system is linearized, leading to a qualitative discrepancy in the interpretation of the state of motion.

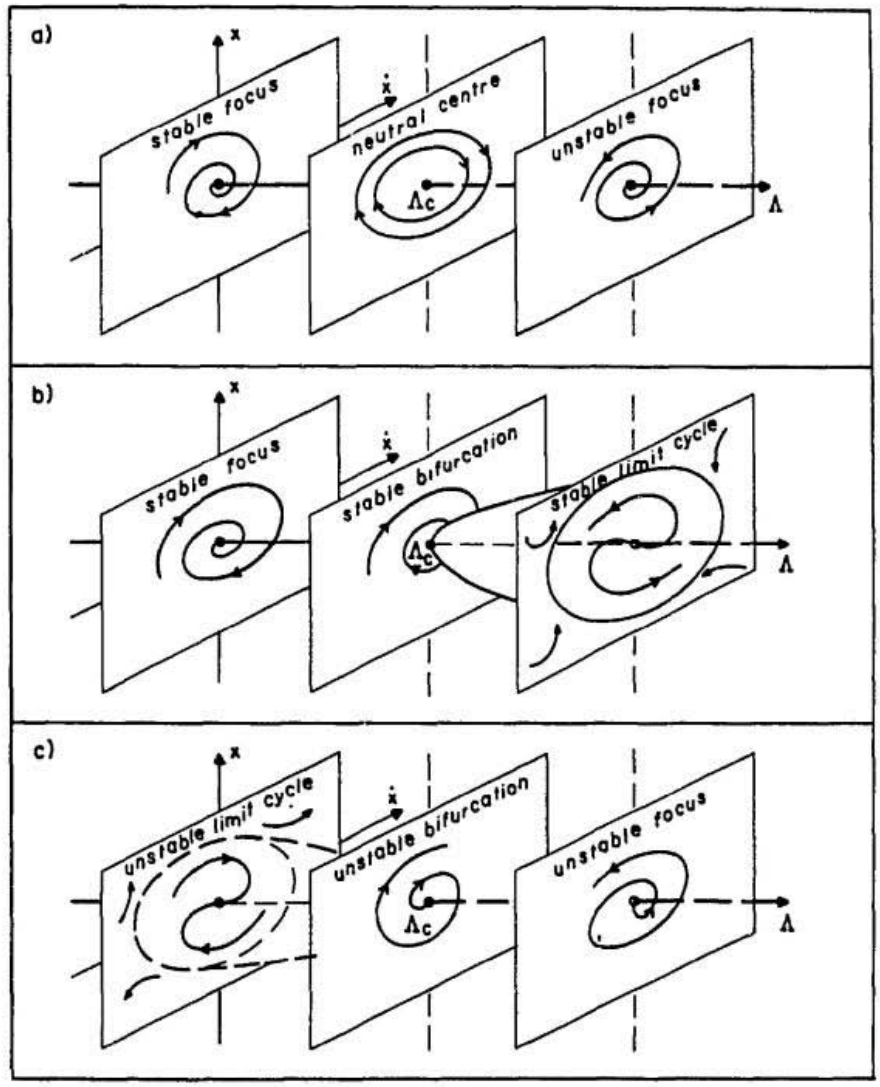

Figure 3.3: Posssible states of motion of a self-excited autonomous oscillator; (a) linear, (b) stable bifurcation, (c) unstable bifurcation.

Non-autonomous system

The motion of a non-autonomous oscillator is described by equation (3.9) in its full form, e.g. $F_{St}(t) \neq 0$. Note that the stability of a damped linear oscillator ($D = 0$) is not affected by stochastic forcing and is given by the characterisitic equation (3.10). Its non-linear effect, however, cannot be treated analytically. This gives motivation to a heuristic study; superposition of linear forced oscillations with non-linear self-excited limit cycles of the autonomous system, [74]. Thus, their coupling is conceptually ignored.

Figure 3.4(a) and Figure 3.4(b) show schematically the separate linear combined oscillations and the self-excited limit cycles for a stable and an unstable bifurcation, respectively. The linear oscillations to combined excitation are exactly defined also *via* superposition; their amplitude rises asymptotically to infinity as the net damping, in equation (3.9), tends to zero for the critical value of the control parameter, $\Lambda = \Lambda_C$. Because coupling is ignored, the self-excited limit cycles are not affected by the forcing term, $F_{St}(t)$. However, the large amplitude linear oscillations clearly interact with the unstable limit cycle (Figure 3.4(b)), modifying the state of stability. This indicates that, even without non-linear coupling between the mechanisms, the system may lose stability for $\Lambda < \Lambda_C$ if the forced linear oscillations exceed the unstable limit cycle. Thus, the critical control parameter for a non-autonomous self-excited oscillator, Λ'_C, may be defined by the intersection of the linear combined response surface with the unstable limit cycle.

This analytical description of possible states of motions and their stabilities of a forced self-excited non-linear oscillator leads to the final conclusion that only asymptotic stability, or infinite degree of stability, defined by non-linear a. can globally guarantee stability of the system.

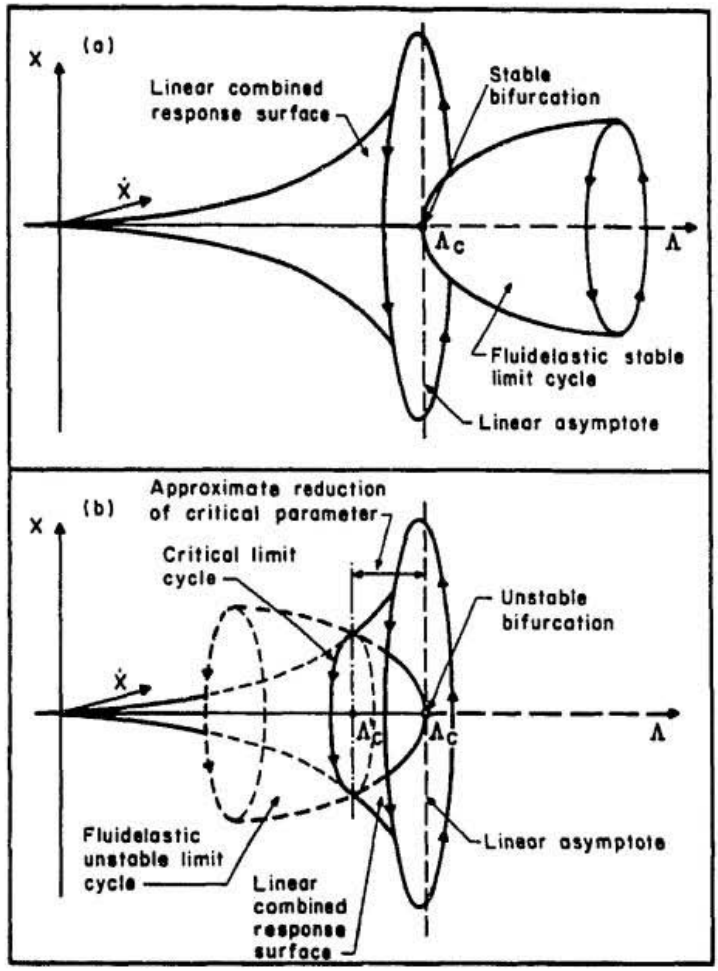

Figure 3.4: Possible states of motion of a self-excited non-autonomous oscillator (superposition of linear forced oscillations with non-linear autonomous limit cycles); (a) stable bifurcation, (b) unstable bifurcation.

3.3 Stability of marine riser

A direct analogy between the dynamic system, presented in Figure 3.2, and the marine riser may be drawn by letting the trivial equilibrium state, $\vec{w}(\vec{w}_0, t_0; t) = \vec{0}$, represent a rigid cluster configuration due to wave load (its stability was assumed by the condition of transformation, equation (3.4)), and letting the perturbed state, $\vec{w}(\vec{w}_0, t_0; t)$, represent relative pipe motions due to current (hydroelastic oscillations: turbulence buffeting, Strouhal periodicity and fluidelastic instability). It follows that

the flexible riser is stable if relative motion between the pipes in a cluster remains as small as desired (within $\bar{\epsilon}$-limit). Since this study is concerned with fluidelastic instability and turbulence buffeting, the latter dictates the size of initial disturbance, $\bar{\delta}(\bar{\epsilon}, t_0)$, and the $\bar{\epsilon}$-limit. Thus, a knowledge of the flow turbulence characteristics is essential for stability analysis.

3.3.1 Response curve

The state of motion, illustrated in Figure 3.2, may be greatly simplified by averaging the perturbed motion, $\vec{w}(\vec{w_0}, t_0; t)$, over an infinitely long time. Thus, its Peak- or RMS-amplitude becomes a function of initial disturbance only which, in turn, depends on local properties of the system defined by the control parameter, Λ. Evidently, practical application requires a finite time and this is usually taken to be 10 *min*. In this way, the initial state of motion creates the response curve and is expressed much as in an experimental investigation; the response amplitude (displacement, velocity, acceleration or strain) *versus* control parameter (fluid load) usually referred to as the reduced flow velocity. Note that based on experimental response curves, two types of post-stable oscillations of pipe arrays have been identified: without and with hysteresis. By analogy with a third order non-linear oscillator, these two cases correspond to stable and unstable bifurcations, respectively.

Practical stability boundary

The stable and unstable bifurcation may also be referred to as soft- and hard-excited system ,[76]. These concepts, indicating the strength of initial disturbance needed to induce instability, are very important for the practical utilization of Lyapunov's definitions. Below, they are applied to ideal (fluidelastic excitation only) and real (combined fluidelastic and turbulence excitation) response curves of pipe arrays in

fluid cross-flow.

The response curves may be idealized by separating turbulence from fluidelastic excitation. Thus, an average response due to turbulence becomes an equilibrium state for fluidelastic instability. To allow a direct analogy with a third order non-linear oscillator, the effect of turbulence buffeting may be removed by subtracting it from overall response (in this way, the equilibrium state for fluidelastic instability becomes trivial). Figures 3.5(a1) and 3.5(b1) show these idealized response curves, while Figures 3.5(a2) and 3.5(b2) show the corresponding dynamic bifurcations for a third order non-linear oscillator. The stable bifurcation (Figures 3.5(a1) and 3.5(a2)) becomes unstable for an infinitesimal (*de nomni* soft) disturbance whenever $\Lambda > \Lambda_C$. The non-linear response is limited by the stable limit cycle whose size increases with Λ from zero at Λ_C. Since the rate of increase may vary, depending on system parameters, the point of dynamic bifurcation, Λ_C, defines the practical stability threshold. Here, a linear model is capable of predicting the stability boundary of the non-linear system but cannot predict its finite post-stable oscillations. The unstable bifurcation (Figures 3.5(b1) and 3.5(b2)) may display hysteresis behaviour; the response jumps at $\Lambda = \Lambda_C$ during the increase of the control parameter and at $\Lambda = \Lambda_H$ during its decrease (the coalescence of limit cycles at Λ_H, secondary point of bifurcation, cannot be displayed by a simple third-order oscillator, unless Λ is not amplitude-dependent). Inside the hysteresis region, the system has a finite domain of attraction bounded by the unstable limit cycle, which is represented by the dashed line in Figure 3.5(b1). Therefore, unlike the soft-excited system, only a finite (*de nomni* hard) disturbance carrying the linearly stable system beyond this cycle would cause instability. In the absence of detailed information on the expected size of these disturbances in real situations, the lower limit of the hysteresis region, Λ_H, must be treated as the practical stability boundary for the cylinder array (it guarantees asymptotic stability). Therefore, the application of a linear theory (which predicts

only Λ_C) may be unconservative, especially when the hysteresis region is relatively broad.

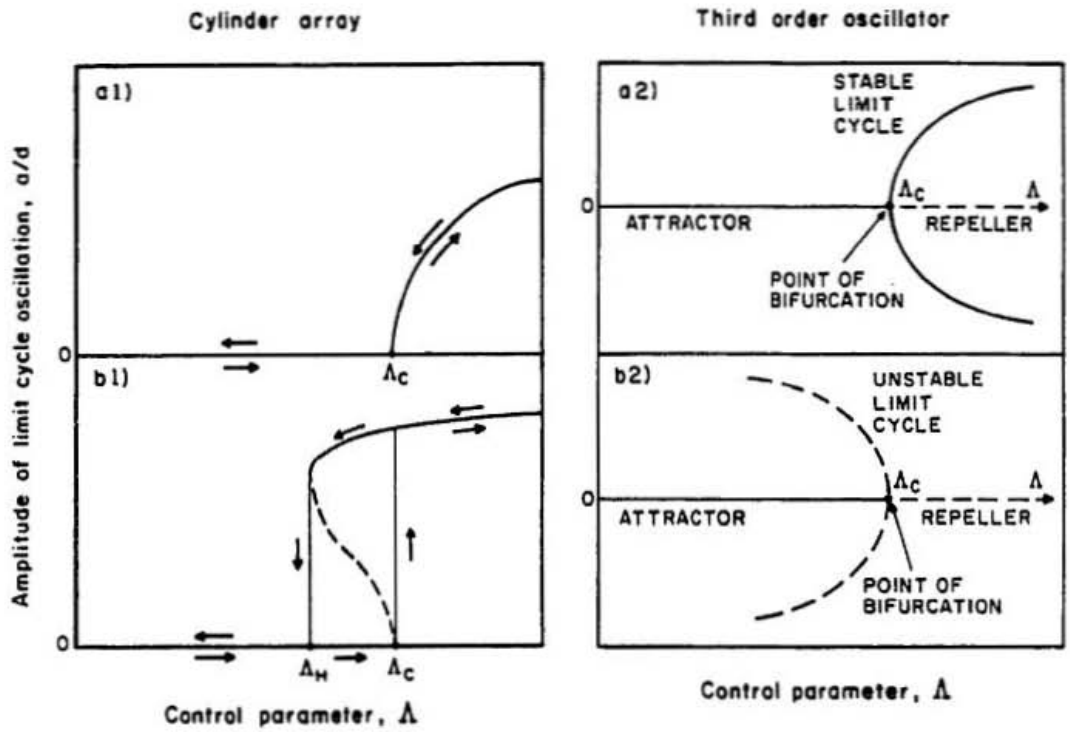

Figure 3.5: Idealized representation of possible fluidelastic oscillations in cylinder arrays and dynamic bifurcations of a third order oscillator; (a) soft- and (b) hard-excited systems.

The critical control parameter, either Λ_C or Λ_H, may be clearly obtained from idealized response curves. In practice, however, it may be difficult to determine, especially, if turbulence strongly contributes to sub-stable oscillations and its effect cannot be easily separated out of experimental measurements. Therefore, the common approach is to determine Λ_C from experimental response curves generated by fluidelastic interaction with turbulence excitation. In this way, the actual interaction mechanism is absorbed by standard threshold definitions (which are purely empirical). Consequently, the coupled system and its stability remain phenomenologically not defined.

The possible nature of fluidelastic interaction with turbulence excitation may be explored by drawing an analogy between the dynamic response of pipe arrays and the buckling (or static instability) of corresponding static systems, where two distinct bifurcations (stable and unstable) are also recognized. Additionally, severe imperfection sensitivities, which can round-off or even destroy the perfect bifurcation, have been observed, [74]. As we shall see, some insight may be gained into the influence of turbulence on fluidelastic instability by treating turbulence response as an imperfection parameter in a coupled system.

The stable bifurcation (soft-excited system) and its imperfection sensitivity may be discussed by considering load-deflection curves for a compressed Euler column, [74], as presented in Figure 3.6. If the column is axially loaded ($\epsilon = 0$, perfect system), the system remains in the trivial equilibrium state as the load slowly increases from zero. At critical load, $P_S = P_{SC}$, the column undergoes a static instability, and for further increases in P_S, its deflection, v, follows a stable equilibrium path. A direct analogy between this load-deflection curve and the stable Hopf bifurcation of the fluidelastic instability may be drawn by allowing the load, P_S, to represent the control parameter, Λ, and the static deflection, v, to represent the amplitude of the limit cycle oscillations, a. However, if an offset of the load is introduced, resulting in an initial out-of-straightness of the column (imperfection parameter ϵ), the column experiences small stable deflections as the load slowly increases from zero, tending asymptotically to the post-stable equilibrium path. By drawing the analogy further, we can allow the imperfection parameter to represent the strength of the turbulence field. Thus, the load-deflection curve becomes the response curve of the pipe array under combined excitation. The imperfection sensitivity diagram indicates that the actual value of Λ_C, resulted from fluidelastic excitation only, may be delayed by turbulence. However, for a gradual increase in the control parameter from zero, the response curve tends asymptotically to the stable limit cycle and

delays in Λ_C cannot be realized. However, depending on the threshold definition used, such a response curve might be assigned a practical threshold below Λ_C, and this value would reduce with increasing turbulence (ϵ).

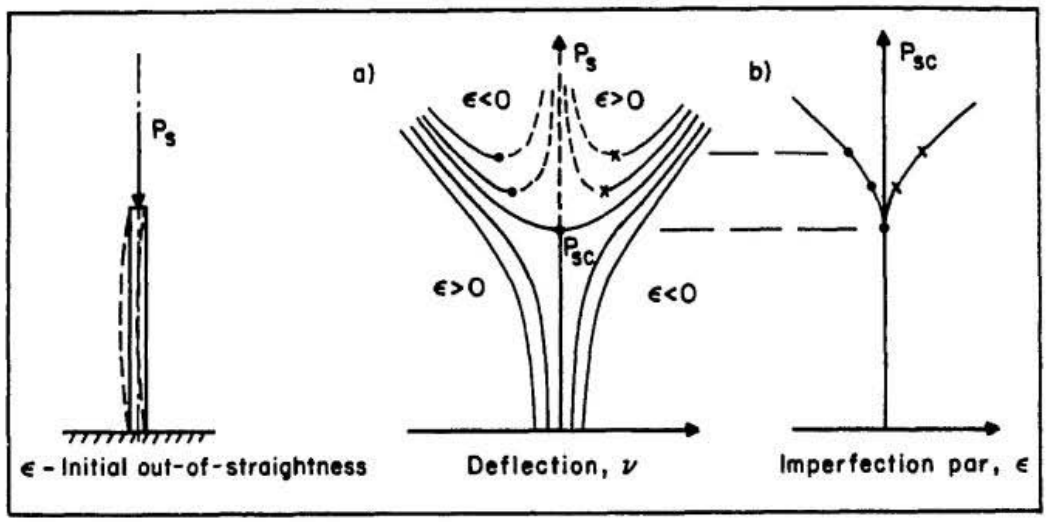

Figure 3.6: A compresed Euler column; (a) load-deflection curve, (b) imperfection sensitivity.

Similarly, the unstable bifurcation (hard-excited system) and its imperfection sensitivity may be discussed by considering load-deflection curves for a deep fixed arch, [74], as shown in Figure 3.7. If the arch is centrally loaded, it represents a perfect system which undergoes a static instability at $P_S = P_{SC}$. However, the system at this point shows non-linear softening and an unstable equilibrium path. Unlike the column discussed above, the arch shows severe imperfection sensitivity, resulting in a reduction in the actual critical load with increasing ϵ. Thus, by analogy with the unstable Hopf bifurcation of a fluidelastic system, turbulence buffeting may reduce the actual fluidelastic stability boundary, Λ_C, due to non-linear coupling of both excitation mechanisms. In this case, prediction of the combined response becomes very important.

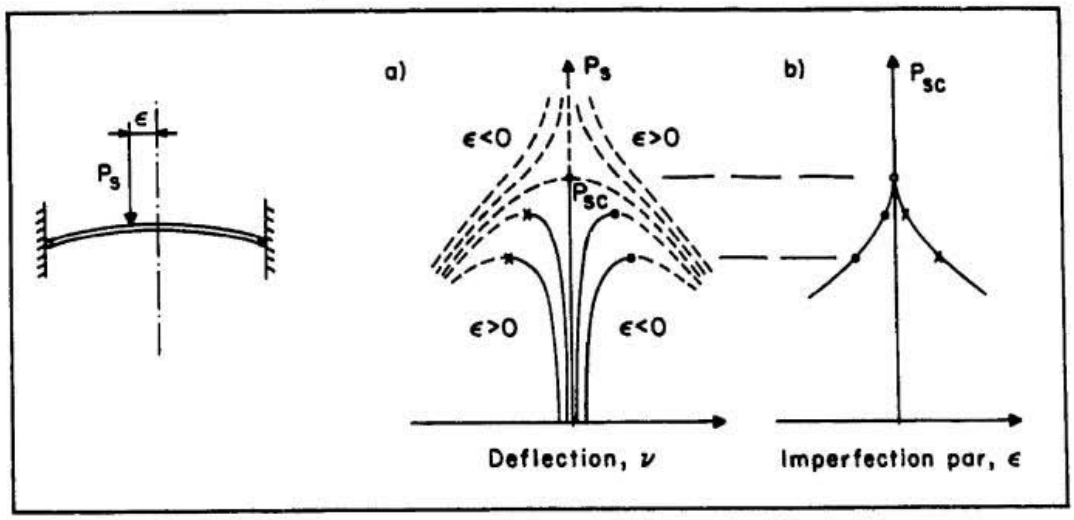

Figure 3.7: A deep fixed arch under load; (a) load-deflection curve, (b) imperfection sensitivity.

Standard stability definitions

It follows, from the above discussion, that the practical determination of the stability of pipe arrays in fluid cross-flow requires a deep understanding of post-stable oscillations and the underlying excitation mechanisms. Otherwise, the experimentally used concept of stability may depend on systems application and not on its physical properties.

Due to a lack of a universal stability definition, different criteria have gained acceptance over the years (summarized graphically in Figure 3.8).

- An abrupt change in slope of the response curve (first defined by Weaver and El-Kashlan, [31]). This is acceptable if the change of slope is very sudden, otherwise it allows only limits of instability, Λ_{C1} and Λ_{C2}, to be specified (see Figure 3.8(a)).

- Intersection of the steepest tangent to the post-stable response curve with the flow velocity (Λ) axis (introduced by Franklin and Soper, [71]). This

underestimates Λ_C, especially if a limit cycle increases very gradually as it may happen in the case of soft-excited oscillations (see Figure 3.8(b)).

- The response curve exceeds a permissible value, typically 1-3 % of pipe diameter (first used by Pettigrew and Gorman, [64]). While this is consistent, it is phenomenologically incorrect (see Figure 3.8(c)).

- intersection of the steepest tangent to the-post stable curve with the response induced by turbulence (recently proposed by Chen, [77]). This gives the exact location of the critical control parameter, Λ_C, in terms of Lyapunov's definition, assuming that the response due to turbulence is known (see Figure 3.8(d)).

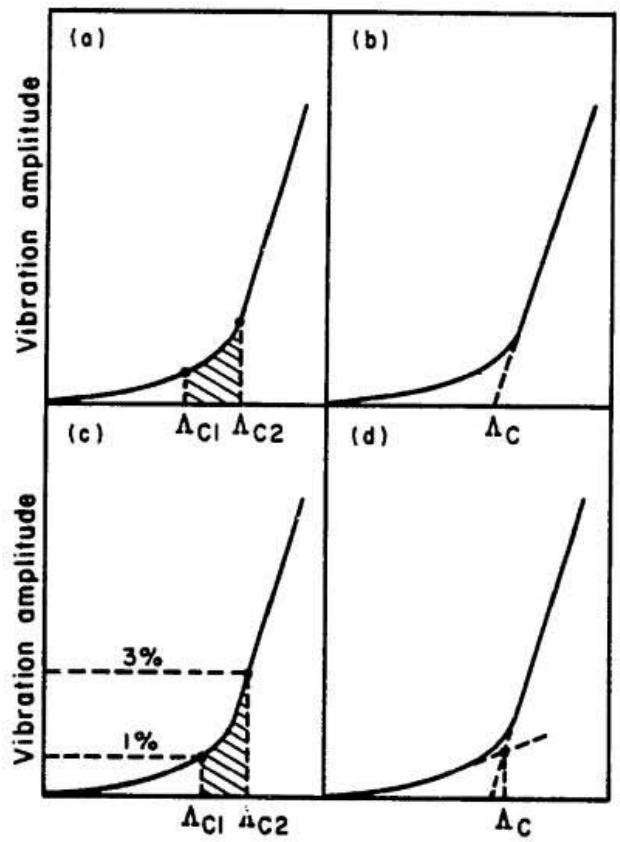

Figure 3.8: Graphic representation of standard threshold definitions; (a) an abrupt change in slope, (b) intersection point of steepest tangent with Λ-axis, (c) amplitude limits, (d) intersection point of steepest tangent with turbulence response.

As a result, the determination of the critical control parameter may be affected, to various degrees, by turbulence, depending on the definition used. This has lead to significant discrepancies in the reporting of experimental data, discussed in References [14,50,55,77], for example. Lever and Rzentkowski, [50], investigated analytically the effect of turbulence on the apparent critical flow velocity of a linearized fluidelastic system. They found that the greater the response due to turbulence the lower the stability point assigned on the basis of the first 3 standard definitions. Even a factor as simple as the plotting scale may affect the results of these methods. Their study suggested that representing the response curve on a logarithmic scale, which apparently reduces the effect of turbulence buffeting, may give more consistent results, [78,79]. However, this method only corrects the size of the problem and does not recognize its nature.

On the basis of this discussion, it follows that the latter criterion of stability (suggested by Chen, [77]) which may be considered as a universal definition in the Lyapunov sense, has the greatest potential for unified presentation of experimental data. The difficulty of this method is in defining the response due to turbulence which, in most practical cases, requires separate measurements. However, turbulence buffeting may be approximated by the tangent to sub-critical curve passing through the origin, assuming that its increasing curvature (as the critical control parameter, Λ_C, is approached) is caused by the fluidelastic excitation which interacts with turbulence. Obviously, this effect becomes increasingly important with the control parameter, Λ. In this way, the presented concept reaches the point of practical application and will be used throughout in this study.

3.3.2 Stability map

The response curve displays the behaviour of the system governed by only one control parameter. However, routine dimensional analysis and energy considerations for

the equation of damped harmonically excited oscillator lead to a Connors-type stability criterion, equation (1.1), as demonstrated by Heinecke, [80]. This equation is expressed in terms of two nondimensional parameters, appearing very commonly in aeroelasticity; the aforementioned reduced flow velocity, $\frac{U}{fd}$, and the mass-damping parameter, $\bar{m}\delta_0$ (where $\bar{m} \stackrel{\text{def}}{=} \frac{m}{\rho d^2}$ denotes the mass parameter and δ_0 is the logarithmic decrement of damping defined in quiescent air). In this way, a response surface may be constructed, [74], and the stability concept becomes three dimensional.

For a pipe array, this surface is folded and may appear as shown in Figure 3.9. When projected on to the control plane (stability map), it forms a cusp. Within the cusp, the system response is a double valued function and either small changes in control parameters or finite disturbance may excite instability (hard-excited system). Indeed, the shape of the cusp defines the size of the hysteresis region as a function of the mass-damping parameter.

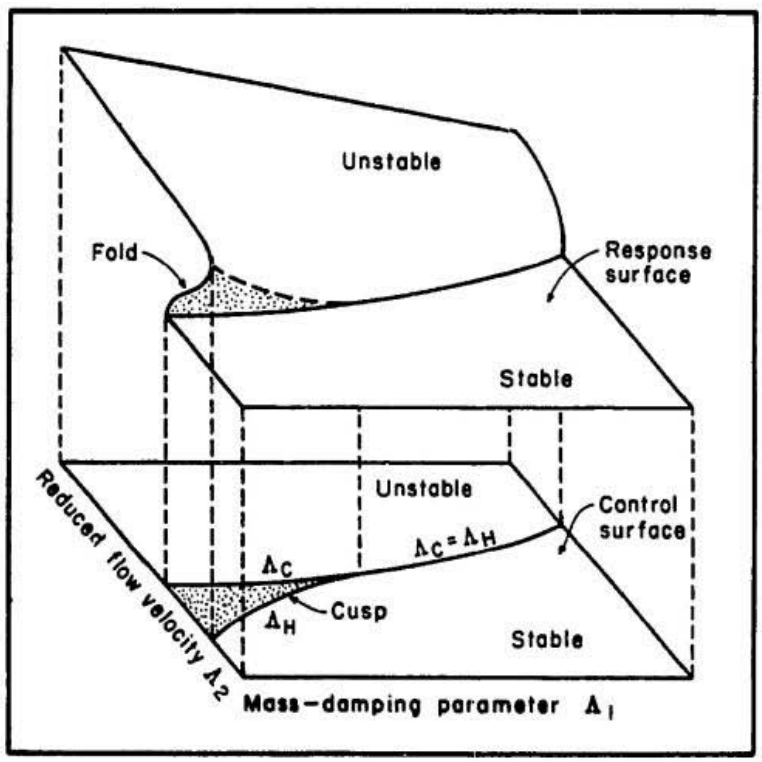

Figure 3.9: Schematic 3-dimensional response of cylinder arrays.

Note that the response surface in Figure 3.9 reflects the experimental observations, discussed earlier, that the hysteresis region disappears at high mass-damping parameters. Clearly, such a response surface may be generated only from a non-linear theory.

Stability maps are commonly used by researchers to summarize experimental results and may serve as a design guideline against flow-induced vibration in pipe arrays (such as the multi-tube marine riser). In this way, Weaver and Fitzpatrick, [16], defined the stability criteria for four standard array configurations shown in functional form in Table 3.1 ($U_{Pr} \stackrel{\text{def}}{=} \frac{U_P}{f_0 d}$). These are based on lower bound curves from most of the experimental data reported in the open literature. The inflection point in the curves for all geometries was taken at the same value of mass-damping parameter, $\bar{m}\delta_0 = 0.3$, for simplicity.

Table 3.1: Experimental stability criteria for four standard array configurations.

Array geometry	$\bar{m}\delta_0$<0.3	$\bar{m}\delta_0$>0.3
Square	$U_{Pr} = 1.4$	$U_{Pr} = 2.5(\bar{m}\delta_0)^{0.48}$
Rotated square	$U_{Pr} = 2.2$	$U_{Pr} = 4.0(\bar{m}\delta_0)^{0.48}$
Normal triangle	$U_{Pr} = 2.$	$U_{Pr} = 3.2(\bar{m}\delta_0)^{0.40}$
Parallel triangle	$U_{Pr} = 1.0$	$U_{Pr} = 4.8(\bar{m}\delta_0)^{0.30}$

Chapter 4

Experimental program

It is now generally believed that the underlying mechanisms responsible for flow-induced instability of pipe arrays in cross-flow are fluid-damping and fluid-stiffness controlled. The first mechanism is the single degree-of-freedom velocity mechanism resulting from negative damping, while the second is the multi degree-of-freedom displacement mechanism resulting from fluid coupling effects, thus requiring relative pipe motion. This hypothesis was established by Chen, [41,42], on the basis of unsteady fluid theory. However, a clearer physical explanation was given by Paidoussis and Price, [81], who, in the framework of quasi-steady fluid theory, showed that there were fundamental similarities between classical galloping and the fluid-damping controlled instability, and between wake-flutter and the fluid-stiffness controlled instability. Both studies suggested that these distinct mechanisms generally coexist, but each is predominant over different ranges of system parameters, [81]; fluid-damping controlled instability over $\bar{m}\delta_0 < 300$ and fluid-stiffness controlled instability over $\bar{m}\delta_0 > 300$ (approximately). However, this conclusion followed from linearized analysis and identified only the mechanisms which initially produce the instability - Hopf bifurcation of trivial equilibrium state. A physical explanation of the various elements of fluid forces, taking part in the generation of limit cycles, was missing.

There are also little data which can shed some light into this problem and may be *a priori* used to establish foundations for non-linear modelling of post-stable

behaviour. The present state of knowledge may be summarized as follows:

- Stable limit cycles exist over the entire range of system parameters; their size decrease with $\bar{m}\delta_0$, as noted in Reference [31,82], for example. The location of the associated points of bifurcation is array and row dependent; generally, the pipe in the third or fourth row yields the lowest critical flow velocity, [82].

- Unstable limit cycles exist only for $\bar{m}\delta_0 < 30$, [21,43,55]. They are responsible for a hysteresis-type behaviour which was observed for a single flexible pipe in the first or second row, [22,54,55], and in a fully flexible array, [23,53,56]; the size and the width of the hysteresis region decreases with $\bar{m}\delta_0$. The effect of array geometry is generally unknown.

Moreover, the work on heat exchangers and the recent model studies on marine risers, [11,61], indicate that the fundamental behaviour of cylinder arrays in liquid and gas flows is phenomenologically very similar. This means that the mechanism of fluidelastic instability is independent of Reynolds number as an effect of fully separated fluid flow. Therefore, by varying independently the two nondimensional parameters, δ_0 and $\bar{m}$, and their product, the experimental results obtained in liquid could be interpreted as the results in gas and *vice versa*.

4.1 Objectives

This experimental study is concerned with the multi-tube marine riser represented by a rectangular array of closely spaced pipes. Two standard array configurations were investigated: parallel triangular and square. The principle motivation for choosing these configurations was to examine the physical behaviour of staggered and in-line arrays (see Figure 1.3). The tested arrays were modelled as infinite in transverse to the flow direction, providing a practical simplification for subsequent theoretical analysis. Thus, only one orientation of the arrays, with respect to the

steady flow direction, was examined.

The major objective of this experimental program was to explore the mechanisms underlying fluidelastic instabilities of pipe arrays in fluid cross-flow with special emphasis on the coexistence of stable and unstable bifurcations (soft- and hard-excited systems). In particular, this study sought to provide usefull insight into the following elements of post-stable oscillations:

- the role of relative pipe motion (fluid coupling)
- the behaviour of a single flexible pipe; two *versus* one degree-of-freedom
- the hysteresis effect
- the excited instability within the hysteresis region
- the velocity- and amplitude-dependant damping

The sequence of tests was designed to gradually eliminate the number of degrees-of-freedom needed to capture the physical essence of an array behaviour in the simplest way possible. Special attention was paid to points of dynamic bifurcation (actual stability threshold), the magnitude of the limit cycle and the width of the hysteresis region (if present). In this way, the foundations for later non-linear modelling were developed *via facti*. These experiments were performed in a wind tunnel, to allow for a clear separation between Strouhal periodicity and fluidelastic instability.

4.2 Facility

4.2.1 Wind tunnel

A newly constructed low speed wind tunnel, which facilitates both atmospheric boundary layer simulation in a main tunnel section and flow-induced vibration studies in an auxiliary flow duct, is located in the Fluids Laboratory at Memorial University. The main tunnel consists of a centrifugal blower with variable angle

inlet vanes driven by a 19 kW motor, a flow conditioning chamber and a 1 m by 20 m roughed floor boundary layer test section. The auxiliary duct facilities consist of a 430 mm by 610 mm test section constructed of plexiglas, several high-loss screens to achieve uniform flow profiles upstream of the tested array, and a flexible coupling to isolate the test section from the main wind tunnel.

4.2.2 Test section

The test section is made of plexiglass plate on all four sides to provide a clear observable testing environment. For ease in installing cylinders and for changing array pattern, the top and bottom plates of the test section are removable. These plates have the same pattern of 10 mm holes, either parallel triangular or square, to allow anchor bolts to fix the cylinders in proper positions. The only difference is in the size of the holes in the bottom plate, at the location of flexible cylinders, which were drilled to a diameter of 35 mm to allow free movement of these cylinders. In order to adjust their damping, the oil-filled cups could be attached to the bottom plate. Additionally, fourteen holes were drilled upstream of the tested array, eight in the side and six in the top plate, so that the hot-wire probe support could be inserted at various positions (Figure 4.1 shows some views of the test section).

In the first stage, experiments were conducted with a 1.375 pitch ratio parallel triangular configuration to permit comparison with the extensive air flow data reported in the literature, [31,82,83]. Since it has been found that only the monitored cylinder, positioned in the third or fourth row, and its immediate neighbours need to be flexible to simulate the behaviour of a fully flexible array, [82], the experimental array consisted of 7 flexible cylinders with the central one in the fourth row. Rigid cylinders and half-cylinders along the side walls were used to complete an, initially, 8 row deep array, as presented in Figure 4.2.

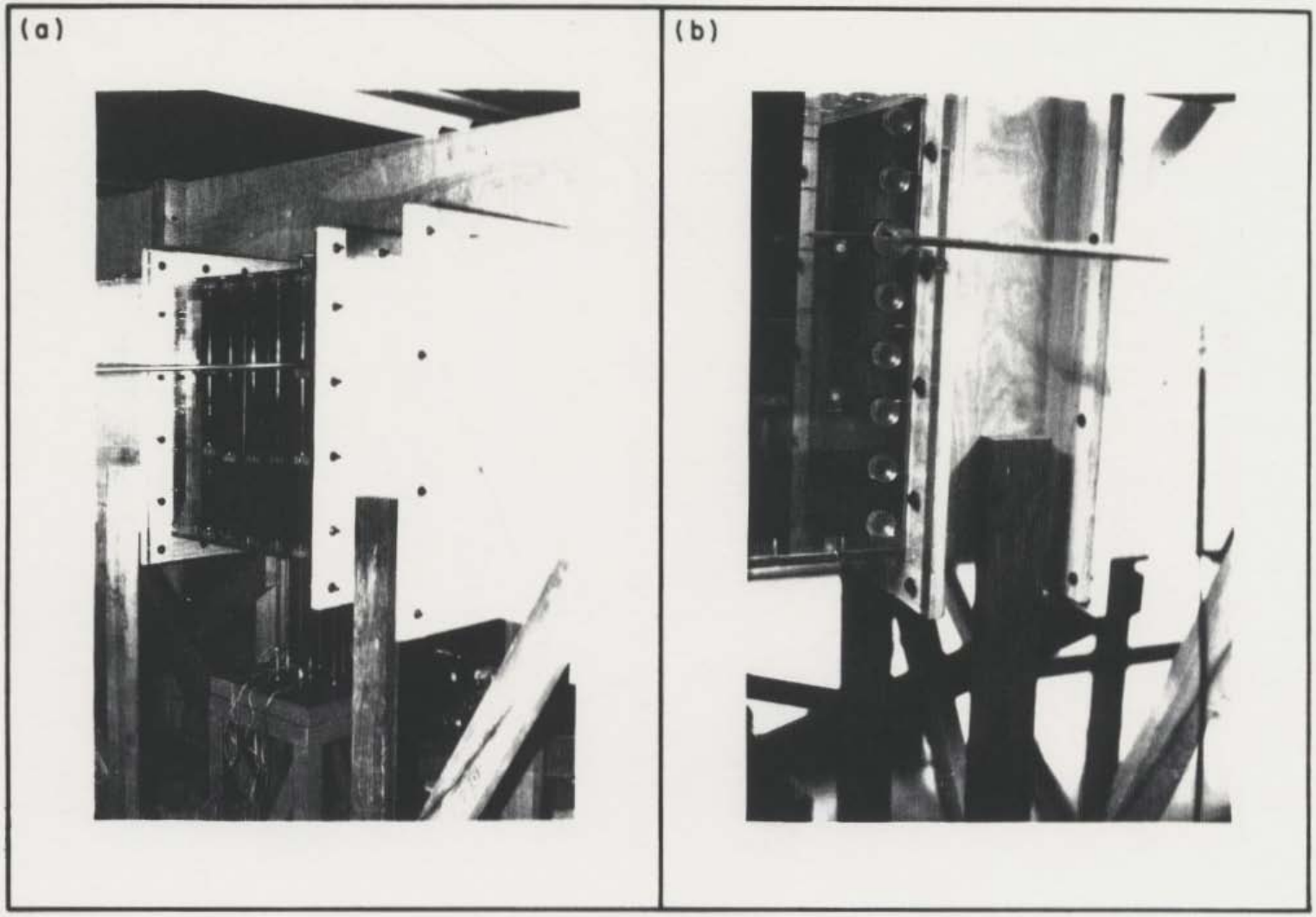

Figure 4.1: Photographs of the test section; (a) an overall view, (b) an inlet and probe location.

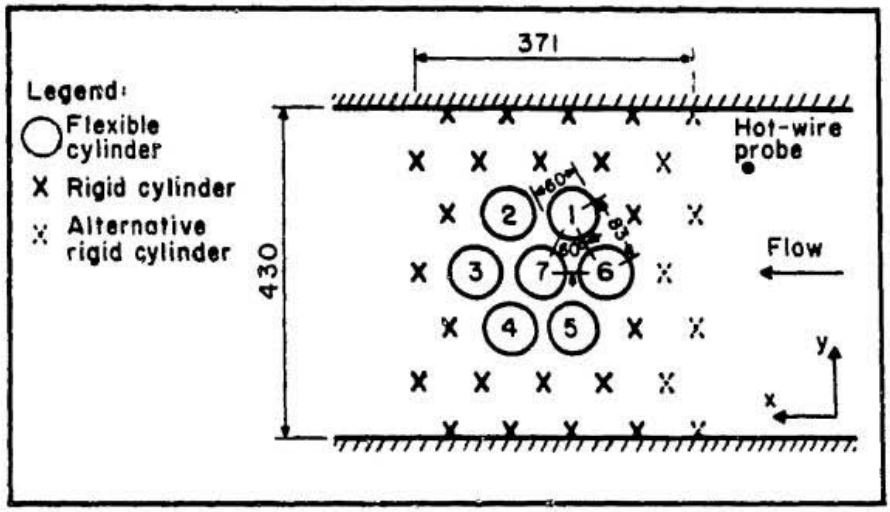

Figure 4.2: A tested parallel triangular array (linear dimensions in *mm*) and cylinders numbering.

In the second stage, the tested array was replaced with a 1.433 square configuration. As with Reference [77,82], a flexible kernel, within a rigid array, was constructed of 9 flexible cylinders, the central one being in the fourth row. Here, the experimental array was initially 6 rows deep (see Figure 4.3).

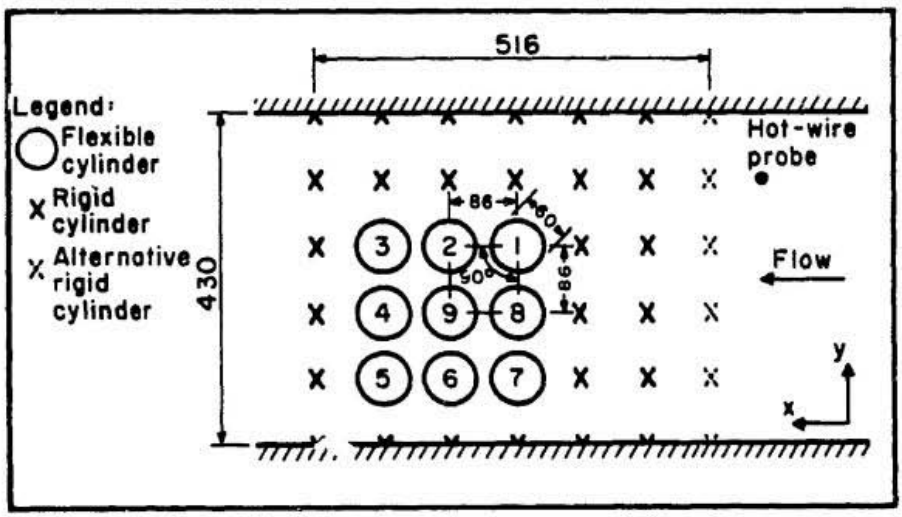

Figure 4.3: A tested square array (linear dimensions in *mm*) and cylinders numbering.

All rigid cylinders and half-cylinders were 610 mm long and made out of 60 mm outside diameter PVC pipe. The rigid cylinders were bolted to both the top and bottom plates, while the half-cylinders were attached to the side plates introduced to simulate flow conditions of the surrounding cylinders. Each flexible cylinder was also 60 mm in an outside diameter but only 600 mm long to provide roughly 5 mm clearance at each end. Each was mounted as a cantilever on a 365 mm long steel rod which in turn was threaded into a steel template (alternatively, a damping paddle, which was free to move within an oil-filled cup, could be attached to the free end of the steel rod). The 50 mm thick template was fixed to a welded steel frame anchored to the floor. This stand was made very stiff, with bending natural frequency in excess of 85 Hz, to minimize mechanical coupling between the cylinders through the base.

Figure 4.4 presents schematically some constructional details of this experimental set-up.

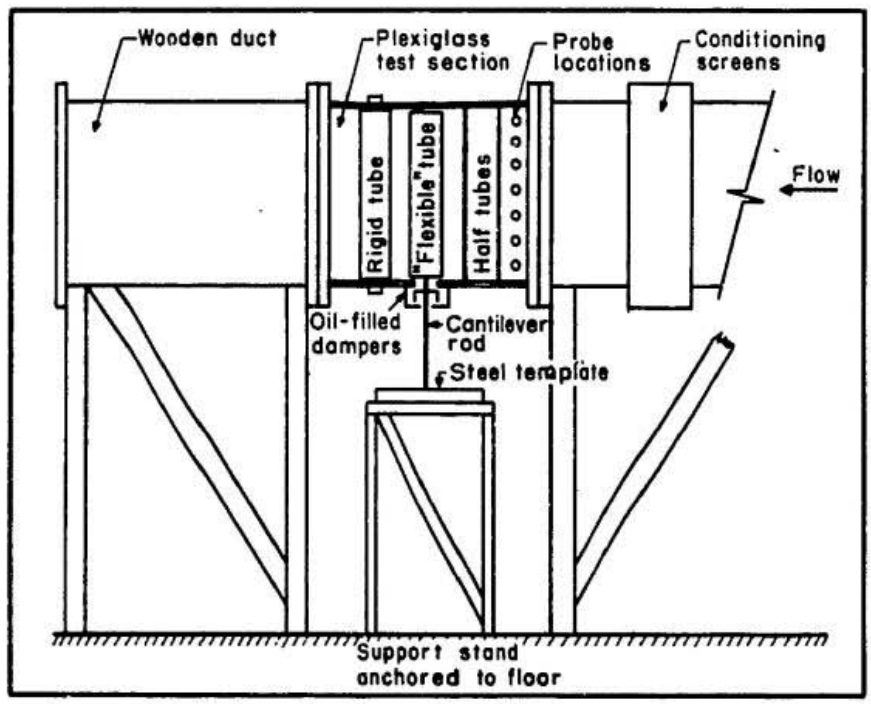

Figure 4.4: Test section layout showing some constructional details.

4.2.3 Flexible cylinder

For simplification of analytical modelling, the flexible cylinder should ideally be a simple spring-dashpot system, such as that shown in Figure 4.5. In this case, it can be seen that only planar motion is allowed which, additionally, is fully correlated along the pipe span. Moreover, the damping and stiffness properties are linear and equal in all directions (later simplified to a single degree-of-freedom system which can vibrate in a transverse-to-flow direction only).

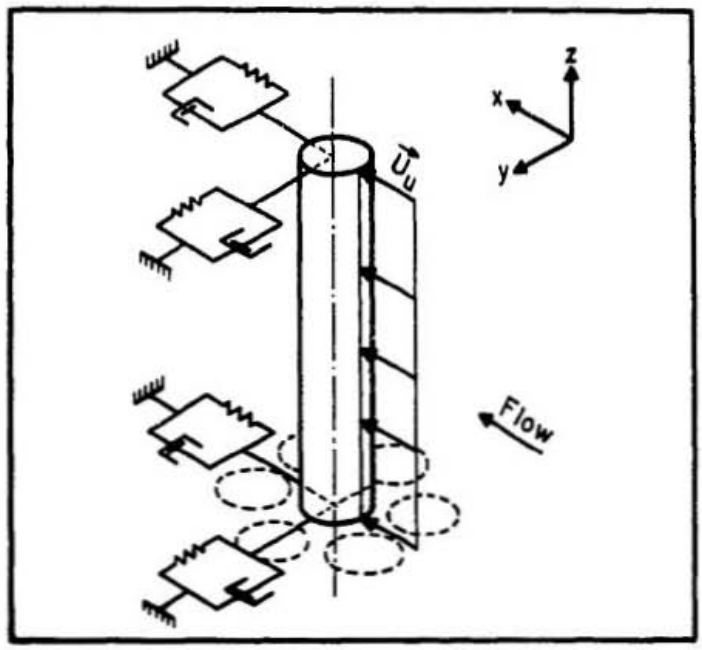

Figure 4.5: An idealized model of a single flexible cylinder in an rigid array.

In practice, it is very difficult and expensive to construct such an ideal system because it generally requires a complex electro-magnetic suspension, such as that described in Reference [55]. The cantilever arrangement, which was implemented in this study, may be considered a reasonable compromise since a routine modal analysis shows that the mode shape effect is almost negligible. However, linear damping requires special precautions to be taken to ensure perfect alignment of the cantilever rod and the cylinder. While this was not always realizable in practice,

the effects of non-linearity and asymmetry in the cylinder behaviour were made as small as possible.

The mass-damping parameter, $\bar{m}\delta_0$, of the flexible cylinder was varied by changing the mass, m, and the damping, δ_0, separately. The cylinder mass was changed by unscrewing it and replacing it with one made of a different material. Three sets of cylinders were used; made from PVC pipe (m=1.04 $\frac{kg}{m}$), steel pipe (m=6.16 $\frac{kg}{m}$) and steel rod covered with PVC pipe (m=12.93 $\frac{kg}{m}$). The cylinder damping could be varied by attaching a paddle to the free end of the cantilever support rod and then by changing the oil level or, alternatively, the oil density in a cup (however, the application of this method was found to be limited for investigation of post-stable oscillations since the oil-damper showed strongly non-linear characteristics). Table 4.1 summarizes the cylinder data for various bundles used throughout this experimental study.

As noted earlier, the cantilever rod, which projected the flexible cylinder into the test section, was 365 mm long. For symmetric stiffness tests, two different rods were used, depending on the cylinder mass: for the low mass PVC pipe case the rod diameter was 9.5 mm while for the higher mass steel pipe and steel rod/PVC cases it was 15 mm. For asymmetric stiffness tests, 30 mm diameter rods with a 20 mm long plate near the base were used to force the flexible cylinder to move in transverse-to-flow direction only (for frequency separation, see Table 4.1). For the low mass case, the plates were 2.5 mm thick and 30 mm wide. For the higher mass cases, they were 5.0 mm by 30 mm. Figure 4.6 shows schematics of this cantilever supporting rod.

Table 4.1: A summary of experimental data for tested arrays (parallel triangular and square).

Array geometry	Cylinder material	Set #	$\bar{m}$ (-)	δ_0 (-)	$\bar{m}\delta_0$ (-)	f_x (Hz)	f_y (Hz)	$\frac{f_x}{f_y}$ (-)	Remarks
Parallel triangular	PVC pipe	1	237	0.009 ± 10%	2.13 ± 10%	5.10 ± 1%	5.10 ± 1%	1.0	Preliminary tests
	PVC pipe	2	250	0.009 ± 10%	2.25 ± 10%	5.00 ± 1%	5.00 ± 1%	1.0	Varied damping
		3	250	0.020 ± 10%	5.00 ± 10%	4.95 ± 1%	4.95 ± 1%	1.0	
		4	250	0.030 ± 10%	7.50 ± 10%	4.90 ± 1%	4.90 ± 1%	1.0	
	PVC pipe	5	237	0.008 ± 10%	1.90 ± 10%	5.10 ± 1%	5.10 ± 1%	1.0	Varied number of degree-of-freedom (varied mass)
			237	0.010 ± 1%	2.37 ± 1%	61.5	5.15	11.9	
	Steel pipe	6	1401	0.008 ± 10%	11.2 ± 10%	5.70 ± 2%	5.70 ± 2%	1.0	
			1401	0.006 ± 1%	8.41 ± 1%	42.5	5.95	7.1	
	Steel rod & PVC pipe	7	2942	0.008 ± 10%	23.5 ± 10%	3.85 ± 2%	3.85 ± 2%	1.0	
			2942	0.0075 ± 1%	22.1 ± 1%	29.0	4.00	7.3	
Square	PVC pipe	8	237	0.008 ± 10%	1.90 ± 10%	5.15 ± 1%	5.15 ± 1%	1.0	Varied number of degree-of-freedom (varied mass)
			237	0.012 ± 1%	2.84 ± 1%	61.0	5.10	12.0	
	Steel pipe	9	1401	0.008 ± 10%	11.2 ± 10%	6.00 ± 2%	6.00 ± 2%	1.0	
			1401	0.007 ± 1%	9.80 ± 1%	42.5	5.95	7.1	
	Steel rod & PVC pipe	10	2942	0.008 ± 10%	23.5 ± 10%	4.15 ± 2%	4.15 ± 2%	1.0	
			2942	0.0075 ± 1%	22.1 ± 1%	29.5	4.10	7.2	

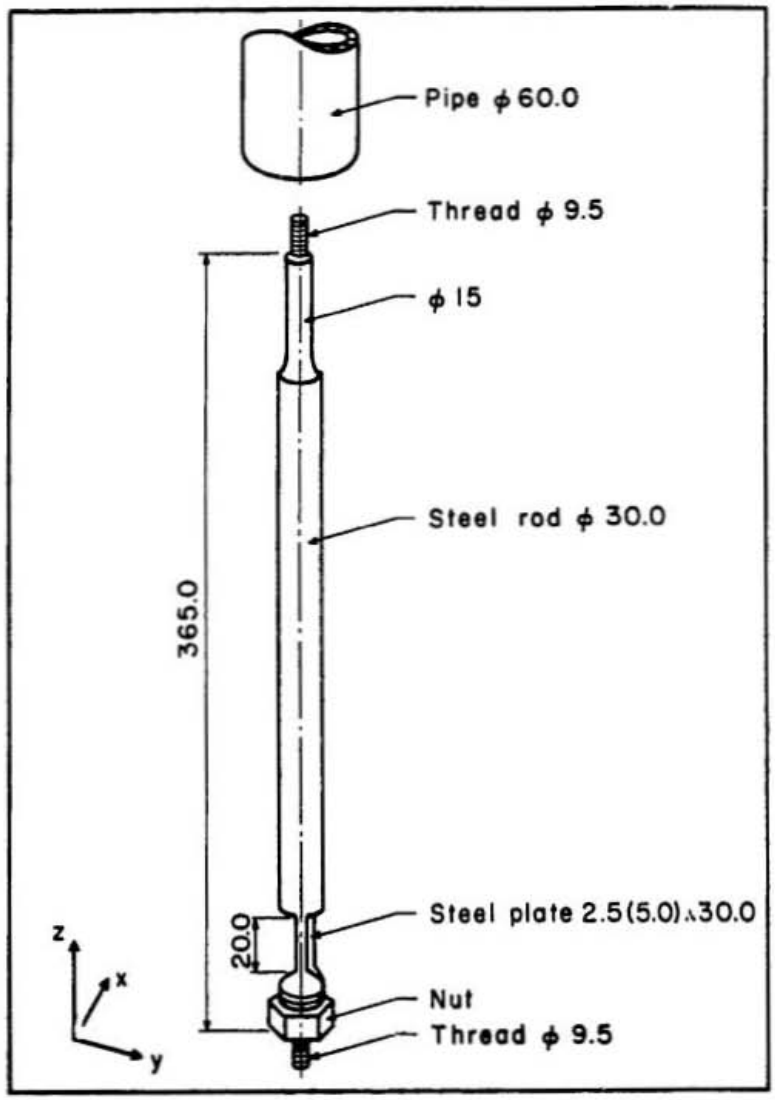

Figure 4.6: A schematic view of an asymmetric cantilever rod (all dimensions in mm).

4.3 Instrumentation

Figure 4.7 shows a view of an instrumentation system which, in general, consisted of flow velocity (hot-wire anemometer) and pipe motion (strain gauge) measuring devices.

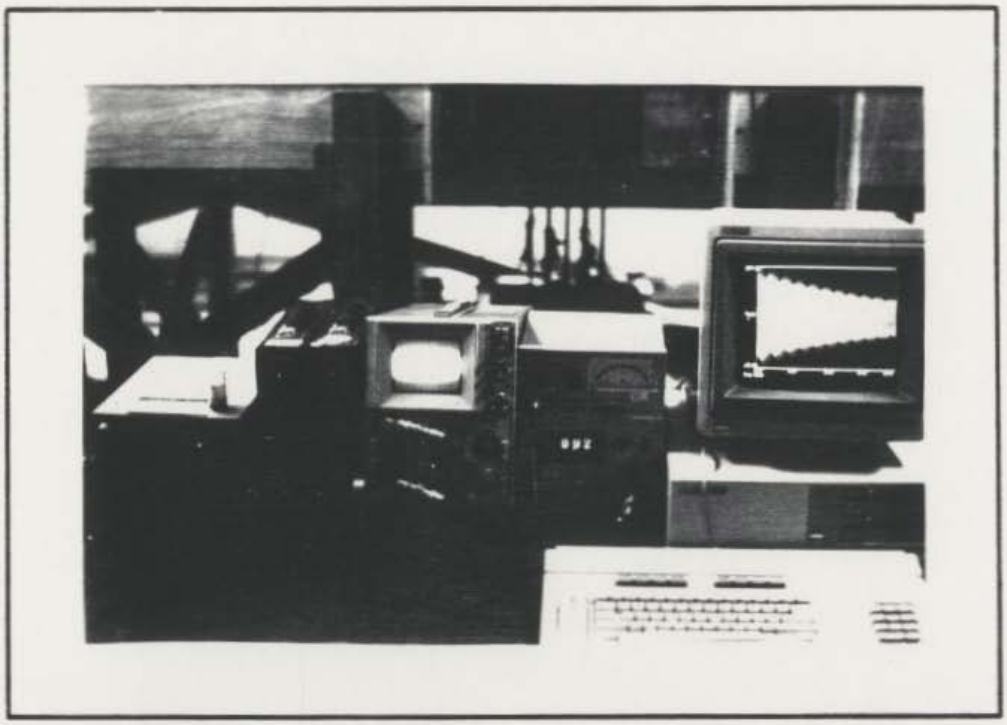

Figure 4.7: A photograph of an instrumentation system.

4.3.1 Flow velocity

The flow velocity was measured upstream of the experimental array using a calibrated DISA constant temperature hot-wire anemometer connected to the DISA 55M system. This system consisted of a 55M01 unit, a 55M10 constant temperature anemometer standard bridge, a 55M05 power pack and a DISA 90 *deg* sensor (type 55P13) parallel to axis probe. The voltage reading during the experiments was performed using a 55D31 digital voltmeter with a 10 *sec* time constant. The hot-wire sensor was installed on the probe support at a fixed position.

Before any test, the instruments were warmed-up and the hot-wire sensor was heated for at least 30 *min* to avoid drift in voltage reading during the experiment. To account for room temperature variation from one day to the next, actual readings in still air were converted to values recorded during calibration runs.

4.3.2 Pipe motion

Vibration response of the cylinder due to air flow was monitored using the following set-up: strain gauges, Wheatstone bridge, filter, oscilloscope, chart recorder and RMS voltmeter. Two VISHAY EA-06-125BT-120 open faced general purpose metallic foil strain gauges were mounted near the base of each cantilever steel rod in both streamwise and transverse-to-flow directions. The strain gauges were connected to the Wheatstone bridges, MICRO-MEASUREMENTS BA-4, giving readings in mA or $micro - strain$. The electric signal from the bridge was transferred through the dual HI/LO filter (cut off frequency was set twice the natural frequency of the cylinder), model Rockland 1022F, to the storage oscilloscope giving a wave pattern which represented the vibration response of the monitored cylinder (hard copy could be obtained using a chart recorder). Its RMS displacement was recorded by a DISA 55D35 RMS digital voltmeter with a 100 *sec* time constant.

For final analysis of the cylinder physical properties (natural frequency and damping) the response pattern was digitized using a KEITHLEY SYSTEM 570 data aquisition instrument, displayed on the monitor screen for control and stored on a floppy disc for further processing on a VAX/VMS mainframe computer.

4.4 Procedure

Prior to the actual testing, a calibration of the instruments and a series of preliminary tests were performed which included close tuning of all flexible cylinders (natural frequencies and dampings) and, because the facility was new, an assesment of its quality in terms of upstream flow conditions (velocity and turbulence intensity profiles) and cylinder mechanical properties.

4.4.1 Instrument calibration

Hot-wire anemometer

During calibration, the hot-wire probe was mounted in air flow, of known variable velocity, over a relevant velocity range, $U = 0.0 - 4.0\ \frac{m}{sec}$. For $U = 0.0 - 1.0\ \frac{m}{sec}$, the hot-wire sensor was placed at the inlet to the water-filled container and the velocity of in-flowing air was calculated, *via* the Bernoulli's equation, from the rate of change of water column level (for details, see reference [84]). The velocity range could be changed by varying the orifice size in the bottom of the cylinder. For $U = 1.0 - 4.0\ \frac{m}{sec}$, a Pitot tube and the hot-wire probe were mounted in the main wind tunnel. Thus, the velocity of air flow was regulated by varying the degree of fan opening and calculated from the measured stagnation pressure. In both cases, the probe operation temperature was set at 200 *deg.C* and decade resistance was calculated from the equation stated on the probe test card. Figure 4.8 shows a typical calibration curve.

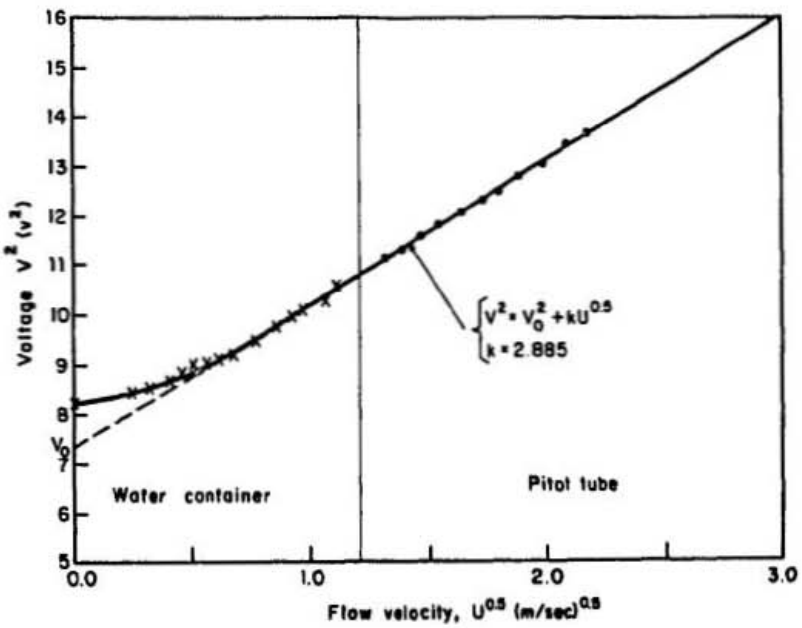

Figure 4.8: Calibration curve for hot-wire probe DISA 55P13.

For calibration, the squares of voltages were plotted against the square roots of velocities to yield a linear characteristic for $U > 0.75 \frac{m}{sec}$. Over this range, the flow velocity was directly calculated using the equation for this line. However, over the lower range, the experimental data had to be compared with the calibration curve to obtain the actual flow velocity. It can be seen that all experimental points correlate very well; the water cylinder readings being a non-linear extension of the Pitot tube readings.

Strain gauges

The strain gauges were calibrated for tip deflections up to one half a cylinder diameter (30 mm), which is more than that needed to cause inter-cylinder clashing, in both streamwise and transverse-to-flow directions, separately. The output from the Wheatstone bridge was found to be a linear function of cylinder static displacement, equal in both directions. Thus, the calibration factor was directly obtained from the calibration curve which is shown in Figure 4.9.

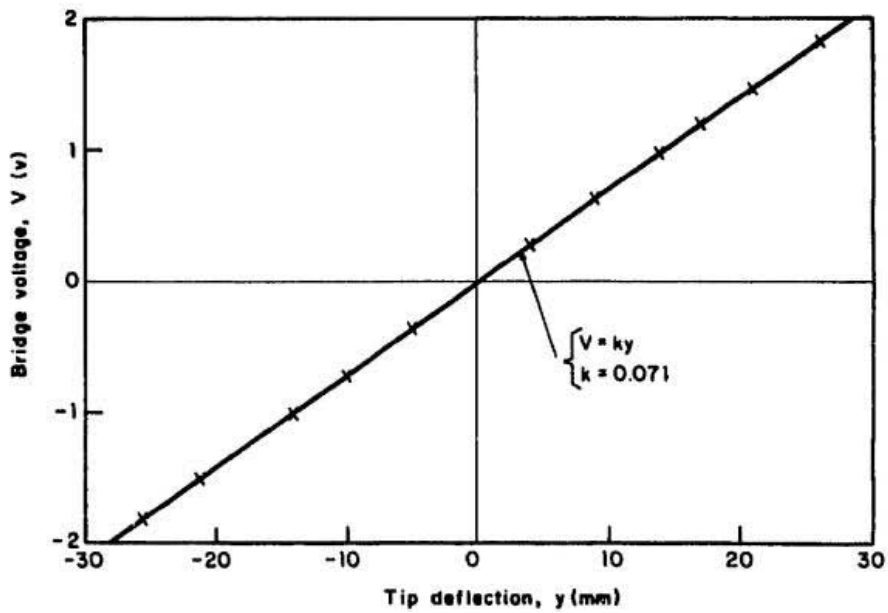

Figure 4.9: Calibration curve for strain gauge VISHAY EA-06-125BT-120.

4.4.2 Preliminary tests

Upstream flow conditions

This measurement was done over the range of critical flow velocities for the tested arrays. The flow velocity and the turbulence intensity were recorded in a cross-sectional plane, 70 *mm* upstream of the test section (measured to the symmetry axis of the first row of cylinders), at 48 uniformly spaced points. It was found that velocity profile showed mean variations between test points less than 17 % and turbulence intensities variations less than 6-10 %. These values, comparable with those reported for other tests rigs (see Reference [55], for example), were felt to be acceptable, given the predominant effect of the pipe bundle geometry on the flow field within the bundle. Figure 4.10 shows typical measured velocity and turbulence intensity profiles (for these, the mean upstream flow velocity was $\bar{U}_U = 0.78\ \frac{m}{sec}$).

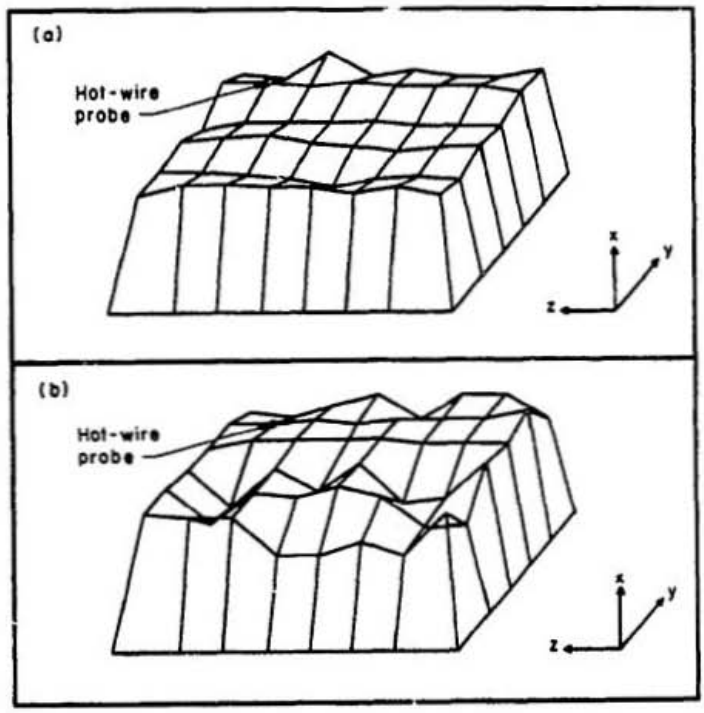

Figure 4.10: Upstream flow conditions for $\bar{U}_U = 0.78\ \frac{m}{sec}$; (a) velocity profile, (b) turbulence intensity profile.

Mechanical *versus* fluid coupling

Although the support stand for the flexible cylinders was intentionally made very stiff, tests were conducted to investigate the relative importance of mechanical *versus* aerodynamic coupling between adjacent PVC flexible cylinders. When a neighbouring cylinder was plucked in still air at a relatively large amplitude (15 % d), the monitored cylinder's vibration amplitude was roughly 40 times smaller, suggesting small coupling, in general. The monitored cylinder was then replaced on its cantilever rod with an equivalent solid steel lumped mass of a diameter 60 mm and 130 mm long which was tuned to the same frequency. The damping for this system dropped by a factor of three from the value for the full PVC cylinder, reflecting the lower aerodynamic damping of the smaller lumped mass. When the neighbouring cylinder was then plucked at large amplitude, the monitored system vibration amplitude was roughly 120 times smaller. That is, the same factor of three reduction was seen for both the damping and the induced vibration of the lump mass in comparison with the full PVC cylinder.

These tests suggested that virtually all the coupling between adjacent flexible cylinders was aerodynamic, with essentially negligible mechanical coupling. Thus, it is very unlikely that heavier cylinders, used in subsequent experiments, could introduce significant mechanical coupling. This, in turn, confirmed the effectiveness of the stiff base plate and support stand.

Natural frequency and damping

The natural frequency, f_0, and the logarithmic decrement of damping, δ_0, of the flexible cylinder were determined using a simple pluck test. Initially, they were obtained from a 20 *sec* recording on the oscilloscope. The number of cycles over this time period was counted and the peak-to-peak cylinder response at the beginning and at the end was determined from the square root of the sum of the squares of

the measured responses in the x- and y-directions. In this way, both the natural frequency and the logarithmic decrement of damping could be calculated and subsequently tuned, by adjusting slightly the length of the cantilever steel rod, to better than 2 % (4 % for an asymmetric rod) for frequency and 20 % for damping.

The final analysis, after the bundle was tuned, was performed by means of a digitizer and a specially developed computer code (it will be described in detail in Section 4.3). The natural frequency and the logarithmic decrement of damping were computed as a function of oscillation amplitude to verify their linear properties (separately, in both streamwise and transverse-to-flow directions). The natural frequency was virtually constant and equal in both directions, while the logarithmic decrement of damping slightly increased over the tested response range (typical plots are shown in Figure 4.11).

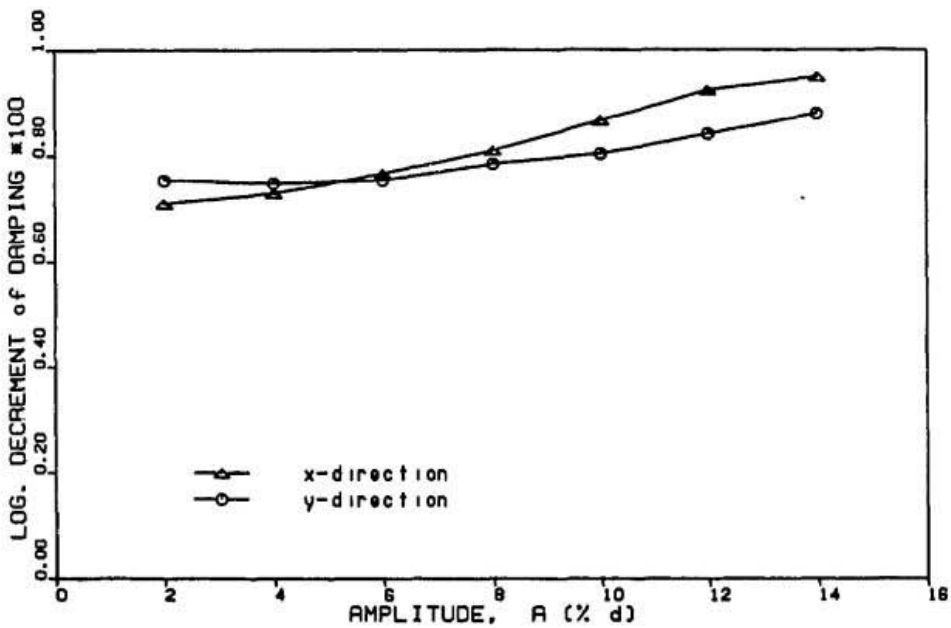

Figure 4.11: Logarithmic decrement of damping in quiescent fluid, δ_0, as a function of amplitude ($\bar{m}\delta_0 = 2.25$).

4.4.3 Response curves

The fluidelastic behaviour of each array was investigated based on response curves; the nondimensional RMS-amplitude of oscillation, $\frac{A_{RMS}}{d}$, plotted against the reduced pitch velocity, $U_{Pr} \stackrel{\text{def}}{=} \frac{U_P}{f_0 d}$, which defined the flow velocity inside the array. The pitch velocity, U_P, was expressed in terms of the upstream flow velocity, as $U_P \stackrel{\text{def}}{=} \frac{P}{P-d} U_U$. The coefficient P defines the array pitch (see Figure 1.3).

Each experiment was commenced at some low flow velocity which was then increased in small steps. The RMS amplitude measuremerts were made in both the streamwise and transverse-to-flow directions (A_{RMS} was calculated as the square root of the sum of the squares of these), with a minimum 10 *min* settling time elapsing at each velocity (to achieve steady state). The flow velocity was increased until the non-linear response plateau was observed or cylinder-to-cylinder clashing occurred. The flow was then decreased in small steps, again allowing a minimum 10 *min* settling time to elapse before response readings were taken, until the vibration amplitudes dropped to their stable levels. In this way, both soft- and hard-excited (hysteresis-type) oscillations were identified. The effectiveness of this procedure was examined in a series of preliminary tests (set 1 in Table 4.1).

Initially, the effect of varied damping on the response curves was investigated. These tests were started at the structural damping level, $\delta_0 \approx 0.01$ and were performed only for a parallel triangular array at the lowest mass, since it was observed that an oil-filled damper caused the damping to be non-linear. A total of six response curves were recorded; one for a "fully flexible" array and one for a single flexible cylinder, which was positioned in the fourth row (see Figure 4.2), at three different damping levels (set 2, 3 and 4 in Table 4.1).

Next, the detailed studies of a minimum number of degrees-of-freedom, needed to capture the essence of array behaviour, were conducted. These tests were first performed on "fully flexible" arrays; flexible kernel of seven (parallel triangular ar-

ray) or nine (square array) cylinders surrounded by rigid neighbours. The cylinder at the center of each kernel was monitored. In this way, the basic response pattern was established and the next tests were intended to reproduce this pattern with a fewer number of degrees-of-freedom. Thus, the flexible kernel was reduced to a tandem cylinder arrangements; the central one and one of the adjacent cylinders. All possible configurations were tested to find those which matched closely the previously recorded response pattern. During these tests, both of the flexible cylinders were monitored to explore the effect of neighbouring cylinder motion and the physical role of fluid coupling. This procedure gradually eliminated some of the cylinders and identified the critical zone within the flexible kernel. Subsequently, a single flexible cylinder in an otherwise rigid array was investigated. This required recording a total of twenty (parallel triangular array) or twenty five (square array) response curves. Finally, the symmetric cantilever rods of the cylinders were replaced with asymmetric ones, allowing oscillations in the transverse-to-flow direction only, thus further reducing the number of degrees-of-freedom. As before, first the tandem flexible cylinder configurations and then the single flexible cylinders were investigated for their behaviour within a rigid array.

Summa summarum; in this procedure the multi degree-of-freedom "flexible array" was gradually reduced to the single degree-of-freedom flexible cylinder.

When one sequence of experiments was completed, two upstream cylinder rows in a parallel triangular array were step by step inserted (see Figure 4.2) and one in a square array (see Figure 4.3), and the whole process repeated. Then, the array was assembled to its initial configurations and the effect of varied mass was investigated by replacing the flexible cylinders. Thus, a total of nine such experiments were run for a parallel triangular array (upto thirty response curves each); three different cylinder masses (set 5, 6 and 7 in Table 4.1) for each of three different array geometries depending on a number of upstream rows. Since in a square array only one

upstream cylinder row was additionally inserted to study the row dependence effect, a total of six such experiments were performed (upto forty one response curves each); three different cylinder masses (set 8, 9 and 10 in Table 4.1) for two different array geometries.

4.4.4 Transient excitation

The transition of an array from stable to post-stable states at the same flow velocity (hard-excited oscillations) was examined using both transient displacement and velocity excitation. These tests were conducted in order to determine the magnitude of the excitation needed to trigger instability of a stable array operating within the hysteresis region.

Displacement excitation

With an array oscillating at steady, stable amplitude near the lower limit of the hysteresis region, the monitored cylinder was plucked. The transient displacement of the cylinder was recorded on a chart recorder to determine the peak amplitude which was converted to an equivalent RMS by dividing by the square root of two. To allow the system to reach steady-state, a minimum of 10 *min* was permitted to elapse before RMS readings were taken. The test was terminated after an elapsed time of more than 30 *min*. At the same flow velocity, the process was then repeated with larger peak displacement excitation until the array went unstable. In this way, the minimum peak (RMS) transient displacement needed to cause transition from stable to post-stable oscillations was determined. The flow velocity was then incremented in steps and the whole procedure repeated until the upper hysteresis limit was reached.

These excitation experiments were performed for parallel triangular and square arrays (set 1 and 8 in Table 4.1), at the lowest cylinder mass where the observed

width of the hysteresis region was the largest.

Velocity excitation

These tests were conducted by starting at a stable vibration level at initial velocity, U_I, near the lowest region of the hysteresis region, increasing the velocity by ΔU for a time period of Δt, then returning to velocity U_I. The time interval was varied over the values 10, 15, 20, 30, 45 and 60 *sec*, and for each ΔU, the minimum Δt needed to trigger instability was determined. After the surge, at least 10 *min* of settling time was permitted to elapse before the cylinder amplitude readings were taken and 30 *min* before the test was terminated. A time series trace of the velocity surge, $U(t)$, was obtained from the hot-wire anemometer for each test (a typical trace is shown in Figure 4.12). Note that the steady flow results (response curves) correspond essentially to $\Delta t > 10\ min$ and $\Delta U_{min} = U_C - U_I$ (the minimum velocity increment needed to raise the system to the stability threshold under steady state conditions). Thus, a Δt of longer than 1 *min* was not used, since it was felt that this would tend to approach the steady flow test conditions.

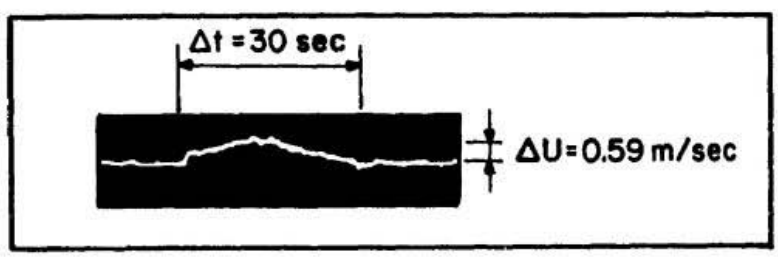

Figure 4.12: Typical trace of velocity surge, $U(t)$, obtained from hot-wire anemometer.

As with displacement excitation, the velocity U_I was incremented in steps towards the upper hysteresis limit. The product of velocity and time increments , $\Delta U \cdot \Delta t$, was taken to be a measure of the overall array excitation. These tests were of practical importance, showing how the velocity surge may trigger instability

within the hysteresis region. However, they gave very little additional insight and were only conducted for a parallel triangular array at the lowest cylinder mass (set 1 in Table 4.1).

4.4.5 Velocity-dependent damping

This experimental study looked at the nature of velocity-dependent damping of cylinders oscillating in both rigid and flexible arrays. The tests were conducted for a parallel triangular and a square array with the monitored cylinder (m=1.04 $\frac{kg}{m}$) positioned in the fourth row.

Analysis of decay curve

Decay curves were used as a common method of assessing the damping in flow-induced vibrations. The monitored cylinder, subjected to steady flow velocities from zero to U_C, was plucked upto a tip peak deflection of $A = 20\ \%\ d$ in the streamwise and transverse-to-flow directions, separately. In each case (below the hysteresis limits), the cylinder oscillations, induced by plucking, decayed to the turbulent buffeting level at a given flow velocity.

The amplitude decay curves were digitized with a sampling rate of approximately 40 points per cycle (200 Hz for $f_0 = 5.00\ Hz$). To reduce the "noise" caused by random turbulence fluctuation in the mean flow, the data files were smoothed using the five-point marching polynomial of Longuet-Higgins and Cokelet, [85]. Additionally, the "mean drift" of the equilibrium state ($A = 0$) was removed to obtain comparable results from the negative and the positive peaks. Figure 4.13 shows a typical experimental decay curve which was obtained, using this procedure, in the presence of fluid flow.

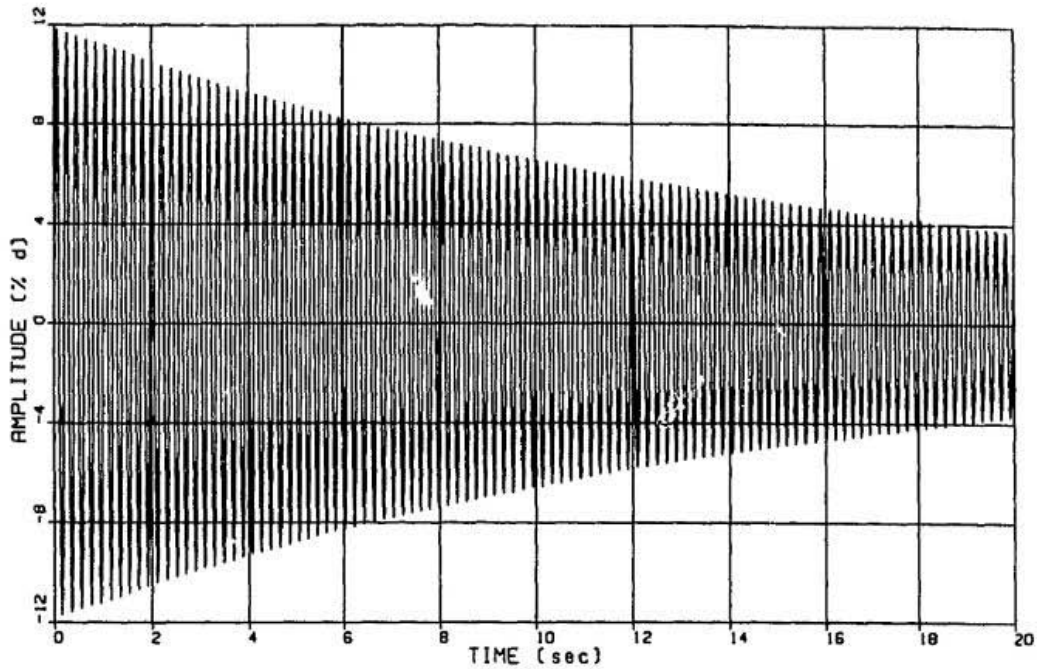

Figure 4.13: Typical decay curve in transverse-to-flow direction ($U_U \approx 0.5U_C$).

The damping factor, $\zeta(A)$, was computed as a function of the peak amplitude, A, over portions of the decay curve in small amplitude intervals, (A_n, A_{n+N}), which were 2 % d. The damping, at each flow velocity, was then obtained by extrapolation of $\zeta(A)$ to the amplitude level induced by turbulence (typically, less than 1 % d). This method was especially convenient within the hysteresis region, where the damping showed a strong dependence on the oscillation amplitude due to the coexistence of stable and unstable domains. The final values of damping were an average of three different pluck tests.

The associated frequency of oscillations which follows from the number of cycles, N, in the equivalent time interval, (t_n, t_{n+N}), is:

$$f = \frac{N}{t_{n+N} - t_n}. \tag{4.1}$$

which yields f_0 in the still fluid.

Methods of damping estimation

Experimental decay data were initially analyzed using three different techniques: (1) a standard logarithmic decrement method, (2) a modified logarithmic decrement method and (3) a numerical parameter identification technique.

The method of logarithmic decrement, which is most commonly used in practice, allows the linear damping to be estimated from the raw decay data *via* equation:

$$\delta = \frac{1}{N} ln \frac{\bar{A}_n}{\bar{A}_{n+N}} \tag{4.2}$$

which yields δ_0 in the still fluid. The amplitude $\bar{A}_n$ at t_n and $\bar{A}_{n+N}$ at t_{n+N} are calculated as average values from the positive and negative peaks, [43]:

$$\bar{A}_n = \frac{A_n + A_{n+1}}{2} \; ; \; \bar{A}_{n+N} = \frac{A_{n+N} + A_{n+N+1}}{2}. \tag{4.3}$$

The logarithmic decrement of damping, δ, was converted to the damping factor (expressed in percentage of actual over critical), ζ, using the approximate relationship:

$$\zeta = \frac{1}{2\pi} \delta * 100\%. \tag{4.4}$$

In this method, only one value of damping was obtained in a given amplitude range, (A_n, A_{n+N}). However, this value varied with the number of cycles, N, posing an important experimental problem.

The modified logarithmic decrement method, [86], is an alternative procedure, independent of the number of cycles in equation (4.2). The expotential decay curve:

$$A = C_0 e^{-2\pi\zeta f t} \tag{4.5}$$

is fitted through the peak points (separately, through positive and negative) of the experimental decay curve. The constant C_0 defines the intersection point ($t = 0$) with the amplitude axis. After taking the logarithm of both sides and substituting for f (equation (4.1)), this expression becomes:

$$lnA = lnC_0 - 2\pi\zeta N. \tag{4.6}$$

The function, which is given by equation (4.6) (plotted against time measured in units of N), represents a straight line on a log-linear basis with equally spaced points, at $\Delta N = 1$, for approximately constant frequency of oscillations. Thus, the departure of the experimental peak points, $\ln A$, from this line is entirely due to non-linearity in the damping. As before, equation (4.6) was applied in amplitude intervals of 2 % d, using a best-fit straight-line representation of experimental data, yielding the actual value of the damping factor. This method was especially convenient if the decay curve was perturbed by flow turbulence.

The parameter identification technique, originally developed by Bass and Haddara, [87], for finding the roll damping of ships, allows a direct assessment of damping non-linearities. This method can be applied to the complete portion of the decay curve, assuming equation of decay motion, induced by plucking, to be of the following non-linear form:

$$\ddot{y}(t) + 2\omega\zeta[1 + \eta_1 \mid \dot{y}(t) \mid + \eta_2 \dot{y}(t)^2]\dot{y}(t) + \omega^2[1 + \mu_1 y(t)^2]y(t) = 0 \qquad (4.7)$$

where the constants η_1, η_2 and μ_1 reflect the fluid-damping and fluid-stiffness non-linearities, respectively. The identification of these constants is performed through a best-fit of equation (4.7) to experimental decay data, either all recorded points or the peak values. This numerical routine requires as an input the initial conditions at the peak point ($y_0 = A_n$, $\dot{y}_0 = 0$), the estimated linear parameters (ω, ζ), and the "guessed" non-linear parameters (η_1, η_2, μ_1). The difference between the predicted and the observed values of the decay amplitude is minimized with respect to the parameters to be identified. Some details of this complex numerical procedure can be found in Reference [87].

To test the validity of the proposed methods, the pluck experiments were first performed in still air and then in fluid flow ($U_U \approx 0.5U_C$). Table 4.2 shows the variation of the damping, with the amplitude of oscillations, derived from numerical analysis of the decay curves. The numerical results, which were obtained from

application of the different techniques (1,2,3), were found to be generally in very close agreement. In view of these results, it could be concluded that each method gave accurate estimates of the damping in a given amplitude interval (2 % of d). However, the logarithmic decrement method (1) and the parameter identification technique (3) showed a sensitivity to flow turbulence "noise" which obscured the true value at the response peaks. Moreover, the parameter identification technique was strongly dependent on its linear inputs; ω and ζ. Thus, on the basis on these observations, the modified decrement method (2) was chosen for the present work since it gave more consistent estimates of damping and was relatively simply to apply.

Table 4.2: Numerical values of damping factor (% of critical); comparison of different techniques.

A	$U_U = 0.0$			$U_U \approx 0.5U_C$		
(% d)	(1)	(2)	(3)	(1)	(2)	(3)
15-13	.142	.140	.141	.180	.182	.177
13-11	.136	.134	.134	.184	.184	.182
11-9	.128	.130	.130	.191	.185	.189
9-7	.127	.127	.129	.179	.178	.175
7-5	.119	.120	.122	.180	.180	.182
5-3	.121	.120	.129	.177	.179	.175
3-1	.120	.121	.124	.167	.174	.168

Chapter 5

Experimental results and discussion

The experimental program, undertaken within this study, was very extensive; approximately five hundred response curves were recorded. Therefore, only those results which were found essential for further model development are reported and discussed in this Chapter. However, viewed in this condensed form, they may appear difficult to interpret. For this reason, the majority of the recorded response curves are presented in the Appendix A, while the detailed damping curves are included in the Appendix B.

To ensure that the trends observed are not distinct phenomena associated with an array geometry, two different configurations were tested; parallel triangular and square.

5.1 Parallel triangular array

The tested cylinder configuration is displayed in Figure 4.2. The monitored cylinder, No.7, is positioned in the fourth row for the basic geometry or, alternatively, in the fifth and sixth rows with additional cylinders installed upstream.

5.1.1 Post-stable behaviour

Preliminary tests

These experiments, which included both steady flow and transient excitation tests, were aimed to recognize the nature of post-stable oscillations.

Figure 5.1(a) shows the initially obtained RMS response curves as a function of reduced pitch velocity, U_{Pr}, for the steady flow tests conducted on both 7 flexible and 1 flexible cylinder arrays (set 1 in Table 4.1), with the monitored cylinder in the fourth row. Notice that the 7 flexible cylinder configuration shows clear hysteresis behaviour, while the single flexible cylinder system does not. For the 7 flexible cylinder array, a stability threshold, U_C, of $U_{Pr} = 13.66$ may be clearly assigned, since the curve is essentially vertical at this point (it should be vertical, in principle, but it is shown here as connections between data points as actually obtained). The post-stable vibration amplitudes saturated at $\sim$ 11.5 % d. Higher flow velocities were found to initiate cylinder clashing, leading to slightly lower RMS amplitudes. As the flow velocity was reduced, the array remained unstable until the velocity dropped below $U_{Pr} \approx 10.80$. The lowest velocity point on the hysteresis curve, U_H, may be taken as $U_{Pr} = 10.42$. For the single flexible cylinder array, the stability threshold may be defined as $U_{Pr} = 14.75$ using the criterion suggested in Section 3.3.1 (intersection of steepest tangent to the post-stable response curve with the response induced by turbulence). The post-stable vibration amplitudes appear to be self-limiting, reaching a plateau of $A_{RMS} \approx 6.7$ % d. It is worth noting that these tests were subsequently repeated and gave virtually identical results.

With the basic post-stable behaviour recognized, the transient excitation tests were conducted. The 7 flexible cylinder array was excited at initial velocities, U_I: $U_{Pr} = 9.95, 10.80, 11.87, 12.95$. For $U_I < U_H$ ($U_{Pr} = 10.42$), the array always returned to its original state (regardless of excitation characteristics), while for $U_H < U_I < U_C$ ($U_{Pr} = 13.66$) these transients could trigger a transition to post-stable

oscillations with all 7 flexible cylinders vibrating at large amplitudes. The final post-stable RMS amplitudes were found to be very close to those levels recorded during the steady flow tests (it should be noted that once unstable, the array showed no tendency to return to its original lower vibration level). Figure 5.1(b) presents these data together with the minimum peak displacement excitation levels converted to equivalent RMS amplitudes (naturally, larger excitations than these minima would also cause transition). As expected, smaller minimum excitations were required to cause transition as U_C was approached. However, these excitation amplitudes all lie above the expected location of the unstable limit cycle which should be positioned within hysteresis region (see Figure 3.5). This is not surprising since additional energy must be put into the system *via* fluid coupling to trigger instability of the neighbouring cylinders (the single flexible cylinder array would always return to its original vibration amplitude after any excitation). It is thus reasonable to expect that the unstable limit cycle would show up at lower excitation levels if all flexible cylinders were excited at the same time.

The overall excitation was accomplished with the velocity transients, however the size of velocity surge could not be converted to an equivalent displacement excitation. Interestingly, the product needed to trigger transition, $\Delta U \cdot \Delta t$, is approximately constant, at a given U_I, and decreases as U_I approaches U_C ($\Delta U \cdot \Delta t \approx 24, 15, 8$ at respective velocities $U_{P_r} = 10.80, 11.87, 12.95$). This suggests that the threshold for transition by surge, at a given U_I, is related to the increased energy in the surge flow as compared with the steady flow. As one would expect, the larger the magnitude of the surge, the less it would need to persist to trigger the transition to post-stable vibration.

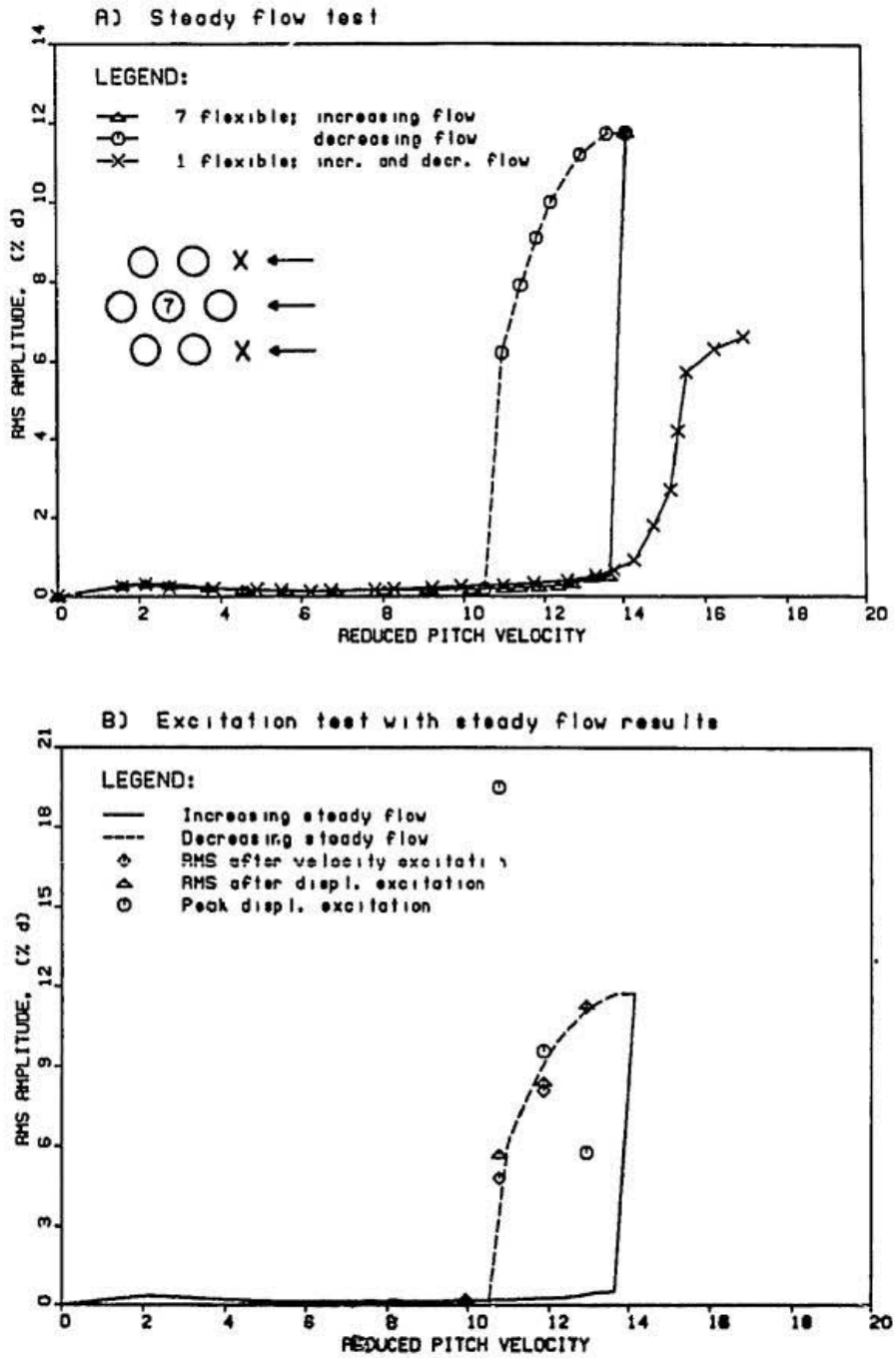

Figure 5.1: RMS response curves for the 7 and 1 flexible cylinder parallel triangular array; (a) steady flow and (b) excitation tests.

Effect of damping

Figure 5.2 presents the effect of damping on the array behaviour (to allow damping variations, paddles were fitted to the top of each cantilever support rod). Steady flow tests were run for $\delta_0 = 0.010, 0.021, 0.030$ (set 2, 3, and 4 in Table 4.1). Notice that the response curve for the 7 flexible cylinder array with $\delta_0 = 0.010$ agrees well qualitatively with that obtained previously for this case which, for easy of comparison, is also presented in Figure 5.2. For some reason, the stability threshold has dropped slightly from $U_{Pr} = 13.66$ to 12.96 while the width of the hysteresis region has decreased from 24 % U_C to 16 % U_C. The most noticeable change, however, is the reduction in the post-stable amplitude plateau from ~ 11.5 % d to ~ 6.3 % d. Since this latter vibration level did not produce cylinder clashing, data were obtained at several velocity points higher than U_C. As can be seen in Figure 5.2, this lower post-stable plateau was observed at all damping values. However, the further increase of damping to $\delta_0 = 0.021$ and 0.030 increased the stability threshold to $U_{Pr} = 14.21$ and 15.35, and reduced the width of the hysteresis region to 10 % U_C and 6 % U_C, respectively. Also, the single flexible cylinder cases all showed slightly higher stability thresholds, less dramatic transition from stable to post-stable behaviour and no hysteresis.

In addition, for each damping value, transient displacement and velocity excitation tests were conducted on the 7 flexible cylinder array at steady velocities, U_I, just below U_H and approximately half way between U_H and U_C. As with the previous test series, transitions generated by either displacement or velocity transients gave final RMS amplitudes virtually identical with the corresponding steady flow results which are presented in Figure 5.2. Also, the single flexible cylinder array always returned to its initial amplitude levels, regardless of the magnitude of the transient.

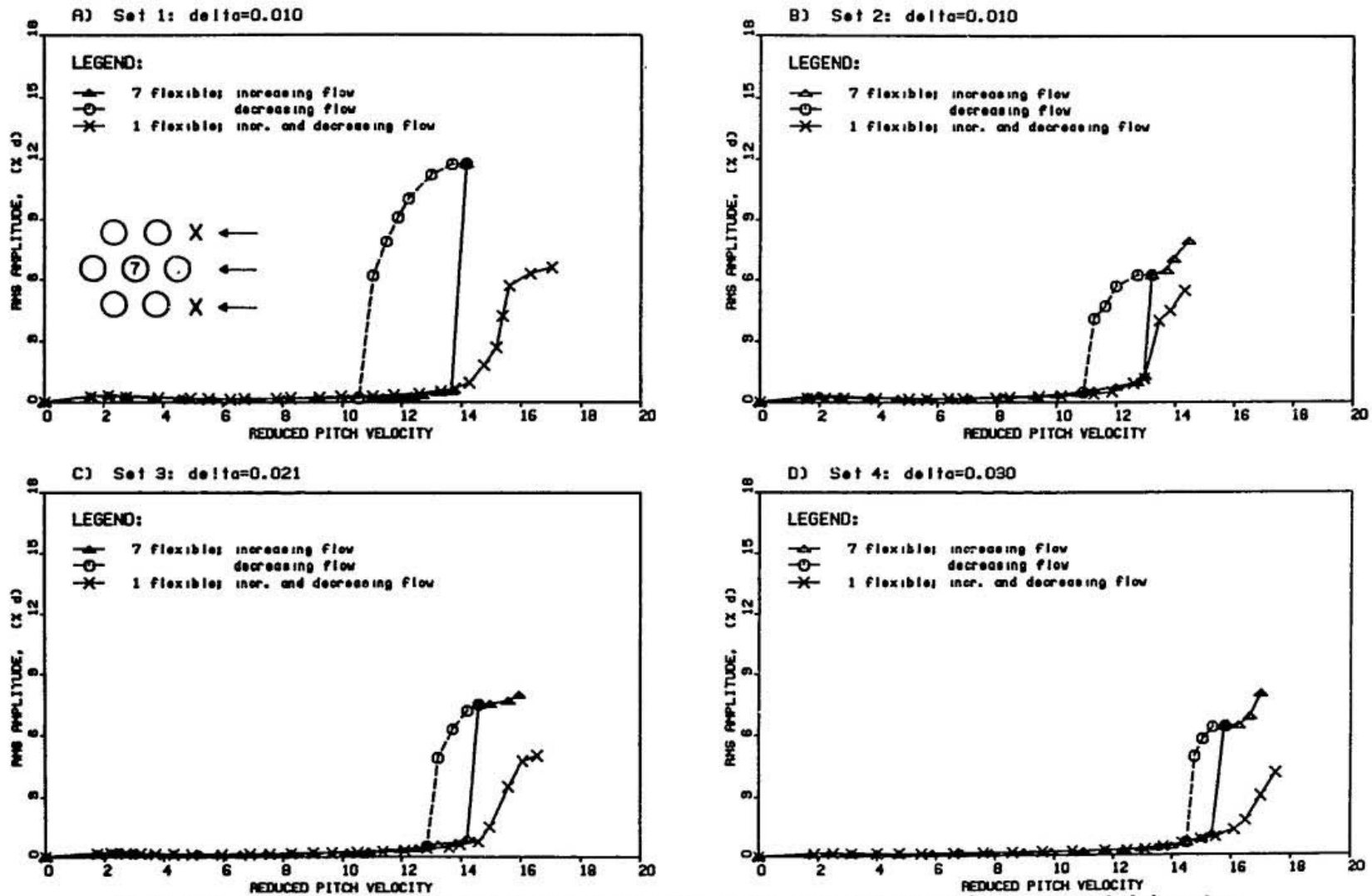

Figure 5.2: RMS response curves for the 7 and 1 flexible cylinder parallel triangular array, varied damping.

Before proceeding further with the experimental investigation, it was necessary to find an explanation for the significant discrepancy in the observed RMS amplitudes of post-stable oscillations for $\delta_0 = 0.010$ (see Figure 5.2(a) and 5.2(b)). For this, the damping paddles were removed and the steady flow test for the 7 flexible cylinder array (set 5 in Table 4.1) was run again. Figure 5.3 shows the new response curve which is drawn without markers (solid for increasing and dashed for decreasing flow velocity) and is denoted as "ideal". Interestingly, this response curve agrees well qualitatively with the previous steady flow tests for $\delta_0 = 0.010$ (set 1 in Table 4.1), yielding the stability threshold $U_{Pr} = 13.75$ and the width of the hysteresis region 20 % U_C. The post-stable amplitude plateau is even higher from observed earlier, reaching $\sim$ 15.4 % d. This suggests that an oil-filled damper introduces non-linear damping, causing additional energy dissipation at large amplitude oscillations. Because of this, damping paddles were not used in subsequent work.

Imperfection sensitivity

As noted earlier, the mass-damping parameter was varied by changing the mass of the flexible cylinders. Unfortunately, this required the reassembly of the array each time, leading to inevitable changes in relative cylinder positions. As shown by Andjelic, [54,55], these changes, although very small, may affect the critical flow velocity. Therefore, before proceeding to actual experiments on a number of degrees-of-freedom, a limited study was performed, showing sensitivity of the post-stable array behaviour to the slight imperfections in the cylinders alignment. To measure the extreme imperfection effect possible, the "dominant" cylinder (e.g. the cylinder which was observed to have the lowest stability threshold and the largest post-stable oscillation amplitude) was slightly displaced, $\sim$ 10 % of the gap between cylinders, from its "ideal" position.

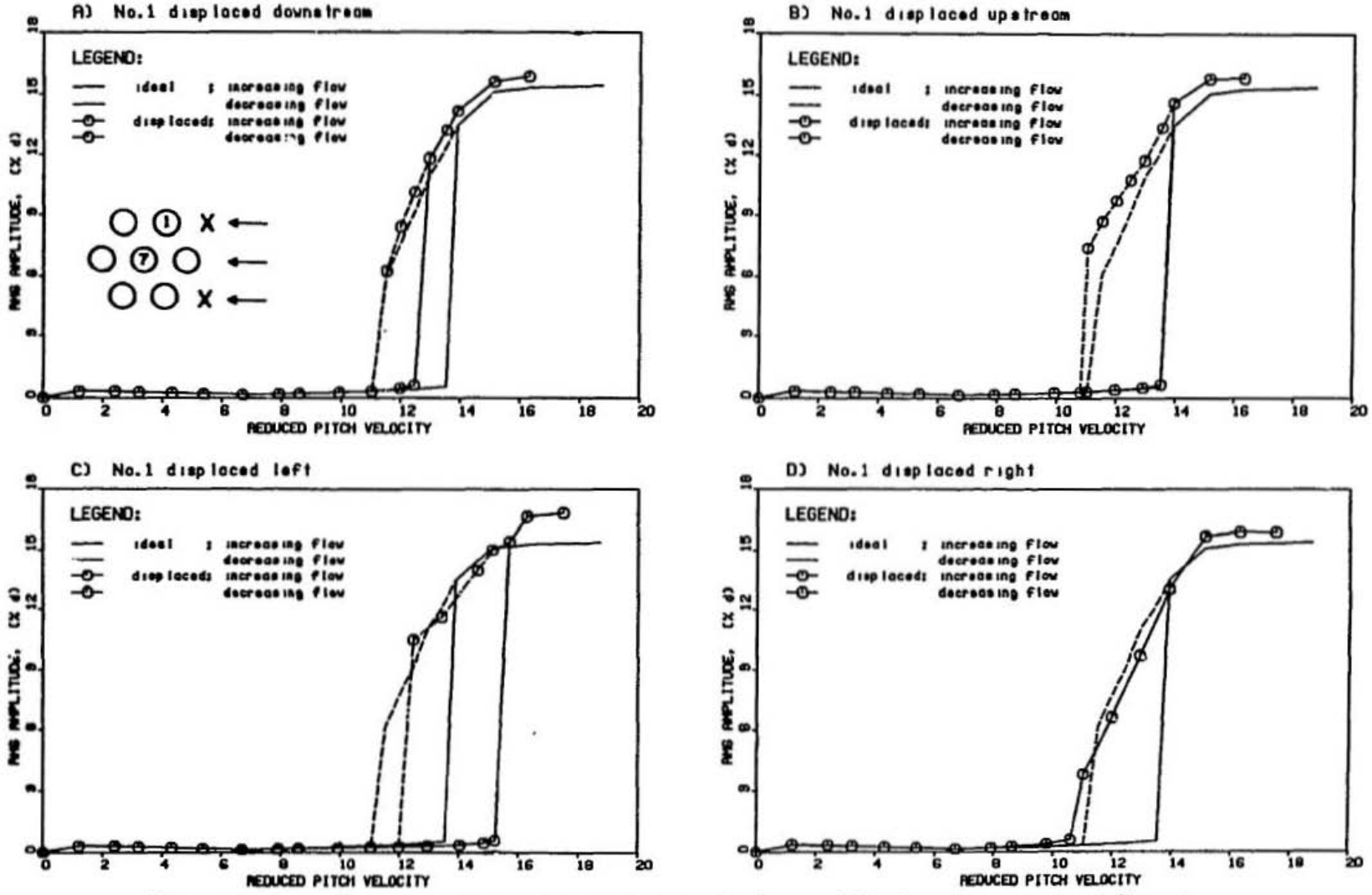

Figure 5.3: Imperfection sensitivity of the 7 flexible cylinder parallel triangular array (±10 % gap).

Figure 5.3 shows the response curves for the 7 flexible cylinder array with the dominant cylinder, No.1, displaced (a) downstream, (b) upstream, (c) left and (d) right (together with the "ideal" which is presented for easy of comparison). Notice that, unlike the previous tests, the response curves display significant qualitative discrepancy. However, the post-stable amplitude plateaux, all in the range $\sim$ 15.8-16.8 % d, are essentially unaffected. The stability threshold, U_C, has varied between $U_{Pr} = 10.61$ (Figure 5.3(d)) and $U_{Pr} = 15.22$ (Figure 5.3(c)), while the lowest point on the hysteresis curve, U_H, has varied only between $U_{Pr} = 10.81$ (Figure 5.3(b)) and $U_{Pr} = 11.99$ (Figure 5.3(c)). The widths of the hysteresis region are in the range 14-21 % U_C. Evidently, the most noticeable change in the array behaviour is the disappearance of hysteresis in Figure 5.3(d). However, the stability threshold,$U_{Pr} = 10.61$, falls close to the U_H range ($U_{Pr} = 10.81 - 11.99$). These results explicitly show that, indeed, even slight imperfection in cylinder alignment may influence the post-stable array behaviour. However, for the limited cases studied, U_H is approximately constant. This suggests that, in the extreme situation of the disappearance of hysteresis, U_C may be interpreted as $U_C = U_H$.

Effect of number of degrees-of-freedom

The detailed experimental studies, to reduce a number of degrees-of-freedom needed to model the post-stable behaviour of a fully flexible array, were conducted in the mass-damping parameter range ($\bar{m}\delta_0 \approx 1.9 - 23.5$ (set 5, 6 and 7 in Table 4.1). Figures 5.4-5.6 give the essence of these experiments. To provide a clear description of the tested arrays, a code is employed (indicating the monitored cylinder and the total number of degrees-of-freedom); No.$l : m \times n$, where l identifies the monitored cylinder (1-7), m denotes the number of flexible cylinders (1-7) and n is the number of degrees-of-freedom for the flexible cylinder (1,2). For a given geometry, each Figure contains four response curves; the central cylinder in the 7 flexible cylinder

array (No.7: 7×2), the central cylinder in the 2 flexible cylinder array (No.7: 2×2) whose strong coupled motion approximately replicated No.7: 7×2, and the single flexible cylinder (1×2 and 1×1) whose motion dominated the behaviour of the 2 flexible cylinder array previously recorded. In this way, the examined array was gradually reduced from 14 to 1 degrees-of-freedom. Viewed in this condensed form, Figures 5.4-5.6 may appear difficult to interpret. Thus, additional results are presented in Appendix A (Figures A1-A21). Below, some observations are noted, regarding the stability behaviour of cylinder arrays (enclosed in brackets are the supplementary observations from examination of Figures A1-A21).

Figure 5.4 shows the results obtained at $\bar{m}\delta_0 \approx 1.9 - 2.4$ (set 5, Table 4.1). Note that (see also Figures A1-A9), although almost all 2×2 configurations tested show coupled motion (e.g. both cylinders move in a well defined mode induced by the "dominant" cylinder), only one closely replicates 7×2 response (fluid coupling in 2×1 was not observed). It appears that there is one cylinder in the bundle which, *via* fluid coupling, dominates 2×2 and 7×2 behaviour; it initiates instability and governs post-stable oscillations.

- Figure 5.4(a) - the central cylinder in 4-th row:
  - No.7: 7×2 displays hysteresis (No.7: 1×2 does not)
  - No.7: 2×2 closely replicates No.7: 7×2 behaviour, showing strong coupled motion (only one 2×2 configuration, No.7 and No.1, behaves similarly to No.7: 7×2, coupled motion for 2×1 is not present)
  - No.1: 1×2 and No.1: 1×1 also show hysteresis, however differ from No.7: 7×2 in exact details (both 3-rd row flexible cylinders, No.1 and No.5, display nearly same 1×2 and 1×1 behaviour)

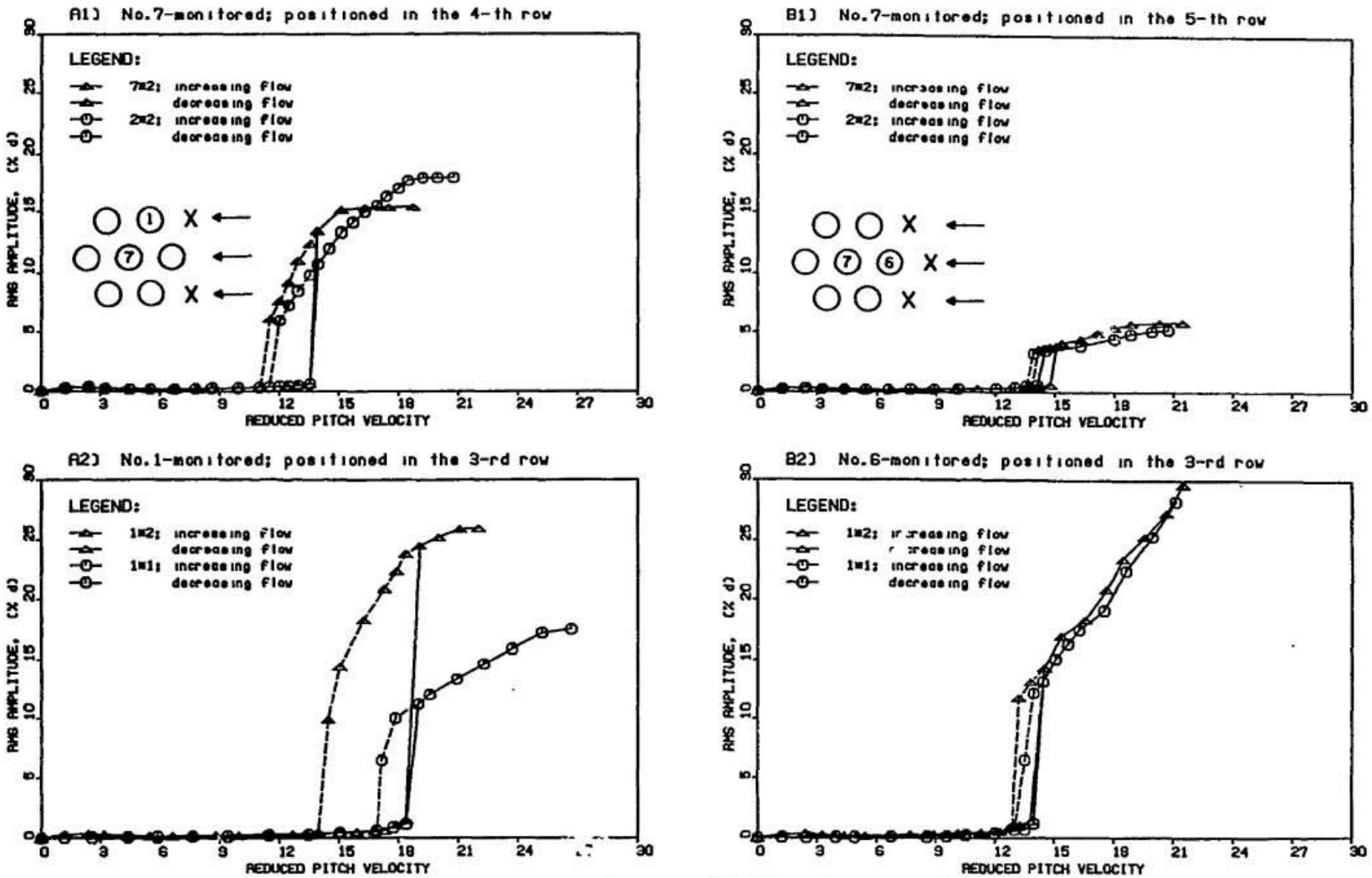

Figure 5.4: RMS response curves for a parallel triangular array, $\bar{m}\delta_0 \approx 1.9 - 2.4$.

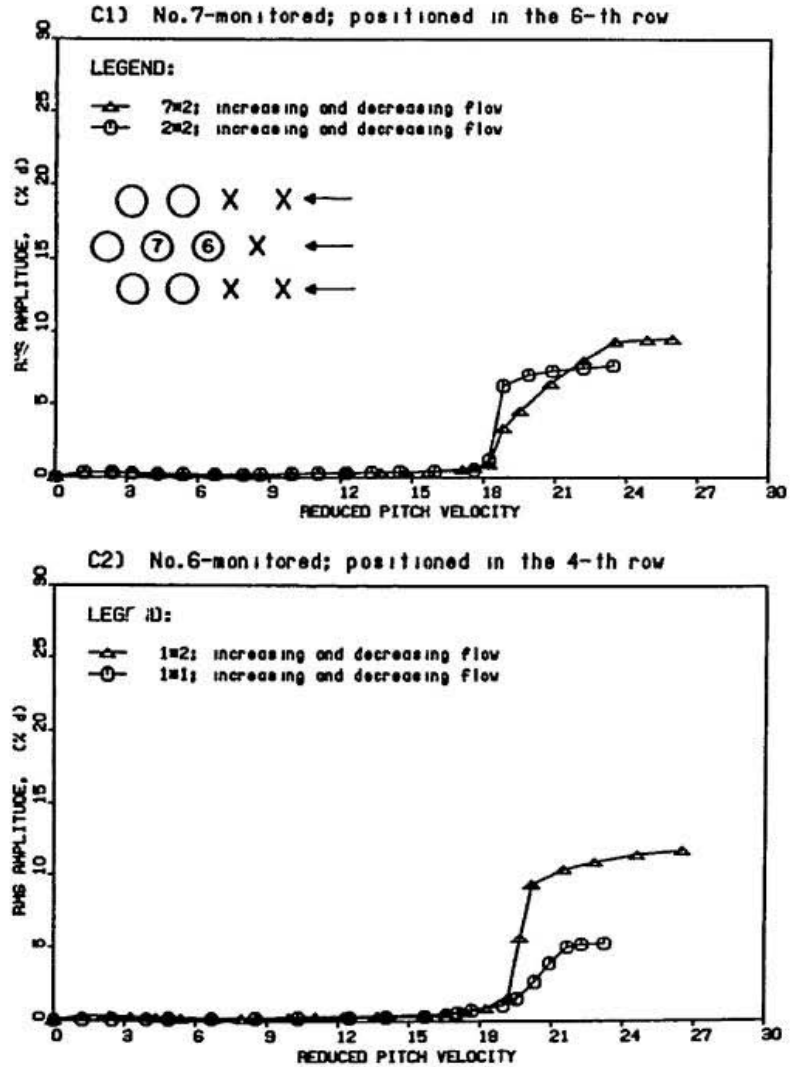

Figure 5.4 (cont'd): RMS response curves for a parallel triangular array, $\bar{m}\delta_0 \approx 1.9 - 2.4$.

- Figure 5.4(b) - the central cylinder in 5-th row:
  - No.7: 7×2 displays hysteresis (No.7: 1×2 is stable in the tested velocity range)
  - No.7: 2×2 closely replicates No.7: 7×2 post-stable behaviour, however becomes unstable earlier (only one 2×2 configuration, No.7 and No.6, shows coupled motion which is not present for 2×1)
  - No.6: 1×2 and No.6: 1×1 show qualitatively similar behaviour to No.7: 7×2, post-stable response is significantly higher (cylinders No.1 and No.5 are almost stable)
- Figure 5.4(c) - the central cylinder in 6-th row:
  - No.7: 7×2 does not display hysteresis (No.7: 1×2 is stable in the tested velocity range)
  - No.7: 2×2 replicates No.7: 7×2 behaviour (no hysteresis), although shows clean response jump at the stability threshold (only one 2×2 configuration, No.7 and No.6, show coupled motion which is not present for 2×1)
  - No.6: 1×2 and No.6: 1×1 behave similarly to No.7: 7×2, No.6: 1×2 shows steeper post-stable response (No.6 is the only clearly unstable cylinder)

Figure 5.5 presents the corresponding results for tests conducted at $\bar{m}\delta_0 \approx 8.4 - 11.2$ (set 6, Table 4.1). The most noticeable difference is the weaker coupling in all tested 2×2 configurations (see also Figures A10-A15). However, the role of the dominant cylinder is clearly established.

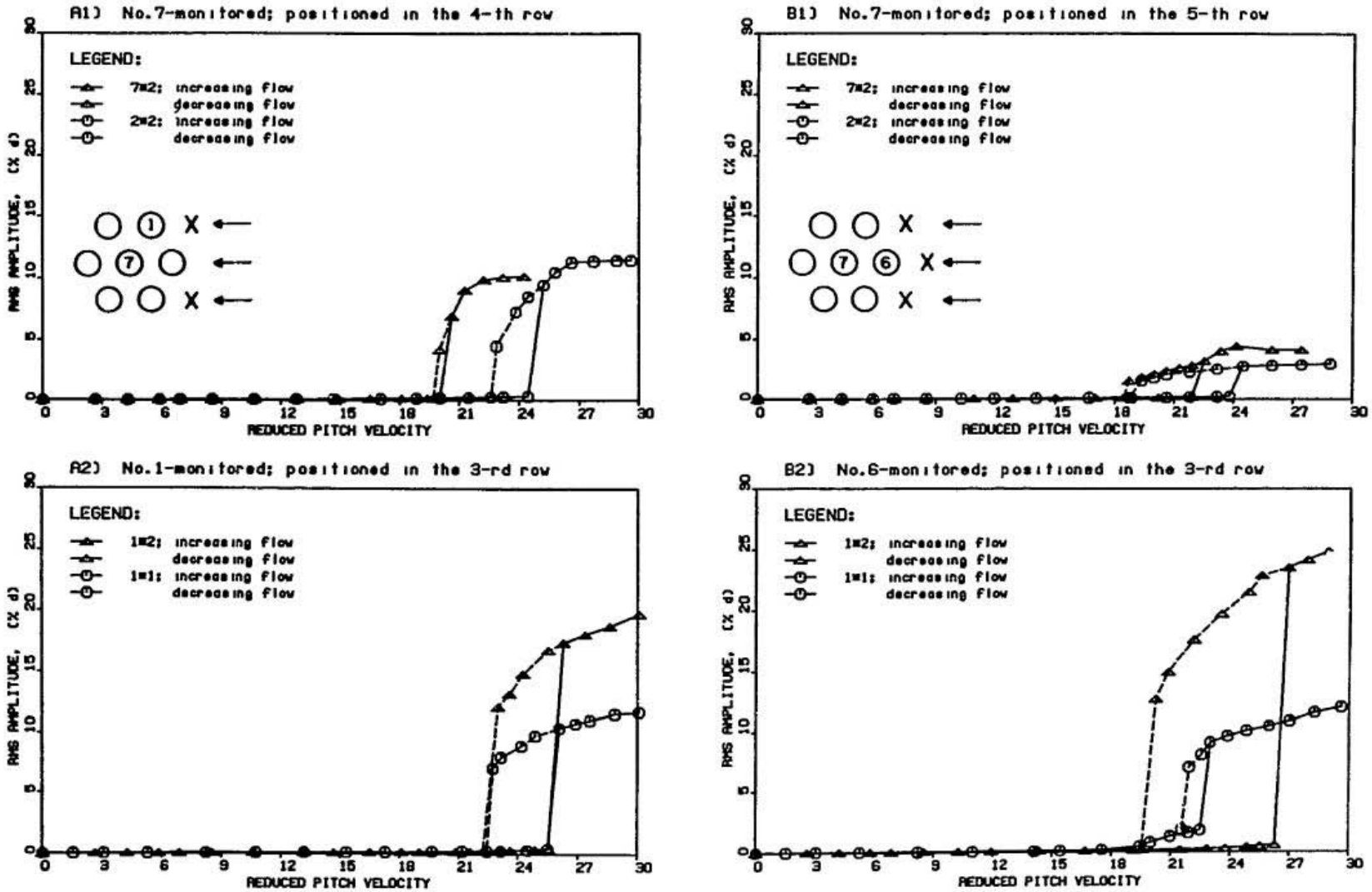

Figure 5.5: RMS response · ves for a parallel triangular array, $\bar{m}\delta_0 \approx 8.4 - 11.2$.

- Figure 5.5(a) - the central cylinder in 4-th row:
  - No.7: 7×2 displays very narrow hysteresis (No.7: 1×2 does not)
  - No.7: 2×2 replicates No.7: 7×2 post-stable behaviour, however initiation of instability is delayed (only one 2×2 configuration, No.7 and No.1, show coupled motion which is not present for 2×1)
  - No.1: 1×2 and No.1: 1×1 closely reflects No.7: 2×2 behaviour, thus initiation of instability is delayed with respect to No.7: 7×2 (No.5: 1×2 shows better qualitative agreement with No.7: 7×2 behaviour, however No.5 and No.7 do not show coupling in 2×2 configuration)
- Figure 5.5(b) - the central cylinder in 5-th row:
  - No.7: 7×2 displays wide hysteresis, post-stable plateau is very low (No.7: 1×2 is stable in the tested velocity range)
  - No.7: 2×2 closely replicates No.7: 7×2 behaviour (only one 2×2 configuration, No.7 and No.6, show coupled motion which is not present for 2×1)
  - No.6: 1×2 displays qualitatively similar hysteresis behaviour to No.7: 7×2 and No.7: 2×2, higher post-stable response (No.6 is the only clearly unstable cylinder)
  - No.6: 1×1 displays significantly narrower hysteresis than No.6: 1×2 and becomes unstable earlier

The results for the central cylinder in 6-th row are not discussed since all configurations (including No.7: 7×2) were found stable in the tested velocity range.

Figure 5.6 shows results obtained at $\bar{m}\delta_0 \approx 22.1 - 23.5$ (set 7, Table 4.1). The recorded response curves are more difficult to interpret due to general lack of coupling in 2×2 configurations (Figures A16-A21 indicate that the case presented in

Figure 5.6(b1) is the only exception). Thus, the dominant cylinder, whose role in an array was so pronounced (as a source of post-stable behaviour) in the lower ranges of the mass-damping parameter, cannot be clearly identified. Here, it appears that the least stable single flexible cylinder (1×2), whose response is presented for comparison, may initiate instability of a flexible array (7×2). However, the post-stable behaviour of this initially dominant cylinder results from coupling between all free-to-move cylinders.

- Figure 5.6(a) - the central cylinder in 4-th row:
  - No.7: 7×2 displays wide hysteresis (No.7: 1×2 does not)
  - No.7: 2×2 is stable in the tested velocity range (No.1: 2×2 replicates qualitatively No.7: 7×2 behaviour)
  - No.1: 1×2 and No.1: 1×1 show essentially identical behaviour as No.1: 2×2, however No.1: 1×1 becomes unstable later (3-rd row flexible cylinders, No.1 and No.5, display similar 1×2 and 1×1 behaviour)
- Figure 5.6(b) - the central cylinder in 5-th row:
  - No.7: 7×2 displays wide hysteresis, post-stable plateau is very low (No.7: 1×2 is stable in the tested velocity range)
  - No.7: 2×2 also shows hysteresis, however it is narrow and induced earlier (only one 2×2 configuration, No.7 and No.6, shows coupled motion which is not present for 2×1)
  - No.6: 1×2 displays qualitatively similar hysteresis behaviour to No.7: 2×2, post-stable response is substantially higher (No.6 is the only clearly unstable cylinder)
  - No.6: 1×1 does not display hysteresis, however post-stable response replicates closely that of No.6: 1×2 for decreasing flow velocity

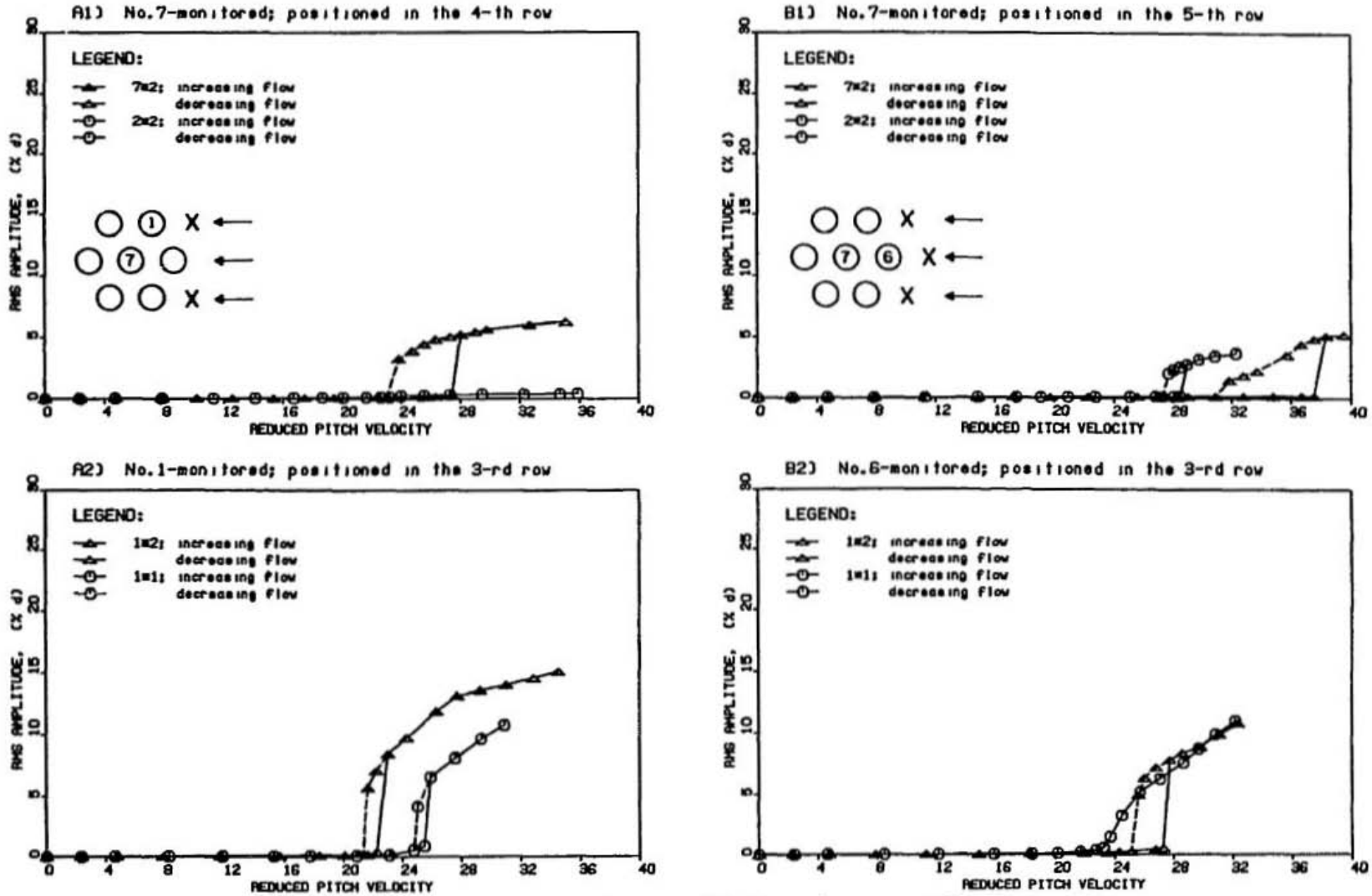

Figure 5.6: RMS response curves for a parallel triangular array, $\bar{m}\delta_0 \approx 22.1 - 23.5$.

As before, for the central cylinder in 6-th row, all tested configurations (including No.7: 7×2) were found stable.

When studied together, the presented Figures indicate that only cylinders in the second and third row display hysteresis (first row was not investigated). These cylinders tend to dominate the 7×2 configuration and their post-stable behaviour is only slightly modified by the motion of flexible neighbours (especially, at a low mass-damping parameter range). Thus, it appears that the observed hysteresis in a 7×2 array is due to the cascade effect, which is caused by fluid coupling, and has its actual source in the behaviour of the dominant cylinder (qualitatively well represented by a 1×1 system). Fluid coupling, however, becomes less significant with increasing mass-damping parameter and clearly coupled modes between cylinders do not occur. Unfortunately, quantitative comparison between the dominant cylinder and a 7×2 array is hindered by shifts in the location of the stability threshold. This could be attributed to geometrical imperfections, resulting from unavoidable modifications to change the number of degrees-of-freedom. Note, however, that the lowest point on the hysteresis curve, which should be chosen as the practical stability threshold, is significantly less affected.

Effect of mass

In view of Figures 5.4-5.6, the overall effect of increasing the mass parameter, $\bar{m}$, is to increase the critical flow velocity and to lower the non-linear plateau of the post-stable amplitudes. Also, fluid coupling becomes less important. The stability threshold is always well defined due to existence of a response jump, characterizing a hysteresis loop. In general, the width of the hysteresis region decreases, suggesting that hysteresis behaviour may disappear at $\bar{m}\delta_0 \approx 30.0$. This observation agrees with the experimental results presented by Hara, [21] and Andjelic, [55].

Table 5.1 gives a summary of the experimental data for the monitored cylinder

in the fourth row of the 7 flexible cylinder array (No.7: 7×2 - these results are most commonly reported in the open literature) and for the single flexible dominant cylinder in an otherwise rigid array (1×2 and 1×1). For completeness, the varied-damping data are also presented.

Table 5.1: A summary of experimental results for a parallel triangular array; varied damping and mass.

Set	$\bar{m}\delta_0$	7×2			1×2			1×1		
		U_C	U_H	$\frac{U_C - U_H}{U_C}$	U_C	U_H	$\frac{U_C - U_H}{U_C}$	U_C	U_H	$\frac{U_C - U_H}{U_C}$
1	2.1	13.66	10.42	24 %						
2	2.3	12.96	10.89	14 %						
3	5.0	14.21	12.81	10 %						
4	7.5	15.35	14.47	6 %						
5	1.9	13.75	11.04	20 %	18.15	13.93	23 %			
	2.4							18.15	16.87	7 %
6	11.2	19.91	19.65	2 %	19.66	18.30	7 %			
	8.4							25.92	22.55	13 %
7	23.5	27.43	23.03	16 %	22.26	21.30	4 %			
	22.1							25.48	24.75	3 %

The critical flow velocities, U_C, and the hysteresis velocities, U_H, are plotted in Figure 5.7 together with the stability threshold limits observed by other researchers (based on Reference [16], the direct comparison with data for a 1.375 pitch ratio parallel triangular array is presented in Section 7.2.1). It can be seen that, while the hysteresis velocities all lie well within these limits, the critical flow velocities are concentrated mainly near the upper stability boundary, in some cases exceeding it. It should be remembered, however, that the stability criterion used in this study is, in general, unconservative (see discussion in Section 3.3.1). Moreover, since the concept of excited instability within the hysteresis region is not clarified in the literature, it is believed that some experimental data reported are in fact within the hysteresis region. Notice that the general trend with respect to the mass-damping

parameter is similar with that suggested by the limits of all experimental data.

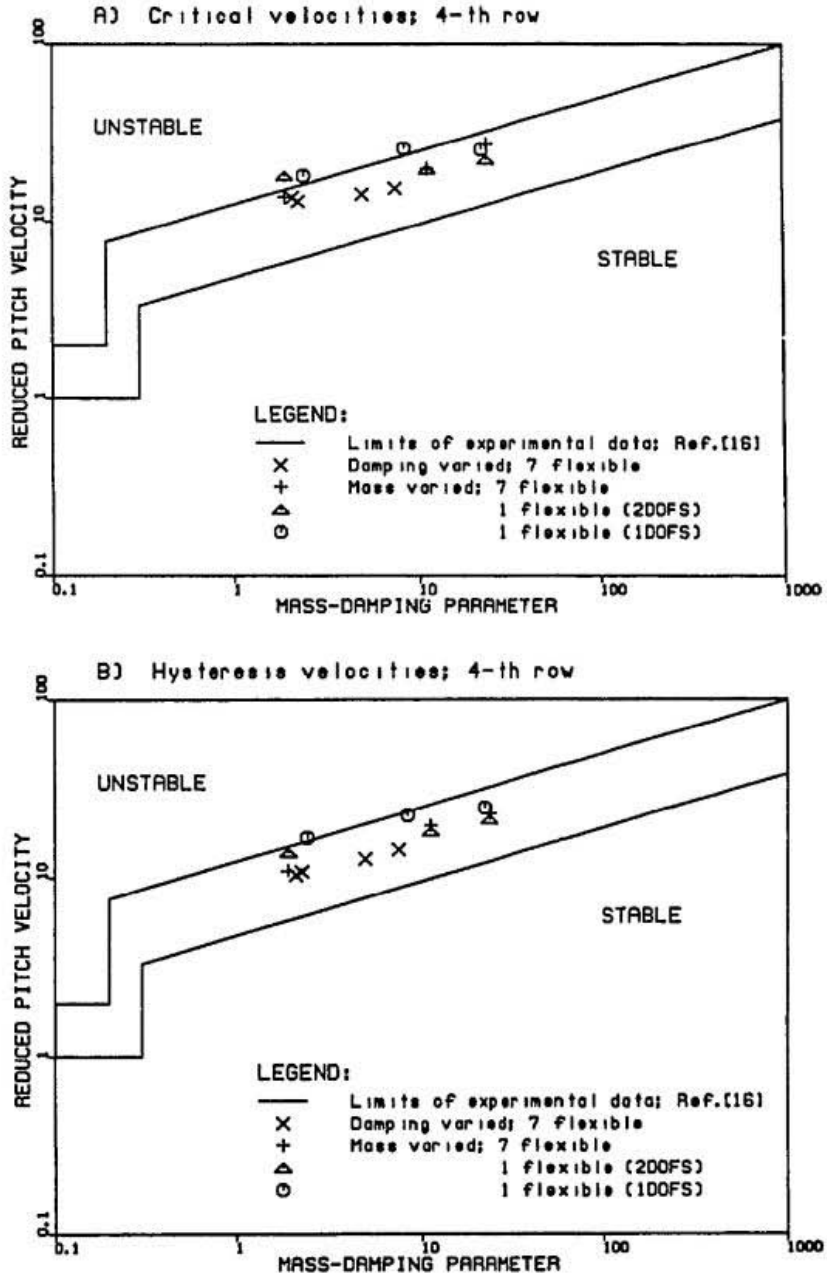

Figure 5.7: Stability plots comparing present experimental data ($\bar{m}\delta_0 \approx 1.9-23.5$) to existing in the literature for a parallel triangular array; (a) critical and (b) hysteresis flow velocities.

5.1.2 Velocity-dependent damping

The velocity-dependent damping was determined for the cylinder positioned in the fourth row of the 7 and 1 flexible cylinder arrays in streamwise and transverse-to-flow directions, separately. Only one cylinder was monitored, since the experimental data reported by Weaver and El-Kashlan, [31], indicate that the damping is virtually independent on the cylinder location within an array. At a given flow velocity, the velocity-dependent damping as a function of amplitude was estimated from pluck-generated decay curves. By subtracting the value of damping in quiescent fluid, the fluidelastic damping factor, ζ, was derived. Figures B1 and B2, which are included in Appendix B, show that the fluidelastic component of damping is essentially independent on the amplitude, except in the amplitude range close to the steady turbulence response level where a significant scatter in measured data was observed (especially, near the stability threshold). It was thus felt that in this range a larger number of tests would be required to obtain reliable estimates of damping. Notice that, within the hysteresis limits, the experiment could not be fully completed due to the existence of an unstable limit cycle which manifested itself in very low damping values at higher response levels.

Figure 5.8 shows the results as a function of reduced pitch velocity, together with the response curves for easy of interpretation. Figure 5.8(a) shows that the fluidelastic component of damping for the 7 flexible cylinder array, after an initial drop, increases linearly with flow velocity upto $\sim$ 60 % U_C and is essentially identical in both the streamwise and transverse-to-flow directions. For higher flow velocities, the damping in the transverse-to-flow direction (y) decreases, approaching zero (quiescent fluid damping) towards the stability threshold, U_C, while the damping in the streamwise direction (x) continues to increase linearly upto the lowest limit of hysteresis region, $U_H \approx 80$ % U_C. Thus, as it was already observed experimentally, the cylinder loses stability in the transverse-to-flow direction. These trends

were compared with those of Weaver and El-Kashlan, [31], who reported the only experimental data for this array available in the literature. They used essentially an identical technique of damping estimation. The measurement, however, was performed close to the actual response level to avoid the effect of eventual non-linearity (the average value of three pluck tests was reported). It can be seen that the trends from both experiments are quite consistent; initially, both curves increase linearly with reduced pitch velocity (proportionality constant ~ 0.015), reaching a peak at $\sim 50-60$ % U_C and then decreasing gradually towards the stability threshold. The quantitative difference results apparently from the lower stability threshold observed by Weaver and El-Kashlan; $U_{P_r} = 8.66$ in comparison to $U_{P_r} = 13.75$ obtained in this study.

Figure 5.8(b) presents the corresponding results for the single flexible cylinder in an otherwise rigid array. It can be seen that, in the velocity range upto ~ 50 % U_C, the fluidelastic component is virtually identical to that of the 7 flexible cylinder array. However, for higher flow velocities, the damping further increases in the transverse-to-flow direction (y), reaching a maximum value at a velocity ~ 90 % U_C where it starts to decrease sharply, approaching zero at the threshold, while the damping in the streamwise direction (x) is approximately constant. As with the 7 flexible cylinder array, the system has only the structural component of damping to overcome to become unstable. Unfortunately, there are no another experimental data in the open literature to compare with.

From comparison of Figures 5.8(a) and 5.8(b), the role of fluid coupling in the sub-critical region becomes apparent. At a velocity ~ 50 % U_C, the damping in the transverse-to-flow direction starts to decrease towards threshold in the 7 flexible cylinder array, while in the 1 flexible cylinder array it continues to grow linearly with flow upto a velocity ~ 90 % U_C. It is felt that this difference can be completely attributed to coupling between flexible cylinders.

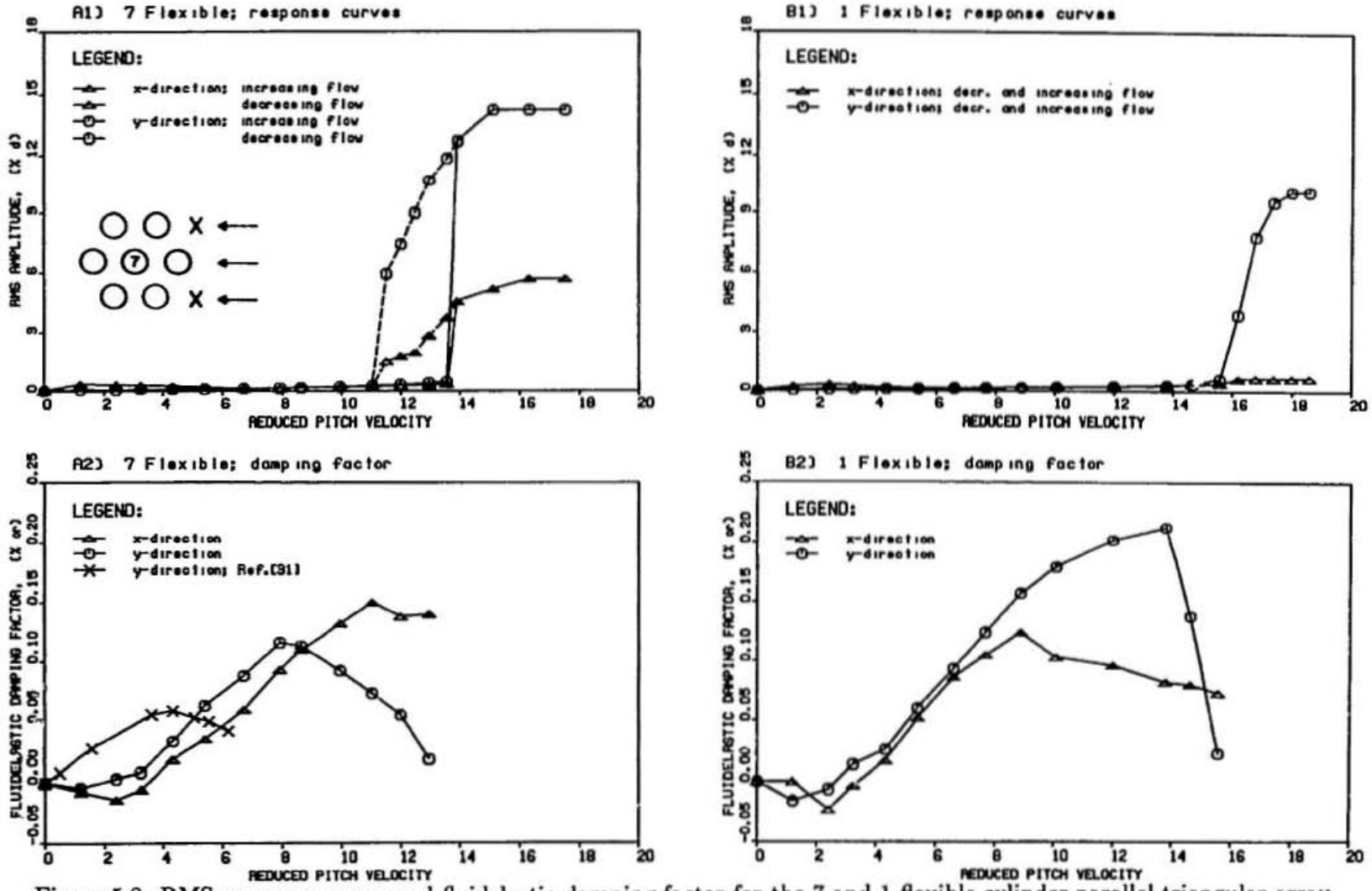

Figure 5.8: RMS response curves and fluidelastic damping factor for the 7 and 1 flexible cylinder parallel triangular array, $\bar{m}\delta_0 = 2.25$.

Interestingly, the damping in the 1 flexible cylinder array shows good qualitative agreement with theoretical prediction of Blevins, [7]. He found that the fluid damping factor for the single structure, oscillating in the fundamental mode, may be expressed as:

$$\zeta_x = \frac{1}{2} C_D \left(\frac{\rho d^2}{m}\right)\left(\frac{U}{\omega_0 d}\right) \tag{5.1}$$

$$\zeta_y = \frac{1}{4} C_D \left(\frac{\rho d^2}{m}\right)\left(\frac{U}{\omega_0 d}\right) \tag{5.2}$$

where ζ_x and ζ_y are the damping factors in the streamwise and transverse-to-flow directions, respectively, C_D denotes the steady fluid drag, and U is the flow velocity in the vicinity of the structure (in the case of cylinder arrays, $U = U_0$, the actual velocity in the gap between the cylinders). These equations are linearized, for the small amplitude oscillations with respect to the flow velocity, since it was found that velocity-dependent damping in cylinder arrays is essentially independent of the oscillatory amplitude (see Figures B1 and B2) and the non-linear terms may be neglected. By fitting the single-flexible-cylinder experimental data to equation (5.2), the value of drag coefficient $C_D \approx 2.20$ was obtained.

It follows from equation (5.1) and (5.2) that the streamwise damping component should be twice higher than that in the transverse-to-flow direction. This is not reflected in the experimental data, perhaps, due to the existence of an upstream wake region, in front of the cylinder oscillating within an array, which reduces steady drag. For comparison, the experimental data for the 7 flexible cylinder array were also fitted to equation (5.2), yielding $C_D \approx 1.90$ and $C_D \approx 1.60$ for the present test and that of Weaver and El-Kashlan, respectively.

5.2 Square array

The tested cylinder array, which consisted of 9 flexible cylinders surrounded by rigid neighbours, is illustrated in Figure 4.3. The monitored cylinder, No.9, was positioned either in the third row, for a basic geometry, or in the fourth row with additional upstream cylinders installed.

5.2.1 Post-stable behaviour

Preliminary tests

As with the parallel triangular array, the nature of post-stable oscillations was first sought, based on both steady flow and transient excitation tests, for the 9 and 1 flexible cylinder arrays. The monitored cylinder was in the third row to ensure flexibility of all cylinders within the critical zone (second to fourth row). Figure 5.9(a) shows results from steady flow tests which are essentially similar to those reported for the parallel triangular array; the 9 flexible cylinder configuration displays hysteresis behaviour, while the single flexible cylinder in an otherwise rigid array does not. The most noticeable difference is the low stability threshold in the latter case, $U_{Pr} = 7.28$, which is within the hysteresis region of the 9 flexible cylinder array ($U_{Pr} = 6.42 - 7.84$). Thus, the lack of hysteresis for the 1 flexible cylinder array must be interpreted with caution since the observed U_C could be U_H (indeed, in subsequent tests, hysteresis behaviour was observed). For the 9 flexible cylinder array, a stability threshold of $U_{Pr} = 7.84$ can be clearly assigned since the monitored cylinder experiences a vertical response jump at this point, reaching a post-stable amplitude of $A_{RMS} \approx 26.0$. The non-linear plateau was not clearly observed, since higher flow velocities resulted in a further increase of post-stable oscillations and, finally, cylinder clashing. The lowest point on the hysteresis curve may be taken as $U_{Pr} = 6.42$, yielding a width of 18 % U_C. For the 1 flexible cylinder array, the stability threshold is also clearly defined. Similarly, the response curve is close to

vertical at this point and does not saturate for slightly higher velocities.

Figure 5.9(b) shows displacement excitation results for the 9 flexible cylinder array; the final RMS amplitudes after transients together with the minimum RMS excitation levels. As with the parallel triangular array, the final post-stable RMS amplitudes (each showing no tendency to return to its original stable vibration level) were very close to those levels recorded during the steady flow tests. Again, for flow velocities less then U_H ($U_{Pr} = 6.42$), the flexible cylinders always remained stable, regardless of the excitation level. For flow velocities between U_H and U_C, minimum excitation levels were found which caused a transition to post-stable oscillations with all 9 flexible cylinders vibrating at large amplitudes. It can be seen that, unlike the parallel triangular array, these excitation amplitudes all lie within the hysteresis region and indicate the actual position of the unstable limit cycle. This suggests that the observed hysteresis results not from coupling with the flexible neighbours, as in the case of the parallel triangular array where a non-dominant cylinder was excited, but rather from the single flexible dominant cylinder characteristics. However, this observation was not confirmed by the experiments on the 1 flexible cylinder array since the single flexible cylinder always returned to its original vibration amplitude after any excitation (this is as expected since, in steady flow tests, no hysteresis was observed).

Notice that the unstable limit cycle for the 9 flexible cylinder array yields the RMS amplitudes ($A_{RMS} \approx 2.5, 2.0, 1.75$ % d for $U_{Pr} = 6.75, 7.18, 7.71$, respectively) which are only slightly higher than the stable response levels ($A_{RMS} = 0.63, 0.76, 1.20$ % d, respectively). In this case, a transition from stable to post-stable behaviour is very easy within the hysteresis region. Thus, severe imperfection sensitivity, perhaps already observed in the response of the single flexible cylinder, may be expected.

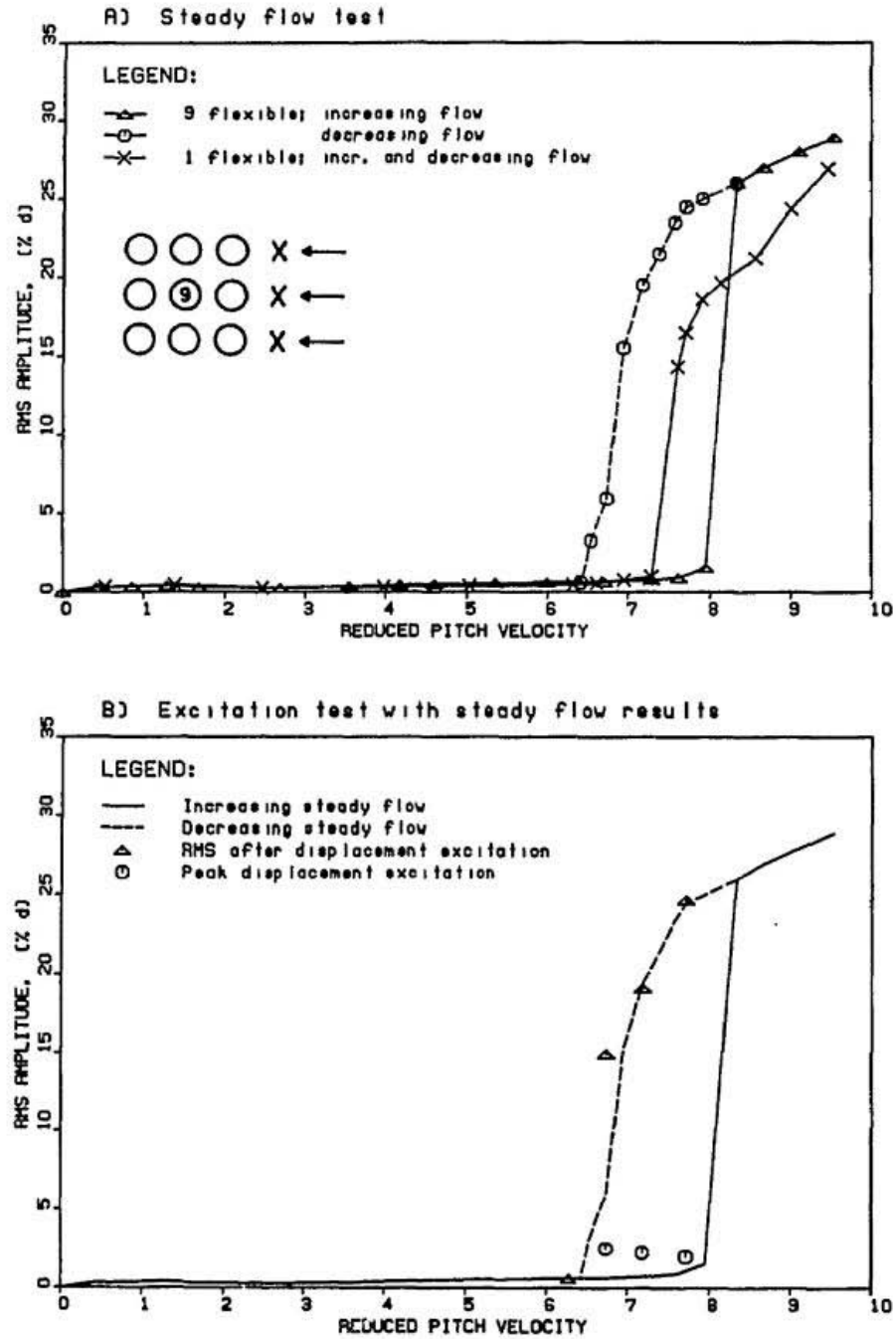

Figure 5.9: RMS response curves for the 9 and 1 flexible cylinder square array; (a) steady flow and (b) excitation tests.

Imperfection sensitivity

The next series of tests were conducted with the motivation to confirm the hypothesis that imperfection sensitivity, associated with cylinder alignment, could cause qualitative difference in the observed behaviour of the 9 and 1 flexible cylinder arrays. The position of the monitored cylinder was almost identical in both configurations (the steady blow-back for the 1 flexible cylinder array was less than ~ 1 % of the gap between the cylinders and, therefore, was not corrected). However, the surrounding flexible cylinders could be slightly displaced due to inevitable change between free-to-vibrate (9 flexible) and fixed (1 flexible) positions. Therefore, steady flow tests were repeated on the 1 flexible cylinder array with the upstream one (No.8) displaced by ~ 10 % of the gap between the cylinders.

Figures 5.10(a)-5.10(d) show the response curves with the cylinder No.8 displaced upstream, downstream, left and right, respectively. Notice that unlike the previously obtained response curve, which is also presented in Figure 5.10 (denoted as "ideal"), all display hysteresis. Interestingly, the post-stable behaviour shown in Figure 5.10(d) is virtually identical to that obtained for the 9 flexible cylinder array. Although the response curves shown in Figures 5.10(a), 5.10(b) and 5.10(d) are qualitatively similar, the strongly delayed stability threshold in Figure 5.10(c) is difficult to explain.

This test suggests that, indeed, slight imperfections in cylinder alignment can not only modify (as in the case of parallel triangular array) but drastically change the post-stable behaviour. Thus, this geometric imperfection sensitivity may account for why the subsequent tests, on a number of degrees-of-freedom needed to model the post-stable behaviour of cylinder arrays, were somewhat confusing and difficult to interpret.

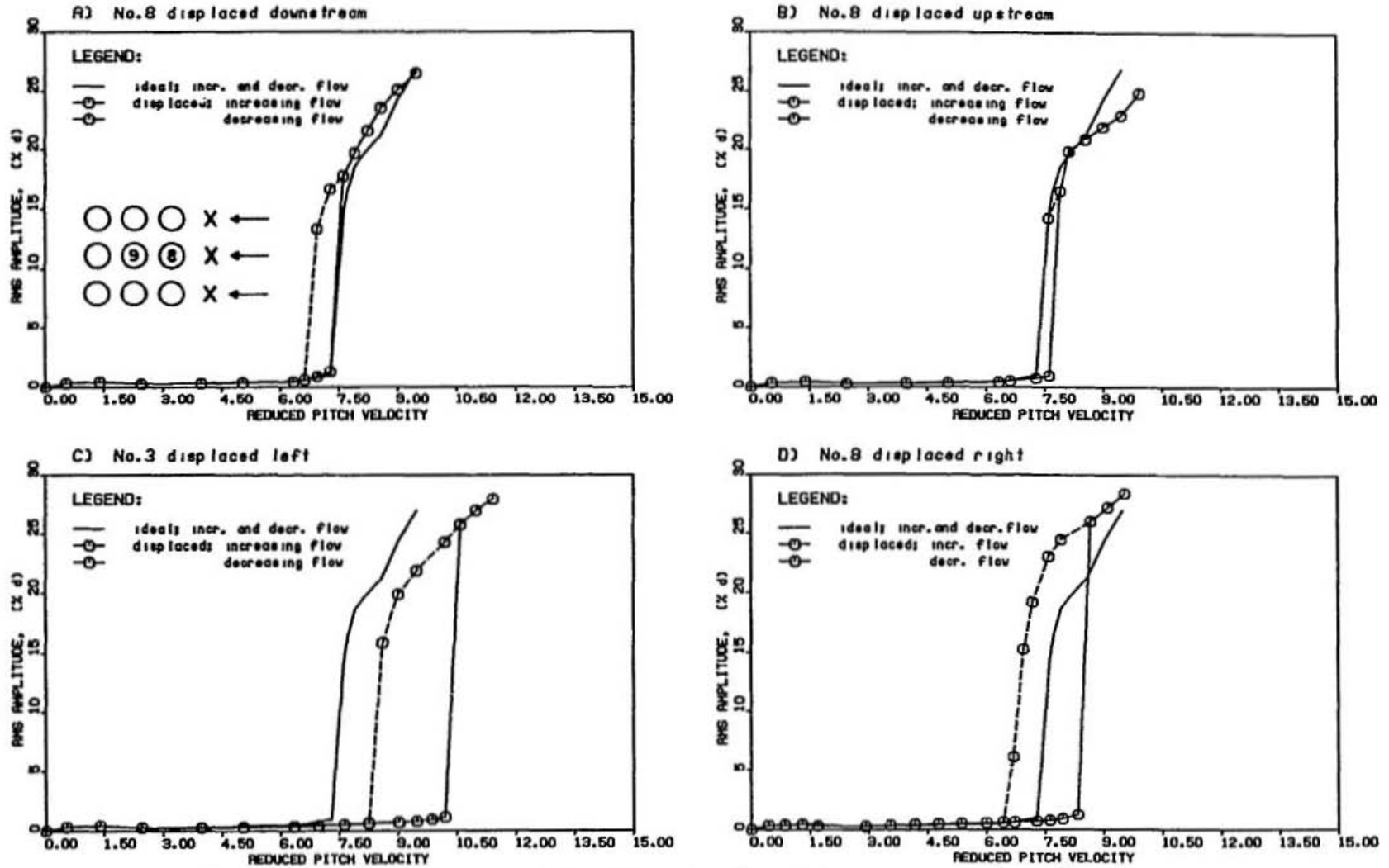

Figure 5.10: Imperfection sensitivity of the 1 flexible cylinder square array (±10 % gap).

Effect of number of degrees-of freedom

An experimental program, virtually identical to that conducted previously for the parallel triangular array, was undertaken to reduce a number of degrees-of-freedom needed to model the post-stable behaviour of a fully flexible array. Figures 5.11-5.13 show the essential results obtained with the mass-damping parameter in the range of $\bar{m}\delta_0 \approx 1.9-23.5$ (set 8, 9 and 10 in Table 4.1). For a given geometry, each Figure contains four response curves (reflecting the process of gradual reduction from 18 to 1 degree-of-freedom); the central cylinder in the 9 flexible cylinder array (No.9: 9×2), the central cylinder in the 2 flexible cylinder array (No.9: 2×2) and the dominant single flexible cylinder (1×2 and 1×1). For completeness, additional results for the upstream (No.8) and the downstream (No.4) cylinders, which show coupled motion in No.9: 2×2 configurations, are presented in Appendix A (Figures A22-A33). Below, some observations are noted following from examination of Figures 5.11-5.13 and Figures A21-33 (in brackets).

Figure 5.11 shows the results of experiments conducted at $\bar{m}\delta_0 \approx 1.9-2.8$ (set 8, Table 4.1). Again, it appears that there is one cylinder in the bundle (No.9: 1×2) which, *via* fluid coupling, dominates 2×2 and 9×2 behaviour. Its role, however, is difficult to establish based on Figure 5.11 alone since all 2×2 configurations tested show strong coupled motion (this requires careful analysis of Figures A22-A25). Unfortunately, 1×2 and 1×1 behaviour of the dominant cylinder, although phenomenologically similar, cannot be directly compared due to a strongly delayed initiation of instability in the 1×1 system (in some cases, U_C is twice higher, as in Figure 5.11(b2), for example). This may be either due to geometric imperfection sensitivity or separation of mass-damping parameter ($\bar{m}\delta_0 = 1.9$ for 1×2 in comparison to $\bar{m}\delta_0 = 2.8$ for 1×1) which causes instability in the higher region (see Section 7.2.1, for details).

- Figure 5.11(a) - the central cylinder in 3-rd row:
  - No.9: 9×2 displays hysteresis
  - No.9: 2×2 closely reflects No.9: 9×2 behaviour, however it shows narrower hysteresis (all 2×2 configurations behave similarly to No.9: 9×2, very weak coupling for 2×1 configurations)
  - No.9: 1×2 does not display hysteresis, however its post-stable response replicates well No.9: 2×2 behaviour for decreasing flow (No.8: 2×1 displays hysteresis)
  - No.9: 1×1 shows hysteresis, however initiation of instability is strongly delayed (No.4: 1×1 and No.8: 1×1 behaviour is qualitatively similar to that of No.9: 1×1)
- Figure 5.11(b) - the central cylinder in 4-th row:
  - No.9: 9×2 does not display hysteresis
  - No.9: 2×2 shows very narrow hysteresis, its post-stable response for decreasing flow velocity is similar to that of No.9: 9×2 (all 2×2 configurations behave similarly to No.9: 9×2, very weak coupling for 2×1 configurations)
  - No.9: 1×2 replicates closely No.9: 9×2 behaviour for decreasing flow (No.8: 2×1 displays clear hysteresis)
  - No.9: 1×1 shows wide hysteresis, however initiation of instability is strongly delayed (No.4: 1×1 and No.8: 1×1 do not display hysteresis, however they show good agreement with No.9: 1×1 post-stable response for decreasing flow velocity)

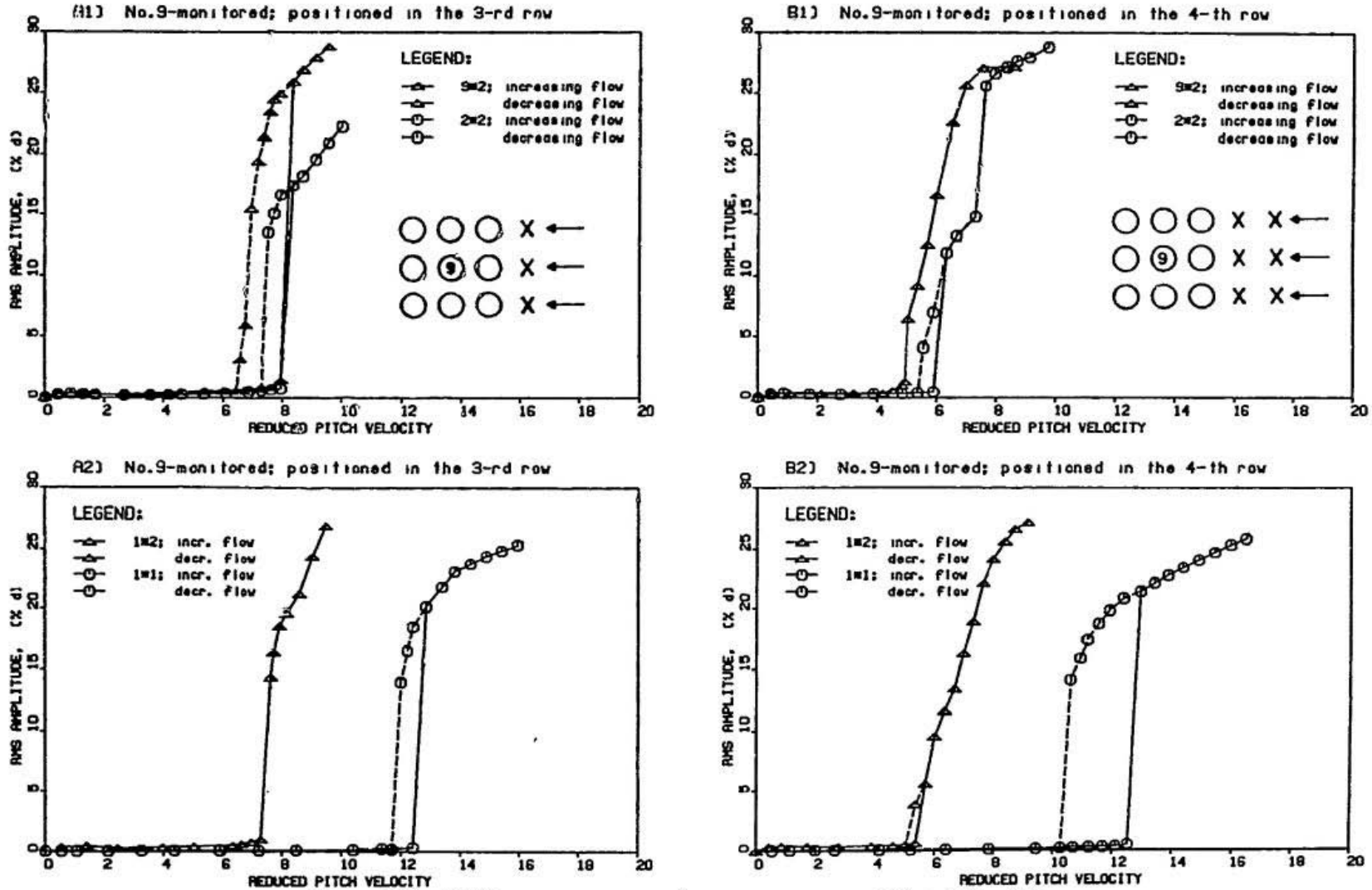

Figure 5.11: RMS response curves for a square array, $\bar{m}\delta_0 \approx 1.9 - 2.8$.

Figure 5.12 shows the next series of results obtained at $\bar{m}\delta_0 \approx 9.8 - 11.2$ (set 9, Table 4.1). These response curves, showing good agreement in exact details of fluidelastic instability, are easier to interpret. The most noticeable difference to the lower $\bar{m}\delta_0$ is the weaker coupling in the tested 2×2 configurations which is present mostly between cylinders in the same row (see Figures A26-A29).

- Figure 5.12(a) - the central cylinder in 3-rd row:
  - No.9: 9×2 displays clear hysteresis (No.9: 1×2 does not, however its post-stable response shows good agreement with No.9: 2×2 behaviour for decreasing flow)
  - No.9: 2×2 closely replicates No.9: 9×2 behaviour (only one 2×2 configuration, No.9 and No.8, behaves similarly to No.9: 9×2, weak coupling for 2×1 configurations)
  - No.8: 1×2 displays qualitatively similar hysteresis, however it becomes unstable earlier
  - No.8: 1×1 does not show hysteresis, however its post-stable response is qualitatively similar to No.9: 2×2 behaviour for decreasing flow velocity (good agreement with No.4: 1×1 and No.8: 1×1 behaviour)
- Figure 5.12(b) - the central cylinder in 4-th row:
  - No.9: 9×2 displays clear hysteresis (No.9: 1×2 does not)
  - No.9: 2×2 closely replicates No.9: 9×2 behaviour (only one 2×2 configuration, No.9 and No.8, behaves similarly to No.9: 9×2, weak coupling for 2×1 configurations)
  - No.8: 1×2 shows good qualitative agreement with No.9: 9×2 behaviour
  - No.8: 1×1 does not display hysteresis, it becomes unstable early (No.9: 1×1 displays hysteresis)

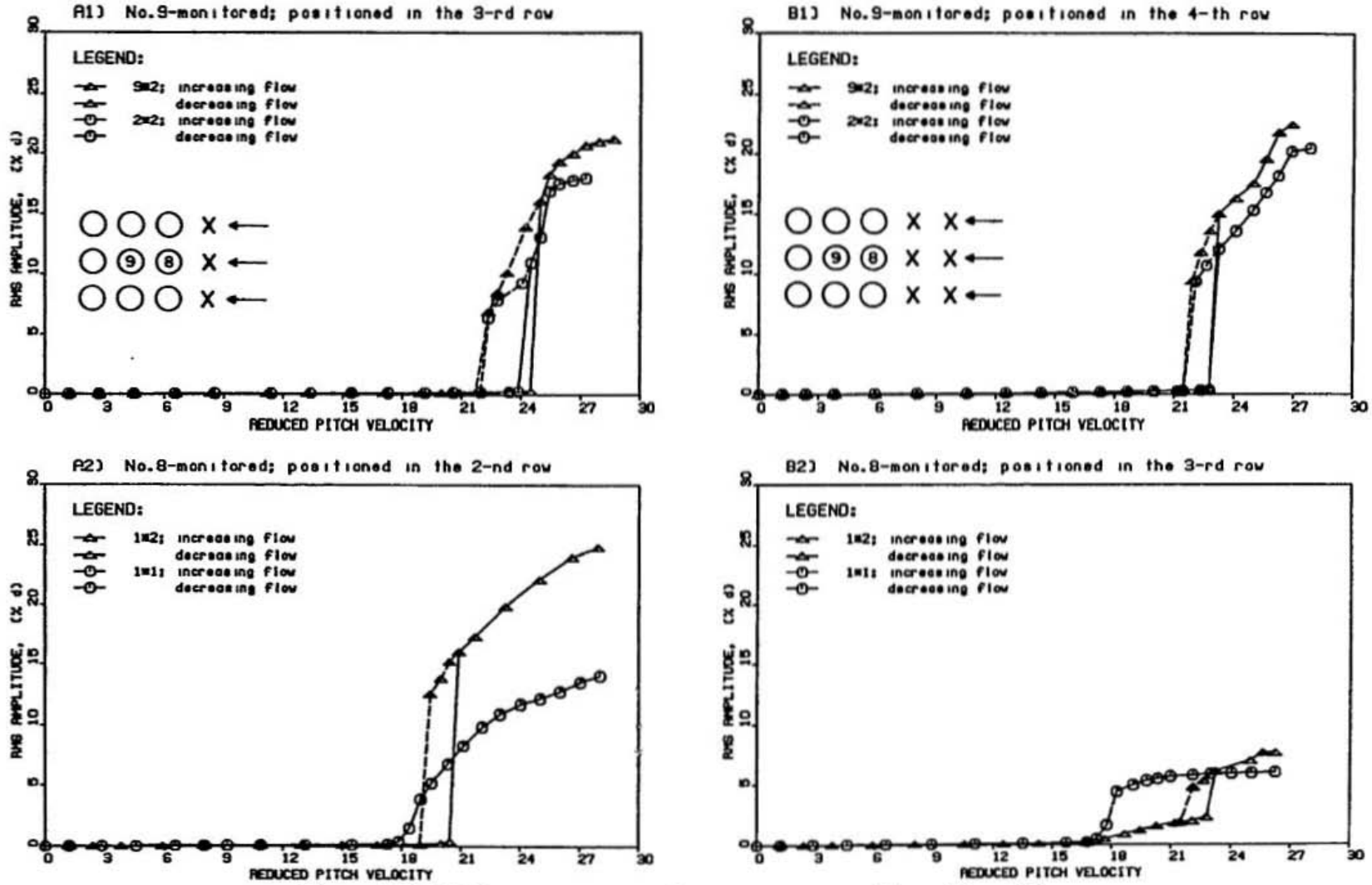

Figure 5.12: RMS response curves for a square array, $\bar{m}\delta_0 \approx 9.8 - 11.2$.

Figure 5.13 shows the corresponding results obtained at $\bar{m}\delta_0 \approx 22.1 - 23.5$ (set 10, Table 4.1). As with the parallel triangular array, the role of the dominant cylinder does not manifest itself as clearly as it did at lower mass-damping parameters due to a general lack of coupling in 2×2 configurations (Figures A30-A33 indicate that the case presented in Figure 5.13(a1) is the only exception). However, fluid coupling is present in all 9×2 configurations, suggesting that more than two flexible cylinders are needed to initiate coupled motions. It was observed that instability, once excited by one of the flexible cylinders, cascades through the array (the post-stable behaviour results from coupling between all free-to-move cylinders). It appears that the least stable single flexible cylinder (No.8: 1×2), whose response is presented for comparison, initiates the instability in the fully flexible array (9×2) at this mass-damping parameter.

- Figure 5.13(a) - the central cylinder in 3-rd row:
  - No.9: 9×2 displays clear hysteresis (No.9: 1×2 does not, however its post-stable response is essentially identical to that of No.9: 9×2 for decreasing flow velocity)
  - No.9: 2×2 does not display hysteresis, however its post-stable response is qualitatively similar to No.9: 9×2 behaviour for decreasing flow velocity (only one 2×2 configuration, No.9 and No.8, shows coupled motion, not present in 2×1)
  - No.8: 1×2 and No.8: 1×1 replicate closely No.9: 9×2 (No.8 is the only clearly unstable cylinder)
- Figure 5.13(b) - the central cylinder in 4-th row:
  - No.9: 9×2 displays clear hysteresis, however the post-stable response plateau is low (No.9: 1×2 does not display hysteresis)

- No.9: 2×2 is stable in the tested velocity range (no coupling in all tested 2×2 and 2×1 configurations)
- No.8: 1×2 does not display hysteresis, however its post-stable response is qualitatively similar to No.9: 9×2 behaviour for decreasing flow velocity
- No.8: 1×1 shows good qualitative agreement with No.9: 9×2 behaviour (No.8 is the only clearly unstable cylinder)

Figures 5.11-5.13, together with Figures A21-A33, clearly indicate that only flexible cylinders in the second, third and fourth rows of a square array can exhibit hysteresis behaviour (first row was not examined). As with a parallel triangular array, these cylinders tend to dominate 9×2 configurations (fluid coupling, however, becomes less significant at higher mass-damping parameters). Again, it appears that the observed hysteresis in a 9×2 array is due to the cascade effect, and has its actual source in the behaviour of the dominant cylinder (well qualitatively represented by a 1×1 system). As expected, the exact details of post-stable behaviour (e.g. critical velocity, hysteresis effects, limit cycle amplitudes) depend strongly on geometrical imperfections, resulting from unavoidable modifications of the tested array. It is worth noting that, again, the lowest point on the hysteresis curve is significantly less affected.

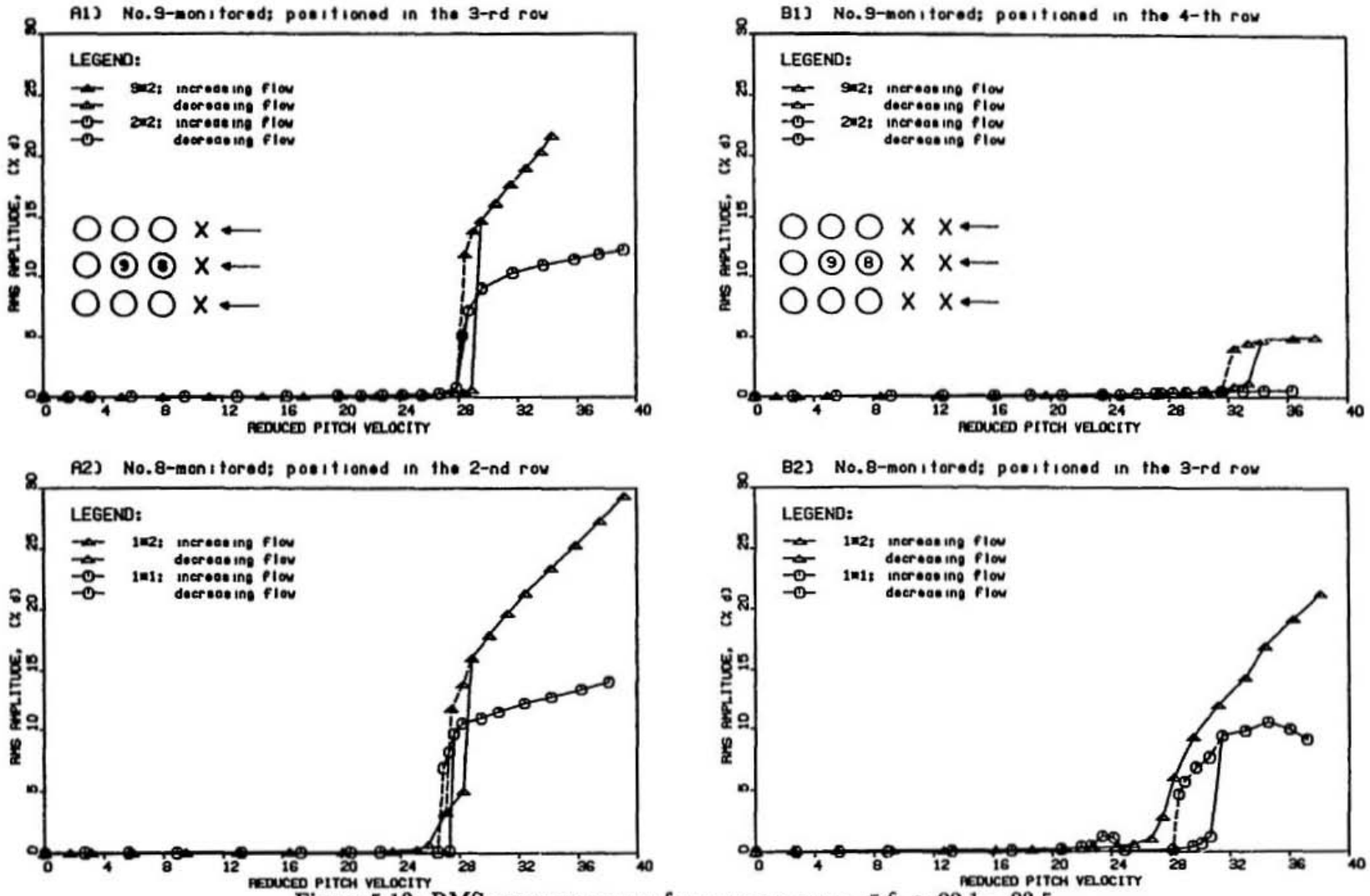

Figure 5.13: RMS response curves for a square array, $\bar{m}\delta_0 \approx 22.1 - 23.5$.

Effect of mass

It follows from Figures 5.11-5.13 that increasing the mass parameter, $\bar{m}$, in the square array generates trends which are similar to those seen in the parallel triangular array. Specifically, it (i) increases the stability threshold, (ii) lowers the non-linear plateau of the post-stable amplitudes, (iii) has less fluid coupling and (iv) reduces the width of the hysteresis regio' Table 5.2 summarizes the experimental data for the monitored cylinder in the third row (stability thresholds of early upstream rows are mainly reported in the open literature) of the 9 flexible cylinder array (No.9: 9×2) and for the single flexible dominant cylinder in an otherwise rigid array (1×2 and 1×1).

Table 5.2: A summary of experimental results for a square array, varied mass.

Set	$\bar{m}\delta$	9×2			1×2			1×1		
		U_C	U_H	$\frac{U_C - U_H}{U_C}$	U_C	U_H	$\frac{U_C - U_H}{U_C}$	U_C	U_H	$\frac{U_C - U_H}{U_C}$
8	1.9	4.90	-	-	5.63	5.03	11 %			
	2.8							12.51	10.26	18 %
9	11.2	22.70	21.45	6 %	22.34	21.45	4 %			
	9.8							18.04	-	-
10	23.5	33.10	31.45	5 %	27.47	-	-			
	22.1							30.68	28.14	8 %

These data, compared with the results of others, are plotted in Figure 5.14. As before, the limits for an experimentally observed stability threshold are defined based on Reference [16]. It can be seen that these limits bracket well all experimental data; the critical and the hysteresis flow velocities. Notice that for cylinders in the fourth row, although the critical flow velocities at the lowest mass-damping parameters are ~ 50 % higher, all results would also fall within the experimental limits.

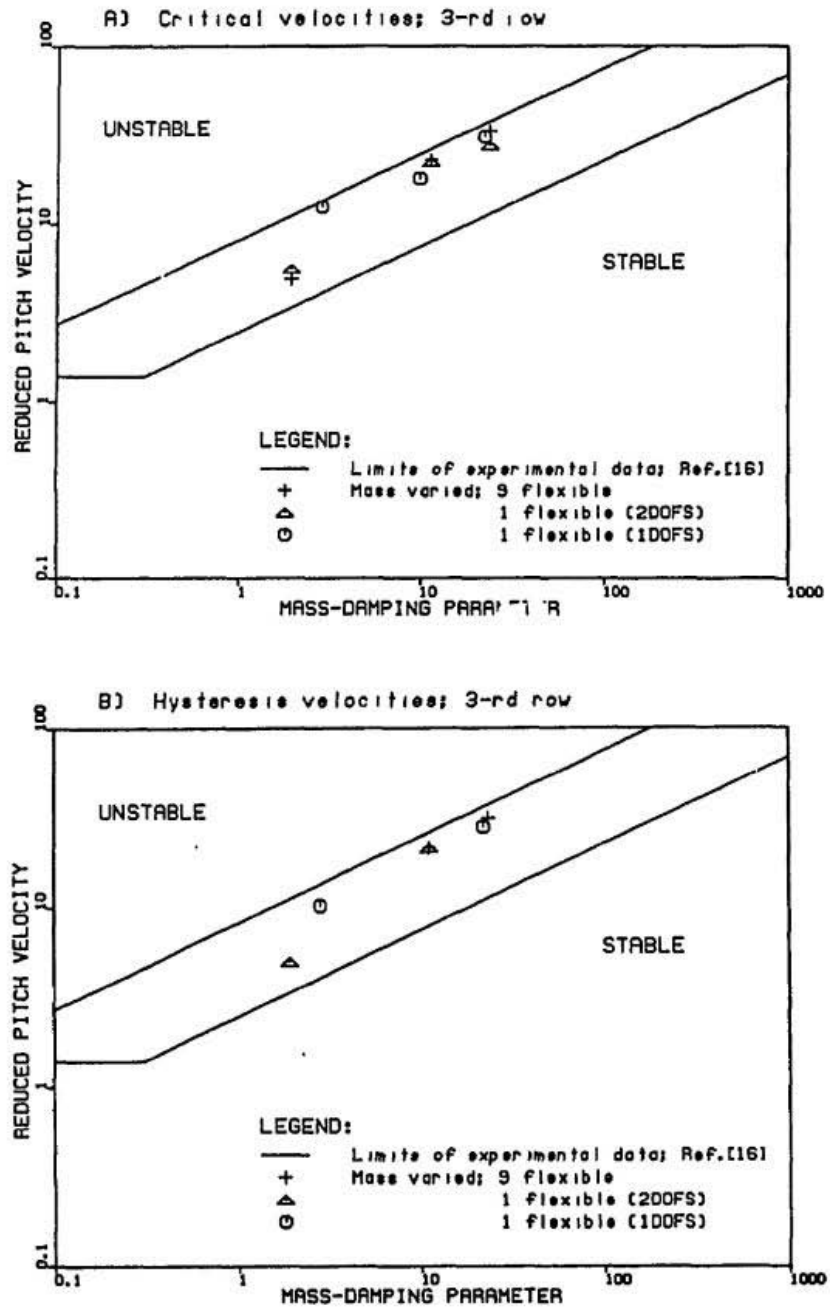

Figure 5.14: Stability plots comparing present experimental data ($\bar{m}\delta_0 \approx 1.9 - 23.5$) to existing in the literature for a square array; (a) critical and (b) hysteresis flow velocities.

5.2.2 Velocity-dependent damping

Damping was estimated using the procedure developed earlier for the parallel triangular array. Here, the monitored cylinder was positioned in the third row. Figures B3 and B4, which are presented in Appendix B, show streamwise and transverse-to-flow components of the fluidelastic damping factor, $\zeta(A)$, as a function of amplitude at a given flow velocity. As before, the damping is essentially independent of the oscillation amplitude.

Figure 5.15 shows the fluidelastic component of damping, obtained by projecting the measured data on the response level induced by turbulence, as a function of reduced pitch velocity (for ease of interpretation, the corresponding response curves are also presented). There are two noticeable changes with relative to the parallel triangular array; (i) the damping is essentially identical for the 1 and 9 flexible cylinder arrays, and (ii) the fluidelastic damping factor in transverse-to-flow direction (y) is, in general, negative (flow does not cause an additional energy dissipation). The first observation suggests that the monitored cylinder is *de facto* dominant in the tested configuration (a similar conclusion may be drawn from an analysis of the response curves presented in Figure 5.11(a)). It can be seen that the damping is initially not affected by the flow but then, at a velocity $\sim$ 50 % U_C, it shows a gradual reduction towards the stability threshold (the net damping approaches approximately zero at this point) in the transverse-to-flow direction and a gradual increase in the streamwise direction (based on equation (5.1), $C_D \approx 0.80$ and $C_D \approx 1.10$ for the 1 and 9 flexible cylinder arrays, respectively). The second observation is that the stability threshold may vary significantly in this configuration due to the very low value of net damping over a large velocity range in the sub-stable region. This, in part, explains the result of the imperfection sensitivity study presented in Figure 5.10.

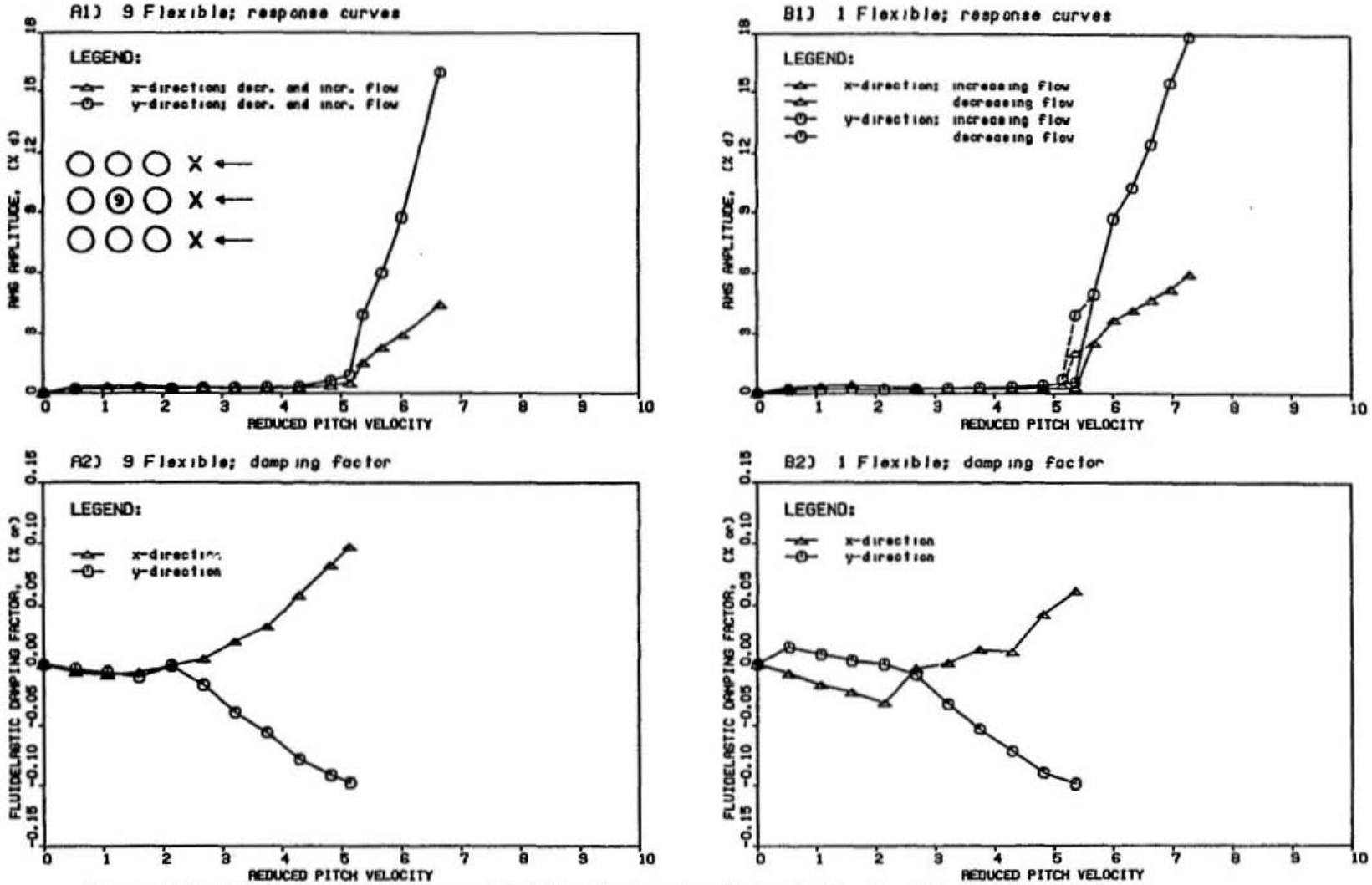

Figure 5.15: RMS response curves and fluidelastic damping factor for the 9 and 1 flexible cylinder square array.

5.3 Conclusions and recommendation for analytical modelling

A detailed experimental study was conducted with the objective to capture the physical essence of the post-stable behaviour of a fully flexible array with a minimum number of degrees-of-freedom. Although the results may appear inconsistent in some aspects, analyzed globally they yield clear trends in the tested mass-damping parameter range.

- The stability behaviour of a fully flexible array results from single flexible cylinder characteristics due to strong coupled motion induced by the dominant cylinder (the effect of coupling, however, decreases with increase of mass-damping parameter). Only two degrees-of-freedom cylinders show coupled motion.

- A single flexible cylinder in an otherwise rigid array may display hysteresis behaviour which appears to vanish at $\bar{m}\delta \approx 30$ (the underlying excitation mechanism is, however, row-dependent and manifests itself in the second and third rows for a parallel triangular array, and in the second to fourth rows for a square array). Thus, coupled motion between flexible cylinders is not required for hysteresis effects.

- The stability behaviour of a single flexible cylinder array may be qualitatively represented by a one degree-of-freedom system which also may display hysteresis. Thus, coupling between streamwise and transverse-to-flow cylinder motions is not essential to the underlying instability mechanism.

- The exact details of the stability behaviour (e.g. critical velocity, hysteresis effects, limit cycle amplitudes) depend strongly on geometric imperfection. Also, turbulence may affect hysteresis behaviour *via* random initiation of instability within the hysteresis region. In the extreme case, $U_C = U_H$.

- The velocity-dependent damping increases approximately linearly with the flow velocity in the sub-critical region (thus, the form suggested by Blevins, [7], may be used to account for the fluid steady drag). The rate of increase, however, depends of the number of flexible cylinders and the array configuration.

- The velocity-dependent damping is essentially independent of the cylinder oscillatory amplitude. Thus, its linearized form, for the small amplitude oscillations with respect to the flow velocity, yields a good approximation.

Briefly, it can be concluded that instability and the post-stable behaviour of a fully flexible array is governed by the dominant cylinder (the least stable) which may be well represented by a one degree-of-freedom system. The velocity-dependent damping, due to the fluid steady drag only, may be modelled using the linearized Blevins' expression.

Chapter 6

Non-linear model for fluidelastic instability

This Chapter describes a theory which is capable of modelling the post-stable behaviour of a cylinder array. Since a complete theoretical analysis of a fully flexible array, due to complexity this would involve, is beyond present capabilities, it was decided to look for a practical alternative. The experimental results, reported and discussed in the previous Chapter provided evidence that fluid damping forces, associated with the motion of a single flexible cylinder within a critical zone in an array, are exclusively operative at stability thresholds and dominant in the post-stable region at the mass-damping parameter range governed by hysteresis-type behaviour ($\bar{m}\delta_0 < 30$). Because of this, the present theory for fluidelastic instability is restricted to a single flexible cylinder in an otherwise rigid array. The flexible cylinder is constrained to move in the transverse-to-flow direction only since it was found from the experiments that this simplified representation is sufficient to capture the essence of its behaviour. The theory includes also the random buffeting due to turbulence which in real situations is always present and can interact with fluidelastic instability. Particularly important is the influence of turbulence on system behaviour near bifurcation points.

6.1 Time-domain formulation

6.1.1 Fluidelastic excitation

The present theory is essentially a modified time-domain version of the linearized steady-state model of Lever and Weaver, [46-48]. Here, the first, [46], more compact version is chosen, to establish foundations for non-linear analysis, due to its simplicity and relatively good agreement with experimental data. However, the latter version, [47,48], is more consistent in terms of physical parameters which describe the arrays of interest (see Figure 1.3); staggered (parallel triangular, normal triangular, rotated square) and normal square. Thus, the geometrical parameters, which define the cylinder-in-channel configuration, are taken from References [47,48]. Since References [46-48] contain the details of the development of this theory, only the modifications necessary to permit a time-domain non-linear formulation will be discussed here. Nevertheless, it is instructive to outline briefly the simplifying assumption, underlying the original model of Lever and Weaver, including extensions to account for the present experimental observations.

- The motion of the neighbouring cylinders is not essential to model the behaviour of the dominant cylinder, either at the stability threshold or in the post-stable region. Fluid coupling is important primarily in triggering instability of adjacent cylinders but its effect on the dominant cylinder may be ignored.

- The mechanisms underlying stability behaviour, in either streamwise or transverse directions, are independent of each other (coupling is not important). Thus, it is legitimate to pursue them individually and to model the dominant cylinder as a single degree-of-freedom system. Instability in the transverse direction has, in general, a significantly lower threshold.

- The motion of a cylinder near its stability threshold is, essentially, periodic at a simple frequency. As the excitation mechanism is a self-excited one, any unsteady flow perturbation, due to cylinder motion, may be assumed to have periodic time dependencies at the cylinder frequency.

- The fluid-elastic excitation mechanism is assumed not to be dependent on wake phenomena. Thus, only perturbations in the free-stream flow along either side of the cylinder are considered.

- A highly regular flow field is defined by each array. The main streamlines tend to pass through an array without crossing from one flow channel to the next. The streamtubes are narrow relative to their length, so that one-dimensional flow assumption can be used.

Figure 6.1 shows the "unit cell" sufficient to describe fully the fluidelastic system controlled by the velocity mechanism. A single flexible cylinder is symmetrically located relative to the apparent position of neighbouring cylinders and undergoes motion $y(t)$ in the transverse-to-flow direction only. The steady streamlines through the array define the boundaries of the "unit cell". Assuming incompressible, one-dimensional flow, the area, velocity and pressure variation along the two streamtubes passing on either side of the cylinder may each be written as the sum of first order functions of position only, plus second order perturbation functions (containing linear and non-linear terms) of both position and time. Employing symmetry conditions, the area, velocity and pressure distribution may be thus written as:

$$A_i(s,t) = \bar{A}(s) + (-1)^{i+1} a(s,t) \qquad a(s,t) < \bar{A}(s) \tag{6.1}$$

$$U_i(s,t) = \bar{U}(s) + (-1)^{i+1} u(s,t) \qquad u(s,t) < \bar{U}(s) \tag{6.2}$$

$$P_i(s,t) = \bar{P}(s) + (-1)^{i+1} p(s,t) \qquad p(s,t) < \bar{P}(s) \tag{6.3}$$

where the subscript $i = 1, 2$ refers to the left and right streamtubes, respectively (see Figure 6.1). From geometry arguments, the area perturbations and, therefore, the velocity and pressure perturbations are limited by the steady-state terms.

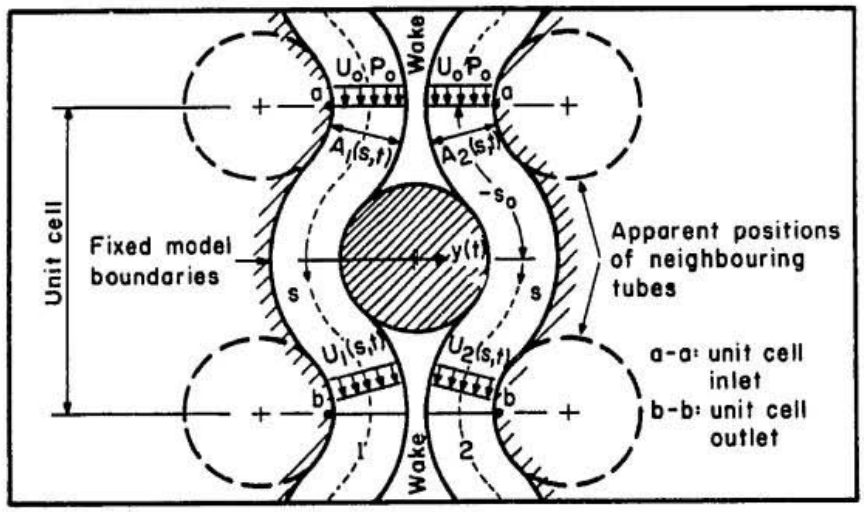

Figure 6.1: "Unit cell" for fluidelastic model.

Whereas the model presented in References [46-48] assumed simple harmonic cylinder motion, the present formulation requires that the time dependence of $y(t)$ and the perturbation functions remain unspecified. In keeping with the hydraulic transient analog presented in Reference [46], it is assumed that the streamtube area perturbation follows the cylinder motion but with a time lag due to fluid inertia. Further, this time lag, τ, varies linearly from $\tau = 0$, at the cylinder centerline ($s = 0$), to $\tau_0 = \frac{l}{U_0}$ at the unit cell inlet ($s = -s_0$), where l is relevant fluid inertia length for small cylinder motion. Thus, to a first approximation, the streamtube perturbation function may be written as:

$$a(s,t) = y(t + \tau_0 \frac{s}{s_0}) \tag{6.4}$$

Note that since s is negative in the direction of the inlet, this area perturbation lags cylinder motion, as required.

Expression (6.4) is here extended to include the effect of viscous flow on the streamtube area perturbation, as suggested by Yetisir and Weaver, [49]. They postulated that the streamtube area perturbation must diminish at large distances from the cylinder and introduced an area decaying function, $f(s)$, to account for this. In the present analysis, this function is taken to be:

$$f(s) = e^{\alpha \frac{s}{s_0}} \tag{6.5}$$

where α is a positive constant in the upstream region and negative in the downstream region. Thus, there is no decay at the attachment points, $f(0) = 1$ (for simplicity, positions of the flow attachment points are defined by the cylinder centerline, $s = 0$), and no perturbation at large distances from the cylinder, $\lim_{s \to \pm\infty} f(s) = 0$, as required. Combining equation (6.4) and (6.5), the streamtube perturbation function can be finally written as:

$$a(s,t) = e^{\alpha \frac{s}{s_0}} y(t + \tau_0 \frac{s}{s_0}). \tag{6.6}$$

With the streamtube perturbation function specified, the velocity and pressure variations may be readily found using the one-dimensional unsteady continuity and Bernoulli equations, respectively:

$$\int_{-s_0}^{s} \frac{\partial A}{\partial t} \partial s + A(s,t)U(s,t) = A(-s_0,t)U(-s_0,t) \tag{6.7}$$

$$\frac{1}{\rho}P(s,t) + \frac{U^2(s,t)}{2} + \int_{-s_0}^{s} \frac{\partial U}{\partial t} \partial s + \frac{h}{2s_0} \int_{-s_0}^{s} U^2 \partial s = \frac{U^2(-s_0,t)}{2} + \frac{1}{\rho}P(-s_0,t) \tag{6.8}$$

where h is the flow resistance coefficient. Here, the simplifying assumptions of constant area streamtubes, $\bar{A}(s) = A_0$, and no velocity and pressure fluctuations at the inlet (boundary conditions), $u(-s_0,t) = p(-s_0,t) = 0$, are applied. Thus, solution of the continuity equation becomes:

$$\frac{u(s,t)}{U_0} = \frac{(1 + \frac{s_0}{l})[e^{-\alpha} y(t - \tau_0) - e^{\alpha \frac{s}{s_0}} y(t + \tau)] + \frac{\alpha}{l} \int_{-s_0}^{s} e^{\alpha \frac{s}{s_0}} y(t + \tau) \partial s}{A_0 + e^{\alpha \frac{s}{s_0}} y(t + \tau)} \tag{6.9}$$

where $y(t+\tau) = y(t+\tau_0\frac{s}{s_0})$. To solve the Bernoulli equation, this solution was expanded into a power series in $e^{\alpha\frac{s}{s_0}\frac{y(t+\tau)}{A_0}}$. Note that this series converges for $|\, y(t)\,| < A_0$ at $s = 0$, as initially defined by equation (6.1). After expansion, the unsteady velocity and pressure perturbation functions are, respectively:

$$\frac{u(s,t)}{U_0} = \{(1+\frac{s_0}{l})[e^{-\alpha}y(t-\tau_0) - e^{\alpha\frac{s}{s_0}}y(t+\tau)] + \frac{\alpha}{l}\int_{-s_0}^{s} e^{\alpha\frac{s}{s_0}}y(t+\tau)\partial s\}\cdot$$
$$\cdot\sum_{n=0}^{\infty}(-1)^n(\frac{1}{A_0})^{n+1}e^{n\alpha\frac{s}{s_0}}y^n(t+\tau) \quad (6.10)$$

$$\frac{p(s,t)}{\rho U_0^2} = \{(1+\frac{s_0}{l})^2[e^{\alpha\frac{s}{s_0}}y(t+\tau) - e^{-\alpha}y(t-\tau_0)] - \frac{\alpha}{l}\int_{-s_0}^{s} e^{\alpha\frac{s}{s_0}}y(t+\tau)\partial s\}\cdot$$
$$\cdot\sum_{n=0}^{\infty}(-1)^n(\frac{1}{A_0})^{n+1}e^{n\alpha\frac{s}{s_0}}y^n(t+\tau) +$$
$$+\frac{1}{2}\{(1+\frac{s_0}{l})[e^{-\alpha}y(t-\tau_0) - e^{\alpha\frac{s}{s_0}}y(t+\tau)] + \frac{\alpha}{l}\int_{-s_0}^{s} e^{\alpha\frac{s}{s_0}}y(t+\tau)\partial s\}^2\cdot$$
$$\cdot\sum_{n=1}^{\infty}(-1)^n(\frac{1}{A_0})^{n+1}ne^{(n-1)\alpha\frac{s}{s_0}}y^{n-1}(t+\tau) +$$
$$-(1+\frac{s_0}{l})e^{-\alpha}\frac{d}{dt}y(t-\tau_0)\frac{1}{U_0}\sum_{n=0}^{\infty}(-1)^n(\frac{1}{A_0})^{n+1}\int_{-s_0}^{s} e^{n\alpha\frac{s}{s_0}}y^n(t+\tau)\partial s +$$
$$+\alpha(\frac{s_0}{l})^2\sum_{n=0}^{\infty}(-1)^n(\frac{1}{A_0})^{n+1}e^{-(n+1)\alpha}y^{n+1}(t-\tau_0) +$$
$$-\frac{\alpha}{l}\sum_{n=0}^{\infty}(-1)^n(\frac{1}{A_0})^{n+1}[(1+\frac{s_0}{l})(n+1)+\frac{s_0}{l}]\int_{-s_0}^{s} e^{(n+1)\alpha\frac{s}{s_0}}y^{n+1}(t+\tau)\partial s +$$
$$+(\frac{\alpha}{l})^2\sum_{n=0}^{\infty}(-1)^n(n+1)(\frac{1}{A_0})^{n+1}\int_{-s_0}^{s}\int_{-s_0}^{s} e^{(n+1)\alpha\frac{s}{s_0}}y^{n+1}(t+\tau)\partial s\partial s +$$
$$+\frac{h}{s_0}\{(1+\frac{s_0}{l})\sum_{n=0}^{\infty}(-1)^n(\frac{1}{A_0})^{n+1}[\frac{1}{2}(1+\frac{s_0}{l})n+1]\int_{-s_0}^{s} e^{(n+1)\alpha\frac{s}{s_0}}y^{n+1}(t+\tau)\partial s +$$
$$-(1+\frac{s_0}{l})e^{-\alpha}y(t-\tau_0)\sum_{n=0}^{\infty}(-1)^n(\frac{1}{A_0})^{n+1}[(1+\frac{s_0}{l})n+1)\int_{-s_0}^{s} e^{n\alpha\frac{s}{s_0}}y^n(t+\tau)\partial s +$$
$$+\frac{1}{2}(1+\frac{s_0}{l})^2e^{-2\alpha}y^2(t-\tau_0)\sum_{n=1}^{\infty}(-1)^n(\frac{1}{A_0})^{n+1}n\int_{-s_0}^{s} e^{(n-1)\alpha\frac{s}{s_0}}y^{n-1}(t+\tau)\partial s +$$
$$-\frac{\alpha}{l}\sum_{n=0}^{\infty}(-1)^n(\frac{1}{A_0})^{n+1}[(1+\frac{s_0}{l})n+1]\int_{-s_0}^{s} e^{n\alpha\frac{s}{s_0}}y^n(t+\tau)\int_{-s_0}^{s} e^{\alpha\frac{s}{s_0}}y(t+\tau)\partial s\partial s +$$
$$+\frac{1}{2}(\frac{\alpha}{l})^2\sum_{n=0}^{\infty}(-1)^n(\frac{1}{A_0})^{n+1}n\int_{-s_0}^{s} e^{(n-1)\alpha\frac{s}{s_0}}y^{n-1}(t+\tau)[\int_{-s_0}^{s} e^{\alpha\frac{s}{s_0}}y(t+\tau)\partial s]^2\partial s +$$
$$+\frac{\alpha}{l}(1+\frac{s_0}{l})e^{-\alpha}y(t-\tau_0)\cdot$$

$$\cdot \sum_{n=0}^{\infty}(-1)^n(\frac{1}{A_0})^{n+1} n \int_{-s_0}^{s} e^{(n-1)\alpha\frac{s}{s_0}} y^{n-1}(t+\tau) \int_{-s_0}^{s} e^{\alpha\frac{s}{s_0}} y(t+\tau)\partial s \partial s]\} \tag{6.11}$$

where the subscript, n, yields the desired order of solution; $n = 0$ for the linear and $n \geq 1$ for the non-linear. It can be seen that the series arising from the expansion of the velocity perturbation function converges faster than that arising from its square (contain n coefficient). This indicates that from those two sources of non-linear terms, which appear in the solution of the Bernoulli equation, the contribution from the square of the velocity perturbation function becomes increasingly important with increasing order of solution. This also suggests that, for adequate convergence of pressure perturbation function, a high order solution may be required.

Equations (6.10) and (6.11) were carefully verified against the solutions for $\alpha = 0$ (no decay of the streamtube perturbation) which were separately derived. These expressions are much simpler and yield a closed form solution of the unsteady continuity equation. In this case, the unsteady velocity (in the closed form and series expansion) and pressure perturbation functions become, respectively:

$$\frac{u(s,t)}{U_0} = (1+\frac{s_0}{l})[\frac{y(t-\tau_0)-y(t+\tau)}{A_0+y(t+\tau)}] \tag{6.12}$$

$$\frac{u(s,t)}{U_0} = (1+\frac{s_0}{l})[y(t-\tau_0)-y(t+\tau)]\sum_{n=0}^{\infty}(-1)^n(\frac{1}{A_0})^{n+1}y^n(t+\tau) \tag{6.13}$$

$$\begin{aligned}\frac{p(s,t)}{\rho U_0^2} = (1+\frac{s_0}{l})\{&(1+\frac{s_0}{l})[y(t+\tau)-y(t-\tau_0)]\sum_{n=0}^{\infty}(-1)^n(\frac{1}{A_0})^{n+1}y^n(t+\tau)+\\ &+\frac{1}{2}(1+\frac{s_0}{l})[y(t-\tau_0)-y(t+\tau)]^2\sum_{n=1}^{\infty}(-1)^n(\frac{1}{A_0})^{n+1}ny^{n-1}(t+\tau)+\\ &-\frac{1}{U_0}\frac{d}{dt}y(t-\tau_0)\sum_{n=0}^{\infty}(-1)^n(\frac{1}{A_0})^{n+1}\int_{-s_0}^{s}y^n(t+\tau)\partial s\}+\\ &+\frac{h}{s_0}\{\sum_{n=0}^{\infty}(-1)^n(\frac{1}{A_0})^{n+1}[\frac{1}{2}(1+\frac{s_0}{l})n+1]\int_{-s_0}^{s}y^{n+1}(t+\tau)\partial s+\\ &-y(t-\tau_0)\sum_{n=0}^{\infty}(-1)^n(\frac{1}{A_0})^{n+1}[(1+\frac{s_0}{l})n+1]\int_{-s_0}^{s}y^n(t+\tau)\partial s+\end{aligned}$$

$$+\frac{1}{2}(1+\frac{s_0}{l})y^2(t-\tau_0)\sum_{n=1}^{\infty}(-1)^n(\frac{1}{A_0})^{n-1}n\int_{-s_0}^{s}y^{n+1}(t+\tau)\partial s]]\} \tag{6.14}$$

As in Reference [46], the fluidelastic force acting on the cylinder, $F_E(t)$, is approximated as the pressure difference across its centerline, $p(0,t)$, times an equivalent area factor, $l_0 D_E$:

$$F_E(t) = 2l_0 D_E p(0,t) \tag{6.15}$$

where l_0 denotes the cylinder length. Note that the fluidelastic force is assumed to be fully correlated along the cylinder span. Thus, the equation of motion of the cylinder, oscillating in the transverse-to-flow direction, may now be written as:

$$m_0\ddot{y}(t) + [c_0 + \frac{1}{2}C_D\rho d l_0\sqrt{U_0^2+\dot{y}^2(t)}]\dot{y}(t) + k_0 y(t) = F_E(t) \tag{6.16}$$

where m_0, c_0 and k_0 are the structural mass, damping and stiffness coefficients, and C_D denotes the steady drag coefficient. Note that the present analysis also includes a non-linear velocity-dependent damping term, due to the fluid drag, which in the linearized form was suggested by Blevins, [7]. As before, this term may be expanded into a power series in $\frac{\dot{y}(t)}{U_0}$. This yields:

$$c_d = \frac{1}{2}C_D\rho d l_0 U_0\{1-\frac{1}{2}[\frac{\dot{y}(t)}{U_0}]^2+\frac{1\cdot 3}{2\cdot 4}[\frac{\dot{y}(t)}{U_0}]^4-\frac{1\cdot 3\cdot 5}{2\cdot 4\cdot 6}[\frac{\dot{y}(t)}{U_0}]^6+\cdots\} \tag{6.17}$$

where $|\frac{\dot{y}(t)}{U_0}|<1$ to ensure convergence.

6.1.2 Combined fluidelastic and turbulence excitation

The random field of turbulence, within a flexible array, is defined here by the spectrum formulated by Pettigrew and Gorman, [64]. They assumed that the power spectral density of the turbulence force field per unit cylinder length, $S(f)$, which is homogeneous and fully correlated, is proportional to the square of flow dynamic head (see Section 2.2 for details). That is:

$$S^{0.5}(f) = \frac{1}{2}C_r(f)\rho d U_P^2 \tag{6.18}$$

where the effective random excitation coefficient, $C_r(f)$, defines the shape of the spectrum and is obtained experimentally. Because random excitation coefficients are nearly constant in the range of the cylinder fundamental frequencies typical for a marine riser or a heat exchanger, a flat power spectrum, $C_r(f) = C_r$, was used to represent the random field of turbulence. The dimensional inconsistency in equation (6.18) is eliminated by introducing a nondimensional excitation coefficient, $C_r' = C_r(\frac{d}{U_0})^{0.5}$, as suggested by Blevins *et al*, [65], and Chen and Jendrzejczyk, [88]. This nondimensionalization yields the final form of the power spectral density function per unit cylinder length as:

$$S^{0.5} = \frac{1}{2}C_r'\rho(dU_P)^{1.5} \tag{6.19}$$

which is used, *via* Fourier transformation, in the time-domain model to construct the turbulence excitation force, $F_T(t)$.

Now, the equation of motion takes the form:

$$m_0\ddot{y}(t) + [c_0 + \frac{1}{2}C_D\rho dl_0\sqrt{U_0^2 + \dot{y}^2(t)}]\dot{y}(t) + k_0y(t) = F_E(t) + F_T(t) \tag{6.20}$$

where the sum of fluid forces consists of fluidelastic force, $F_E(t)$, and turbulence force, $F_T(t)$.

6.2 Analytical solution

6.2.1 Limit cycle and dynamic bifurcation under fluidelastic excitation

The non-linear equation of motion (6.16) is solved using the first approximation method of Kryloff and Bogoliuboff, [89].

Initially, this equation is reduced to the basic differential form:

$$\ddot{y}(t) + \omega^2y(t) + F[y(t), \dot{y}(t)] = 0 \tag{6.21}$$

where, unlike the original theory of Lever and Weaver, $F[y(t), \dot{y}(t)] = \mu f[y(t), \dot{y}(t)]$ is a non-linear function of cylinder displacement and velocity which perturbs the

simple linear system oscillating with the frequency $\omega = \sqrt{\frac{k}{m_0}}$ (this frequency differs from ω_0 due to fluidelastic stiffness terms). The constant, μ, is a small positive quantity which defines the size of the perturbation, $\mu \ll \omega^2$. This means that the contribution of non-linear terms to the final solution must be very small.

Then, the solution of equation (6.21) is assumed to be periodic:

$$y(t) = a(t)cos[\omega t + \Phi(t)] \tag{6.22}$$

where the amplitude, $a(t)$, and the phase, $\Phi(t)$, are slowly varying functions of the time, t, in the state of equilibrium. It can be shown that they are given by the following formulas (see Appendix C, for details) which satisfy equation (6.21) to order μ^2;

$$\dot{a}(t) = \frac{1}{2\pi\omega}\int_0^{2\pi} F(acos\Theta, -a\omega sin\Theta)sin\Theta d\Theta \tag{6.23}$$

and

$$\dot{\Theta}(t) = \omega(a) \tag{6.24}$$

where $\Theta(t) = \omega t + \Phi(t)$ denotes the total phase. The frequency of oscillation $\omega(a)$ depends on amplitude *via*:

$$\omega^2(a) = \omega_0^2 + \frac{1}{\pi a}\int_0^{2\pi} F(acos\Theta, -a\omega sin\Theta)cos\Theta d\Theta \tag{6.25}$$

Note that the function $F(acos\Theta, -a\omega sin\Theta)$ enters into equations (6.23) and (6.25) directly and not only through its non-linear part. Since the limit cycle of constant amplitude is expected, its rate of change may be set equal to zero ($\dot{a}(t) = 0$ in equation (6.23)).

Unfortunately, the full form of the function $F[y(t), \dot{y}(t)]$, which is given for $\alpha \neq 0$, does not yield analytical solutions. Thus, equation (6.21) was solved for $\alpha = 0$ (no decay of the streamtube perturbation). For simplicity, the function $F[y(t), \dot{y}(t)]$ was reduced to third order ($n = 2$ in equation (6.14)), leading to the following nondimensional forms of the limit cycle amplitude and the associated frequency of

oscillation, respectively:

$$(\frac{a}{d})^2 = \{\bar{m}\delta_0 + \frac{1}{2}\pi C_D(\frac{l}{s_0})(\frac{s_0}{d})(\frac{\omega}{\omega_0})U_r - 2\pi(\frac{D_E}{d})(\frac{d}{A_0})(\frac{l}{s_0})^2(\frac{s_0}{d})^2(1+\frac{s_0}{l})(\frac{\omega}{\omega_0})\cdot$$
$$\cdot U_r^2[(1+\frac{s_0}{l})sin\frac{1}{U_r} - \frac{s_0}{l}\frac{1}{U_r}cos\frac{1}{U_r} + h(sin\frac{1}{U_r} + U_r cos\frac{1}{U_r} - U_r)]\}/$$
$$\{2\pi(\frac{D_E}{d})(\frac{d}{A_0})^3(\frac{l}{s_0})^2(\frac{s_0}{d})^2(1+\frac{s_0}{l})(\frac{\omega}{\omega_0})U_r^2\{sin\frac{1}{U_r}[\frac{3}{4}+\frac{s_0}{l}+$$
$$-\frac{1}{2}(1+\frac{s_0}{l})cos\frac{1}{U_r}] - \frac{1}{2}\frac{s_0}{l}\frac{1}{U_r}cos\frac{1}{U_r} + h\{sin\frac{1}{U_r}[\frac{3}{2}+\frac{s_0}{l} - \frac{1}{2}(1+\frac{s_0}{l})U_r sin\frac{1}{U_r}] +$$
$$+(\frac{7}{4}+\frac{s_0}{l})U_r(cos\frac{1}{U_r}-1)\}\} - \frac{1}{4}\pi C_D(\frac{d}{s_0})(\frac{s_0}{l})(\frac{\omega}{\omega_0})\frac{1}{U_r}\} \tag{6.26}$$

$$(\frac{\omega_0}{\omega})^2 = 1 + 2(\frac{1}{\bar{m}})(\frac{D_E}{d})(\frac{s_0}{l})^2(\frac{s_0}{d})^2(1+\frac{l}{s_0})(\frac{d}{A_0})(\frac{a}{d})^2U_r^2\{(\frac{A_0}{d})^2(\frac{d}{a})^2\cdot$$
$$\cdot[(1+\frac{s_0}{l})(1-cos\frac{1}{U_r}) - \frac{s_0}{l}\frac{1}{U_r}sin\frac{1}{U_r}] + \frac{9}{4}(1+\frac{s_0}{l})(1-cos\frac{1}{U_r}) +$$
$$-\frac{1}{2}sin\frac{1}{U_r}[(1+\frac{s_0}{l})sin\frac{1}{U_r} + \frac{s_0}{l}\frac{1}{U_r}] + h\{(\frac{A_0}{d})^2(\frac{d}{A_0})^2(U_r sin\frac{1}{U_r} - cos\frac{1}{U_r}) +$$
$$+\frac{1}{2}U_r sin\frac{1}{U_r}[(1+\frac{s_0}{l})cos\frac{1}{U_r} + 2 + \frac{s_0}{l}] - (\frac{3}{2}+\frac{s_0}{l})cos\frac{1}{U_r}\}\} \tag{6.27}$$

where U_r denotes reduced velocity which is defined as:

$$U_r = \frac{U_0}{\omega l} \tag{6.28}$$

These expressions satisfy equation (6.21) to order μ^2 for $\mu \ll \omega^2$. This implies that:

$$3(\frac{d}{A_0})(\frac{D_E}{d})(\frac{U_0}{\omega d})^2 \ll \bar{m}. \tag{6.29}$$

An estimate for the range of applicability of the solution can be made using the stability criterion of Connors (equation (2.1)). This yields:

$$\delta_0 \ll \frac{4}{3}(\frac{\pi}{K})^2(\frac{A_0}{d})(\frac{d}{D_E}) \tag{6.30}$$

where $K = 9.9$ is the stability constant found by Connors. Physically, for lightly damped systems, condition (6.29) does not impose restrictions on the derived solution.

As follows from equations (6.26) and (6.27), the trivial linear solution ($a = 0$), which defines the dynamic point of bifurcation, takes the form:

$$0 = \bar{m}\delta_0 - 2\pi(\frac{D_E}{d})(\frac{d}{A_0})(\frac{s_0}{l})^2(\frac{s_0}{d})^2(1+\frac{s_0}{l})(\frac{\omega}{\omega_0})U_r^2[(1+\frac{s_0}{l})sin\frac{1}{U_r} + \\ -\frac{s_0}{l}\frac{1}{U_r}cos\frac{1}{U_r} + h(sin\frac{1}{U_r} + U_r cos\frac{1}{U_r} - U_r)] - \frac{1}{2}\pi C_D(\frac{l}{s_0})(\frac{s_0}{d})(\frac{\omega}{\omega_0})U_r \quad (6.31)$$

$$(\frac{\omega_0}{\omega})^2 = 1 + 2(\frac{1}{\bar{m}})(\frac{D_E}{d})(\frac{s_0}{l})^2(\frac{s_0}{d})^2(1+\frac{s_0}{l})(\frac{d}{A_0})U_r^2[(1+\frac{s_0}{l})(1-cos\frac{1}{U_r}) + \\ -\frac{s_0}{l}\frac{1}{U_r}sin\frac{1}{U_r} + h(U_r sin\frac{1}{U_r} - cos\frac{1}{U_r})] \quad (6.32)$$

In general, these equations represent the net mass-damping parameter $\bar{m}\delta_n$ and the frequency of oscillations, ω, at a given flow velocity, U_r. As can be seen, the net mass-damping parameter, which at the point of bifurcation becomes zero, incorporates the positive structural parameter $\bar{m}\delta_0$ and the negative fluidelastic parameter (flow-dependent terms), $\bar{m}\delta_{fe}$. Similarly, the frequency, ω, differs from ω_0 due to the the fluidelastic stiffness (note that for $(\frac{\omega_0}{\omega}) = 1$ equations (6.31) is identical to that presented in Reference [46]).

For completeness, the trivial linear solutions were also derived for $\alpha \neq 0$ (decay of the streamtube perturbation). In nondimensional form these are:

$$0 = \bar{m}\delta_0 + \frac{1}{2}\pi C_D(\frac{l}{s_0})(\frac{s_0}{d})(\frac{\omega}{\omega_0})U_r - 2\pi(\frac{D_E}{d})(\frac{l}{s_0})^2(\frac{d}{A_0})(\frac{s_0}{d})^2(\frac{\omega}{\omega_0})U_r^2 \cdot \\ \cdot\{e^{-\alpha}sin\frac{1}{U_r} + 2\frac{s_0}{l}\frac{1}{U_r}\frac{1}{\alpha_1}[\alpha + \frac{1}{U_r}e^{-\alpha}sin\frac{1}{U_r} - (\alpha+\frac{1}{2}\alpha_1)e^{-\alpha}cos\frac{1}{U_r}] + \\ +(\frac{s_0}{l})^2(\frac{1}{U_r})^2(\frac{1}{\alpha_1})^2[(\alpha\alpha_1+\alpha_2)e^{-\alpha}sin\frac{1}{U_r} + 2\frac{1}{U_r}\alpha + \frac{1}{U_r}(2\alpha+\alpha_1)e^{-\alpha}cos\frac{1}{U_r}] + \\ -h\frac{1}{U_r}\frac{1}{\alpha_1}\{[U_r(\alpha+\alpha_1) + \frac{1}{U_r}(\frac{s_0}{l}+\frac{\alpha}{\alpha_1})]e^{-\alpha}sin\frac{1}{U_r} + \\ +[1 - \frac{s_0}{l}(\alpha+\frac{\alpha_2}{\alpha_1})]e^{-\alpha_1}cos\frac{1}{U_r} + \frac{s_0}{l}\frac{\alpha_2}{\alpha_1} - 1\}\} \quad (6.33)$$

$$(\frac{\omega_0}{\omega})^2 = 1 + 2(\frac{1}{\bar{m}})\frac{D_E}{d})(\frac{d}{A_0})(\frac{l}{s_0})^2(\frac{s_0}{d})^2U_r^2\{1 - e^{-\alpha_1}cos\frac{1}{U_r} + \\ +2\frac{s_0}{l}\frac{1}{U_r}\frac{1}{\alpha_1}[\frac{1}{U_r} - \frac{1}{U_r}e^{-\alpha_1}cos\frac{1}{U_r} - (\alpha+\frac{1}{2}\alpha_1)e^{-\alpha}sin\frac{1}{U_r}] +$$

$$+(\frac{s_0}{l})^2(\frac{1}{U_r})^2(\frac{1}{\alpha_1})^2[\frac{\alpha_2}{\alpha_1}-(\frac{\alpha_2}{\alpha_1}-\alpha)e^{-\alpha_1}cos\frac{1}{U_r}-\frac{1}{U_r}(1+2\alpha\alpha_1)e^{-\alpha}sin\frac{1}{U_r}]+$$
$$+h\frac{1}{U_r}\frac{1}{\alpha_1}\{\alpha(U_r+\alpha_1\frac{1}{U_r})+(1-\frac{s_0}{l}\alpha+\frac{s_0}{l}\frac{\alpha_2}{\alpha_1})e^{-\alpha}sin\frac{1}{U_r}+$$
$$-[U_r(\alpha^2+\alpha)+\frac{1}{U_r}(1+\frac{s_0}{l}+\alpha\alpha_1)]e^{-\alpha_1}cos\frac{1}{U_r}\}\} \quad (6.34)$$

where $\alpha_1 = \alpha^2 + (\frac{1}{U_r})^2$ and $\alpha_2 = \alpha^2 - (\frac{1}{U_r})^2$.

6.2.2 Linear response and dynamic bifurcation under combined excitation

The non-linear equation of motion (6.20) cannot be solved analytically (its numerical solution is presented in Section 6.4). Here, an approximate method is formulated; superposition of the response for fluidelastic excitation only with that excited by turbulence.

First, the combined response for linear fluidelastic excitation was found. As follows from random vibration theory, the RMS response of a lightly damped, single degree-of-freedom, linear system to broad band excitation is given by:

$$A_{RMS} = \frac{\pi}{\sqrt{2}}[\frac{S(f_0)f_0 l_0^2}{\delta_0 k_0^2}]^{0.5} \quad (6.35)$$

where l_0 is the cylinder length, k_0 is the structural stiffness, δ_0 is the logarithmic decrement of structural damping, and $S(f_0)$ denotes the power spectral density function of the turbulence force at the cylinder's natural frequency, as given by equation (6.19). Because both excitation mechanisms superimpose, the structural terms in equation (6.35) are directly affected by the fluidelastic force. Thus, k_0 becomes k_n, the net system stiffness, and f_0 becomes f, the frequency at a given velocity. After substitution of equation (6.19) into (6.35), the RMS cylinder response to combined turbulence and linear fluidelastic excitation takes the nondimensional form:

$$\frac{A_{RMS}}{d} = \frac{C'_r}{8\sqrt{2}\pi}(\frac{f}{f_0})^{1.5}U_{Pr}^{1.5}[\frac{1}{\bar{m}(\bar{m}\delta_0 - \bar{m}\delta_{fe})}]^{0.5} \quad (6.36)$$

where the net mass-damping parameter, $\bar{m}\delta_0 - \bar{m}\delta_{fe}$, is given by the set of equations (6.31) and (6.32) for $\alpha = 0$, and (6.33) and (6.34) for $\alpha \neq 0$. Because the net system damping decreases with flow velocity towards the dynamic point of bifurcation for fluidelastic excitation ($\bar{m}\delta_0 - \bar{m}\delta_{fe} = 0$), the linear response excited by turbulence rises asymptotically to infinity at this point. In actual fact, however, these large amplitude oscillations are controlled by non-linear fluidelastic effects: stable and unstable bifurcations.

Next, the dynamic point of bifurcation under combined excitation was found. To predict its location correctly, a truly non-linear solution of the equation of motion (6.20) is needed. However, some insight may be gained by superimposing the combined linear response with the non-linear limit cycle due to fluidelastic excitation only, both of which are described analytically (see Figure 6.2). Thus, based on this heuristic representation which conceptionally ignores coupling mechanism, the intersection point may approximate the dynamic point of bifurcation.

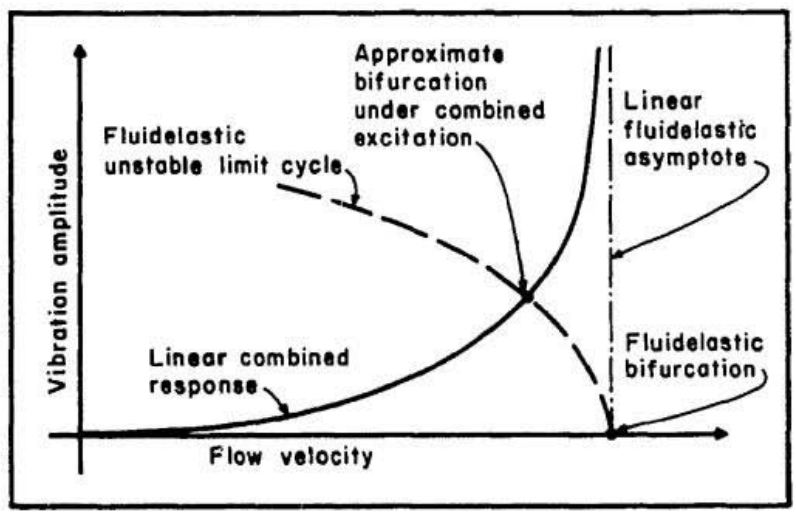

Figure 6.2: Heuristic representation of linear combined response and fluidelastic unstable limit cycle.

This intersection point was determined by combining equation (6.36) with expression for the unstable limit cycle, equations (6.26) and (6.27), which may be

formulated as $(\frac{a}{d})^2 = -\frac{\bar{m}\delta_n}{D}$. This yields:

$$0 = \bar{m}\delta_n - \frac{1}{8\pi}C_r'(\frac{1}{\bar{m}})^{0.5}(\frac{f}{f_0})^{1.5}U_{Pr}^{1.5}(-D)^{0.5} \tag{6.37}$$

where the non-linear operator, D, which arises from fluid load, is defined to third order as:

$$D = -2\pi(\frac{D_E}{d})(\frac{d}{A_0})^3(\frac{l}{s_0})^2(\frac{s_0}{d})^2(1+\frac{s_0}{l})(\frac{\omega_0}{\omega})U_r^2\{sin\frac{1}{U_r}[(\frac{3}{4}+\frac{s_0}{l}) + -\frac{1}{2}(1+\frac{s_0}{l})cos\frac{1}{U_r}] + \frac{1}{2}\frac{s_0}{l}\frac{1}{U_r}cos\frac{1}{U_r} + h\{sin\frac{1}{U_r}[\frac{3}{2}+\frac{s_0}{l} - \frac{1}{2}(1+\frac{s_0}{l})U_r sin\frac{1}{U_r}] + +(\frac{7}{4}+\frac{s_0}{l})U_r(cos\frac{1}{U_r}-1)\}\} - \frac{1}{4}\pi C_D(\frac{s_0}{l})(\frac{d}{s_0})(\frac{\omega}{\omega_0})\frac{1}{U_r} \tag{6.38}$$

with $(\frac{\omega_n}{\omega})$ given by equation (6.27).

Expression (6.38) requires the geometric conversion between the reduced pitch velocity, U_{Pr}, and U_r. This will be defined in the next Chapter, together with the other parameters which enter in the model.

It follows from equation (6.37) that the dynamic point of bifurcation, under combined excitation, can be approximated using superposition only for unstable bifurcations, $D < 0$, where both curves intersect (see also Figure 6.2).

6.3 Stability analysis

6.3.1 Dynamic stability

The concept of dynamic stability was discussed in details in Chapter 3. Briefly, it was shown that only asymptotic stability, which is defined by a stable bifurcation, can guarantee stability of self-excited oscillations. Thus, a dynamic bifurcation formula is needed which can be obtained from non-linear solution of equation of motion.

From the solution of the first approximation, it follows that the equation of

motion (6.16) is satisfied by the cubic expression:

$$D(\frac{a}{d})^3 + \bar{m}\delta_n(\frac{a}{d}) = 0 \tag{6.39}$$

where D is the non-linear coefficient arising from fluid load. This expression yields the bifurcation formula, which is defined by its two solutions; first, $(\frac{a}{d})^2 = -\frac{\bar{m}\delta_n}{D}$, for the limit cycle amplitude which is given by the set of equations (6.26) and (6.27) for $\alpha = 0$, and second, $(\frac{a}{d}) = 0$, for the trivial equilibrium solution which is given by the set of equations (6.31) and (6.32) for $\alpha = 0$, and the set of equations (6.33) and (6.34) for $\alpha \neq 0$. Depending on the sign of the non-linear coefficient, this formula gives possible dynamic bifurcation; stable for $D > 0$ and unstable for $D < 0$. It can be seen that both bifurcations are symmetric of Hopf type. They are shown schematically in Figure 3.3, together with the separate linear response curves due to combined excitation (solid and dashed lines represent the stable and unstable states, respectively). By describing the net mass-damping parameter as the sum of control parameters, $\bar{m}\delta_n = \Lambda_C - \Lambda$, which incorporates the positive structural parameter (stabilizing component), Λ_C, and negative flow-induced parameter (destabilizing component), Λ, a dynamic instability arises at the bifurcation point, $\Lambda = \Lambda_C$.

Stable bifurcation

The instability signalled by a stable bifurcation can be qualitatively described by the trivial equilibrium solution ($(\frac{a}{d}) = 0$), since for $\Lambda < \Lambda_C$ all local motions are asymptotically stable. However, at the point of bifurcation, $\Lambda = \Lambda_C$, the non-linear solution is bounded by a limit cycle, while the linear solution becomes infinite. Thus, the linear solution to combined excitation tends asymptotically to infinity at the point. Because the curve does not intersect the stable limit cycle, the linear asymptote becomes the lowest stability boundary for the combined system. Therefore, the equations which specify the location of the dynamic point of bifurcation, (6.31) and (6.32) for $\alpha = 0$, and (6.33) and (6.34) for $\alpha \neq 0$, are generally sufficient to establish

the dynamic stability criterion for stable bifurcations subjected to turbulence. It should be remembered, however, that turbulence does affect our interpretation of response curves for stable bifurcation. Specifically, an increase in turbulence response leads to an apparent decrease in the critical velocity assigned on the basis of standard threshold definitions (see Section 3.3.1).

Unstable bifurcation

The instability signalled by an unstable bifurcation cannot be qualitatively described by the trivial equilibrium solution, since it is not asymptotically stable for $\Lambda < \Lambda_C$. It follows that, even without non-linear coupling between the turbulence and fluidelastic mechanisms, the linear response to combined excitation is sufficient to initiate instability below the fluidelastic stability boundary (trivial equilibrium solution $\Lambda = \Lambda_C$) when it exceeds the unstable limit cycle. Thus, it may be concluded that the stability threshold for combined fluidelastic and turbulence excitation may be approximately defined by the intersection point of the linear combined response curve with the unstable limit cycle, as given by equation (6.37).

Note, however, that any finite disturbance which carries the system beyond the unstable limit cycle may cause instability. Since this disturbance arises from turbulence buffeting, the RMS response underestimates it and random vibration theory must be applied to define its possible peak size (see Reference [7], for example). For narrow-banded random cylinder motion excited by turbulence, the displacement peak will be governed by the Rayleigh probability density distribution function:

$$p(y) = \frac{y}{\sigma^2} e^{\frac{1}{2}(-\frac{y}{\sigma})^2} \tag{6.40}$$

where $p(y)dy$ is the probability of a peak falling within interval $y + \Delta y$ and σ is the standard deviation. The average number of cycles before a peak displacement $Y_{max} \geq Y$ is experienced may be shown to be:

$$N(Y) = e^{\frac{1}{2}(\frac{Y}{\sigma})^2} \tag{6.41}$$

Therefore, for a cylinder vibrating at frequency f, the average return period in seconds is:

$$T(Y) = \frac{1}{f} e^{\frac{1}{2}(\frac{Y}{\sigma})^2} \tag{6.42}$$

In the present experimental investigation, $f = 5.1\,Hz$ (the frequency of oscillations) and $T(Y) = 10\ min$ (the time during which the cylinder motion was allowed to stabilize at a given flow velocity). It follows from equation (6.43) that the maximum peak displacement expected, Y_{max}, is four times higher than the average RMS response for these conditions. Thus, to account for this effect, the random excitation coefficient in equation (6.37) must be defined *via* expression (6.43) to represent the maximum displacement in the average return period. This gives:

$$C_r'' = \sqrt{2ln[fT(Y)]}C_r' \tag{6.43}$$

where C_r' was obtained experimentally based on the RMS cylinder response. Thus, the stability criterion for unstable bifurcations subjected to turbulence, still ignoring fluid coupling, becomes:

$$0 = \tilde{m}\delta_n - \frac{1}{8\pi} C_r' \{2ln[fT(Y)]\}^{0.5} (\frac{1}{\tilde{m}})^{0.5} (\frac{f}{f_0})^{1.5} U_{Pr}^{1.5} (-D)^{0.5} \tag{6.44}$$

Note, however that to ensure asymptotic stability independent of turbulence excitation, the non-linear fluidelastic analysis must be extended to define a secondary stable point of bifurcation which, in real situations, defines the lower limit of the hysteresis region. That is, U_H is the stability threshold independent of turbulence. Because operation of the array within the hysteresis region risks turbulence-induced transitions to instability, U_H may also be taken as the practical stability boundary.

6.3.2 Static stability

It is interesting to note that, based on equation (6.34), the transition from dynamic to static instability may be defined. Physically, this manifests itself in the frequency

reduction towards zero at the stability threshold, yielding:

$$\frac{U_0}{\omega_0 d} = \sqrt{\frac{\bar{m}}{(\frac{d}{A_0})\{1 - e^{-\alpha} + \frac{h}{\alpha}[1 - e^{-\alpha}(\alpha + 1)]\}}}. \tag{6.45}$$

Note that this expression is defined only for $\alpha \neq 0$. Thus, the present theory predicts static instability only if the area perturbation function diminishes at large distances from the cylinder (as already noted by Yetisir and Weaver, [49]).

6.4 Numerical procedure

With the approximate analytical solution behind, numerical time-domain procedure was developed with two objectives. First, to perform a fully non-linear analysis since the simplified analytical solution ($\alpha = 0$), reduced to third order, might be insufficient to describe accurately the cylinder behaviour under fluidelastic excitation. Second, to quantify the influence of turbulence on fluidelastic instability based on the true non-linear interaction mechanism.

The equations of motion (6.16) and (6.20) were integrated using a fourth order corrector-predictor technique [90]. To verify the effectiveness of the numerical integration scheme and to specify certain parameters for its operation, such as the time step and the number of corrector iterations, this technique was first applied to the standard non-linear equations: Van der Pol's and Rayleigh's oscillators (the details of this study are contained in the Appendix D). It was found that for a lightly damped system, the chosen integration scheme gives accurate results for a time step of $\Delta t = \frac{T_n}{40}$ with three corrector iterations per step.

The numerical evaluation of the equation of motion requires, at each time step, the time history of previous cylinder response, the fluidelastic force, which is calculated from equation (6.15) after substitution of equation (6.11) for $\alpha \neq 0$ and (6.14) for $\alpha = 0$, and the turbulence force which *via* inverse Fourier transformation is obtained from the spectrum, equation (6.19). The integrals in equations (6.11)

and (6.14) are solved in the time-domain after introducing the integration variable, $\xi = t + \tau$ or equivalently $\xi = t + \tau_0 \frac{s}{s_0}$. Since calculation of the fluidelastic force requires that an estimate of cylinder displacement be made at the same instant of time, the integration procedure is iterated at each time step until the desired degree of convergence is obtained. It was found that two iterations for the chosen time step were sufficient for accurate and effective simulations.

6.4.1 Operation of the fluidelastic model

Figure 6.3 shows a flow chart for the operation of fluidelastic model, that is the numerical evaluation of equation (6.16). This numerical procedure may be described as follows. First, the physical parameters are chosen which define the array and the cylinder. Simultaneously, the numerical parameters, such as time and velocity steps, initial disturbance, number of corrector iterations, and order of solution, are defined. Next, the critical velocity is calculated from linear equations (6.31) and (6.32) for $\alpha = 0$, and equations (6.33) and (6.34) for $\alpha \neq 0$. This velocity specifies starting flow conditions such as streamtube velocity and time lag. Since the time-domain simulation requires the time history of cylinder response, $y(t)$ and $\dot{y}(t)$, these are generated for $0 \leq t \leq \tau_0$ as harmonic motion of small amplitude Y_0. Then, the fluidelastic simulation proceeds until the state of equilibrium (stable attracting limit cycle) is reached or instability occurs (unstable repelling limit cycle). Note that the unstable limit cycle is defined by the amplitude of initial harmonic disturbance, Y_0, for which unstable growth occurs. During the simulations, the RMS amplitude is computed and saved at each time step together with the segment of displacement and velocity records which are required for further analysis (phase plane, Fourier transform). If desired, the final amplitude response curve is obtained by incrementing (stable limit cycle) or decrementing (unstable limit cycle) the flow velocity.

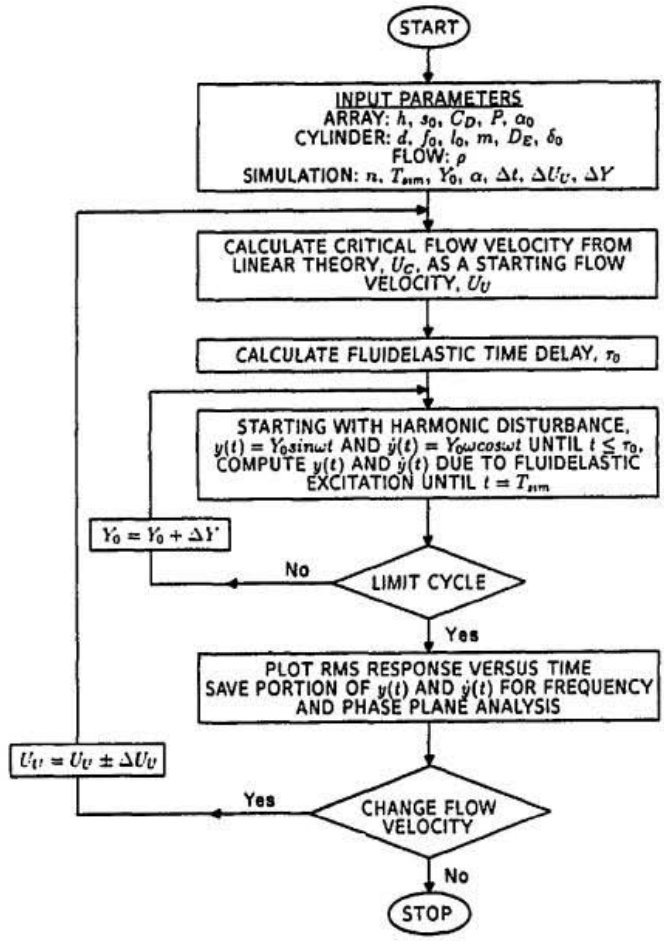

Figure 6.3: Flow chart of fluidelastic numerical simulation.

6.4.2 Operation of the coupled model

Figure 6.4 shows the operation of the coupled model, that is the numerical evaluation of equation (6.20). As before, the physical parameters defining the array and flow conditions are first chosen, together with the simulation parameters such as time step and length of simulation. At each flow velocity, the turbulence force time series is then generated from the spectrum (equation (6.19)) using an inverse Fourier transformation. Next, the fluidelastic streamtube velocity and time lag are calculated. The simulation begins with zero initial cylinder displacement and velocity.

The response to turbulence only is generated until $t = \tau_0$, using the central difference method as a starting procedure. At time τ_0, it becomes possible to calculate the fluidelastic excitation force as in the fluidelastic model. The simulation proceeds, for the prechosen length of time, with the RMS cylinder displacement computed and saved at each time step, together with a segment of $y(t)$ itself. For a given flow velocity, the results are examined and, if desired, the flow velocity is incremented and the simulation repeated. In this way, a simulation is conducted much like an experimental investigation, the final output being an amplitude versus flow velocity response curve.

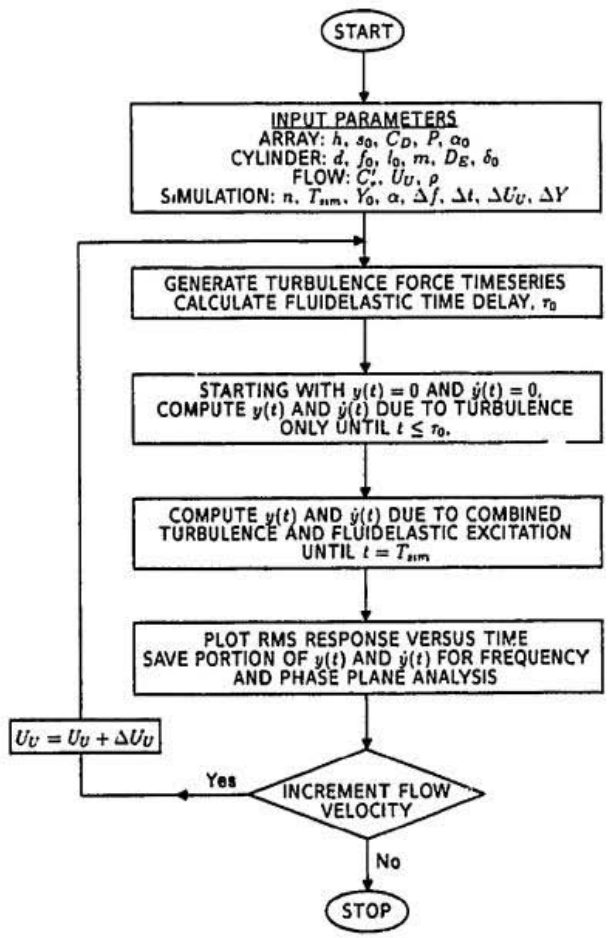

Figure 6.4: Flow chart of coupled turbulence and fluidelastic numerical simulation.

The numerical time-domain model requires certain simulation parameters for its operation. As before, it was found that a time step of $\Delta t = \frac{T_n}{40}$ is sufficiently small for accurate and effective simulation. The frequency resolution of the turbulence force spectrum, Δf, was set based on a consideration of the bandwidth of the cylinder transfer function in still fluid:

$$\Delta f = \frac{2}{K}\zeta f_0 \tag{6.46}$$

where ζ is the damping ratio. The constant, K, denote. the minimum number of frequency components in the bandwidth needed to assure accurate turbulence response simulations. The resolution error can be calculated by comparing the amplitude of linear resonance under harmonic excitation with the amplitude given by equation (6.36). For $K = 1$ (harmonic excitation), this was found to be 25 %, while $K = 2$ reduced this error below 10 %. Combined excitation, however, requires practically infinitely small Δf in the immediate vicinity of a stability threshold ($\delta_n \rightarrow 0$). Thus, $K = 10$ was chosen for the lowest damping value, $\delta_0 = 0.01$. The resulting Δf was used for all subsequent simulations.

Having selected the time and the frequency steps, the maximum frequency in the turbulence force spectrum is given by the Nyquist criterion:

$$F_{max} = \frac{1}{2\Delta t} \tag{6.47}$$

and the length of the corresponding time series of the turbulence force generated by inverse Fourier transform is

$$T_{max} = \frac{1}{\Delta f} \tag{6.48}$$

For a cylinder frequency of $f_0 = 5.1\ Hz$ (as in the experimental study), this yields $T_{max} = 12.5\ min$. If required, simulations of arbitrary length can be conducted, without the prohibitive computational effort associated with very long inverse Fourier Transform, by piecing together turbulence force time series of $T_{max} = 12.5\ min$. This technique was checked against the use of one very long unique time

series and was found to yield equivalent results.

The random nature of the turbulence force was expressed by assigning random phases to each frequency component in the inverse Fourier transformation. Thus each set of random phases produces a different turbulence force time series. However, it was found that the steady-state cylinder response is essentially independent of this randomizing effect, especially if Δf is small compared with the bandwith of the transfer function. For example, the maximum discrepancy resulting from random phase is within 5 % for $K = 2$ and 0.2 % for $K = 80$. Therefore, to reduce computational effort, one set of random phases was used for all subsequent simulations.

Chapter 7

Theoretical results: comparison and discussion

The objective of this Chapter is to compare the first principles non-linear model for fluidelastic instability with experimental results. In this regard, the analytical model is applied to the two array geometries investigated experimentally; a parallel triangular of 1.375 pitch ratio and a square of 1.433 pitch ratio. Comparison is made on the basis of stability thresholds and response curves for the linear system, and limit cycle of post-stable oscillations, with special emphasis on a turbulence effect on unstable bifurcation, for the non-linear system.

First, the theoretical results from equations of the first approximation are generated. These are then compared with the present experimental data to assess the accuracy of the theoretical predictions and to investigate their sensitivity to variations in model parameters. Next, numerical simulation is performed to generate fully non-linear theoretical results and to investigate the actual effect of turbulence on the fluidelastic system. This numerical procedure is verified against analytical expressions of the first approximation.

7.1 Model parameters

To generate theoretical results, the array and cylinder parameters required by the fluidelastic model must be defined. As with the experiment, the cylinder parameters

are; $d = 60\,mm$, $f_0 = 5.00\,Hz$ and $\delta_0 = 0.01$, while the fluid density is $\rho = 1.221\,\frac{kg}{m^3}$. Similarly, the array parameters are expressed in terms of the physical parameters, describing the tested configurations, which can be divided into two groups.

The first group includes those which directly follow from geometry considerations of the flow pattern and the unit cell (see Figure 6.1) and were already specified in References [47,48]. Thus, without further explanation, they are defined in Table 7.1 which also gives their numerical values. Note, however, that the steady streamtube area, $\frac{A_0}{d}$, is expressed based on the minimum gap between the cylinders which for staggered arrays (parallel triangular) is $\frac{A_0}{d} = min(\frac{T}{d} - \frac{1}{2}, \frac{P}{d} - 1)$.

Table 7.1: The nondimensional geometric parameters and their numerical values for the theoretical model.

Array geometry	Streamtube shape	$\frac{T}{d}$	$\frac{A_0}{d}$	$\frac{s_0}{d}$	$\frac{D_E}{d}$
Parallel triangular: $\alpha_0 = \frac{1}{6}\pi$, $\frac{P}{d} = 1.375$	Circular segment	$\frac{P}{d}cos\alpha_0$	$\frac{P}{d} - 1$	$\frac{P}{d}\alpha_0$	$\frac{d}{P}\alpha_0$
		1.191	0.375	0.720	0.381
Square: $\alpha_0 = \frac{1}{2}\pi$, $\frac{P}{d} = 1.433$	Straight	$\frac{P}{d}$	$\frac{P}{d} - 1$	$\frac{P}{d}$	$\frac{1}{8}\alpha_0$
		1.433	0.433	1.433	0.196

Also, a geometric conversion is required to compare the reduced pitch velocity, $U_{Pr} \stackrel{\text{def}}{=} \frac{U_P}{f_0 d}$, usually deployed in stability analyses to express flow dynamics, with the reduced velocity relevant to the theoretical model, $U_r \stackrel{\text{def}}{=} \frac{U_0}{\omega l}$. For staggered arrays, this conversion takes the form:

$$U_{Pr} = 2\pi(\frac{l}{s_0})(\frac{s_0}{d})\frac{(\frac{A_0}{d})}{(\frac{T}{d})}(\frac{\frac{P}{d}}{\frac{P}{d} - 1})(\frac{f}{f_0})U_r, \tag{7.1}$$

while, for a square array, it is:

$$U_{Pr} = 2\pi(\frac{l}{s_0})(\frac{s_0}{d})(\frac{f}{f_0})U_r \tag{7.2}$$

The second group includes parameters which are measured or, in the absence of appropriate experimental data, simply "guessed" based on common sense (they

are summarized in Table 7.2). As with Reference [48], the relevant fluid stream length is set $l = 4s_0$, reflecting the likehood that perturbations generated by a flexible cylinder may persist upto two rows upstream and downstream, $s = \pm 2s_0$ (in staggered arrays, nearest neighbours are two rows away). From this assumption it follows that $\alpha \approx 1$. This means that further upstream and downstream from the flexible cylinder, the effect of perturbation is negligible (86.5 % reduction at $s = \pm 2s_0$). The pressure loss coefficient, h, depends on the array configuration, and the values recommended in Reference [48] are shown in Table 7.2. The drag coefficient, C_D, may be expressed in terms of h based on the following relation, [48];

$$C_D = 2(\frac{A_0}{d})h. \tag{7.3}$$

For a parallel triangular array, this yields $C_D = 0.225$. Note that the value obtained from Blevins' formulae, for drag-dependent damping (equations (5.1) and (5.2)) which was measured experimentally, is approximately ten times higher. Nevertheless, for the overall stability analysis, it was decided to use the value suggested in Reference [48]. Also, the measured flow-velocity dependent damping, although it increased linearly with flow as suggested by Blevins, represents the net and not just the drag-dependent term. However, the effect of increase in C_D and h will be also investigated. The random excitation coefficient, C'_r, was obtained directly from damping measurements at the RMS response level *via* expression (6.36). It is worth noting that the values of C'_r are approximately constant in the sub-stable region and are in close agreement with those reported by Pettigrew and Gorman, [64].

Table 7.2: The empirical parameters for the theoretical model.

Array geometry	$\frac{l}{s_0}$	α	h	C_D	C_r
Parallel triangular: $\alpha_0 = \frac{1}{6}\pi$, $\frac{P}{d} = 1.375$	4	1	0.30	0.225	0.065
Square: $\alpha_0 = \frac{1}{2}\pi$, $\frac{P}{d} = 1.433$	4	1	0.35	0.300	0.200

It follows that, for a given array of specified geometry (angle, α_0, pitch, $\frac{P}{d}$, and pattern, $\frac{T}{d}$), there are seven independent parameters required by the theoretical model: $\frac{A_0}{d}$, $\frac{s_0}{d}$, $\frac{D_E}{d}$, $\frac{l}{s_0}$, h, C_r and α. Complete results of the sensitivity analysis, on the linear stability equations, in which first five of those parameters were independently varied ± 10 % and ± 50 % from the baseline values shown in Table 7.1 and 7.2, are reported in Reference [48]. It was found that the model, although qualitatively unaffected by those changes, is governed primarily by the parameters which describe the relevant fluid streams on either side of the cylinder; the steady streamtube area, $\frac{A_0}{d}$, and the relevant fluid stream length, $\frac{l}{s_0}$. Since the variations of streamtube area are limited to ± 10 % by the minimum gap between cylinders, it may be concluded that the model virtually depends on the assumed flow redistribution mechanism which is described by the time lag, $\tau_0 = \frac{l}{U_0}$.

7.2 Analytical solution

The theoretical model predicts the linear and non-linear stability behaviour of cylinder arrays as a function of the mass-damping parameter and the reduced pitch velocity. The predictions are greatly simplified if the relevant fluid inertia length is expressed in terms of the streamtube length, $l = 4s_0$.

7.2.1 Linear stability boundary

The linear stability curves may be written as:

(a) Dynamic instability for $\alpha \neq 0$

$$\bar{m}\delta_0 = 32\pi(\frac{D_E}{d})(\frac{d}{A_0})(\frac{s_0}{d})^2(\frac{\omega}{\omega_0})U_r^2\{e^{-\alpha}sin\frac{1}{U_r} +$$
$$+\frac{1}{2}\frac{1}{U_r}\frac{1}{\alpha_1}[\alpha + \frac{1}{U_r}e^{-\alpha}sin\frac{1}{U_r} - (\alpha + \frac{1}{2}\alpha_1)e^{-\alpha}cos\frac{1}{U_r}] +$$
$$+\frac{1}{16}(\frac{1}{U_r})^2(\frac{1}{\alpha_1})^2[(\alpha\alpha_1 + \alpha_2)e^{-\alpha}sin\frac{1}{U_r} + 2\frac{1}{U_r}\alpha + \frac{1}{U_r}(2\alpha + \alpha_1)e^{-\alpha}cos\frac{1}{U_r}] +$$

$$-h\frac{1}{U_r}\frac{1}{\alpha_1}\{[U_r(\alpha+\alpha_1)+\frac{1}{U_r}(\frac{1}{4}+\frac{\alpha}{\alpha_1})]e^{-\alpha}sin\frac{1}{U_r}+$$
$$+[1-\frac{1}{4}(\alpha+\frac{\alpha_2}{\alpha_1})]e^{-\alpha_1}cos\frac{1}{U_r}+\frac{1}{4}\frac{\alpha_2}{\alpha_1}-1\}\}-2\pi C_D(\frac{s_0}{d})(\frac{\omega}{\omega_0})U_r \quad (7.4)$$

$$(\frac{\omega_0}{\omega})^2=1+32(\frac{1}{\bar{m}})\frac{D_E}{d})(\frac{d}{A_0})(\frac{s_0}{d})^2U_r^2\{1-e^{-\alpha_1}cos\frac{1}{U_r}+$$
$$+\frac{1}{2}\frac{1}{U_r}\frac{1}{\alpha_1}[\frac{1}{U_r}-\frac{1}{U_r}e^{-\alpha_1}cos\frac{1}{U_r}-(\alpha+\frac{1}{2}\alpha_1)e^{-\alpha}sin\frac{1}{U_r}]+$$
$$+\frac{1}{16}(\frac{1}{U_r})^2(\frac{1}{\alpha_1})^2[\frac{\alpha_2}{\alpha_1}-(\frac{\alpha_2}{\alpha_1}-\alpha)e^{-\alpha_1}cos\frac{1}{U_r}-\frac{1}{U_r}(1+2\alpha\alpha_1)e^{-\alpha}sin\frac{1}{U_r}]+$$
$$+h\frac{1}{U_r}\frac{1}{\alpha_1}\{\alpha(U_r+\alpha_1\frac{1}{U_r})+(1-\frac{1}{4}\alpha-\frac{1}{4}\frac{\alpha_2}{\alpha_1})e^{-\alpha}sin\frac{1}{U_r}+$$
$$-[U_r(\alpha^2+\alpha)+\frac{1}{U_r}(\frac{5}{4}+\alpha\alpha_1)]e^{-\alpha}cos\frac{1}{U_r}\}\} \quad (7.5)$$

where $\alpha_1=\alpha^2+(\frac{1}{U_r})^2$ and $\alpha_2=\alpha^2-(\frac{1}{U_r})^2$. The flow velocity U_r is converted to the reduced pitch velocity U_{Pr} *via* equations (7.1) and (7.2), yielding $U_{Pr}=20.891U_r$ and $U_{Pr}=36.015U_r$ for a parallel triangular and a square array, respectively.

(b) Static instability for $\alpha \neq 0$

$$U_{Pr}=2\pi(\frac{\frac{P}{d}}{\frac{P}{d}-1})U_r(\frac{A_0}{d})^{1.5}(\frac{d}{T})\sqrt{\frac{\bar{m}}{1-e^{-\alpha}+\frac{h}{\alpha}[1-e^{-\alpha}(\alpha+1)]}} \quad (7.6)$$

(c) Dynamic instability for $\alpha = 0$

$$\bar{m}\delta_0=40\pi(\frac{D_E}{d})(\frac{d}{A_0})(\frac{s_0}{d})^2(\frac{\omega}{\omega_0})U_r^2[\frac{5}{4}sin\frac{1}{U_r}-\frac{1}{4}\frac{1}{U_r}cos\frac{1}{U_r}+$$
$$+h(sin\frac{1}{U_r}+U_rcos\frac{1}{U_r}-U_r)]-2\pi C_D(\frac{s_0}{d})(\frac{\omega}{\omega_0})U_r \quad (7.7)$$

$$(\frac{\omega_0}{\omega})^2=1+40\pi(\frac{1}{\bar{m}})(\frac{D_E}{d})(\frac{s_0}{d})^2(\frac{d}{A_0})U_r^2[\frac{5}{4}(1-cos\frac{1}{U_r})+$$
$$-\frac{1}{4}\frac{1}{U_r}sin\frac{1}{U_r}+h(U_rsin\frac{1}{U_r}-cos\frac{1}{U_r})] \quad (7.8)$$

Figure 7.1 shows these stability curves for a parallel triangular and a square array in the form of a stability map. For direct comparison with experimental results, the model parameters are selected as presented in Table 7.1 and 7.2 (the damping values chosen, $\delta_0=0.01$ and $\delta_0=0.10$, bracket nearly all data reported in the open literature). The stability curves, presented in Figure 7.1, reflect a number of interesting features of this model.

- The existence of multiple stability boundaries at low mass-damping parameters. This results from the time delay between cylinder motion and the associated fluid forces which, as follows from equations (7.4) and (7.5), varies harmonically with flow velocity. It is unlikely, however, that these harmonic pressure perturbations would be communicated through a real fluid indefinitely. Thus, it is probable that, in practice, only two or three upper stability branches may exist. It is interesting to note that multiple stability regions were observed experimentally by Andjelic, [55], and were also predicted by other theoretical models which incorporate the velocity mechanism (see References [41,42,81], for example).

- The separation in the two dimensionless parameters, δ_0 and $\bar{m}$, which results from fluidelastic stiffness. This has also been predicted by Price *et al.*, [38].

- The transition from fluid-damping controlled to fluid-stiffness controlled instabilities *via* frequency reduction towards zero. This process takes place gradually, over the low ($\bar{m}\delta_0 < 1$) and high ($\bar{m}\delta_0 >$ 300-500) range of the mass-damping parameter, where the dynamic and static stability boundaries start to approach each other (clearly visible for $\delta_0 = 0.10$). This is in agreement with other theoretical models which, however, predict fluid-stiffness controlled instability by including the effect of relative cylinder motion (see References [37,39], for example).

- The existence of static stability boundary. The slope of this line is proportional to $(\bar{m}\delta_0)^{0.5}$, limiting the increase of dynamic stability curve which is directly proportional to $\bar{m}\delta_0$ at high $\bar{m}\delta_0$. While the predicted static instability has not been observed experimentally for these arrays, its impact on dynamic instability significantly improves the agreement with experimentally observed stability curves (see Table 3.2) and with other theoretical models [28,30,37,39].

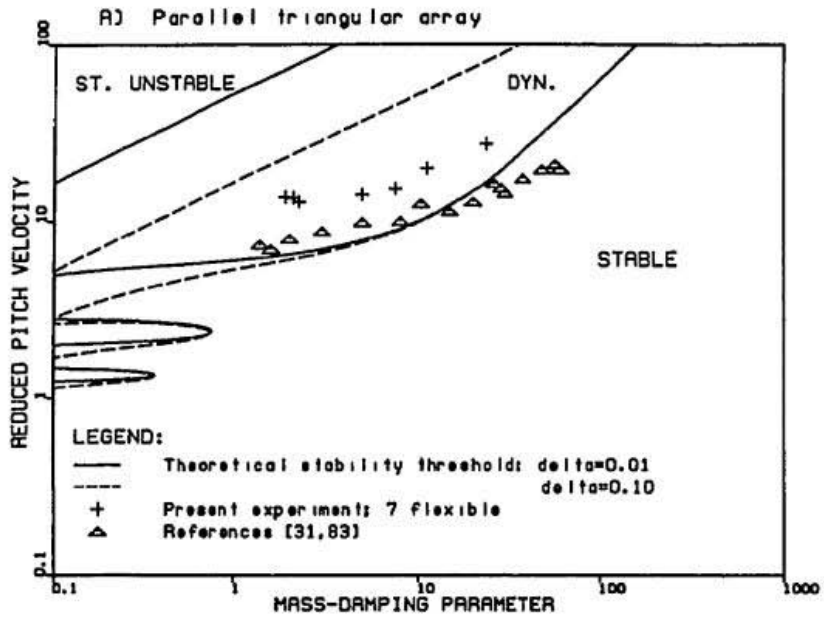

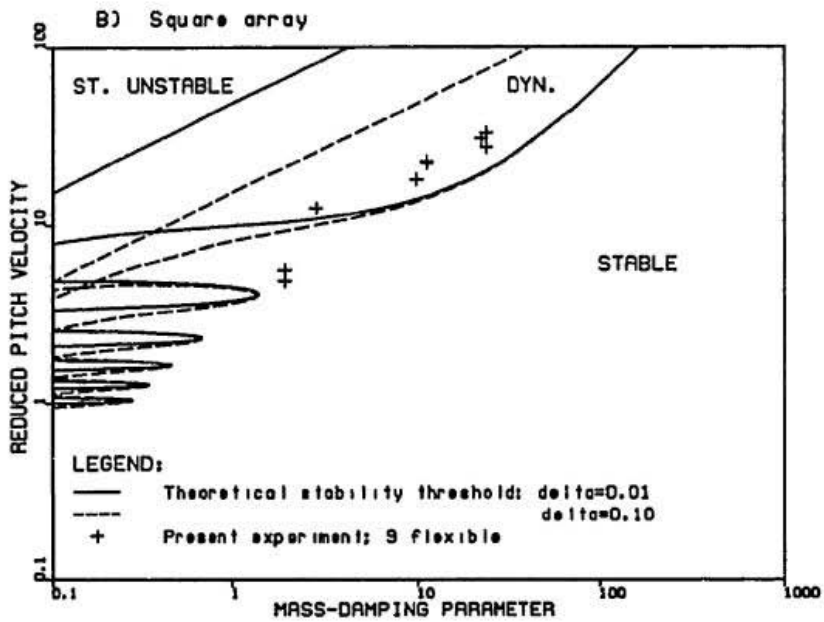

Figure 7.1: Theoretical stability curves, in comparison to experimental data, for a parallel triangular array and a square array (varied δ_0).

Figure 7.1 shows that the stability curves are reasonably well predicted by the model. While a very good agreement can be seen with the experimental data of Weaver *et al*, [31,83], for a parallel triangular array (Figure 7.1(a)), the present results exceed the theoretical prediction. However, they show the correct dependance with respect to $\bar{m}\delta_0$. This indicates that the recommended values of the C_D and h coefficients may be too low for this array (recall that an approximately ten times higher C_D was obtained from Blevins' expression for velocity-dependent damping). Better overall agreement can be seen for a square array (Figure 7.1(b)). Note that the scatter in critical flow velocities, observed experimentally in the range of $\bar{m}\delta_0 \approx 1.9 - 2.8$, can be attributed to the existence of multiple stability regions. This may explain the significant difference in critical flow velocity for the dominant cylinder (1×2 and 1×1, see Table 5.2).

Figure 7.2 shows the effect of the decaying of the area perturbation function on the stability curves. The strength of the decay term (α) was varied ± 100 % from the baseline value suggested in Table 7.2. Since the decay term contributes to energy dissipation in the fluidelastic system, it increases the stability boundary, as expected. This effect is particularly important at high $\bar{m}\delta_0$. Note that at low $\bar{m}\delta_0$ the increase in decaying strength reduces the size of multiple stability regions, while the upper stability boundary is virtually unaffected.

Figure 7.3(a) presents the stability curves for a parallel triangular array for various values of the C_D and h coefficients. As mentioned earlier, these parameters have virtually no influence on the predicted stability boundary if changed ± 100 %. Thus, it was decided to increase the drag coefficient to $C_D = 0.65$ (value suggested in Reference [46]) and to $C_D = 2.20$ (value found in this study). Respectively, the flow resistance coefficient was increased, based on equation (7.3), to $h = 0.87$ and $h = 2.93$. It can be seen that this only slightly improves the agreement with the experimental data. Thus, it does not account for the difference between the present

results and those reported in References [31,83]. A similar analysis was performed for a square array (see Figure 7.3(b)). As before, there is a little effect on the stability curves.

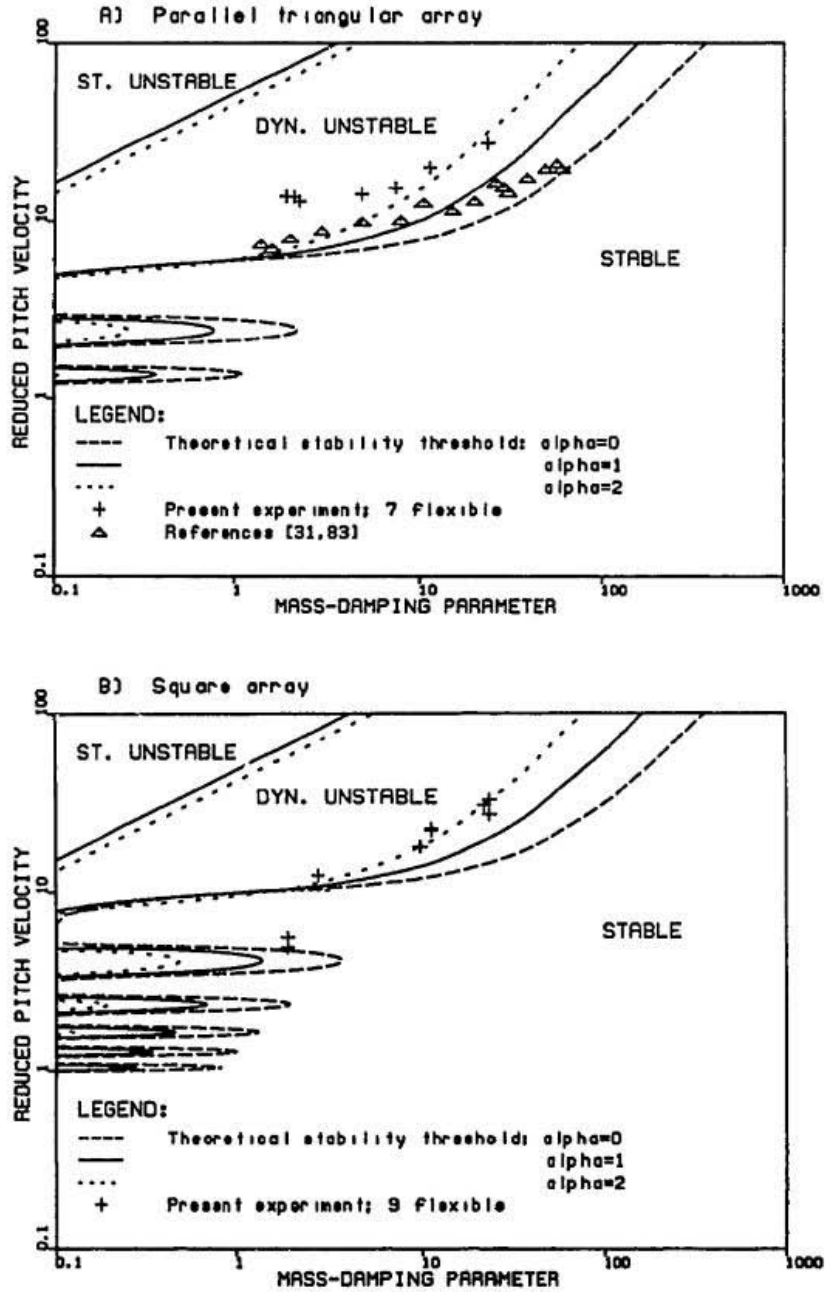

Figure 7.2: Theoretical stability curves, in comparison to experimental data, for a parallel triangular array and a square array (varied α).

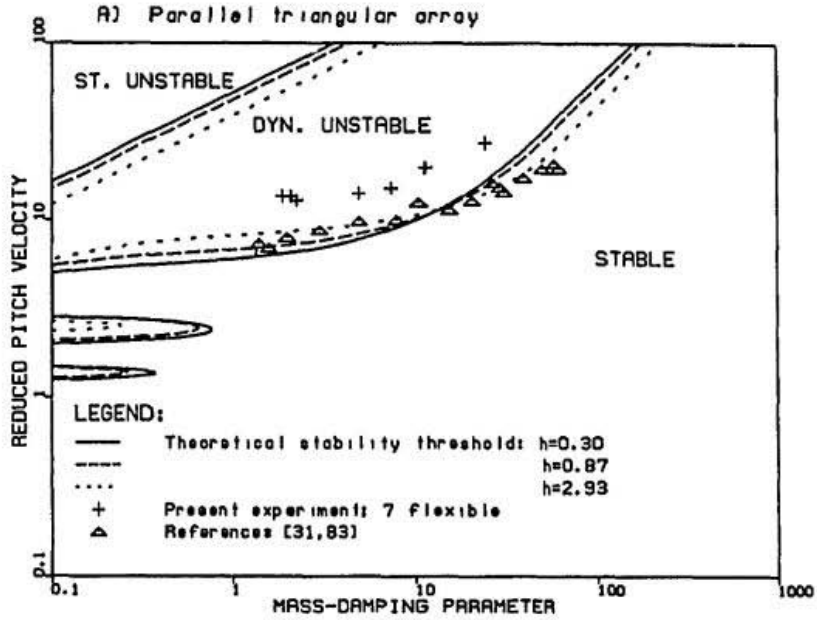

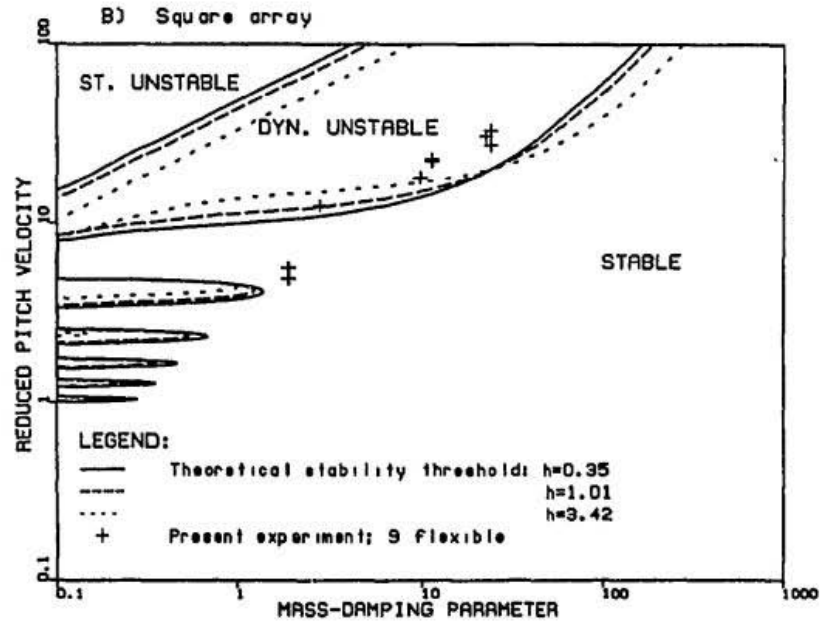

Figure 7.3: Theoretical stability curves, in comparison to experimental data, for a parallel triangular array and a square array (varied h).

7.2.2 Linear response curves

The linear response curve, under combined turbulence and fluidelastic excitation, was formulated as:

$$\frac{A_{RMS}}{d} = \frac{C'_r}{8\sqrt{2}\pi}\left(\frac{f}{f_0}\right)^{1.5} U_{Pr}^{1.5}\left[\frac{1}{\bar{m}(\bar{m}\delta_0 - \bar{m}\delta_{fe})}\right]^{0.5} \tag{7.9}$$

where $\bar{m}\delta_{fe}$ denotes the fluidelastic mass-damping parameter (the RHS of equation (7.7)) which includes the drag-dependent term. This is the term which accounts for the reduction in the net damping and, hence, the increase in turbulence response as the stability threshold ($\bar{m}\delta_0 = \bar{m}\delta_{fe}$) is approached. Note, however, that because in a linear formulation both excitation mechanisms superimpose, the predicted stability threshold location is unaffected by turbulence. Thus, only the effect of the variation in $\bar{m}\delta_{fe}$ on the shape of the linear response curve is investigated here (the random excitation coefficient, C'_r, is set at the baseline value).

Figure 7.4 compares the experimentally obtained fluidelastic damping factor (expressed in percentage of critical as a function of reduced flow velocity) with that predicted by the model. Since the Blevins' velocity-dependent damping term is subjected to some uncertainty, two sets of C_D and h were used for the model predictions; first, the baseline values suggested in Table 7.2 (Figures 7.4(a1) and 7.4(b1)) and next, the values obtained from experiment (Figures 7.4(a2) and 7.4(b2)).

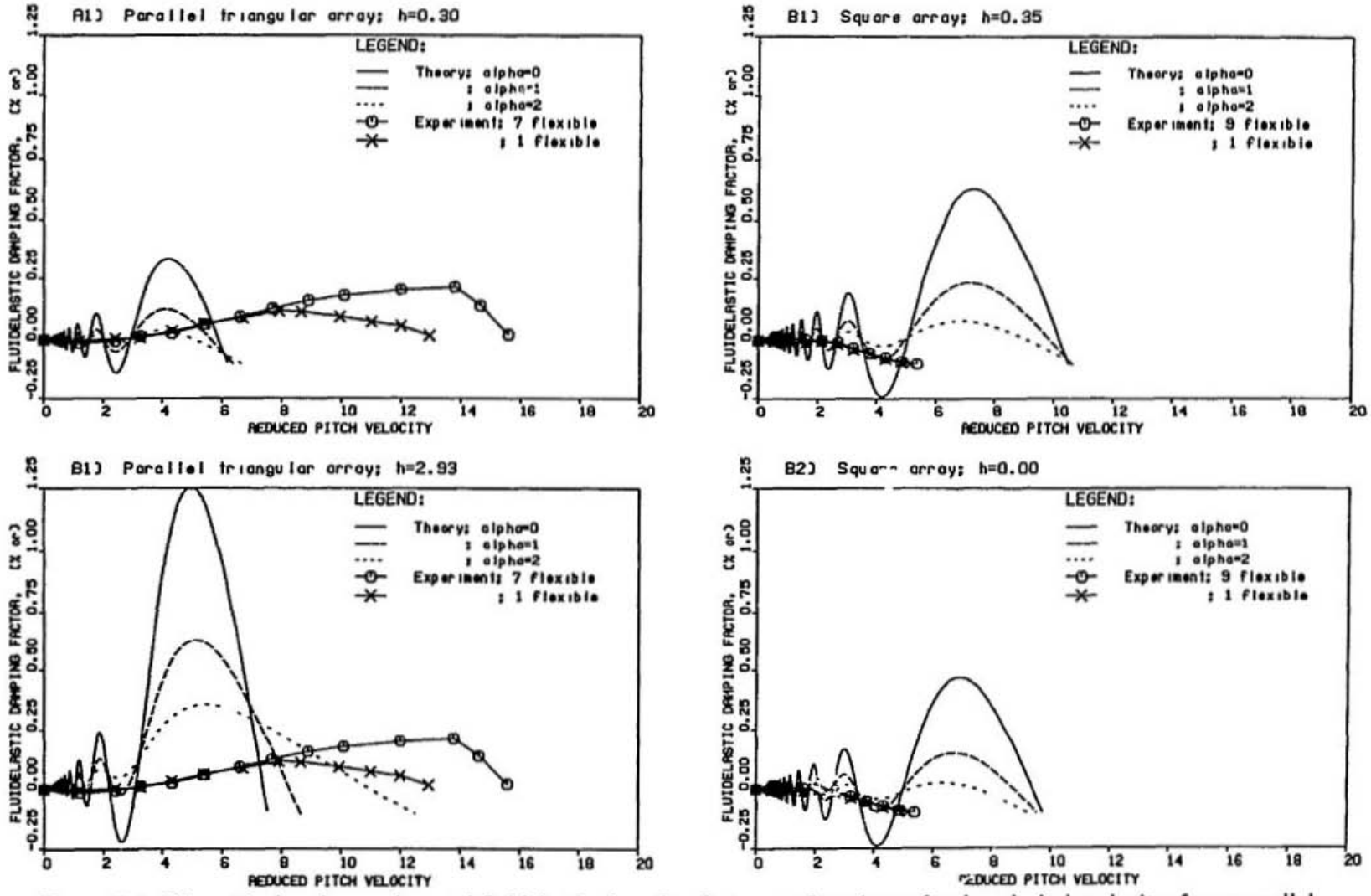

Figure 7.4: Theoretical and experimental fluidelastic damping factor, as functions of reduced pitch velocity, for a parallel triangular array and a square array.

It can be seen that unlike the measured damping curves, which smoothly vary with flow velocity, the theoretical damping curves oscillate around the mean which is defined by the Blevins' term. These oscillations produce the multiple instability regions (as shown in Figures 7.1-7.3) and their magnitude increases with h. Somewhat more realistic modelling is achieved with the decaying of area perturbation function (α) which strongly reduces the strength of the oscillatory term and delays the initiation of instability. Reasonably good agreement is seen between the observed and predicted damping curves for $\alpha = 2$ (C_D and h as with the experiment). Note that for a square array, the stability threshold is located at the lower branch of instability.

Figure 7.5 shows the corresponding experimental and theoretical response curves which are computed from equation (7.9) (vertical scale is exagerated for easy of comparison). For a parallel triangular array (Figures 7.5(a1) and 7.5(a2)), all curves show a smooth increase in RMS response towards an essentially vertical asymptote at the critical flow velocity. The rate of increase is similar fo. all response curve. However, the predicted critical flow velocities, except for $\alpha = 2$ ($h = 2.93$), differ significantly from that experimentally observed. For a square array (Figures 7.5(a2) and 7.5(b2)), a similarly smooth increase in predicted RMS amplitude, towards a vertical asymptote, is seen for $\alpha = 2$ only (other curves show local response "bumps" due to more severe damping oscillations). The measured amplitudes, however, are significantly higher, reflecting the observed lack of positive damping induced by flow. Note that for $\alpha = 0$ only, does the system become unstable at the lower instability branch, revealing good agreement with experiment.

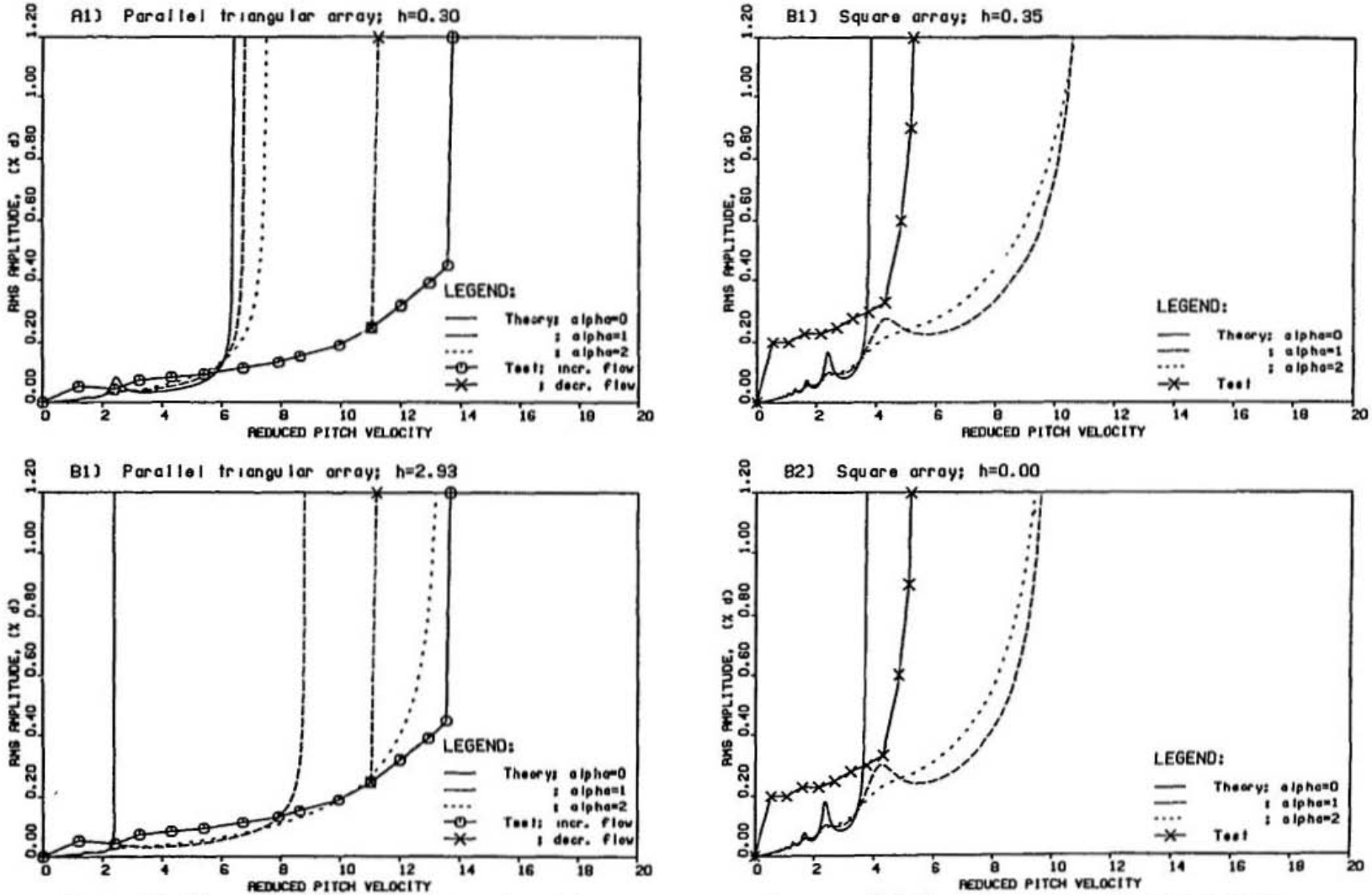

Figure 7.5: Theoretical (linear) and experimental response curves for a parallel triangular array and a square array.

7.2.3 Limit cycle oscillations

For $\alpha = 0$, the third order non-linear solution yields the following amplitude of limit cycle oscillations:

$$(\frac{a}{d})^2 = \{\bar{m}\delta_0 + 2\pi C_D(\frac{s_0}{d})(\frac{\omega}{\omega_0})U_r - 40\pi(\frac{D_E}{d})(\frac{d}{A_0})(\frac{s_0}{d})^2(\frac{\omega}{\omega_0})U_r^2[\frac{5}{4}sin\frac{1}{U_r} + -\frac{1}{4}\frac{1}{U_r}cos\frac{1}{U_r} + h(sin\frac{1}{U_r} + U_r cos\frac{1}{U_r} - U_r)]\}/ \{40\pi(\frac{D_E}{d})(\frac{d}{A_0})^3(\frac{s_0}{d})^2(\frac{\omega}{\omega_0})U_r^2\{sin\frac{1}{U_r}[1 - \frac{5}{8}cos\frac{1}{U_r}] - \frac{1}{8}\frac{1}{U_r}cos\frac{1}{U_r} + +h\{sin\frac{1}{U_r}[\frac{7}{4} - \frac{5}{8}U_r sin\frac{1}{U_r}] + 2U_r(cos\frac{1}{U_r} - 1)\}\} - \frac{1}{16}\pi C_D(\frac{d}{s_0})(\frac{\omega}{\omega_0})\frac{1}{U_r}\} \quad (7.10)$$

$$(\frac{\omega_0}{\omega})^2 = 1 + 40(\frac{1}{\bar{m}})(\frac{D_E}{d})(\frac{s_0}{d})^2(\frac{d}{A_0})^3(\frac{a}{d})^2U_r^2\{(\frac{A_0}{d})^2(\frac{d}{a})^2[\frac{5}{4}(1 - cos\frac{1}{U_r}) + -\frac{1}{4}\frac{1}{U_r}sin\frac{1}{U_r}] + \frac{45}{16}(1 - cos\frac{1}{U_r}) - \frac{1}{2}sin\frac{1}{U_r}[\frac{5}{4}sin\frac{1}{U_r} + \frac{1}{4}\frac{1}{U_r}] + +h\{(\frac{A_0}{d})^2(\frac{d}{A_0})^2(U_r sin\frac{1}{U_r} - cos\frac{1}{U_r}) + \frac{1}{2}U_r sin\frac{1}{U_r}[\frac{5}{4}cos\frac{1}{U_r} + \frac{9}{4}] - \frac{7}{4}cos\frac{1}{U_r}\}\} \quad (7.11)$$

Figure 7.6 shows the amplitudes of limit cycle oscillations for the two arrays of interest and the values of C_D and h which were suggested in the linear analysis. The amplitudes are computed for a variety of mass-damping parameters; $\bar{m}\delta_0 = 1$ (two branches), 10, 20, 30, 50, 100 with $\delta_0 = 0.01$. For a parallel triangular array, stable limit cycle oscillations are predicted below $\bar{m}\delta_0 = 5.10$ for $h = 0.30$ (Figure 7.6(a1)) and below $\bar{m}\delta_0 = 20.30$ for $h = 2.93$ (Figure 7.6(a2)). Interestingly, these oscillations show non-linear softening (i.e. a transition to unstable limit cycle oscillations) at larger amplitudes, particularly explicit at the upper instability branch for $\bar{m}\delta_0 = 1$. This results from fluidelastic stiffness which reduces the natural frequency. In the higher mass-damping parameter range, only the unstable limit cycle oscillations are predicted. For a square array, the model yields essentially similar results; stable limit cycle oscillations below $\bar{m}\delta_0 = 8.95$ for $h = 0.35$ (Figure 7.6(b1)) and below $\bar{m}\delta_0 = 44.10$ for $h = 3.42$ (Figure 7.6(b2)), and unstable limit cycle oscillations in the higher range.

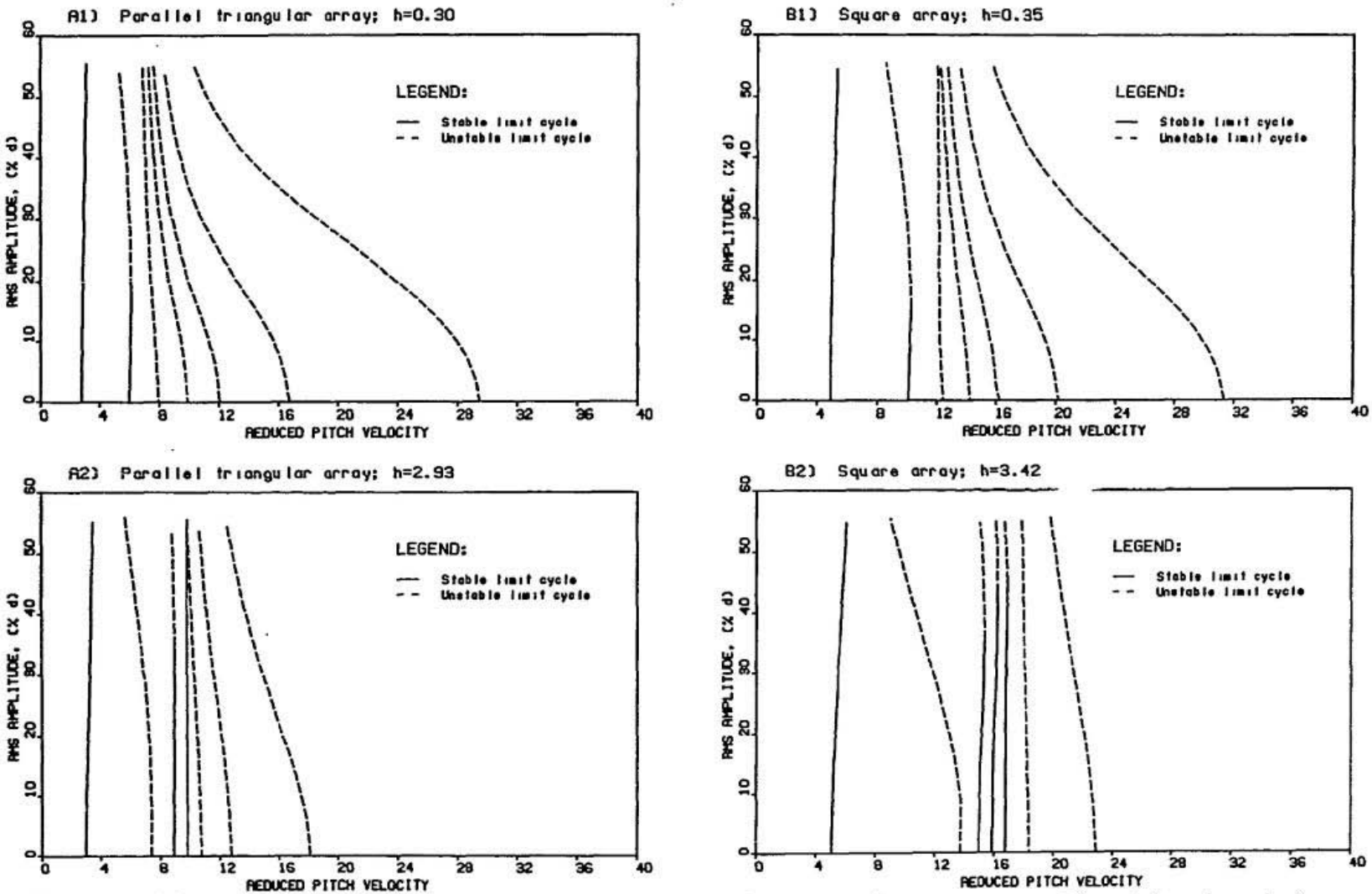

Figure 7.6: Theoretical limit cycle oscillations for a parallel triangular array and a square array; $\bar{m}\delta_0 = 1$ (two branches), 10, 20, 30, 50, 100 - from left to right.

7.2.4 Non-linear stability boundary under combined excitation

The non-linear stability curve under combined excitation was approximately expressed, using superposition of the linear response to combined excitation with the non-linear limit cycle due to fluidelastic excitation only, as:

$$\bar{m}\delta_0 = \bar{m}\delta_{fe} + \frac{1}{8\pi} C_r' \{2ln[fT(Y)]\}^{0.5} (\frac{1}{\bar{m}})^{0.5} (\frac{f}{f_0})^{1.5} U_{Pr}^{1.5} (-D)^{0.5} \qquad (7.12)$$

where $\bar{m}\delta_{fe}$ denotes the fluidelastic mass-damping parameter and D is the non-linear operator (denominator in equation (7.10)). Note that expression (7.12) gives the effect of turbulence on the dynamic bifurcation which defines the stability threshold for the fluidelastic excitation only ($\bar{m}\delta_0 = \bar{m}\delta_{fe}$). It follows that the threshold reduction is directly proportional to the amplitude of turbulence buffeting, C_r', and inversely proportional to the amplitude of unstable limit cycle, $\sqrt{-D}$.

Table 7.3 presents the solution of equation (7.12) for $\bar{m}\delta_0 = 50$ where the fluidelastic system is governed by the unstable bifurcation ($D < 0$), as required. Results were obtained for the baseline values of the random excitation coefficient (suggested for both arrays in Table 7.2) and twice these values to show the effect of increasing turbulent response on the stability threshold. The average return period was set $T(Y) = 10\ min$ (the time at which cylinder was allowed to stabilize, at a given flow velocity, during the experimental investigation) and $T(Y) = 25\ years$ (typical in-service period for production platform). As expected, superposition of turbulence lowers the fluidelastic stability threshold for the unstable bifurcation. Since, in the practical range of C_r', the rate of reduction was found to be very small for $\delta_0 = 0.01$, the analysis was also performed for $\delta_0 = 0.10$ where the reduction is more pronounced due to the larger turbulence response (it is inversely proportional to $\sqrt{\bar{m}}$).

The small effect of turbulence on the fluidelastic stability threshold results from the extreme steepness of the unstable limit cycle predicted by the model (see Fig-

ures 7.6(a1) and 7.6(b1)). It must be appreciated, however, that the experimentally observed unstable limit cycle (within the hysteresis region, see Figure 5.9) is significantly lower. Thus, more severe turbulence sensitivity may be expected.

Table 7.3: Turbulence sensitivity of the unstable bifurcation for $\bar{m}\delta_0 = 50$ (coupling ignored).

Array geometry	δ_0	C'_r	$T(Y)$	$(U_{Pr})_{cr}$	Reduction (%)
Parallel tringular	0.01	0.000	0	16.622	0.00
		0.065	10 *min*	16.587	0.21
			25 *years*	16.564	0.35
		0.130	10 *min*	16.552	0.42
			25 *years*	16.506	0.70
	0.10	0.000	0	16.585	0.00
		0.065	10 *min*	16.475	0.66
			25 *years*	16.404	1.09
		0.130	10 *min*	16.368	1.31
			25 *years*	16.230	2.14
Square	0.01	0.000	0	20.056	0.00
		0.200	10 *min*	19.938	0.59
			25 *years*	19.869	0.93
		0.400	10 *min*	19.819	1.18
			25 *years*	19.685	1.85
	0.10	0.000	0	19.988	0.00
		0.200	10 *min*	19.626	1.81
			25 *years*	19.425	2.82
		0.400	10 *min*	19.297	3.46
			25 *years*	18.848	5.70

7.3 Numerical simulation

Physical arguments suggest that stronger non-linear hardening, leading to stable limit cycles at large amplitudes, should be predicted by the single flexible cylinder model used here. This non-linear hardening may arise from higher order terms or, alternatively, decaying of streamtube area function ($\alpha \neq 0$). To examine these effects and to model the actual coupling between turbulence and fluidelastic excitations, the numerical procedure, described in Section 6.4, is applied here.

7.3.1 Fluidelastic excitation

The initial series of simulations was conducted to determine the linear stability threshold ($n = 0$ in equation (6.13)). The cylinder was harmonically excited in the vicinity of the threshold (defined by the analytical solution, equations (7.3) and (7.4)) and the response record (10 min) was carefully examined by checking for exponential increase or decrease of the oscillation envelope. If desired, the flow velocity was corrected and the procedure repeated until a constant amplitude sinewave (neither decay nor growth) was observed. This was taken as the stability threshold. Comparing the results to the analytical solution, the absolute simulation error in the linear threshold estimation, for mass-damping parameter of 1-100, was found to be in the range 0.02-0.20 % ($\alpha = 0$) and 0.05-0.40 % ($\alpha \neq 0$) for a parallel triangular array, and in the range 0.10-0.30 % ($\alpha = 0$) and 0.20-0.60 % ($\alpha \neq 0$) for a square array. The simulation error increased at higher mass-damping parameter due to the shorter time lag, τ_0. This error can be significantly reduced by finer time stepping, Δt. However, a discrepancy within 1 % is acceptable for this kind of numerical simulation.

The next series of tests was conducted to determine limit cycle oscillations. Initially, the third order solution was computed for $\alpha = 0$ ($n = 2$ in equation (6.13)) to compare directly with the analytical expressions of the first approximation (equations (7.10) and (7.11)). These simulations were performed for $\bar{m}\delta_0 = 1$ (stable limit cycle) and for $\bar{m}\delta_0 = 50$ (unstable limit cycle). Numerical determination of the stable limit cycle was conducted on two upper stability branches. This could be done only over a very limited velocity range due to the extreme steepness of the equilibrium path. As shown in Figures 7.7, agreement between analytical and numerical solutions was excellent. In all cases investigated, both solutions predicted the same type of limit cycle (stable or unstable) at a given flow velocity, indicating that the numerical implementation of the non-linear fluidelastic model is correct.

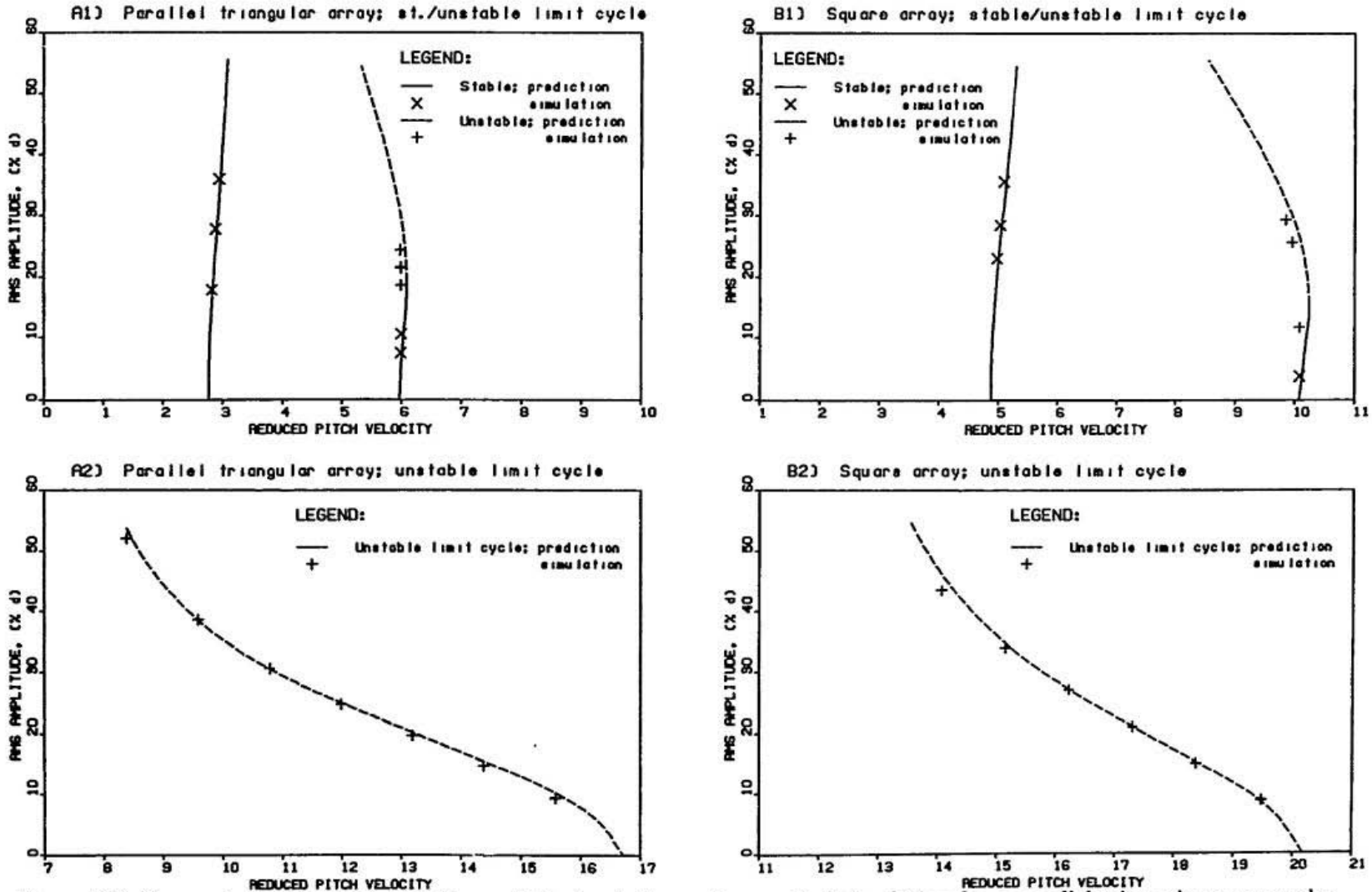

Figure 7.7: Comparison between 3-rd order analytical solution and numerical simulation for a parallel triangular array and a square array ($\bar{m}\delta_0 = 1$ - stable bifurcation and $\bar{m}\delta_0 = 50$ - unstable bifurcation).

Next, the numerical simulation was extended to include higher order terms. To recognize the nature of the limit cycle oscillations, the computation was performed for mass-damping parameter in the range $\bar{m}\delta_0 = 1 - 100$. These simulation results were found to be qualitatively identical to those of the third order (see Figure 7.7). As an example, Table 7.4 presents the limit cycle amplitudes obtained for $\bar{m}\delta_0 = 50$ at three different velocity levels (note that the even terms were found to be zero). It can be seen that convergence to the limit cycle amplitude increases as the stability threshold is approached ($U_{Pr} = 16.62$ for a parallel triangular array and $U_{Pr} = 20.06$ for a square array). A third order solution yields the correct qualitative assessment (stable *versus* unstable limit cycles) and is very close to a fully non-linear solution (within 10 %) in the vicinity of the stability threshold. Thus, it may be concluded that the third order analytical solution of the first approximation is sufficient to capture the essential features of the present model.

Table 7.4: Convergence test of numerical solution.

Array geometry	U_{Pr}	Limit cyle amplitude, A_{RMS} (% d)					
		3-rd	5-th	7-th	9-th	11-th	13-th
Parallel triangular	11.98	24.70	20.50	19.55	19.25	19.15	19.15
	13.18	19.75	17.10	16.50	16.40	16.35	16.35
	14.38	14.90	13.60	13.20	13.15	13.10	13.10
Square	16.23	26.98	22.45	21.70	21.60	21.50	21.50
	17.31	20.90	18.45	18.05	18.00	17.95	17.95
	18.39	14.95	13.95	13.75	13.75	13.70	13.70

The last series of tests was conducted to determine limit cycle oscillations including the decaying effect of streamtube area function ($\alpha \neq 0$). The simulations results were found to be qualitatively identical to those already presented ($\alpha = 0$), with only the bifurcation point and limit cycle amplitudes changing. Unfortunately, the simulations with $\alpha \neq 0$ do not show non-linear hardening with increase of amplitude and mass-damping parameter. That is, the decaying function does not reproduce

the non-linear behaviour expected on physical grounds, pointing to a weakness in the model formulated here.

7.3.2 Combined fluidelastic and turbulence excitation

Initially, linear numerical simulations were conducted to determine RMS cylinder response for separate turbulence buffeting and combined excitation at $\bar{m}\delta_0 = 50$ over broad ranges of damping, δ_0, and random excitation coefficient, C_r'.

As an example, Figure 7.8 shows the simulated time series RMS cylinder response to combined excitation for a parallel triangular array at the baseline value of C_r' (the curves obtained for a square array were essentially identical). Two values of damping were used, $\delta_0 = 0.01$ and $\delta_0 = 0.10$, which bracket all numerical tests. Since the heavier damped cylinder shows larger turbulence response (3.16 times, as follows from equation (7.9)), a 3 times higher scale in Figure 7.8(b) was used to approximately compensate for this effect. According to equations (7.7) and (7.8), the fluidelstic stability boundary is $U_{P_r} = 16.62$ for $\delta_0 = 0.01$ and $U_{P_r} = 16.59$ for $\delta_0 = 0.10$. As can be seen, the combined response achieves steady-state for each flow velocity lower than critical before the end of $T_{max} = 12.5min$, except for $U_{P_r} = 16.51$ (Figure 7.8(a)) where a longer transient time was observed. Therefore, to perform simulations near the stability threshold without the prohibitive computational effort, the steady-state response value, given by equation (7.9), was used as a starting parameter.

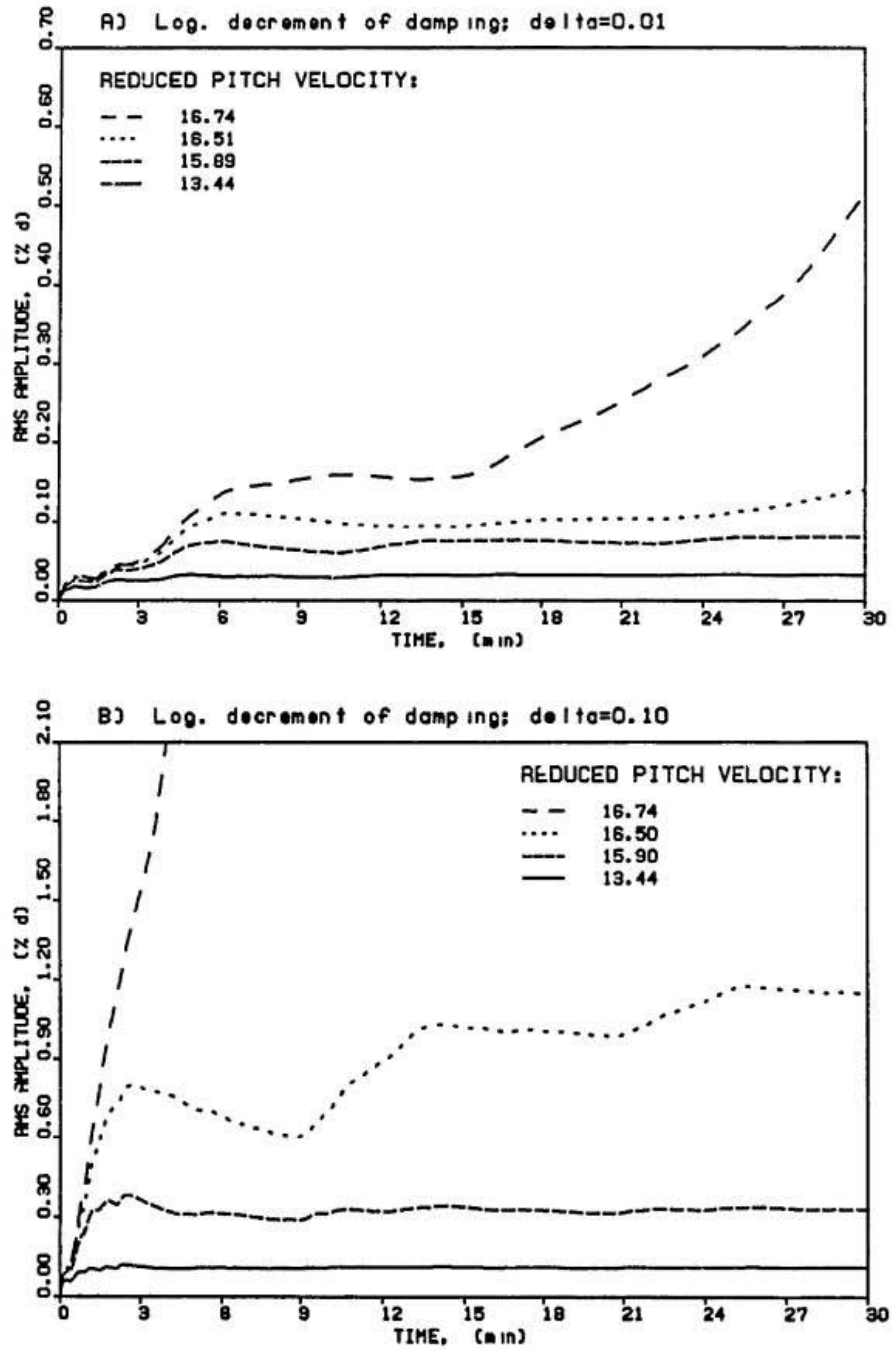

Figure 7.8: Simulated RMS response to combined linear excitation for a parallel triangular array ($\bar{m}\delta_0 = 50$; $\delta_0 = 0.01$ and $\delta_0 = 0.10$).

Table 7.5 compares the simulation results (examined only in the steady-state), in part presented in Figure 7.8, with the corresponding analytical solution to turbulence and combined excitation (equation (7.9)). As can be seen, the turbulence RMS response agreed to better than 2.5 % for $\delta_0 = 0.01$ and to better than 1.0% for $\delta_0 = 0.10$ at each velocity point. The combined RMS response agreed to better than 10 %, except very near the stability threshold. In this region, the response was sensitive to the randomizing effect of turbulence because of discretization errors associated with the decreasing bandwith of the system (very small δ_n). It should be noted, however, that some variations in the simulated response were expected since specific timeseries of finite length were generated, whereas equation (7.9) applies, strictly speaking, to infinitely long records. It is thus felt that the numerical implementation of the combined turbulence/fluidelastic model (at least its linear part) yields accurate and reliable results.

Table 7.5: Validation tests for linear system (A_{RMS} in % d).

U_{Pr}	δ_0	Analytical		Numerical	
		Turbulent	Combined	Turbulent	Combined
12.22	0.01	0.0156	0.0253	0.0153	0.0272
13.44	0.01	0.0180	0.0346	0.0176	0.0364
14.67	0.01	0.0206	0.0507	0.0201	0.0517
15.89	0.01	0.0232	0.0938	0.0227	0.0883
16.51	0.01	0.0246	0.2550	0.0240	0.1824
16.74	0.01	0.0251	unstable	0.0245	unstable
12.22	0.10	0.0494	0.0806	0.0491	0.0945
13.44	0.10	0.0570	0.1103	0.0566	0.1246
14.67	0.10	0.0650	0.1619	0.0644	0.1761
15.90	0.10	0.0733	0.3083	0.0727	0.3385
16.50	0.10	0.0775	0.9155	0.0768	1.3122
16.74	0.10	0.0792	unstable	0.0784	unstable

Next, two separate sets of non-linear simulations were conducted; at $\bar{m}\delta_0 = 1$ ($\delta_0 = 0.01$) for stable limit cycle (Figure 7.9(a)) and at $\bar{m}\delta_0 = 50$ ($\delta_0 = 0.10$)

for unstable limit cycle (Figure 7.9(b)). In each set, both non-linear and linear RMS amplitudes were computed and compared to the analytical expressions for linear combined excitation (equation (7.9)) and non-linear fluidelastic excitation only (limit cycle, equations (7.10) and (7.11)). Therefore, a 3-rd order non-linear simulation was run to allow direct comparison with limit cycle predictions.

As seen in Figure 7.9, the overall effect of non-linearity on the simulated response curves was very weak in both cases since the limit cycle oscillations were nearly vertical at the practical response range ($A_{RMS} = 0 - 20\ \%\ d$). Nevertheless, the non-linear simulated response curves show qualitatively correct behaviour. For stable bifurcations, the combined response tends asymptotically to the analytically predicted limit cycle and remains stable for flow velocities greater than critical. For unstable bifurcations, the non-linear response curve shows a lowering of the stability boundary (as predicted by the analytical solution) although this reduction was quite small. Note that these numerical results confirmed a direct analogy, suggested in Section 3.2.2, between a dynamic system under combined excitation and an equivalent static system by considering turbulence as an imperfection parameter.

To exactly examine the effect of turbulence on unstable bifurcation, a separate series of third order simulations was conducted (higher order terms were almost negligeable in the immediate vicinity of the stability threshold). For a direct comparison with the analytical results presented in Table 7.4 (equation (7.12)), the running time, after reaching steady state response level, was set $T(Y) = 10\ min.$ Table 7.6 gives a summary of this computations for a parallel triangular and a square array. The numerically observed reduction in critical flow velocity was ~ 60 % of that predicted from equation (7.12) by ignoring coupling. This suggests that, perhaps, for a randomly oscillating system more than one consecutive excursions, exceeding the unstable limit cycle, are required to trigger instability. Note, that in both cases the reduction was approximately proportional to turbulence strength.

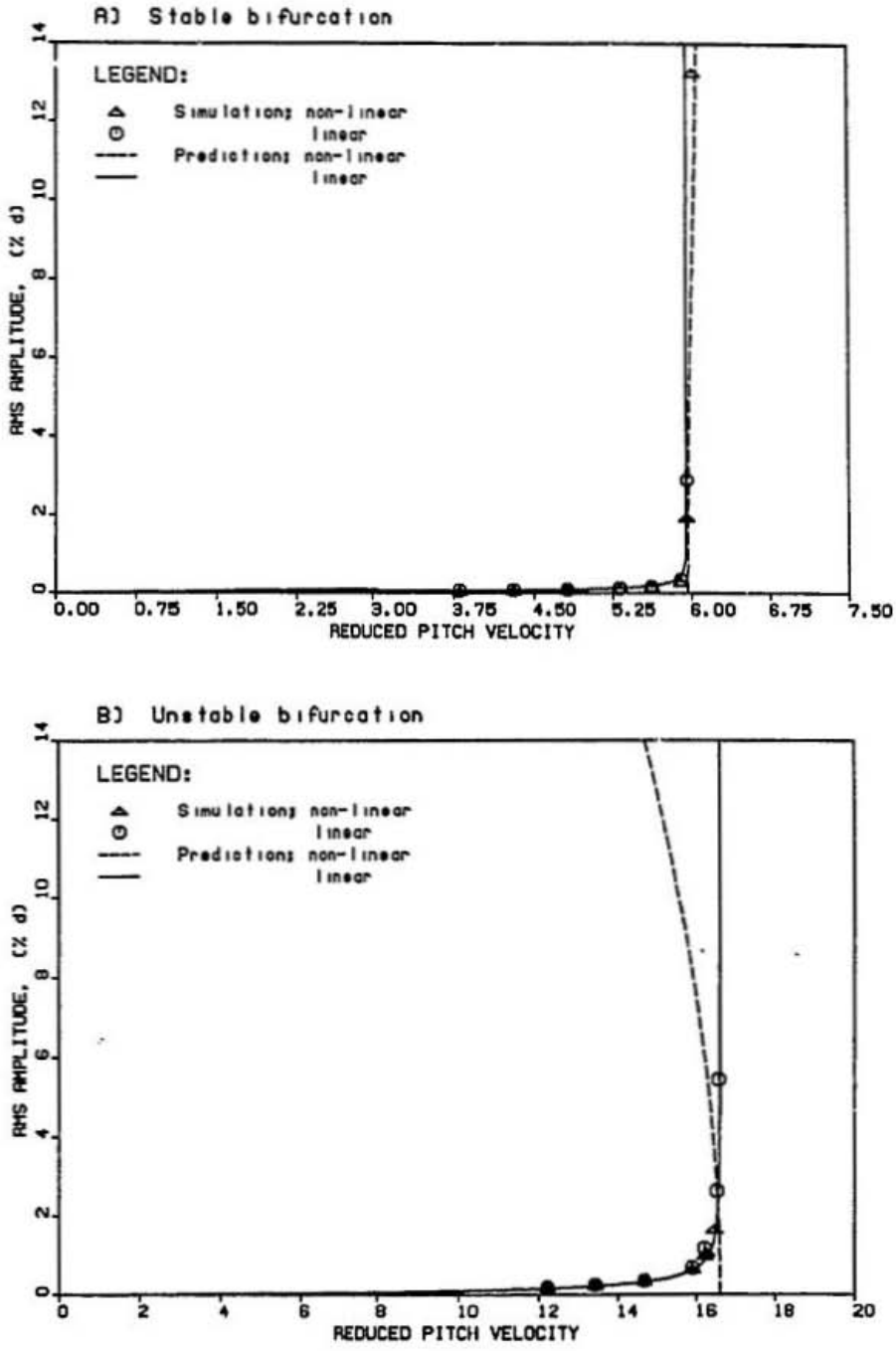

Figure 7.9: Comparison between analytical predictions and numerical simulations to combined excitation for a parallel triangular array ($\bar{m}\delta_0 = 1$ - stable bifurcation and $\bar{m}\delta_0 = 50$ - unstable bifurcation).

Table 7.6: Turbulence sensitivity of the unstable bifurcation ($\bar{m}\delta_0 = 50$, $\delta_0 = 0.10$).

Array geometry	C_r'	$(U_{Pr})_{cr}$		Reduction (%)	
		Numerical	Eq. (7.12)	Numerical	Eq. (7.12)
Parallel triangular	0.000	16.565	16.585	0.00	0.00
	0.065	16.500	16.475	0.39	0.66
	0.130	16.440	16.368	0.76	1.31
Square	0.000	19.938	19.988	0.00	0.00
	0.200	19.725	19.626	1.07	1.81
	0.400	19.530	19.297	2.05	3.46

7.4 Conclusions

The theoretical model has been applied to perform the stability analysis of a single flexible cylinder, in an array of rigid cylinders, subjected to the fluidelastic and turbulence excitation.

The model proved successful in its prediction of linear stability boundaries and linear response curves. Interestingly, it reflects all essential features of the experimentally observed behaviour of a fully flexible array: (i) the presence of dynamic and static stability boundaries, (ii) the separation in the two dimensionless parameters, δ_0 and $\bar{m}$, at the dynamic stability boundary and (iii) the transition from fluid-damping controlled instability, which manifests itself by multiple stability boundaries in a low mass-damping parameter range, to fluid-stiffness controlled instability which dominates in a high mass-damping parameter range. Note that these features are not critically dependent on model parameters.

The non-linear analysis gives only limited agreement with the observed post-stable behaviour due to its lack of non-linear hardening in the high mass-damping parameter range. Nevertheless, it predicts stable and unstable points of bifurcation, as experimentally observed. Through theoretical considerations, based on superposition of the linear combined response with the fluidelastic limit cycle, and a series

of numerical simulations, a direct correspondence with equivalent static systems is shown by considering turbulence response as an imperfection parameter. This allows us to draw some general conclusions regarding the effect of turbulence on the fluidelastic stability boundary.

- For stable bifurcations linear theory yields the lowest stability threshold; the fluidelastic boundary cannot be reduced by interaction with turbulence. However, the response to turbulence below the threshold can lead to apparent reductions in the practical stability boundary assigned on the basis of standard definitions.

- For unstable bifurcations a non-linear theory is required for stability analysis; interaction with turbulence lowers the fluidelastic stability threshold. The rate of reduction, which was found to be directly proportional to the amplitude of the turbulence buffeting and inversely proportional to the amplitude of the unstable limit cycle, can be approximated based on the superposition principle. The numerical simulation, however, suggests that more than one consecutive excursions due to turbulence, exceeding the unstable limit cycle, may be required to trigger instability.

Chapter 8

Proposed modification of theoretical model

The present theoretical model predicts reasonably well linear stability boundaries and combined turbulence and fluidelastic response curves. However, it gives only limited agreement with the observed post-stable behaviour of cylinder arrays due to, particularly, its lack of non-linear hardenig. This raises a fundamental question; does the underlying "cylinder-in-channel" theory warrant non-linear analysis? The detailed experimental investigation, conducted here, demonstrates that a single degree-of-freedom cylinder displays similar non-linear behaviour as a fully flexible array. It also showed that non-linear hardening results from fluidelastic and not structural cylinder characteristics. These observations suggest that the model shortcomings result from failure of the one-dimensional fluid mechanics used here. Indeed, at large amplitude unstable oscillations, main streamlines may pass from one flow channel to the next. Thus, the assumption that the flow field area changes with cylinder motion, due to the presence of solid boundaries, may not be valid in the post-stable region. In this case, variations in magnitude and direction in the flow field have to be addressed by defining its non-uniform distribution based on two-dimensional fluid mechanics.

The modification of underlying fluid mechanics requires formulation of an essentially new theory. Thus, rather than consider the increasingly complex flow field, this

chapter looks into the possible improvement of the assumed one-dimensional flow redistribution mechanism which accounts for most of the observed characteristics of the fluidelastic instability.

8.1 Flow redistribution as amplitude-dependent mechanism

The postulated flow redistribution mechanism, formulated from an analogous transient problem (see Reference [46]), appears well founded for a small cylinder motion. In this case, fluid inertia predominates viscous effects in a near wake region whose size is strongly limited by the constrained streamlines, passing along both sides of the flexible cylinder. Thus, the phase lag is a function of flow velocity only. However, for increasing amplitude of unstable oscillations, perhaps allowance should be made for an unsteady wake effect resulting in shifting of flow separation points. The net force exerted on the cylinder becomes a combination of the perturbation in the free-stream flow, due to the cylinder motion, and the perturbation in the near wake. Without taking into consideration the magnitude of the near wake oscillations, it is reasonable to assume that this force affects the flow/cylinder feedback mechanism. For large amplitude cylinder oscillations, this mechanism may be self-limiting due to the presence of the large-magnitude unsteady wake (a "peacemaker" for the underlying instability).

Indeed, Hara, [92], suggests that the movement of flow separation points governs the phase relation between flow adjustment and the large amplitude cylinder motion. In an interesting experimental study on a cylinder row, Hara found that the phase between the fluidelastic force and cylinder motion is strongly displacement dependent in the post-stable region. Initially, it increases with the amplitude of oscillations and generates negative net damping. Then, approaching the limit cycle, it decreases sharply and generates, in turn, positive net damping leading to

non-linear hardening. In this experiment, however, the adjacent cylinders were free to move, affecting the measurement through fluid coupling effects. Nevertheless, the results may be qualitatively correct also for a single flexible cylinder array. Note that Hara's observed damping variations clearly suggest hysteresis behaviour, as in the single flexible cylinder case.

To simulate a possible amplitude dependent phase lag between the fluidelastic force and cylinder motion, it was decided that the relevant fluid inertia length decreases linearly with the amplitude ratio, $(\frac{a}{d})$, from its initial value at the stable equilibrium state, l, to $l' = [1 - \beta(\frac{a}{d})]$, at a given amplitude ($\beta$ is a proportionality constant). Thus, the streamtube area perturbation, as expressed in equation (6.4), follows the post-stable cylinder motion with a time lag, τ, which at the unit cell inlet is formulated as:

$$\tau_0 = \frac{l}{U_0}[1 - \beta(\frac{a}{d})]. \tag{8.1}$$

At present, there is little justification for this expression, except that it has a proper physical meaning, limiting the underlying fluidelastic feedback mechanism.

8.2 Modified limit cycle oscillations

Figure 8.1 shows the amplitude of the limit cycle oscillations obtained from equations (7.10) and (7.11) after substitution of equation (8.1) for the relevant fluid inertia length (note that the linear stability boundaries are not affected). Typical sets of results are given for $\beta = 1$ ($\tau_0 = 0$ at $(\frac{a}{d}) = 100\ \%\ d$) and $\beta = 2$ ($\tau_0 = 0$ at $(\frac{a}{d}) = 50\ \%\ d$). To allow for direct comparison with Figure 7.6 ($\beta = 0$), the amplitude is computed for the same values of mass-damping parameter; $\bar{m}\delta_0 =$ 1, 10, 20, 30, 50, 100 ($\delta_0 = 0.01$). It can be seen that the assumed reduction of the time delay results in a dramatic change and a significant improvement in the predicted post-stable behaviour. It causes an increasing non-linear hardening with increase in amplitude and mass-damping parameter. Particularly interesting is the

transition from unstable to stable limit cycle for $\bar{m}\delta_0 \approx 30 - 50$. This reflects the experimentally observed hysteresis behaviour which, for both arrays, disappears at $\bar{m}\delta_0 \approx 30$. For high values of mass-damping parameter, only stable limit cycles are predicted. As with the experiment, the rate of increase of post-stable amplitude becomes lower with increasing $\bar{m}\delta_0$.

Note that the variations of β allow accurate adjustment of the predicted limit cycle amplitude (for a square array, the value of β must be slightly higher), leading to remarkable agreement with the observed stability behaviour of cylinder arrays. At the present time, however, expression (8.1) is just a hypothesis. Nevertheless, it suggests that the flow-adjustment phase lag may be both flow velocity and cylinder amplitude dependent.

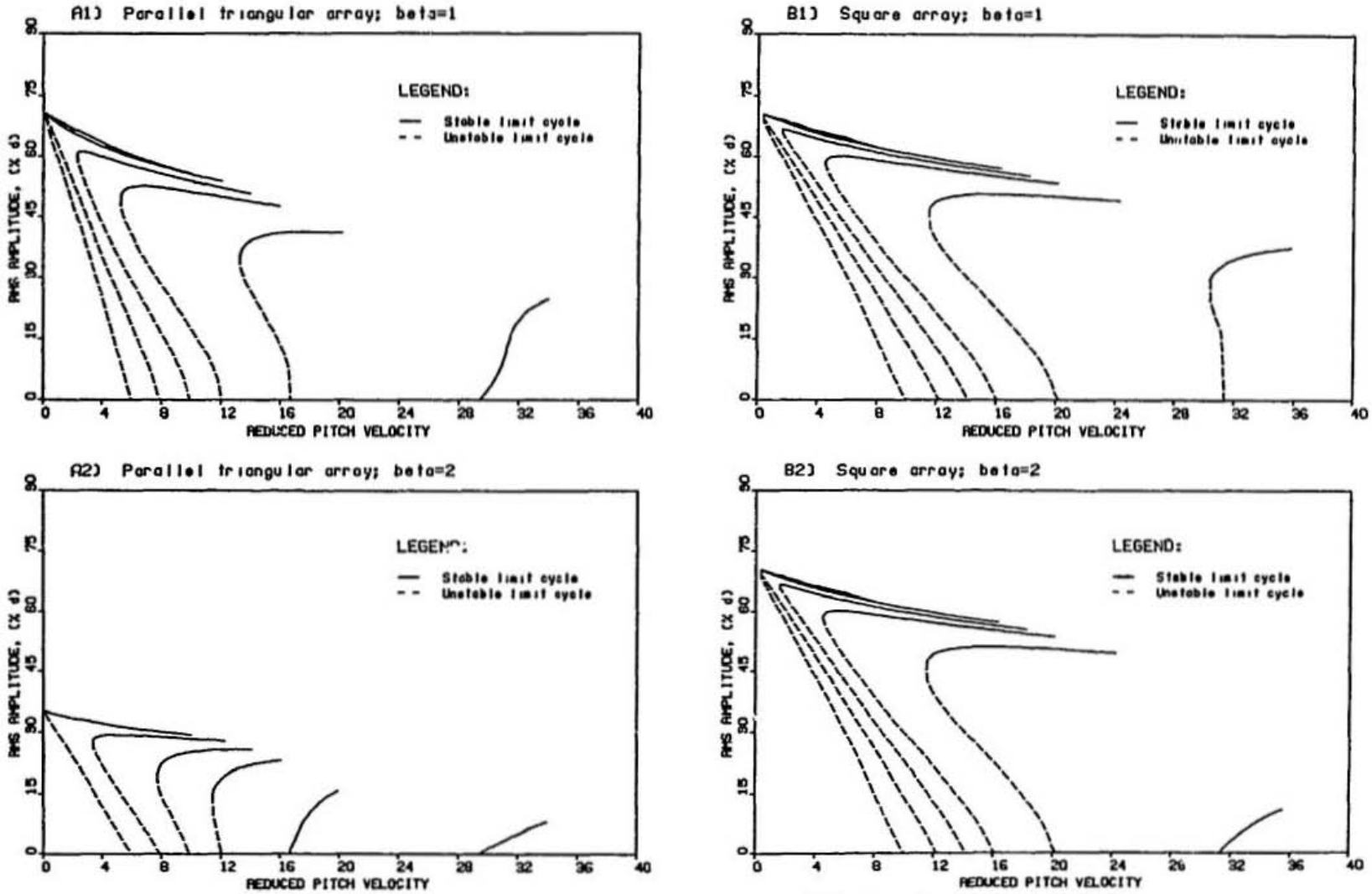

Figure 8.1: Modified theoretical limit cycle oscillations for a parallel triangular array and a square array; $\bar{m}\delta_0 = 1, 10, 20, 30, 50, 100$ - from left to right.

Chapter 9

Summary and conclusions

The main objective of this work was to develop foundations for the design of multi-tube marine risers against current-induced vibration through establishing characteristics of the underlying fluidelastic excitation mechanism. Despite research efforts, undertaken in recent years, and the substantial progress made in understanding fluidelastic instability in cylinder arrays, the basic practical question still remains unanswered. Namely, what is the critical flow velocity from an operational point of view? The experimental study, undertaken as a part of this research program, suggests that prediction based on linear fluidelastic models may be unconservative, particularly, in a low mass-damping parameter range, typical for marine risers, where strongly non-linear hysteresis phenomena can dominate. Since stability of cylinder arrays cannot be guaranteed within the hysteresis region (unstable oscillations may be excited by a sufficiently large disturbance caused, for example, by turbulence), reliability considerations dictate that its lower bound defines the critical flow velocity. This finding clearly emphasies the necessity for experimental investigations into the post-stable behaviour of cylinder arrays subjected to fluid-cross flow or, alternatively, for development of accurate non-linear models for fluidelastic instability, as initiated in this work.

9.1 Summary

An experimental program was conducted with the objective to investigate the post-stable fluidelastic behaviour of cylinder arrays subjected to fluid cross-flow (the arrays were modelled as infinite in transverse-to-flow direction). A wind tunnel was used to allow a clear separation between Strouhal periodicity and fluidelastic instability. This study was performed at the mass-damping parameter range, $\bar{m}\delta_0 \approx 1.9 - 23.5$, where hysteresis-type behaviour has been observed. The sequence of tests was designed to gradually isolate the degrees-of-freedom needed to capture the physical essence of an array vibrational behaviour in the simplest way possible. It was found that instability and post-stable behaviour of a fully flexible array are governed by a dominant cylinder and may be well represented by a one degree-of-freedom system constrained to move in the transverse-to-flow direction only (non-linear hardening resulted from fluidelastic and not from structural cylinder characteristics). Thus, coupled motion between flexible cylinders is not required for hysteresis effects. Although the response curves were recorded for increasing and decreasing steady flow velocity under ideal conditions possible, the effects of system imperfections (e.g. transient turbulence excitations, array misalignments) were also considered. It was shown that the exact details of the stability behaviour (e.g. critical flow velcity, hysteresis effects, limit cycle amplitudes) depend strongly on these imperfections. To ensure that the trends observed are not distinct phenomena associated with an array geometry, two different configuration were tested; parallel triangular and square.

Based on this detailed experimental study, the non-linear theoretical model for fluidelastic instability in cylinder arrays was formulated. The present model is a modified time-domain version of an earlier steady-state "cylinder-in-channel" formulation (the experiments provide physical justification for the modelling of a single flexible cylinder, constrained to move in the transverse-to-flow direction only). The

underlying theory employs one-dimensional fluid dynamics and a phase lag between cylinder motion and flow adjustment. It accounts for both fluid-damping and fluid-stiffness forces acting on the flexible cylinder. Here, an area perturbation decay function was included which expresses the amplitude reduction of perturbations in the free-stream flow away from the cylinder. The equation of motion was then developed with the non-linearity associated with the fluid forces only. This equation was solved analytically to third order using the first approximation method of Kryloff and Bogoliboff.

The third-order non-linear solution gives only limited agreement with the observed post-stable behaviour of cylinder arrays due to, in particular, its lack of non-linear hardening. Nevertheless, it predicts stable and unstable points of bifurcation, allowing us qualitative assessment of the effect of turbulence on the fluidelastic stability boundary. An approximate method was formulated using superposition of both excitation mechanisms (a flat power spectrum was used to represent the random field of turbulence within a cylinder array). This heuristic representation suggests that turbulence affects the unstable point of bifurcation and lowers the actual stability threshold. The rate of reduction was found to be proportional to the amplitude of turbulence buffeting and to the amplitude of the unstable limit cylce.

Physical arguments suggest that stronger non-linear hardening, leading to stable limit cycles at large amplitudes, should be predicted by the single flexible cylinder model used here. To check this, the fully non-linear solution was found using a direct numerical integration of the equation of motion. Unfortunately, the analytical and higher order numerical results were found to be qualitatively identical, pointing to a weakness in the fluidelastic model formulated here (worth noting is the excellent agreement between the closed form solution and the third order numerical simulation). Nevertheless, the developed numerical scheme was applied to simulate array behaviour under combined fluidelastic and turbulence excitation based on the

true non-linear interaction mechanism. Again, the attention was restricted to stable and unstable bifurcations, because both types of stability behaviour were observed experimentally. Particularly important was the influence of turbulence on unstable bifurcations since it was shown, based on superposition, that the interaction mechanism may lower the fluidelastic stability boundary. The numerical simulation confirmed this hypothesis. However, it was found that more than one consecutive excursions may be required to trigger instability. Little overall effect was noticed due to the extreme steepness of the predicted unstable limit cycles near the stability threshold. A direct comparison with equivalent static systems was made in which turbulence response was considered as an imperfection parameter.

The theoretical model can be significantly improved with the assumption that the flow-adjustment phase lag is dependent on cylinder motion and decreases with increasing oscillatory amplitude. This causes an increasing non-linear hardening with increase in amplitude and the mass-damping parameter. Particularly interesting is the transition from unstable to stable limit cycles for $\bar{m}\delta_0 \approx 30 - 50$. This reflects the experimentally observed hysteresis behaviour which, for both arrays, disappears for $\bar{m}\delta_0 \approx 30$. For high values of the mass-damping parameter, only stable limit cycle are predicted. As with the experiment, the rate of increase of the post-stable amplitude becomes lower with increasing $\bar{m}\delta_0$. These resuts suggest that the flow-adjustment phase lag may be both flow velocity and cylinder amplitude dependent.

9.2 Conclusions

Several concluding remarks, regarding the details of experimental and theoretical investigations, have been noted separately at the end of Chapter 5 and Chapter 7. Here, the major conclusions, regarding the fluidelastic instability in cylinder arrays subjected to fluid cross-flow, are restated based on the presented work as a whole.

- The non-linear effects, in the mass damping parameter range governed by the hysteresis behaviour, are as important for the onset of instability as array pitch and pattern. In the absence of a reliable coupled turbulence and fluidelastic model, the lower limit of the hysteresis region must be considered as a practical threshold for fluidelastic instability.

- The fluidelastic instability mechanism of a single flexible cylinder is a row-dependent phenomenon. The least stable (dominant) row reflects all essential features of the stability behaviour of a fully flexible array including hysteresis effects. Within the mass-damping parameter range studied, the motion of neighbouring cylinders is not fundamental to the fluidelastic instability. Instead, fluid coupling tends to cascade instability through the array.

- The non-linear stability characteristics of an array (including hysteresis effects) may be qualitatively represented by a single flexible cylinder constrained to move in the transverse-to-flow direction only. That is, the underlying fluidelastic mechanism requires only one degree-of-freedom to operate.

- For unstable bifurcations, characterized by hysteresis behaviour, interaction with turbulence reduces the fluidelastic stability threshold. The rate of reduction was found to be directly proportional to the amplitude of the turbulence buffeting and inversely proportional to the amplitude of the unstable limit cycle. For stable bifurcations, turbulence does not affect the fluidelastic stability boundary, but its apparent value reduces with increasing turbulence.

- The "cylinder-in-channel" model lacks the non-linear hardening needed to yield good prediction of cylinder behaviour. It appears that the phase lag, between cylinder motion and flow adjustment, must be smaller at the final limit cycle than that at the stable equilibrium state.

- The numerical procedure appears to be a promising starting point for the modelling of fluidelastic oscillations in cylinder arrays, particularly the post-stable behaviour. However, improvements to the underlying fluidelastic model are needed.

9.3 Further development

This work, both experimentally and analytically, contributes to better understanding of the fluidelastic instability in cylinder arrays. The attention was focused on the simplest physical system, retaining the behaviour of full arrays. Many of the assumptions, made in the formulation of the theoretical model, require further experimental justification. Consequently, considerable scope for subsequent research exists.

- The postulated flow redistribution mechanism, which accounts for most of the observed characteristics of the fluidelastic instability, requires experimental validation. Particularly important is the experimental determination of the velocity and amplitude dependence of the assumed phase lag. Unfortunately, these experiments are rather difficult to perform due to the high turbulence levels generated by cylinder arrays.

- The utilized one-dimensional fluid mechanics and the presence of "solid boundaries", limiting the fluid field, must be verified experimentally for large amplitude oscillations of the flexible cylinder. If required, work can then be directed towards the application of two-dimensional flow. In view of the presented level of effort, this is believed to be very challenging.

- Experimental studies on cylinder arrays in water flows indicate that Strouhal periodicity and fluidelastic instability nearly coincide and, as shown by Price *et al.*, [11], cannot be separated in some cases. It follows that Strouhal pe-

riodicity may excite fluidelastic instability, leading to significantly stronger reduction in the critical flow velocity than that predicted here for turbulence buffeting. Thus, the interaction effect between Strouhal periodicity and fluidelastic instability should recive further research attention.

- The arrays, considered for application in production marine risers, have a limited number of flowlines. Thus, the internal flow field may differ from that in an infinite array. However, as suggested by Blevins, [7], the change in the flow field is very small for arrays consisting of more than four cylinders. Nevertheless, further experimental work, on a finite array in water flow, is recommended to determine the applicability of theories based on infinite arrays.

References

[1] Lock G. A.: *Technological factors in offshore hydrocarbon production*, presented in; *The future of offshore petroleum*, McGraw-Hill Publishing, New York, 1981

[2] Griffin O.M. and Ramberg S.E.: *Some recent studies of vortex shedding with application to marine tubulars and risers*, ASME, J. of Energy Resources Technology, Vol. 104(3), 1982

[3] Sarpkaya T.: *Vortex-induced oscillations, a selective review*, J. of Applied Mechanics, Vol. 46(6), 1979

[4] Wooton L.R. *et al.*: *Oscillations of piles in marine structures*, CIRIA, Report 40, 1970, England

[5] Wiegel R.L. *et al.*. *Ocean waves forces on cylindrical piles*, ASCE, J. of Hydr. Div., Vol. 83, HY2, 1957, pp. 1-34

[6] Sarpkaya T. and Isaacson M.: *Mechanics of wave forces on offshore structures*, Van Nostrand Reinhold, New York, 1981

[7] Blevins R.D.: *Flow-induced vibration*, Van Nostrand Reinhold, New York, 1977

[8] Bokain A. and Geola F.: *Hydrodynamic forces on a pair of cylinders*, OTC 5007, Houston, 1985

[9] Jendrzejczyk J.A., Chen S.S. and Wambsganass M.W.: *Dynamic response of a pair of circular tubes subjected to liquid cross flow*, J. of Sound and Vibration, Vol. 67, 1979, pp. 263-273

[10] Zdravkovich M.M.: *The effects of interference between circular cylinders in cross flow*, J. of Fluids and Structures, Vol. 1, pp. 239-261

[11] Price S.J., Paidoussis M.P., Mark B. and Mureithi W.N.: *Current-induced oscillations and instabilities of a multi-tube flexible riser: water tunnel experiments*, OMAE, 1989, pp. 447-454

[12] Demirbilek Z. and Halvorson T.: *Hydrodynamic forces on multitube production riser exposed to current and waves*, OMAE, Dallas, 1985

[13] Pettigrew M.J.: *Flow-induced vibration phenomena in nuclear power station components*, Power Industry Research, Vol. 1, 1981, pp. 97-133

[14] Paidoussis M.P.: *A review of flow-induced vibrations in reactors and reactor components*, Nuclear Engineering and Design, Vol. 74(1), 1983, pp. 31-60

[15] Chen S.S.: *Guidelines for the instability flow velocity of tube arrays in crossflow*, J. of Sound and Vibration, Vol. 93(3), 1984, pp. 439-455

[16] Weaver D.S. and Fitzpatrick J.A.: *A review of flow-induced vibrations in heat exchangers*, Int. Conf. on Flow Induced Vibrations, BHRA, Bowness-on-Windermere, England, 1987, Paper A1, pp. 1-17

[17] Singh K.P. and Soler A.J.: *Mechanical design of heat exchangers and pressure vessel components*, Arcturus Publishers Inc., New Jersey, U.S.A., 1984

[18] Weaver D.S. and Yeung H.C.: *The effect of tube mass on the flow induced response of various tube arrays in water*, J. of Sound and Vibration, Vol. 93(3), 1984, pp. 409-425

[19] Weaver D.S. and Abd-Rabbo A.: *A flow visualization study of a square array of tubes in water crossflow*, J. of Fluids Engineering, Vol. 107, 1985, pp. 354-363

[20] Abd-Rabbo A. and Weaver D.S.: *A flow visualization study of flow development in a staggered tube array*, J. of Sound and Vibration, Vol. 106(2), 1986, pp. 241-256

[21] Hara F.: *Vibration of a single row of circular cylinders subjected to two-phase bubble cross-flow*, BHRA, Int. Conf. on Flow Induced Vibrations, Bowness-on-Windermere, England, 1987, Paper E1, pp. 203-210

[22] Chen S.S. and Jendrzejczyk J.A.: *Characteristics of fluidelastic instability of tube rows in crossflow*, BHRA, Int. Conf. on Flow Induced Vibrations, Bowness-on-Windermere, England, 1987, Paper B3, pp. 77-84

[23] Halle H., Chenoweth J.H. and Wamaganass M.W.: *Flow-induced tube vibration thresholds in heat exchangers from shellside water tests*, ASME, Symp. on Flow Induced Vibration, Vol. 3, 1984, pp. 17-32

[24] Chen Y.N.: *Flow-induced vibration and noise in tube bank heat exchangers due to von Karman streets*, ASME, J. of Engineering for Industry, Vol. 90, 1968, pp. 134-146

[25] Putnam A.A.: *Flow induced noise and vibration in heat exchangers* , ASME, Paper 64-WA/HT-21, 1964

[26] Owen P.R.: *Buffeting excitation of boiler tube vibration*, J. of Mechanical Engineering Science, Vol. 7, 1965, pp. 431-439

[27] Roberts B.W.: *Low frequency, aeroelastic vibrations in a cascade of circular cylinders*, Mechanical Engineering Science, Monograph No.4, London: I. Mech. E., 1966

[28] Connors H.J.Jr.: *Fluidelastic vibration of tube arrays excited by cross flow*, ASME, Flow-Induced Vibrations in Heat Exchangers, New York, 1970, pp. 42-56

[29] Blevins R.D.: *Fluid elastic whirling of the tube row*, ASME, J. of Pressure Vessel Technology, Vol. 96, 1974, pp. 263-267

[30] Blevins R.D.: *Fluid elastic whirling of tube rows and tube arrays*, ASME, J. of Fluids Engineering, Vol. 99, 1977, pp. 457-461

[31] Weaver D.S. and El-Kashlan M.: *The effect of damping and mass ratio on the stability of the tube bank*, J. of Sound and Vibration, Vol. 76(2), 1981, pp. 283-294

[32] Paidoussis M.P.: *Fluidelastic vibration of cylinder arrays in axial and cross flow: state of the art*, J. of Sound and Vibration, Vol. 76, 1981, pp. 329-361

[33] Chen S.S.: *A mathematical model for cross-flow induced vibration of tube rows*, 3rd Int. Conf. Pressure vessel Technology, Part 1, 1977, pp. 415-426

[34] Chen S.S.: *Cross flow induced vibrations of heat exchanger tube banks*, Nuclear Engineering and Design, Vol. 47, 1978, pp. 67-86

[35] Tanaka H. and Takahara S.: *Unsteady fluid dynamic force on tube bundle and its dynamic effect of vibration*, ASME, Flow-Induced Vibration of Power Plant Components, New York, 1980, pp. 77-92

[36] Price S.J., Paidoussis M.P.: *Fluidelastic instability of a double row of circular cylinders subject to cross flow*, J. of Vibration, Acoustics, Stress, Reliability in Design, Vol. 105, 1983, pp. 59-66

[37] Price S.J. and Paidoussis M.P.: *An improved mathematical model for the stability of cylinder rows subject to cross-flow*, J. of Fluid Mechanics, Vol. 146, 1984, pp. 615-640

[38] Price S.J. and Paidoussis M.P.: *A theoretical investigation of the fluidelastic instability of a single flexible cylinder surrounded by rigid cylinders*, ASME, Symp. on Flow-Induced Vibration, New Orleans, 1984, pp. 117-133

[39] Price S.J. and Paidoussis M.P.: *A constrained-mode analysis of the fluidelastic instability of a double row of flexible circular cylinders subject to cross-flow: a theoretical investigation of system parameters*, J. of Sound and Vibration, Vol. 105(1), 1986, pp. 121-142

[40] Price S.J. and Valerio N.R.: *A non-linear investigation of single-degree-of-freedom instability in cylinder arrays subject to cross-flow*, ASME, Symp. on Flow-Induced Vibrations, Honolulu, 1989, pp. 1-10

[41] Chen S.S.: *Instability mechanism and stability criteria of a group of circular cylinders subjected to cross-flow. Part I: theory*, J. of Vibration, Acoustics, Stress and Reliability in Design, Vol. 105, 1983, pp. 51-58

[42] Chen S.S.: *Instability mechanism and stability cryteria of a group of circular cylinders subjected to cross-flow. Part II: numerical results and discussions*, J. of Vibration, Acoustics, Stress and Reliability in Design, Vol. 105, 1983, pp. 253-260

[43] Gasteiger G.: *Ein Beitrag zur ermittlung fluidelastischer Koppelschwingungen in Rohrbundelwarmetauschern (A contribution towards solving coupled fluidelastic vibrations in tube bundle heat exchangers)*, VDI-Verlag, Reihe 6, Nr. 24, Dusseldorf, W. Germany, 1983, (in German)

[44] Andjelic M., Bardowicks H. and Popp K.: *Non-linearities in fluidelastic vibrations in tube bundels*, Inter. Conf. on Flow Induced Vibrations, Bowness-on-Windermere, England, Paper K5, 1987, pp. 477-485

[45] Ducci A.: *Identifikation eines stromungsselbsterregten Schwingers mit Hopfverzweigung (Identification of flow-self-excited oscillators with Hopf bifurcation)*, ZAMM (J. of Applied Mathematics and Mechanics), Vol. 69, No. 5, 1989, pp. 359-361, (in German)

[46] Lever J.H. and Weaver D.S.: *A theoretical model for fluidelastic instability in heat exchangers tube bundles*, ASME, J. of Pressure Vessel Technology, Vol. 104, 1982, pp. 147-158

[47] Lever J.H. and Weaver D.S.: *On the stability of heat exchangers tube bundles, Part I: modified theoretical model*, J. of Sound and Vibration, Vol. 107(3), 1986, pp. 375-392

[48] Lever J.H. and Weaver D.S.: *On the stability of heat exchangers tube bundles, Part II: numerical results*, J. of Sound and Vibration, Vol. 107(3), 1986, pp. 393-410

[49] Yetisir M. and Weaver D.S.: *On an unsteady theory for fluidelastic instability of heat exchanger tube arrays*, ASME, Vol. 3, Chicago, 1988, pp. 181-195

[50] Lever J.H. and Rzentkowski G.: *Determination of the fluidelastic stability threshold in the presence of turbulence: a theoretical study*, ASME, Symp. on Flow Induced Vibration and Noise, Vol. 2, Chicago, 1988, pp. 131-150

[51] Paidoussis M.P., Mavriplis D. and Price S.J.: *A potential flow theory for the dynamics of cylinder arrays in cross flow*, J. of Fluid Mechanics, Vol. 146, 1984, pp. 147-158

[52] Balsa T.F.: *Potential flow interactions in an array of cylinders in cross flow*, J. of Sound and Vibration, Vol. 50, 1977, pp.285-303

[53] Lever J.H. and Rzentkowski G.: *An investigation into the post-stable behaviour of a tube array in cross-flow*, ASME, Symp. on Flow Induced Vibration and Noise, Vol. 3, Chicago, 1988, pp. 95-110

[54] Andjelic M. and Popp K.: *Stability effects in a normal triangular cylinder array*, ASME, Symp. on Flow Induced Vibrations and Noise, Vol. 3, Chicago, 1988, pp. 57-76

[55] Andjelic M.: *Stabilitatsverhalten querangestromten Rohrbundel mit versetzten Dreieckteilung (Stability behaviour of a normal triangular array in cross-flow)*, Doktor Arbeit (Ph.D Thesis), Der Fakultat fur Maschinenwesen der Universtat Hannover, W. Germany, 1988, (in German)

[56] Godon J.L.: *Flows and flow induced vibrations in large condensors*, ASME, Symp. on Flow Induced Vibration, Vol. 3, 1984, pp. 1-16

[57] Moe G. and Overvik T.: *Current induced motion of multiple riser*, The Norwegian Institute of Technology, Trondheim, 1982

[58] Panicker N.N. and Yancey J.R.: *Deepwater production riser*, OTC 4512, Houston, 1983, pp. 9-18

[59] Ottesen Hansen N.E. and Panicker N.N.: *Self-exited vibrations in linear riser arrays*, OMAE, Dallas, 1985, pp. 518-526

[60] Ishigai S.E., Nishikawa P. and Yagi E.:*Structure of gas flow in vibration in tube banks in two axes normal to flow*, ISME, Tokyo, 1973, pp. 1.5.23-1.5.33

[61] Paidoussis M.P., Price S.J. and Mark B.: *Current-induced oscillations and instability of a multi-tube flexible riser*, OMAE, Houston, 1988, pp. 383-389

[62] Ottesen Hansen N.E., Jacobsen V. and Larneas G.: *Hydro-elastic instability of pipe arrays in waves*, Int. Symp. on Hydrodynamics in Ocean Engineering, Norway, Trondheim, 1981, pp. 289-306

[63] Brzozowski V.J. and Hawks R.: *Wake induced full-span instability of bundle conductoor transmission lines*, J. of AIAA, Vol. 14(2), 1976

[64] Pettigrew M.J. and Gorman D.J.: *Vibration of heat exchanger tube bundles in liquid and two-phase cross-flow*, BNES, Int. Conf. on Vibration in Nuclear Plant, Keshwick, U.K., 1978, Paper 2.3

[65] Blevins R.D., Gibert R.J. and Villard B.: *Experiments on vibration of heat exchanger tube arrays in cross flow*, SMIRT, 6th Int. Conf. on Structural Mechanics in Reactor Technology, 1981, Paper B6/9

[66] Sandifer J.B. and Bailey R.T.: *Turbullent buffeting of tube arrays in liquid crossflow*, ASME, Symp. on Flow-Induced Vibrations, Vol. 2, New York, 1984, pp. 211-226

[67] Taylor C.E., Pettigrew M.J., Axisa F. and Villard B.: *Experimental determination of single and two-phase cross flow-induced forces on tube rows*, ASME, Symp. on Flow-Induced Vibrations, PVP-Vol. 104, Chicago, 1986, pp. 31-39

[68] Price S.J., Paidoussis M.P., McDonald R. and Mark B.: *The flow-induced response of the single flexible cylinder in an array of rigid cylinders: a comparison between air- and water-flow results*, ASME, Symp. on Flow-Induced Vibration, PVP-Vol. 104, Chicago, 1986, pp. 107-117

[69] Price S.J. and Paidoussis M.P.: *The flow induced response of a single flexible cylinder in an in-line array of rigid cylinders*, Int. Conf. on Flow Induced Vibrations, BHRA, Bowness-on-Windermare, England, 1987, Paper B1, pp. 51-62

[70] Southworth P.J. and Zdravkovich M.M.: *Effect of grid-turbulence on the fluidelastic vibrations of in-line tube banks in cross flow*, J. of Sound and Vibration, Vol. 39, 1975, pp. 461-469

[71] Franklin R.E. and Soper B.M.H.: *An investigation of fluidelastic instabilities in tube banks subjected to fluid cross-flow*, 4-th Int. Conference on Structural Mechanics in Reactor Technology, Paper F6/7, San Francisco, 1977, pp. 1-14

[72] Chen S.S. and Jendrzejczyk J.A.: *Experiments on fluidelastic instability in tube banks subjected to liquid cross flow*, J. of Sound and Vibration, Vol. 78(3), 1981, pp. 355-381

[73] Husein K.: *Vibrations and stability of multiple parameter systems*, Nordhoff International Publishing, 1978

[74] Thompson J.M.T.: *Instabilities and catastrophes in science and engineering*, John Wiley & Sohn, 1982

[75] Leipholz H.: *Stability of elastic systems*, Sijthoff & Nordhoff, 1980

[76] Andronov A.A, Vitt A.A and Khaikin S.E.: *Theory of oscillations* , Addison-Wesley Publishing Co., 1966

[77] Chen S.S.: *Some issues concerning fluidelastic instability of a group of circular cylinders in crossflow*, ASME, Symp. on Flow Induced Vibration and Noise, Vol. 1, Chicago, 1988, pp. 1-24

[78] Axisa F. *at al.*: *Vibration of tube bundles subjected to air-water and steam-water cross flow: preliminary results on fluidelastic instability*, ASME, Symp. on Flow Induced Vibration, Vol. 2, New York, 1984, pp. 269-284

[79] Paidoussis M.P.: *Flow-induced instabilities of cylindrical structures*, Applied Mechanics Reviews, Vol. 40(2), 1987, pp. 163-175

[80] Heinecke E.P.:"Fluidlastic vibrations in heat exchangers with tubes in cross-flow", BNES, Int. Conf. on Vibration in Nuclear Plant, Keswick, 1978, Paper 2.4

[81] Paidoussis M.P. and Price S.J.: *The mechanism underlaying flow-induced instabilities of cylinder arrays in crossflow*, J. of Fluid Mechanics, Vol. 187, 1988, pp.45-59

[82] Weaver D.S. and El-Kashlan M.: *On the number of tube rows required to study cross-flow induced vibrations in tube banks*, J. of Sound and Vibration, Vol.75, 1981,pp. 265-273

[83] Weaver D.S and Grover L.K.: *Cross-flow induced vibrations in a tube bank - turbulent buffeting and fluidelastic instability*, J. of Sound and Vibration, Vol. 59, 1978, pp. 277-294

[84] DISA: *Instruction and service manual for type 55D01 anemometer unit*

[85] Hornbec R.W.: *Numerical methods*, Quantum Publishing, New York, 1975

[86] James M.L., Smith G.M. and Wolford J.C.: *Applied numerical methods for digital computation with Fortran and CSMP*, Harper & Row Publishers Inc., 1977

[87] Bass D.W. and Haddara M.R.: *Nonlinear models of ship roll damping*, Int. Shipbuild. Progr., Vol. 35, No. 401, 1988, pp. 5-24

[88] Chen S.S. and Jendrzejczyk J.A.:*Fluid excitation forces acting on a square tube array*, J. Fluids Engineering, Vol. 109, 1987, pp. 415-423

[89] Kryloff N. and Bogoliuboff N.: *Introduction to non-linear mechanics*, Princetown University Press, Princetown, 1947

[90] Hornbeck R.W.: *Numerical methods*, Quantum Publishing, New York, 1975

[91] Urabe M.: *Non-linear autonomous oscillations*, Academic Press, New York, 1967, pp. 216-225

[92] Hara F.:*Unsteady fluid dynamic forces acting on a single row of cylinders vibrating in cross flow*, ASME, Symp. on Flow-Induced Vibrations, 1987

Appendix A

Response curves

This Appendix shows the post-stable response response curves, for increasing and decreasing flow velocity, obtained for $\bar{m}\delta_0 \approx 1.9 - 23.5$; Figures A1-A21 are for a parallel triangular array of pitch ratio 1.375 and Figures A22-A33 are for a square array of pitch ratio 1.433.

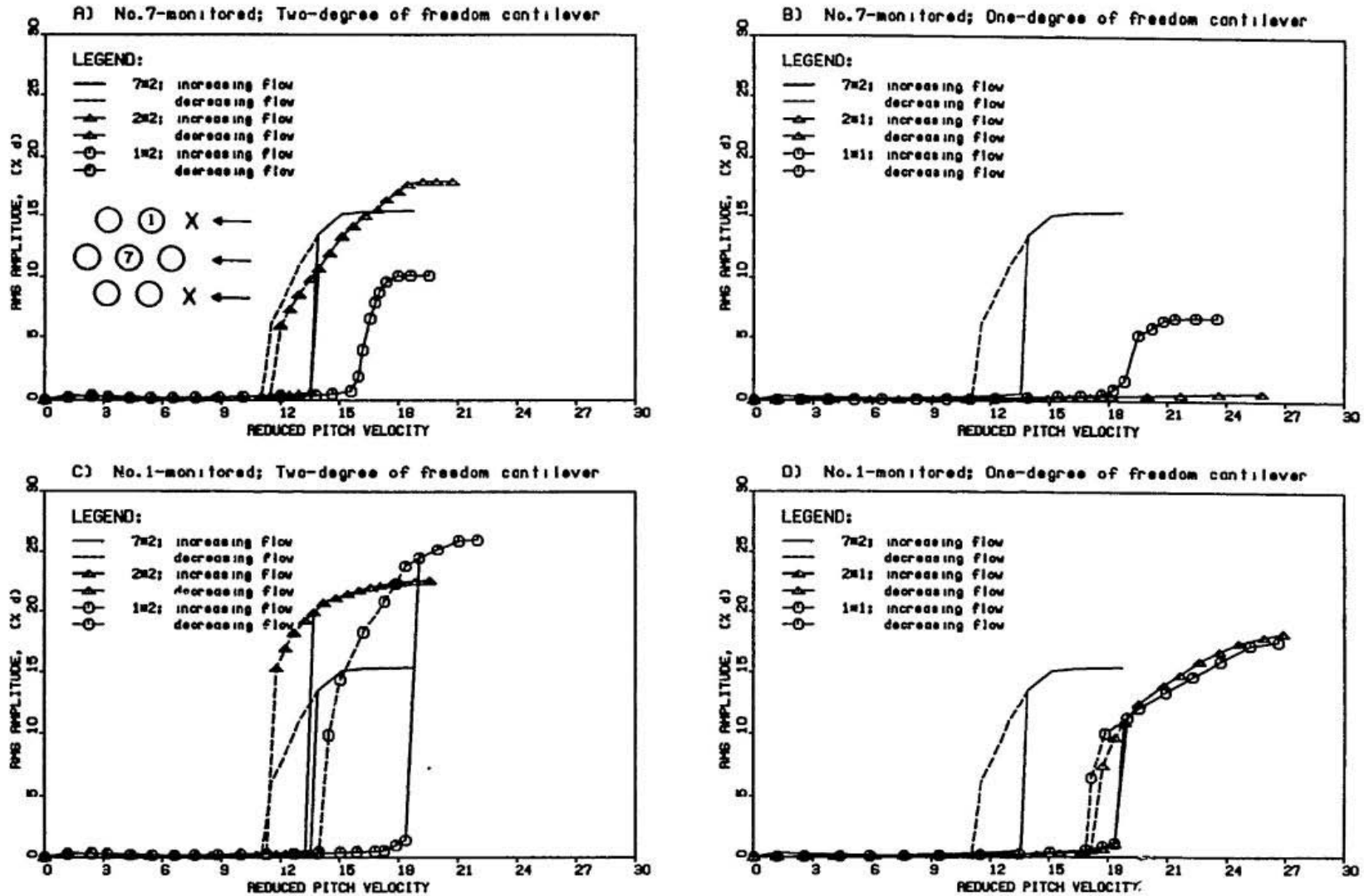

Figure A.1: RMS response curves for the cylinders No.1 and No.7 in a parallel triangular array (No.7 in 4-th row), $\bar{m}\delta_0 \approx 1.9 - 2.4$.

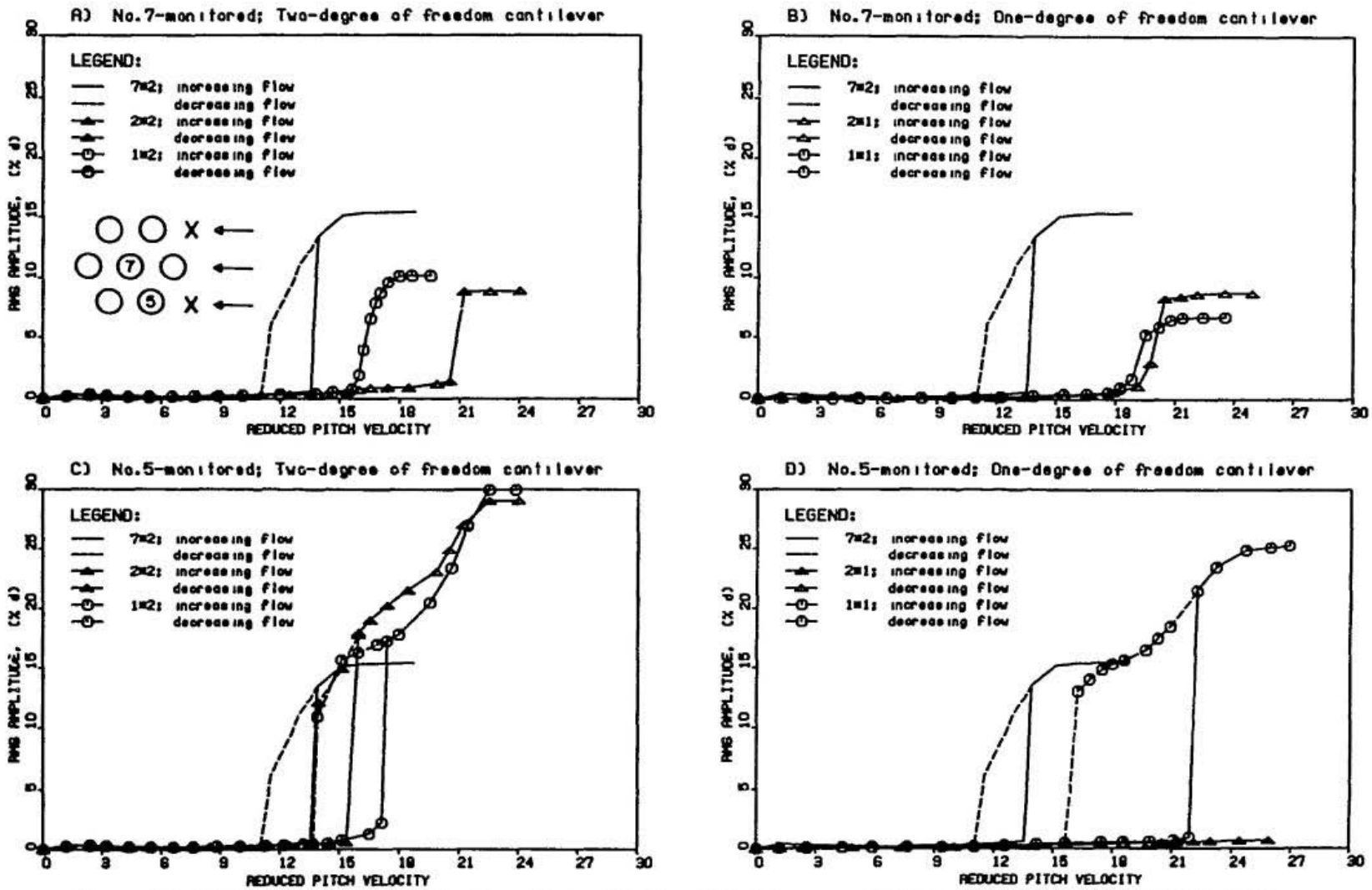

Figure A.2: RMS response curves for the cylinders No.5 and No.7 in a parallel triangular array (No.7 in 4-th row), $\bar{m}\delta_0 \approx 1.9 - 2.4$.

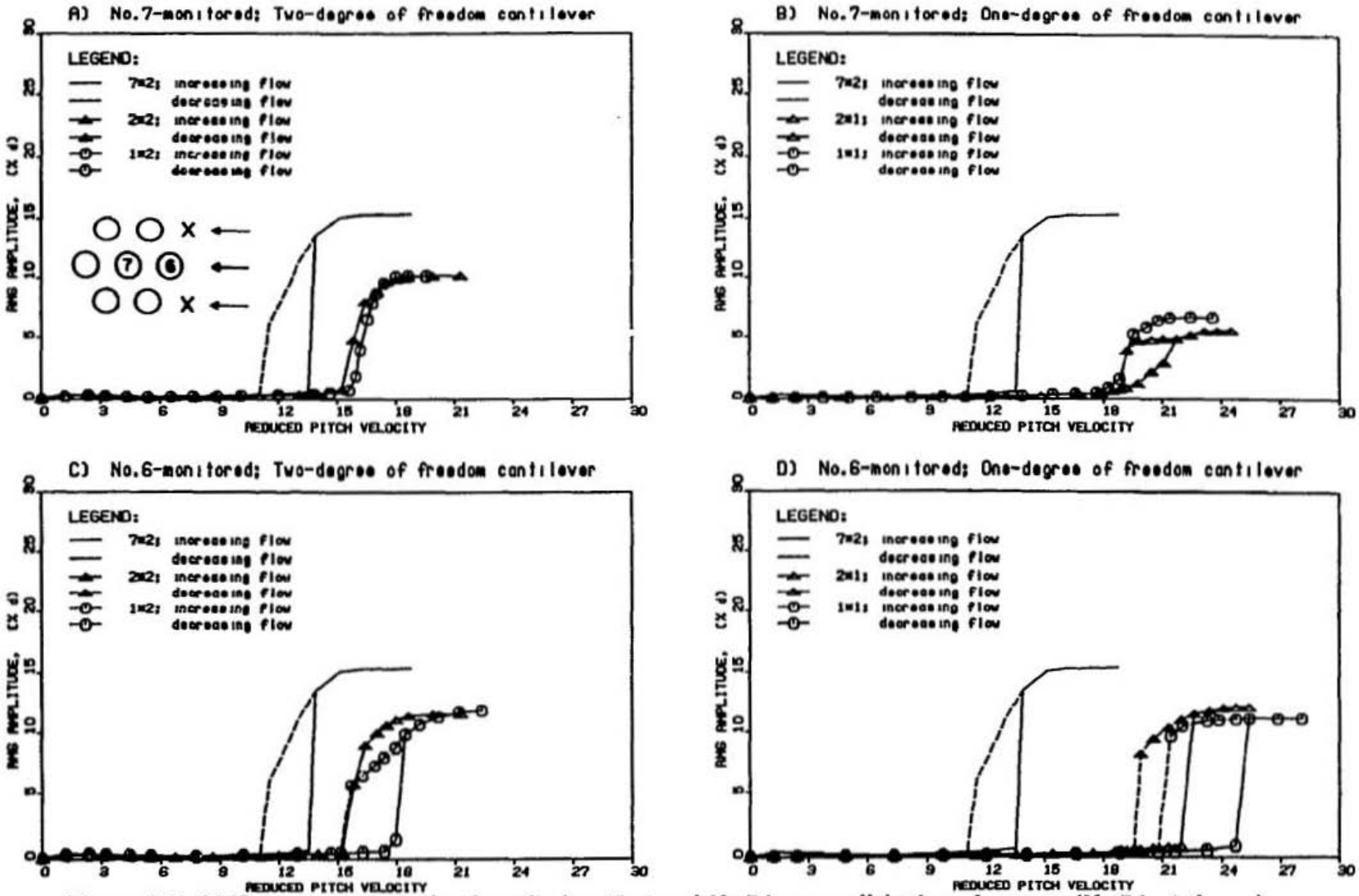

Figure A.3: RMS response curves for the cylinders No.6 and No.7 in a parallel triangular array (No.7 in 4-th row), $\bar{m}\delta_0 \approx 1.9 - 2.4$.

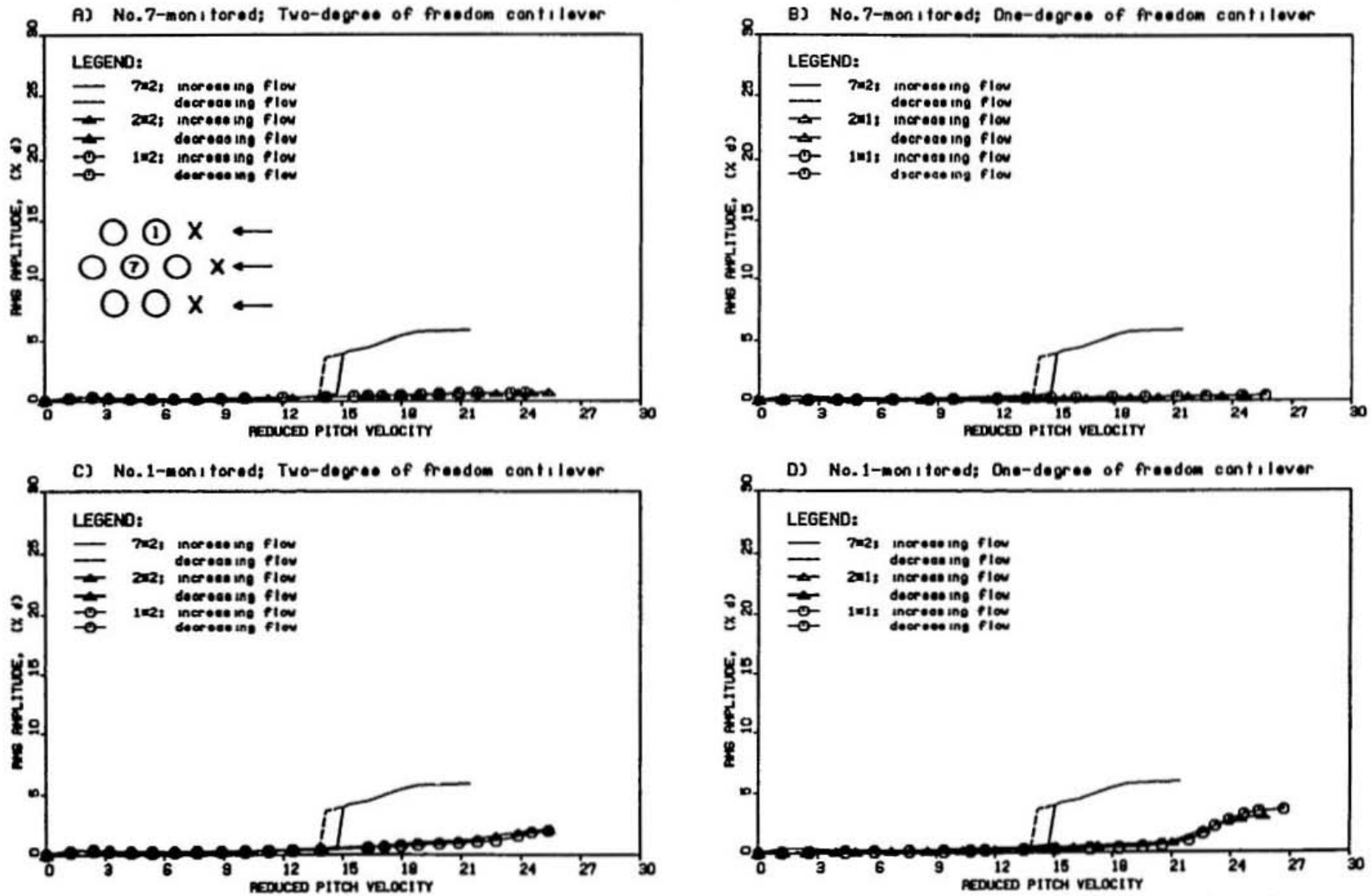

Figure A.4: RMS response curves for the cylinders No.1 and No.7 in a parallel triangular array (No.7 in 5-th row), $\bar{m}\delta_0 \approx 1.9 - 2.4$.

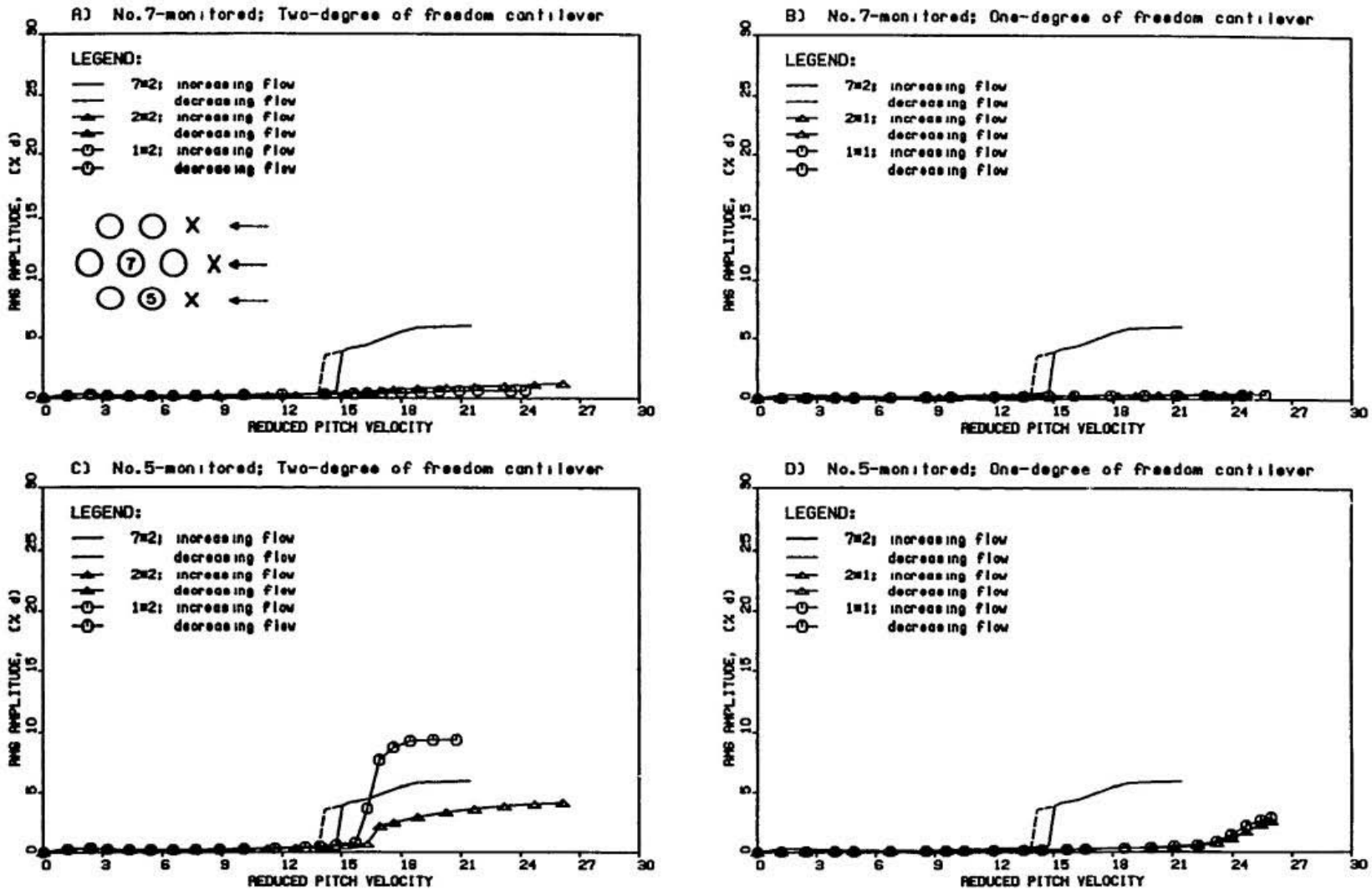

Figure A.5: RMS response curves for the cylinders No.5 and No.7 in a parallel triangular array (No.7 in 5-th row), $\bar{m}\delta_0 \approx 1.9 - 2.4$.

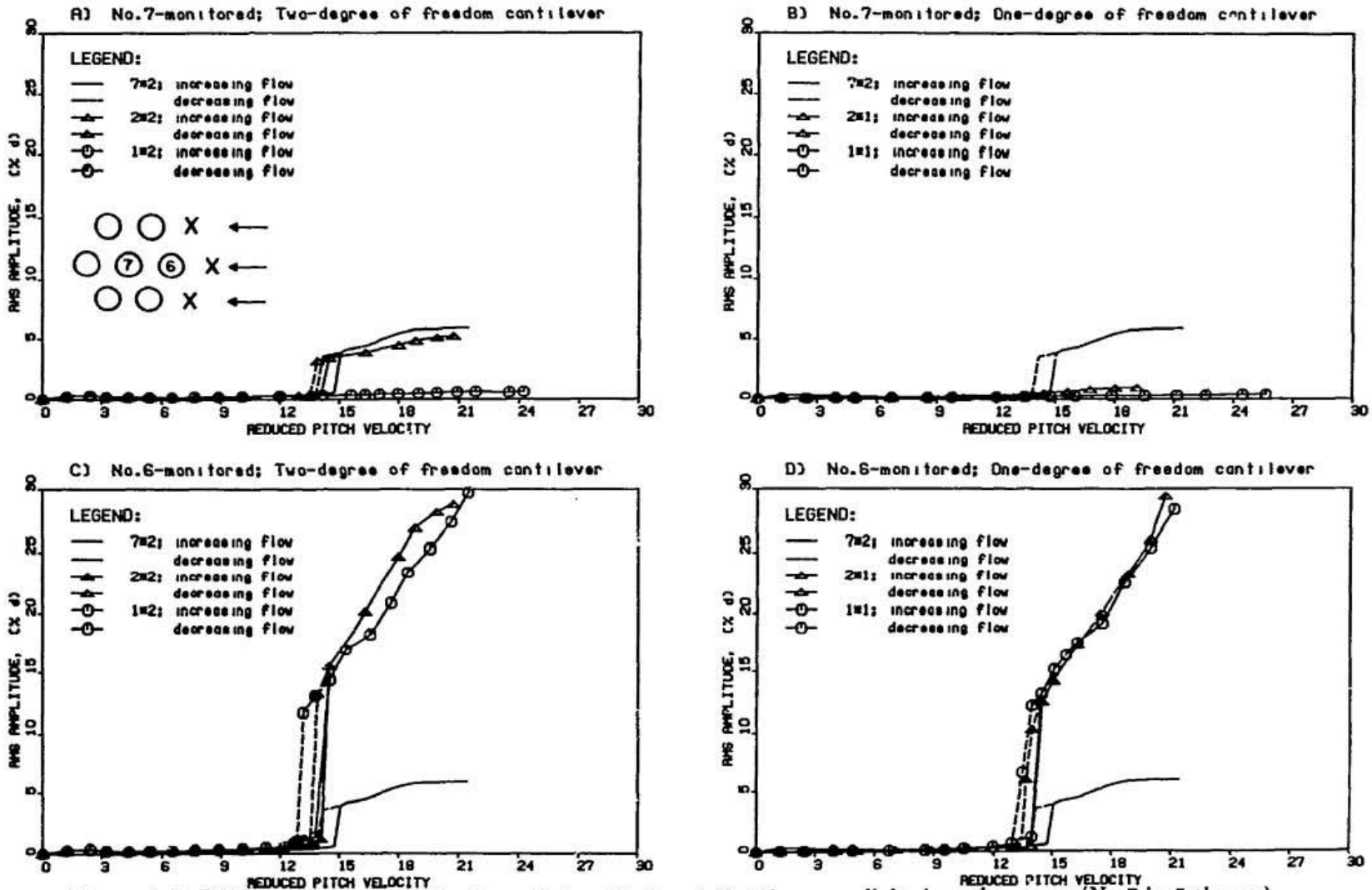

Figure A.6: RMS response curves for the cylinders No.6 and No.7 in a parallel triangular array (No.7 in 5-th row), $\bar{m}\delta_0 \approx 1.9 - 2.4$.

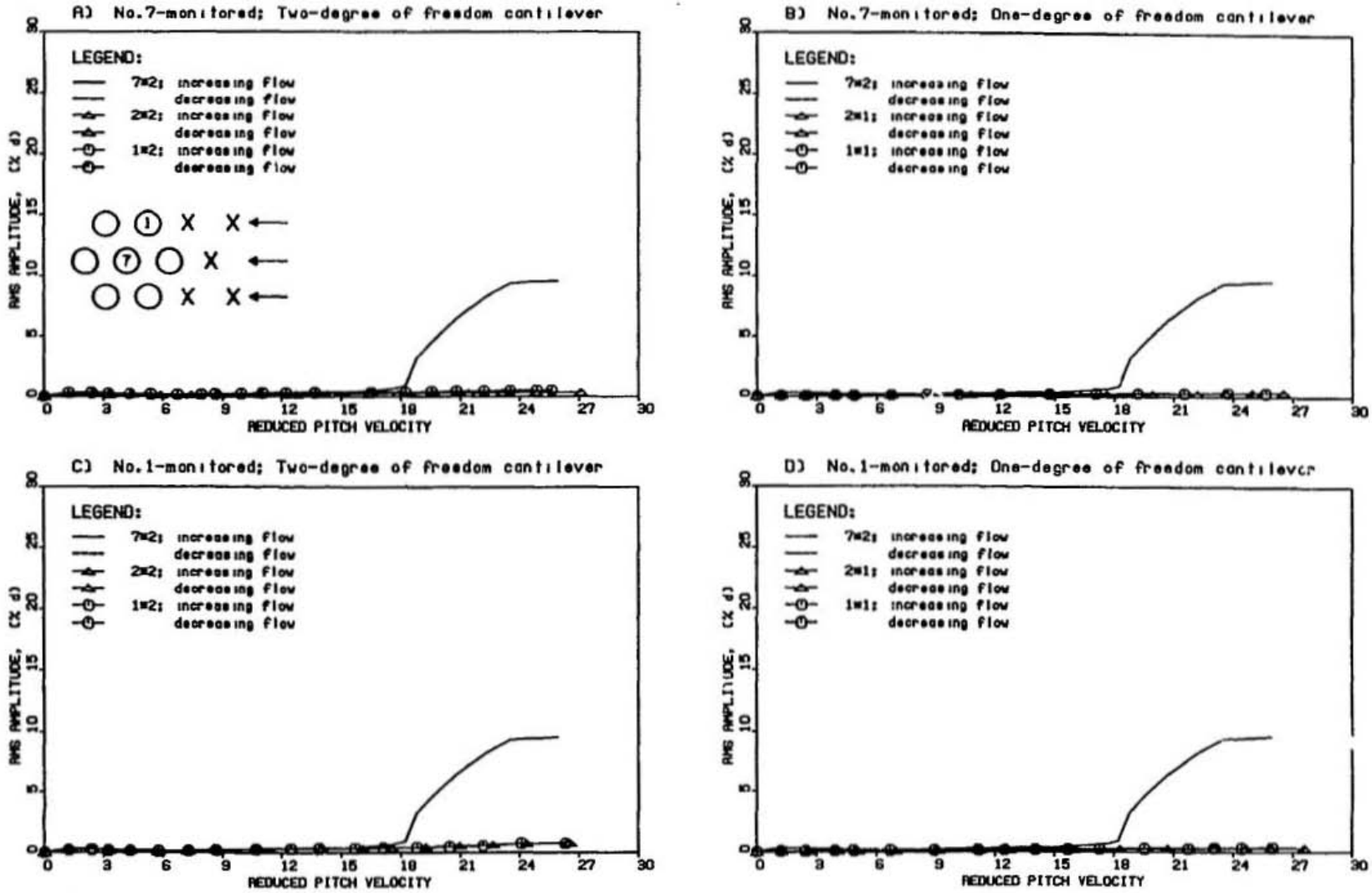

Figure A.7: RMS response curves for the cylinders No.1 and No.7 in a parallel triangular array (No.7 in 6-th row), $\bar{m}\delta_0 \approx 1.9 - 2.4$.

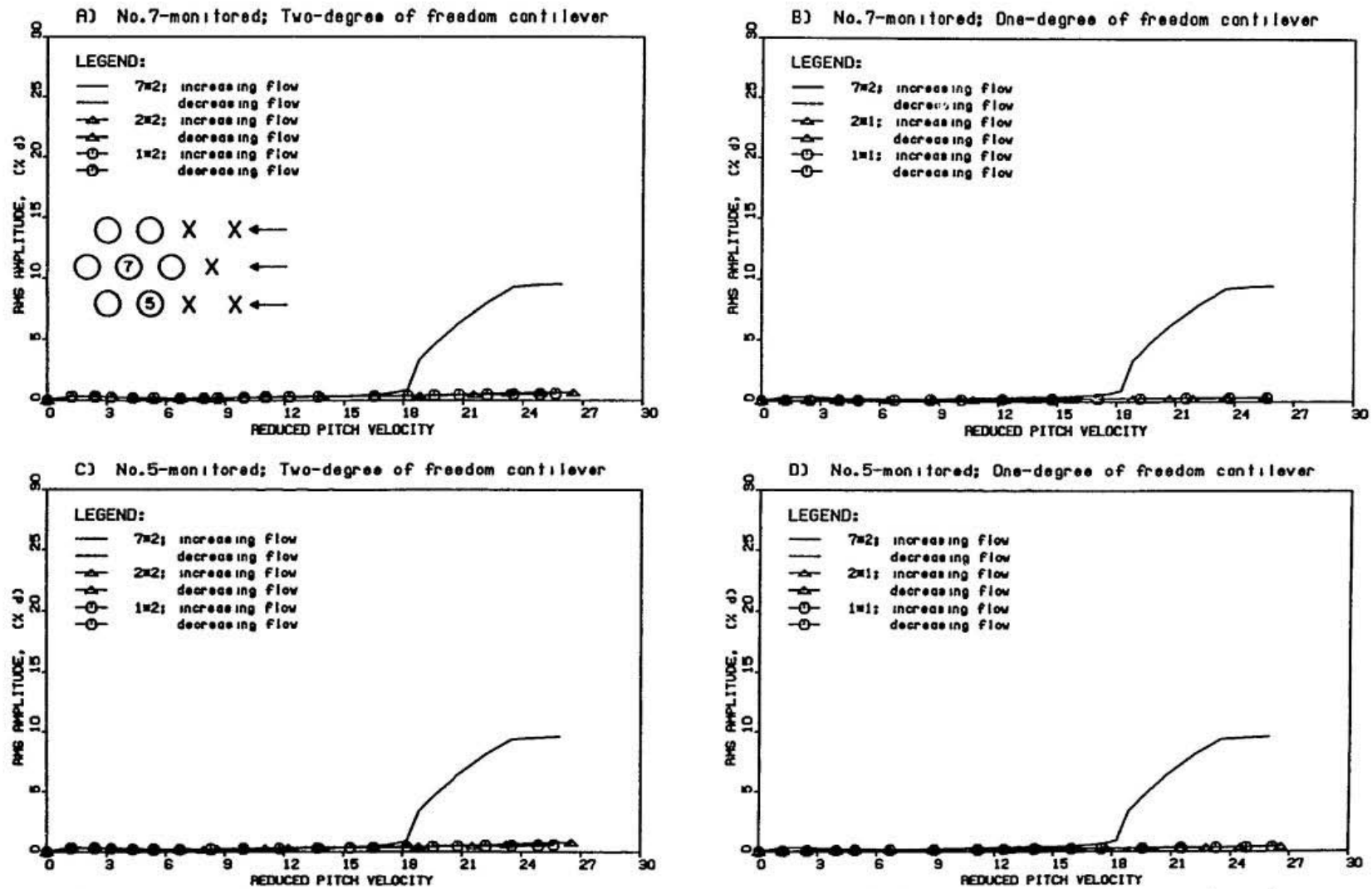

Figure A.8: RMS response curves for the cylinders No.5 and No.7 in a parallel triangular array (No.7 in 6-th row), $\bar{m}\delta_0 \approx 1.9 - 2.4$.

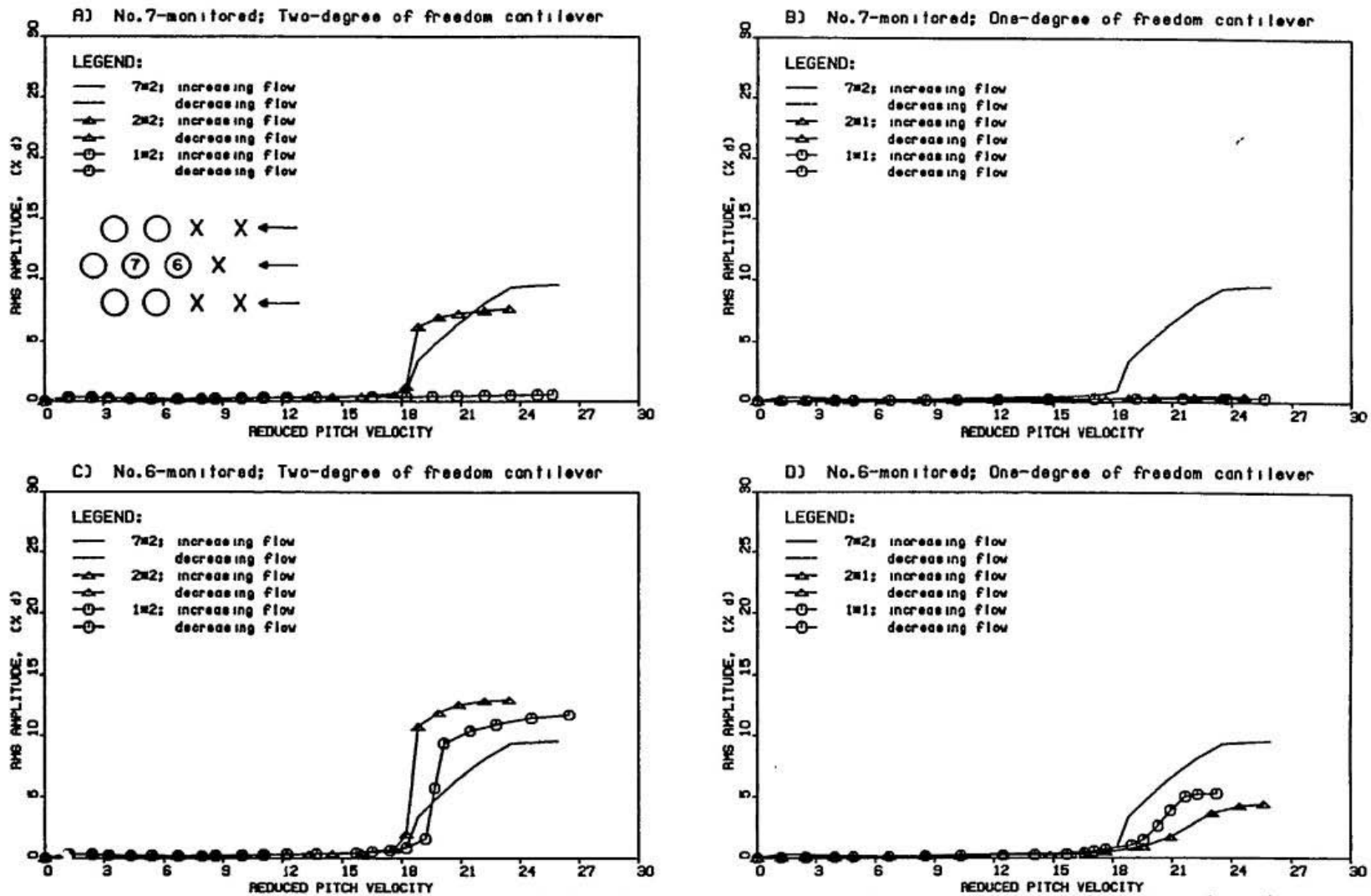

Figure A.9: RMS response curves for the cylinders No.6 and No.7 in a parallel triangular array (No.7 in 6-th row), $\bar{m}\delta_0 \approx 1.9 - 2.4$.

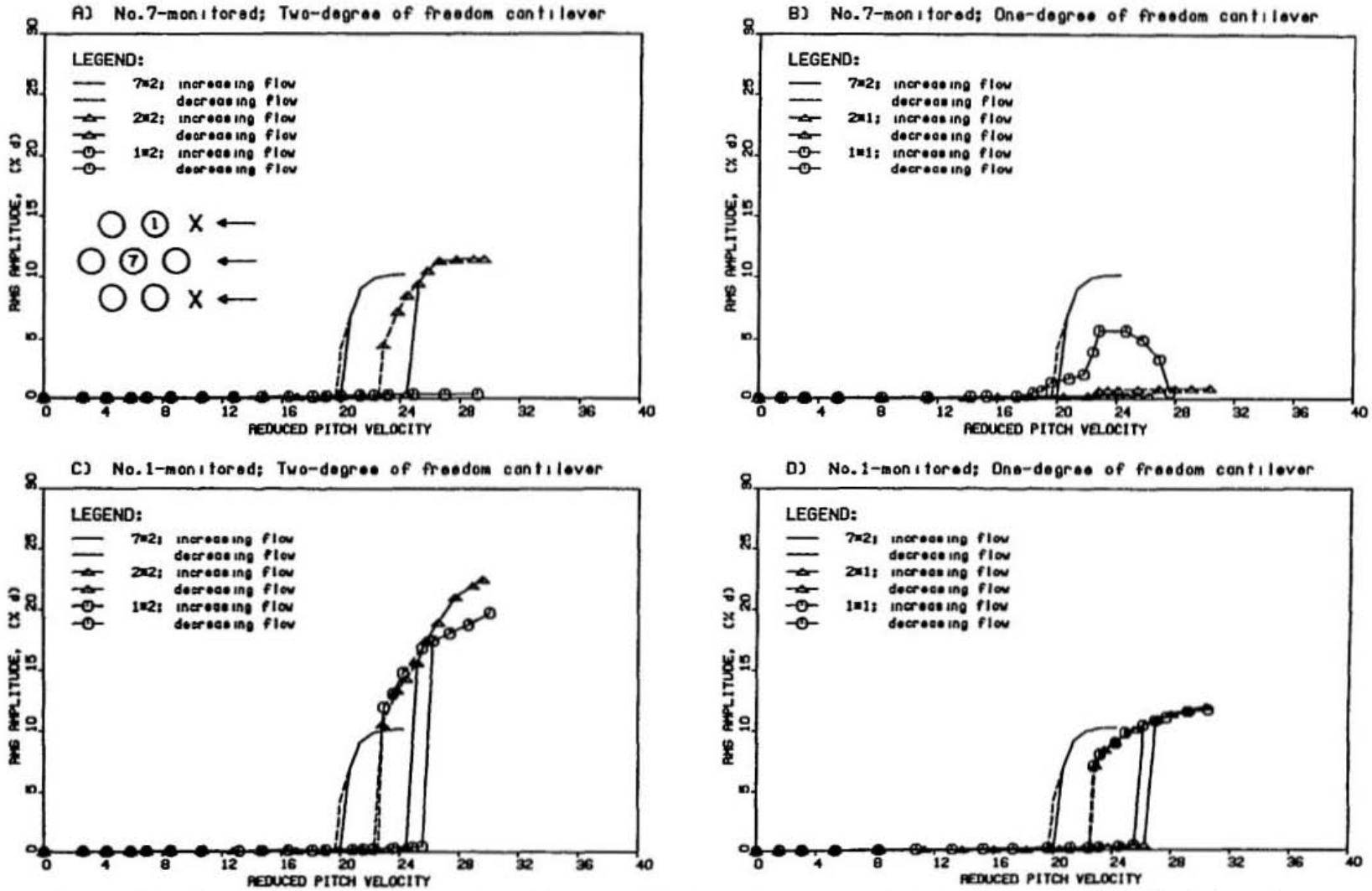

Figure A.10: RMS response curves for the cylinders No.1 and No.7 in a parallel triangular array (No.7 in 4-th row), $\bar{m}\delta_0 \approx 8.4 - 11.2$.

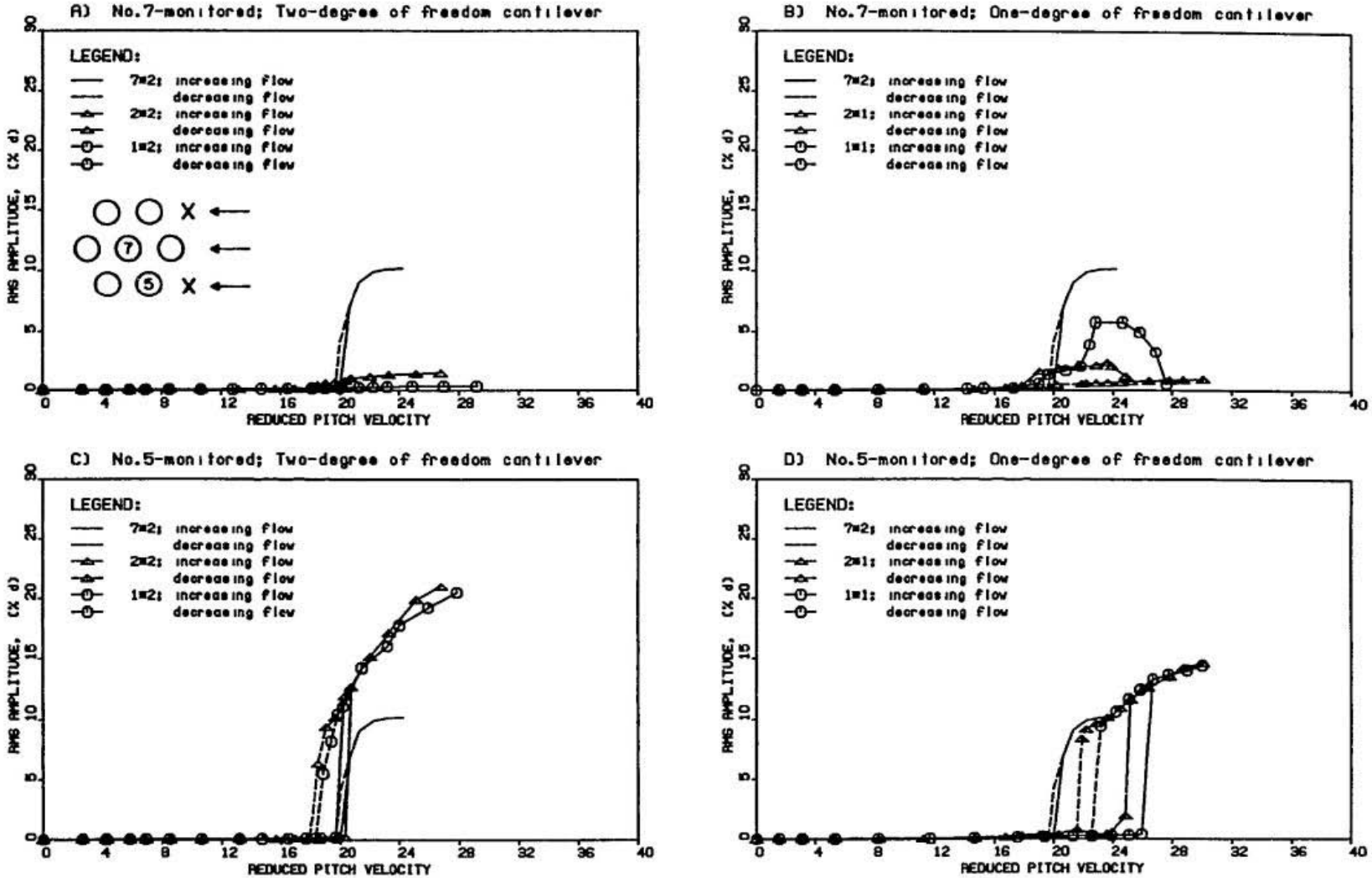

Figure A.11: RMS response curves for the cylinders No.5 and No.7 in a parallel triangular array (No.7 in 4-th row), $\bar{m}\delta_0 \approx 8.4 - 11.2$.

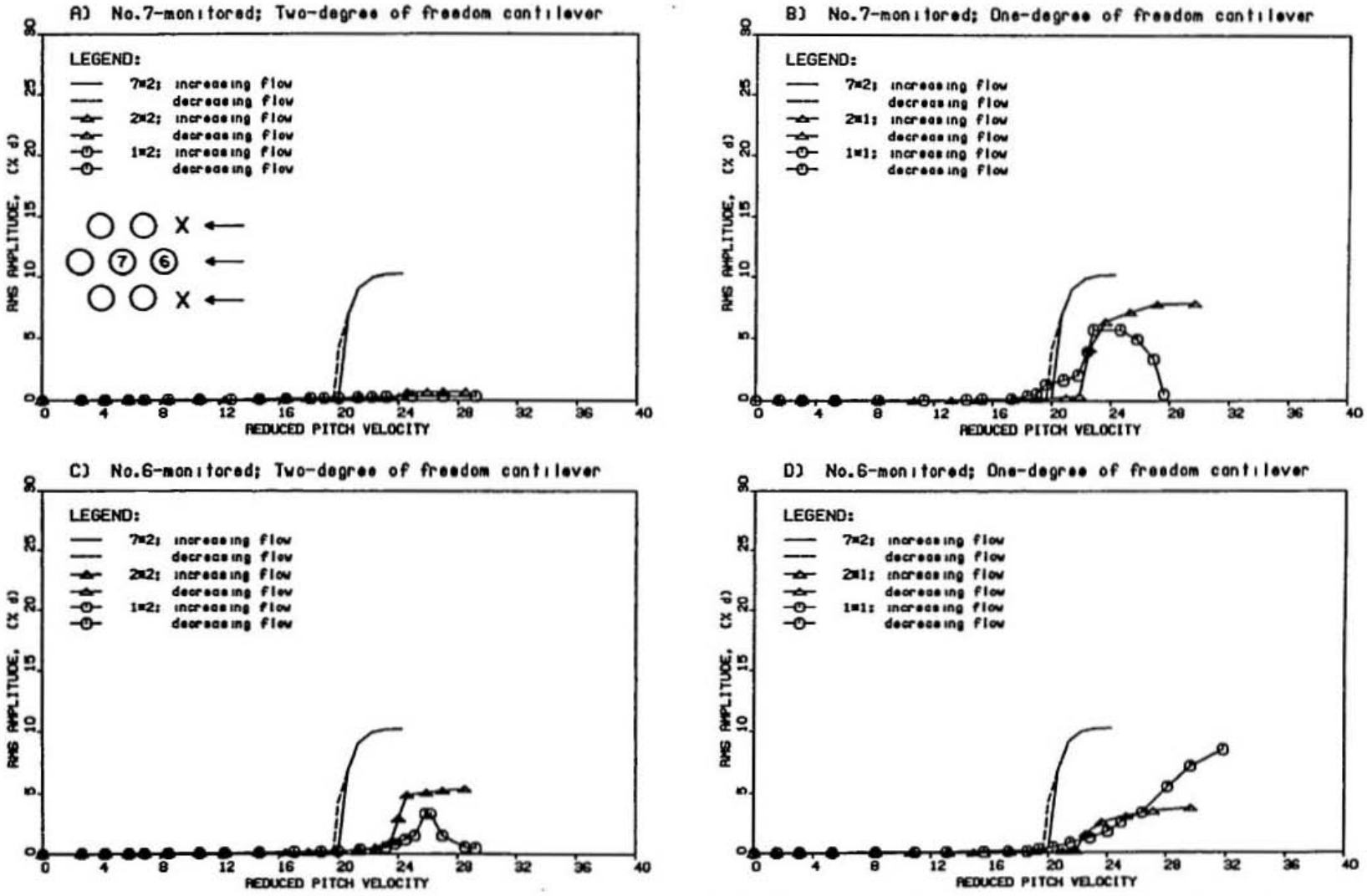

Figure A.12: RMS response curves for the cylinders No.6 and No.7 in a parallel triangular array (No.7 in 4-th row), $\bar{m}\delta_0 \approx 8.4 - 11.2$.

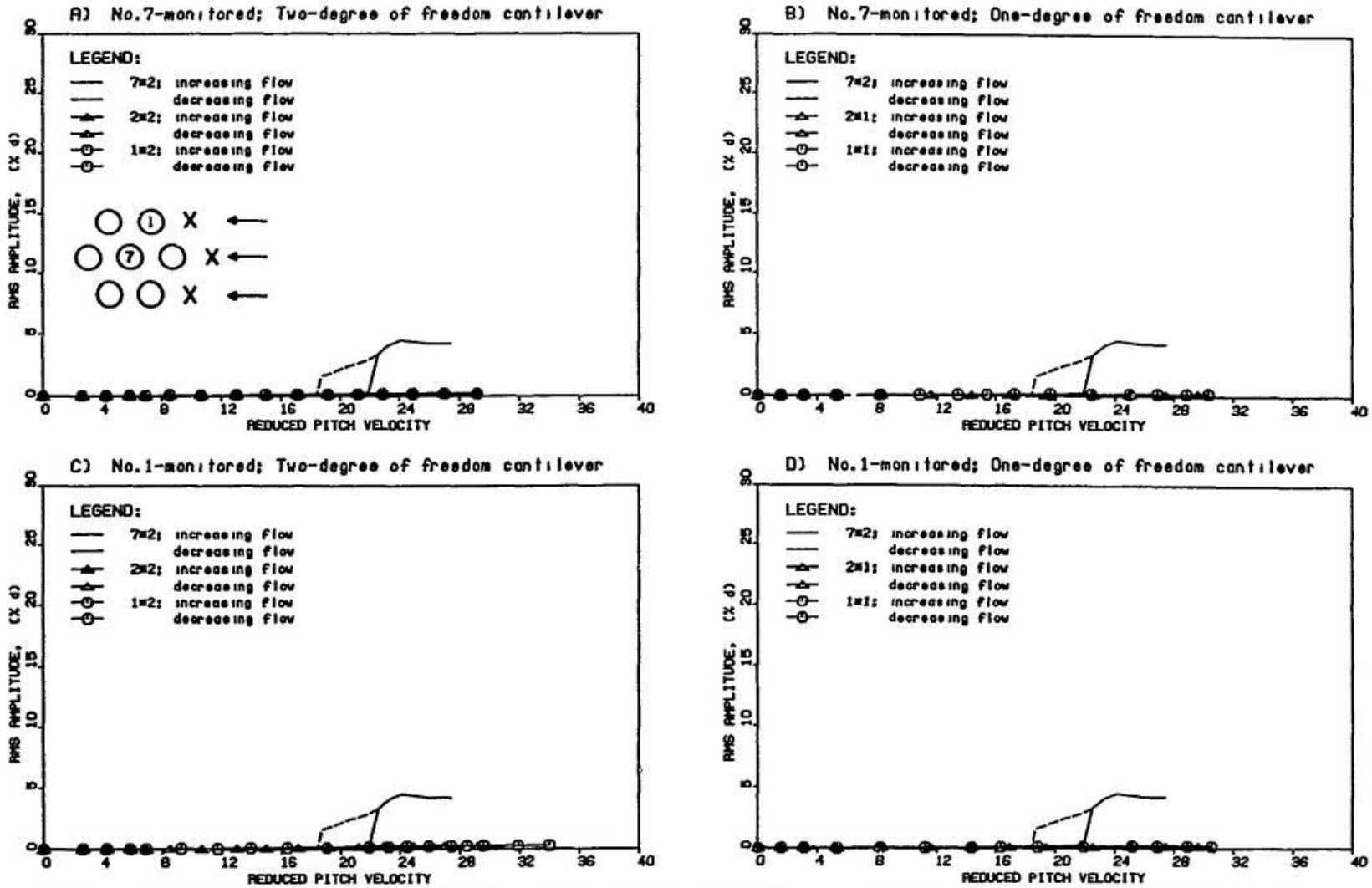

Figure A.13: RMS response curves for the cylinders No.1 and No.7 in a parallel triangular array (No.7 in 5-th row), $\bar{m}\delta_0 \approx 8.4 - 11.2$.

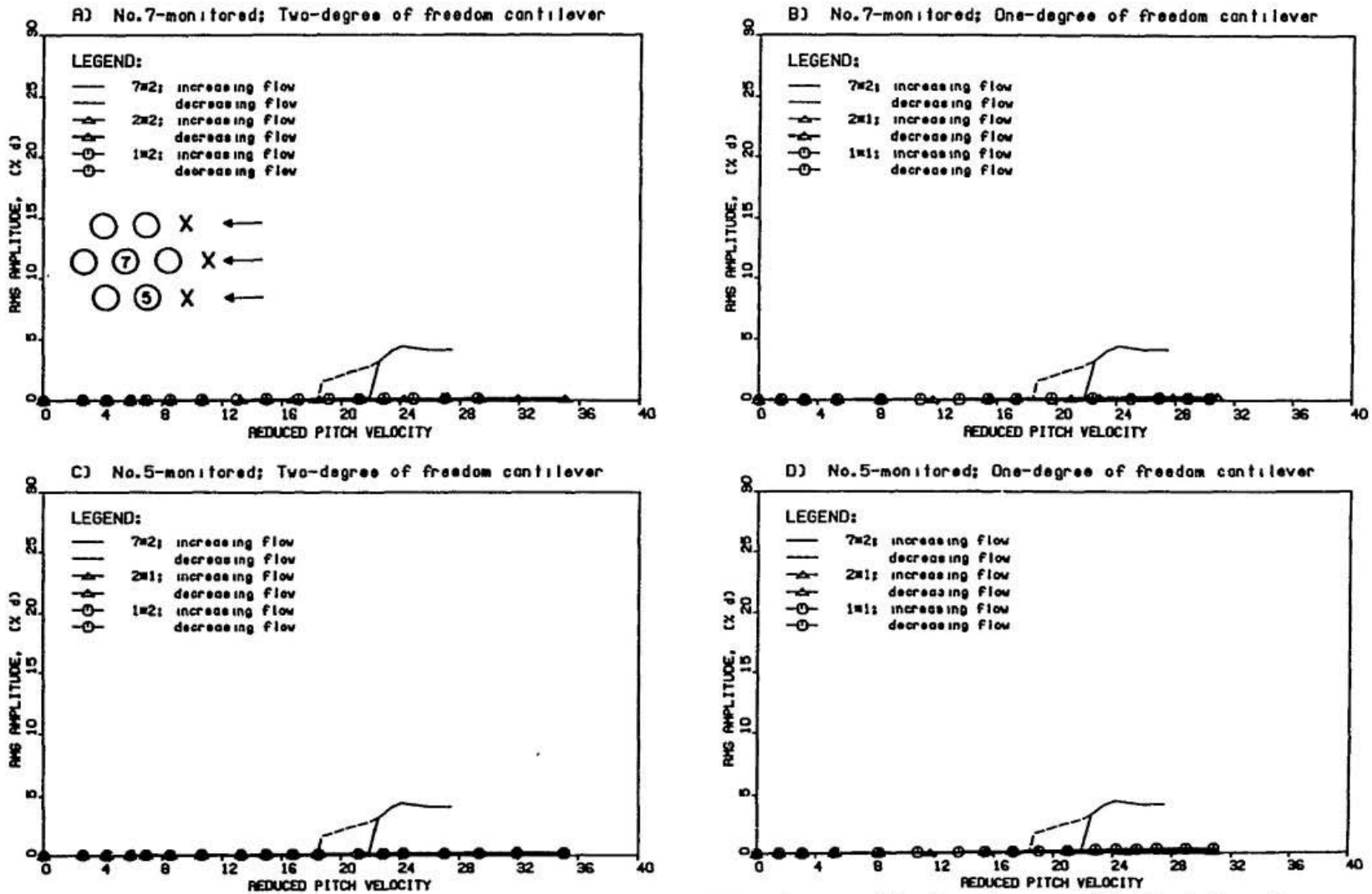

Figure A.14: RMS response curves for the cylinders No.5 and No.7 in a parallel triangular array (No.7 in 5-th row), $\bar{m}\delta_0 \approx 8.4 - 11.2$.

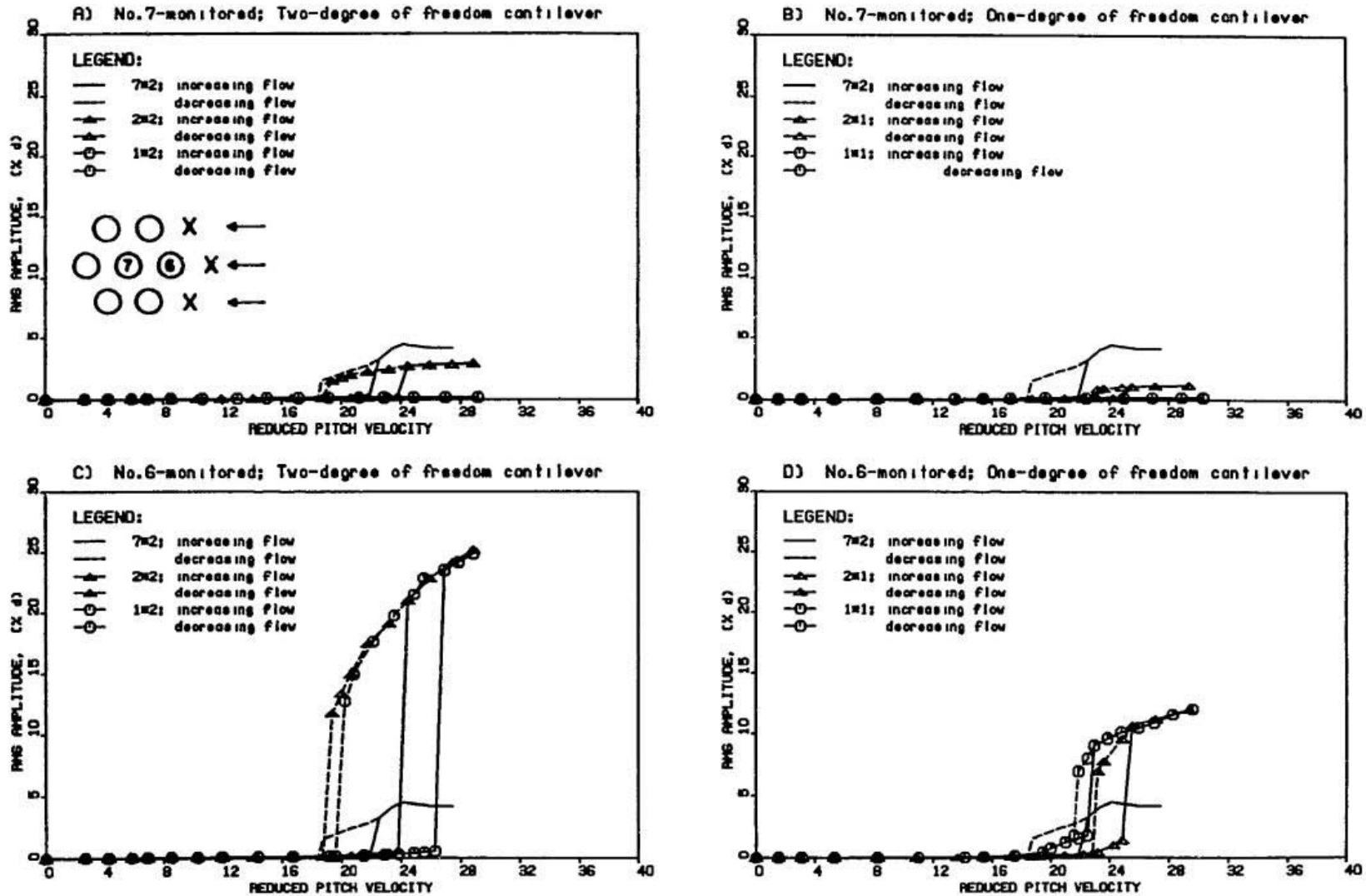

Figure A.15: RMS response curves for the cylinders No.6 and No.7 in a parallel triangular array (No.7 in 5-th row), $\bar{m}\delta_0 \approx 8.4 - 11.2$.

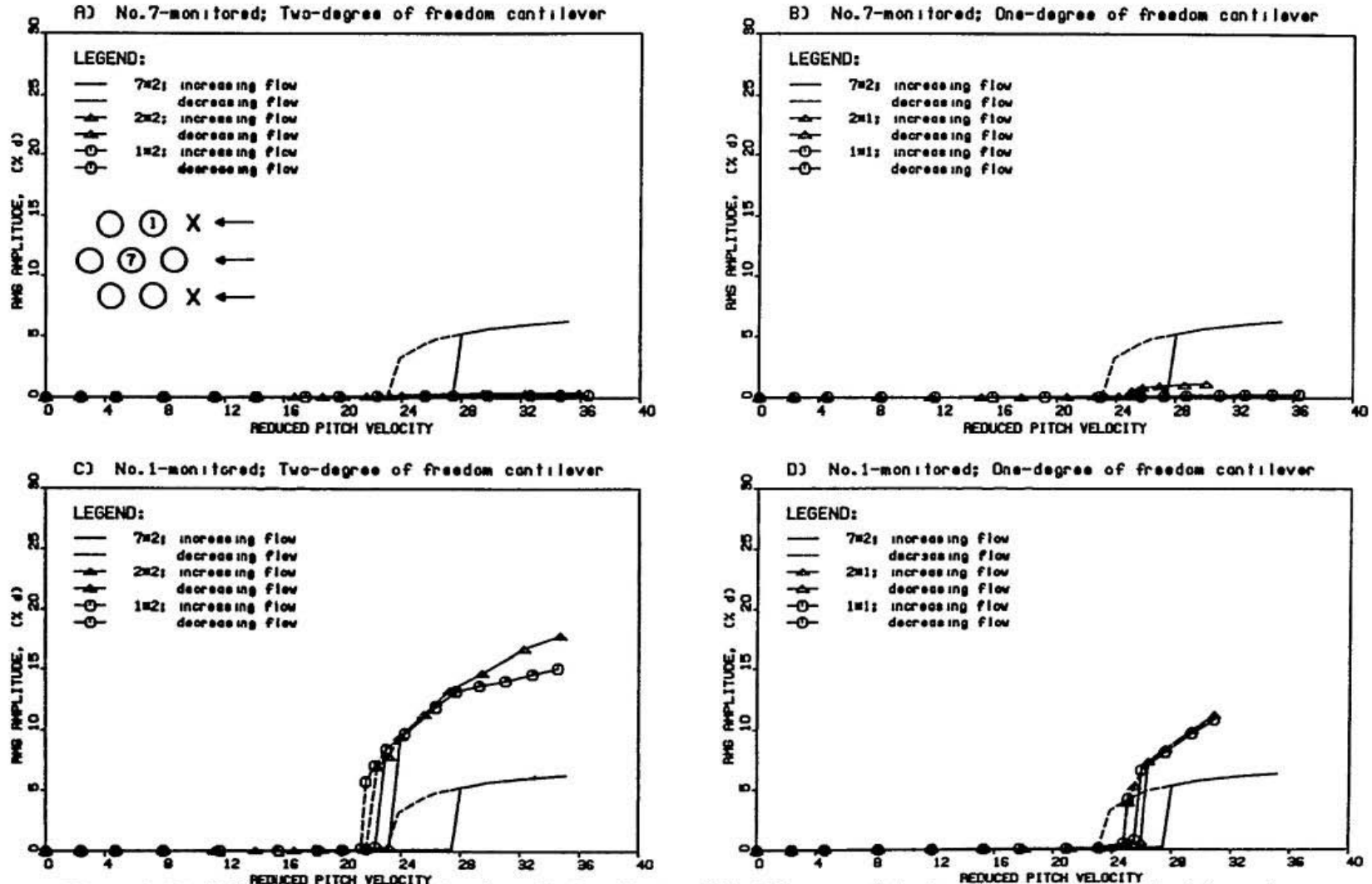

Figure A.16: RMS response curves for the cylinders No.1 and No.7 in a parallel triangular array (No.7 in 4-th row), $\bar{m}\delta_0 \approx 22.1 - 23.5$.

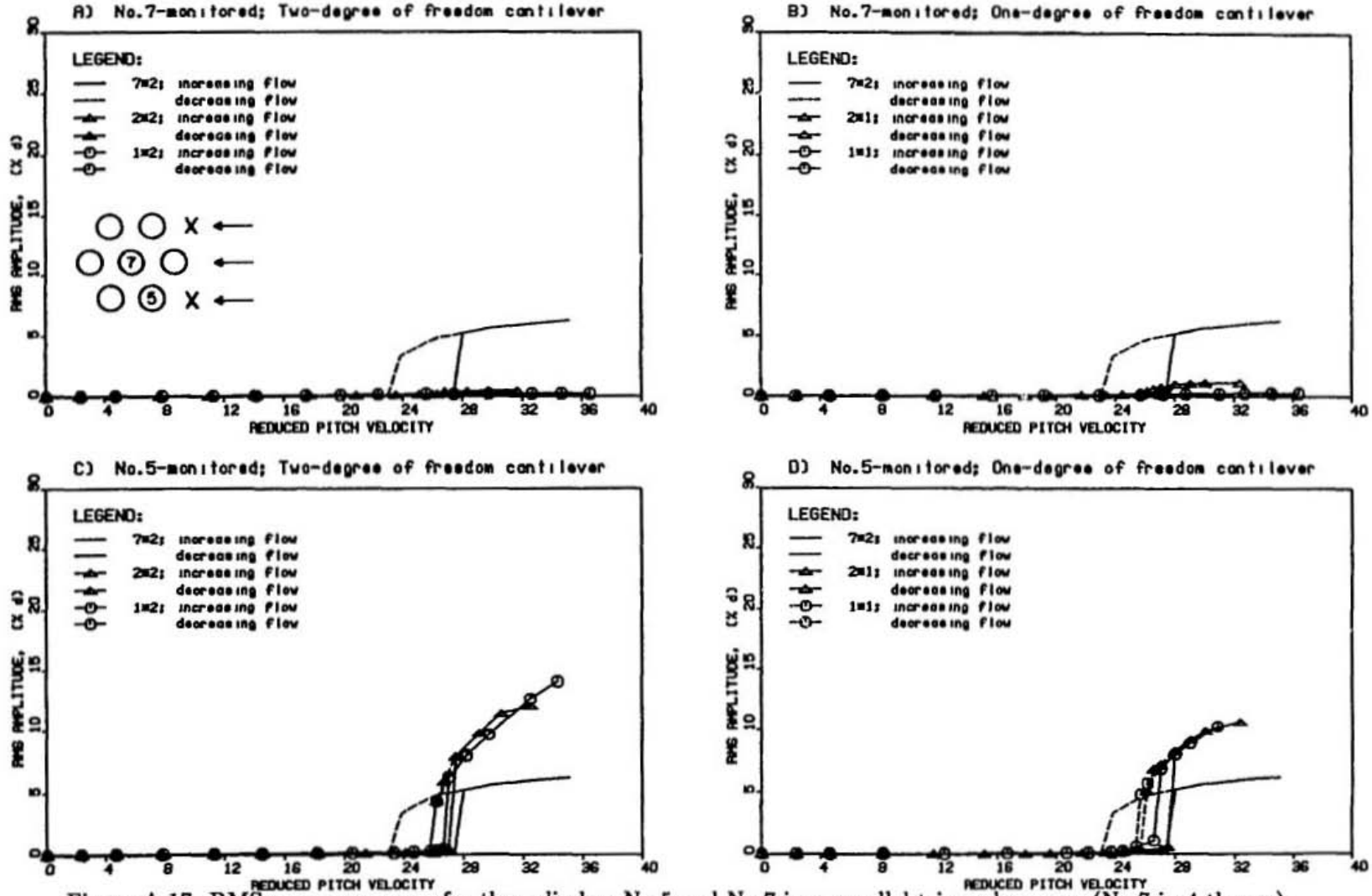

Figure A.17: RMS response curves for the cylinders No.5 and No.7 in a parallel triangular array (No.7 in 4-th row), $\bar{m}\delta_0 \approx 22.1 - 23.5$.

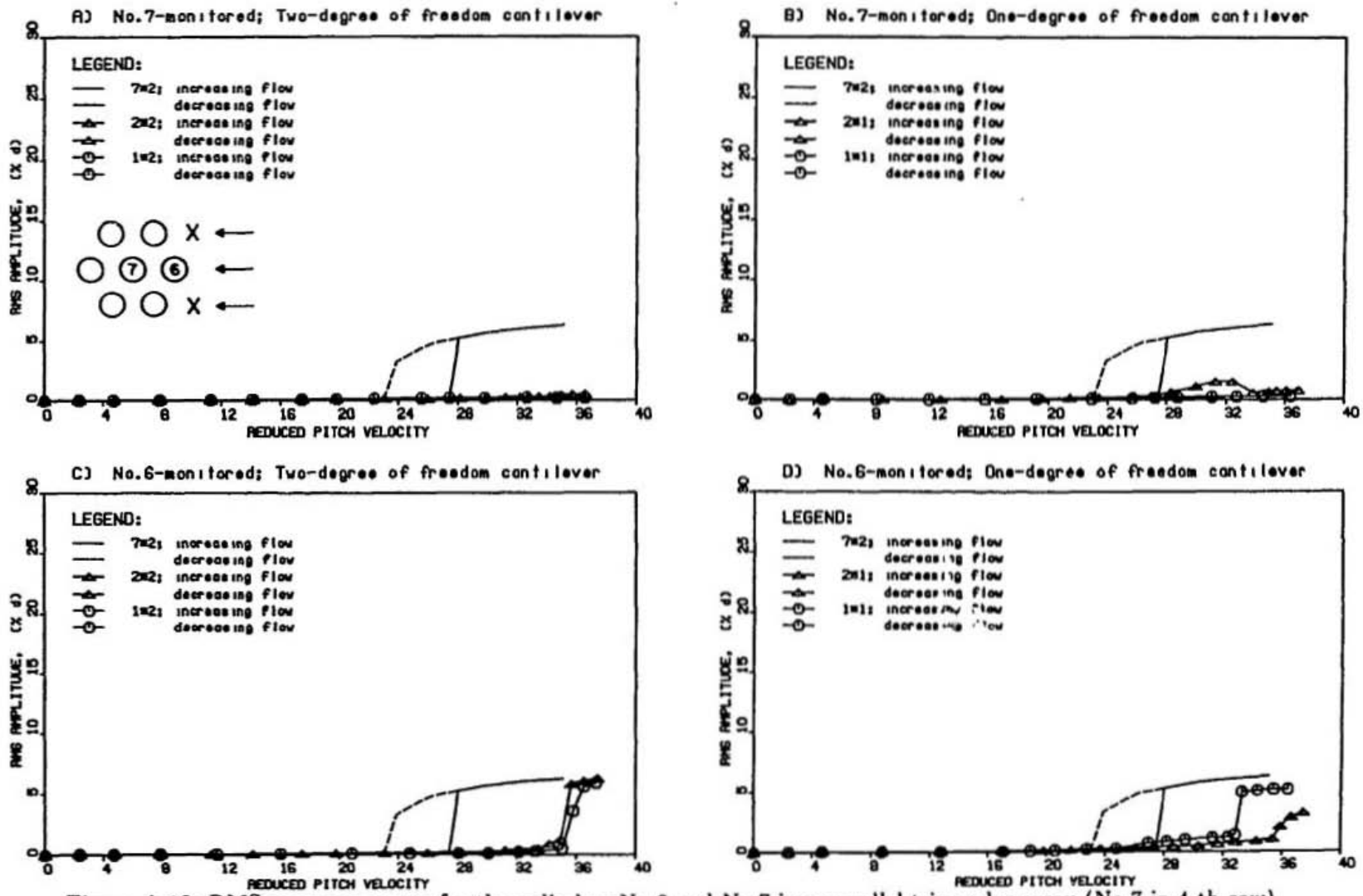

Figure A.18: RMS response curves for the cylinders No.6 and No.7 in a parallel triangular array (No.7 in 4-th row), $\bar{m}\delta_0 \approx 22.1 - 23.5$.

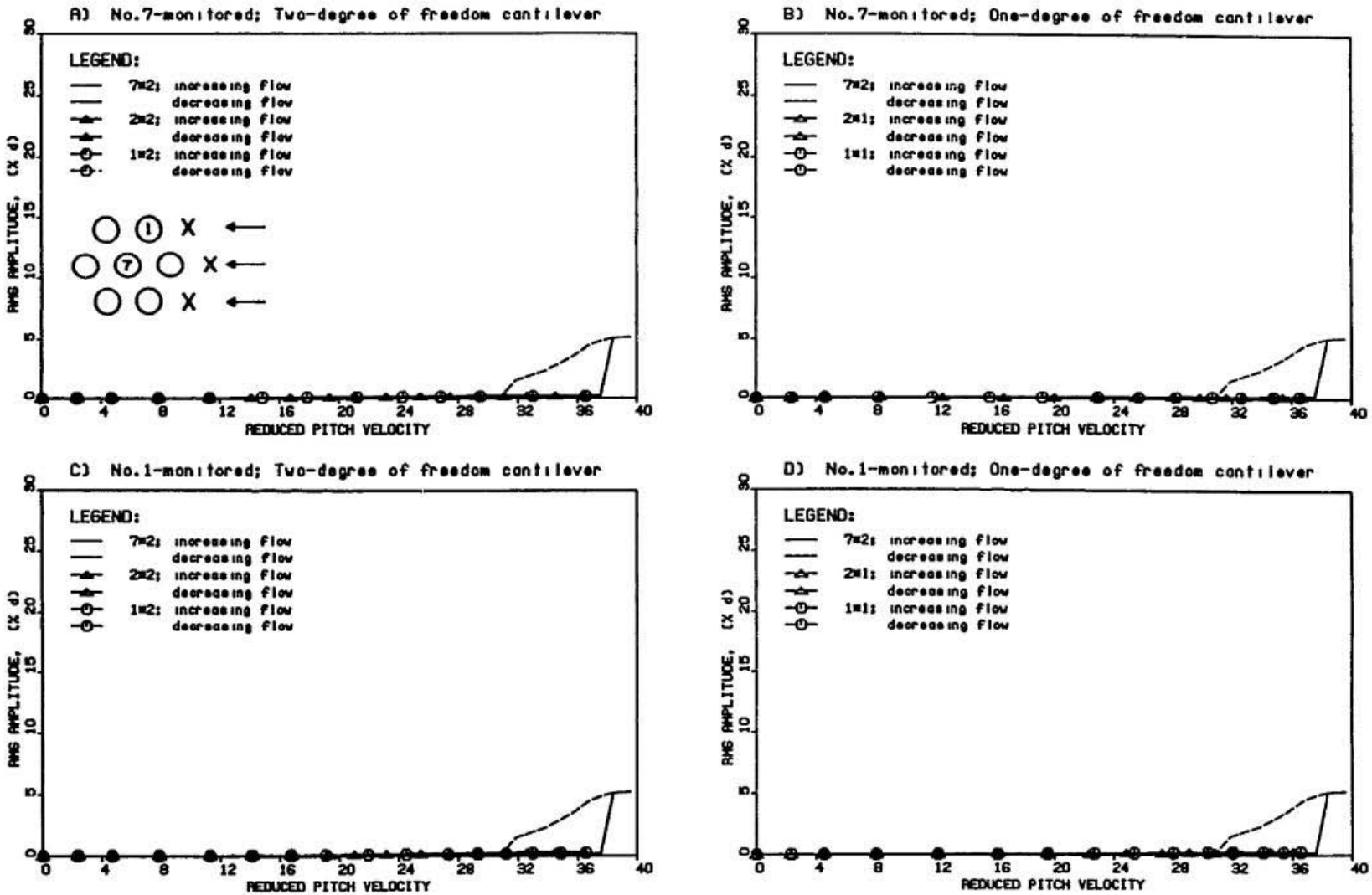

Figure A.19: RMS response curves for the cylinders No.1 and No.7 in a parallel triangular array (No.7 in 5-th row), $\bar{m}\delta_0 \approx 22.1 - 23.5$.

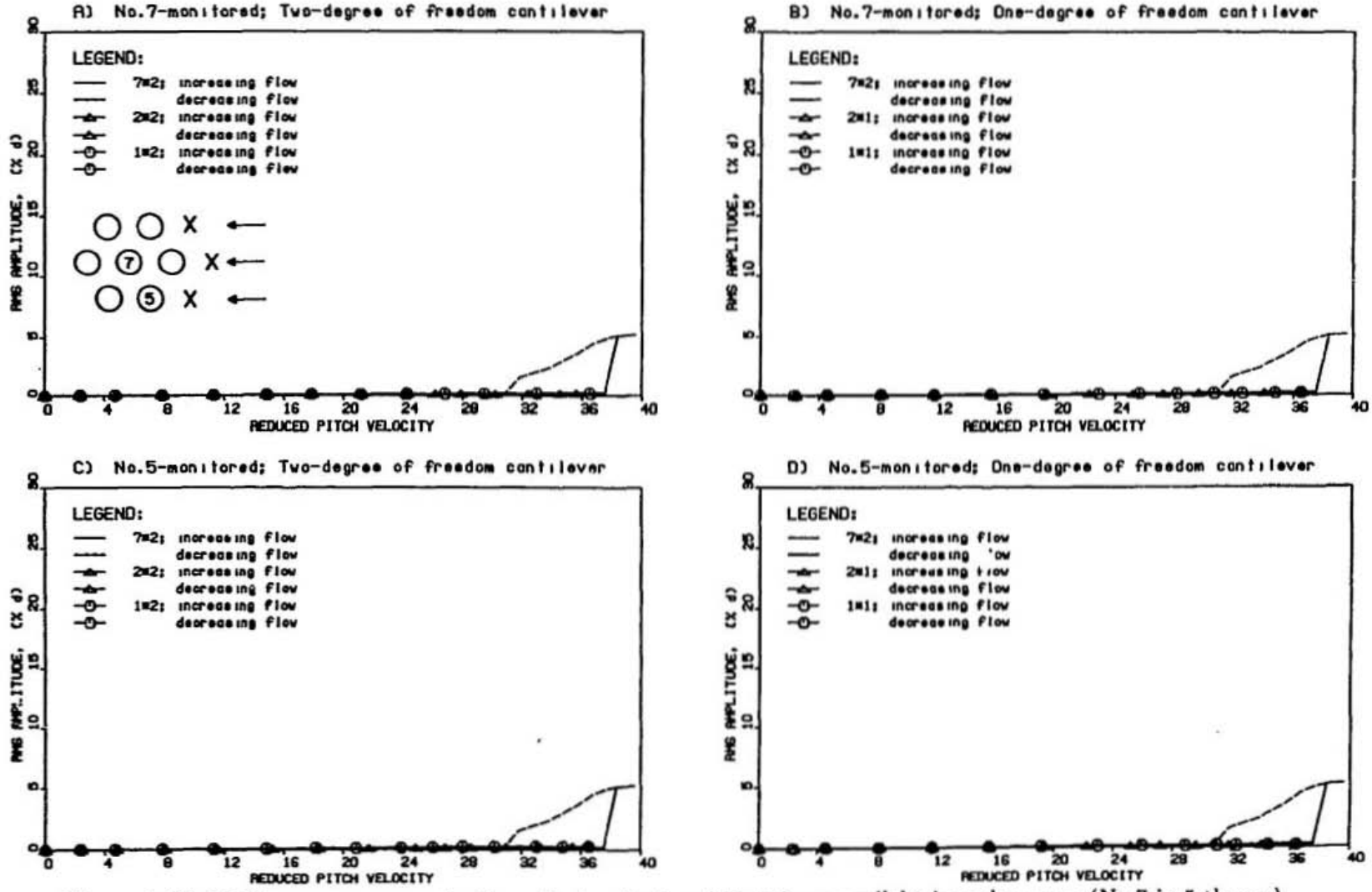

Figure A.20: RMS response curves for the cylinders No.5 and No.7 in a parallel triangular array (No.7 in 5-th row), $\bar{m}\delta_0 \approx 22.1 - 23.5$.

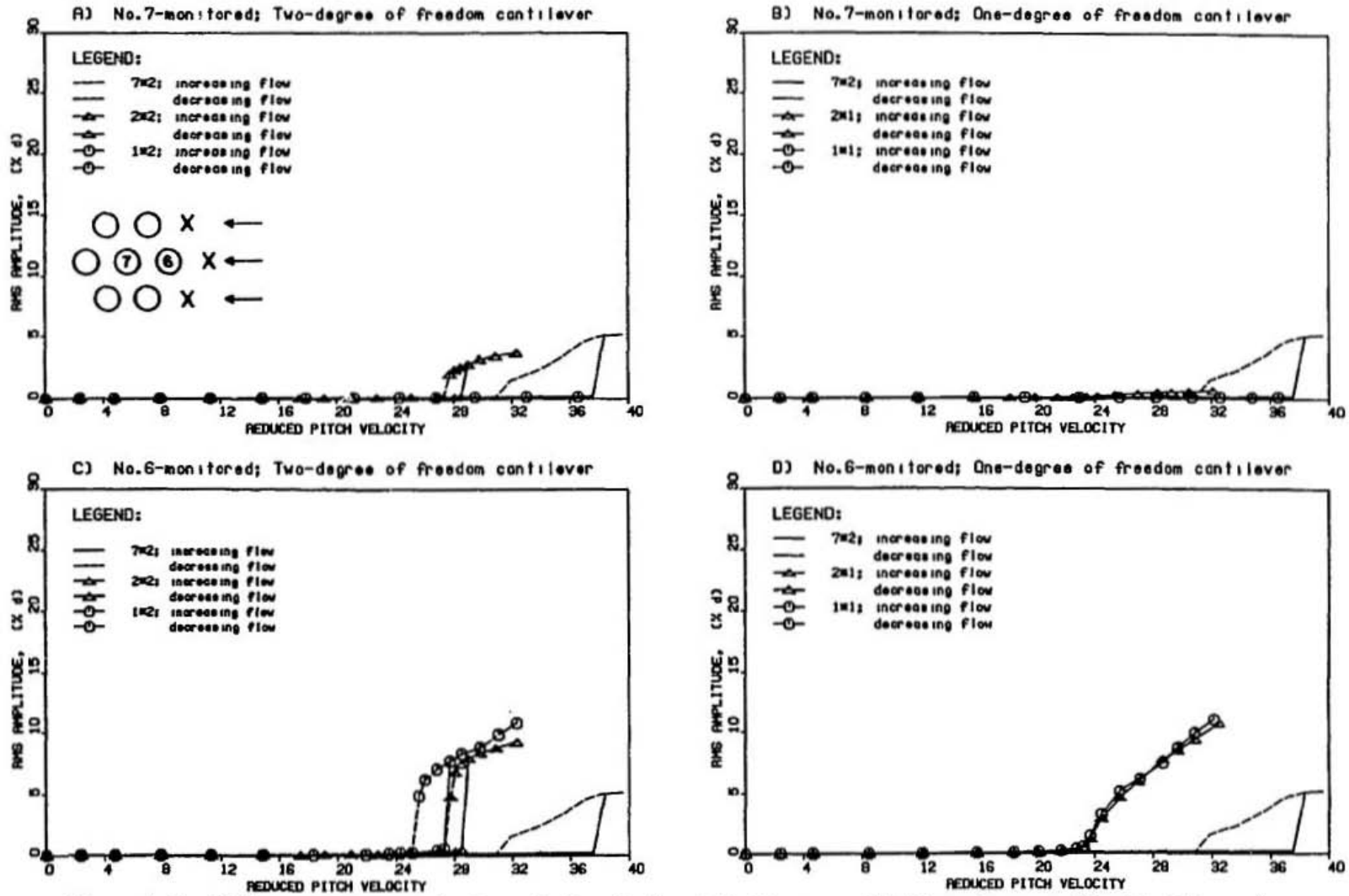

Figure A.21: RMS response curves for the cylinders No.6 and No.7 in a parallel triangular array (No.7 in 5-th row), $\bar{m}\delta_0 \approx 22.1 - 23.5$.

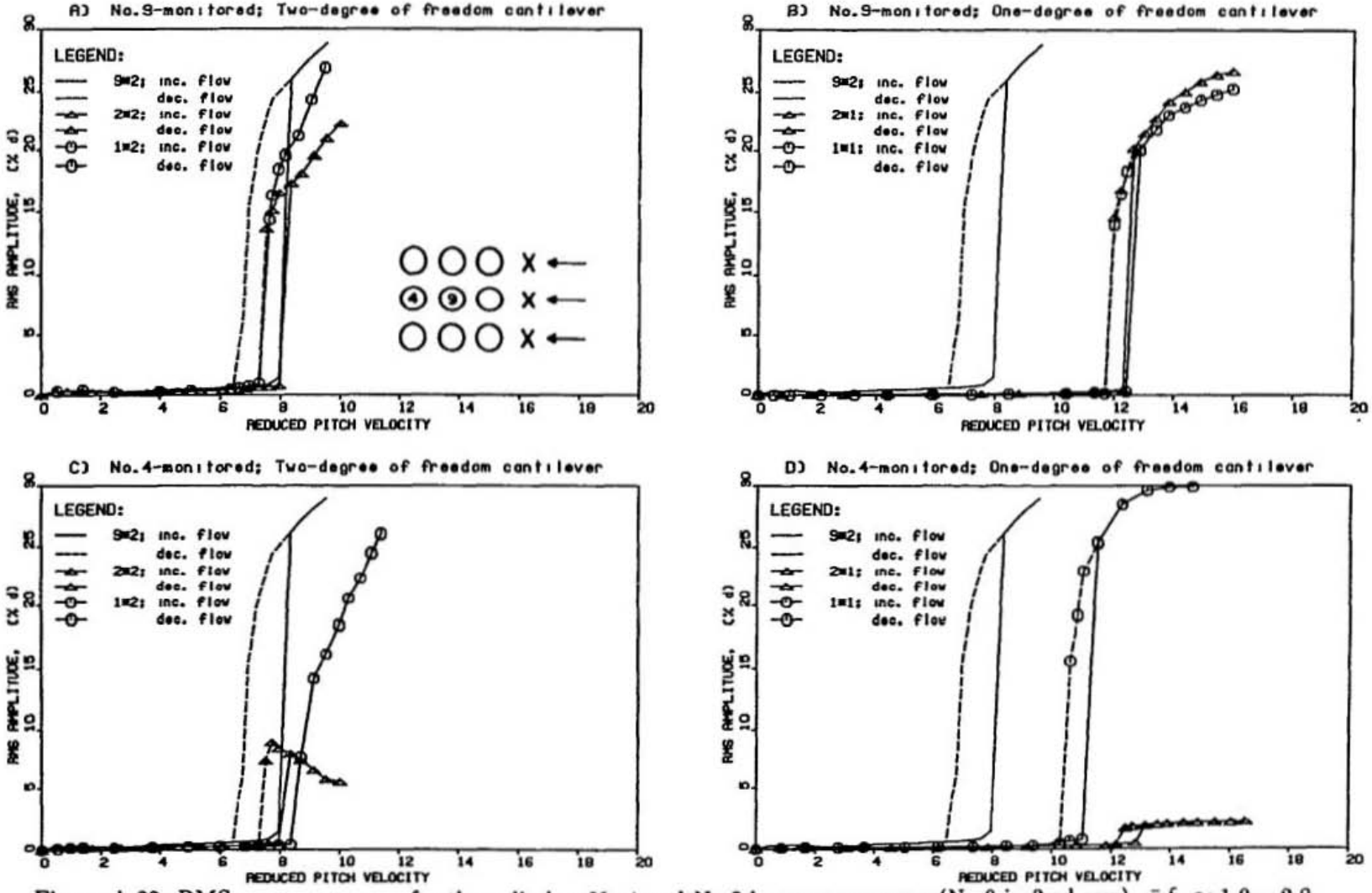

Figure A.22: RMS response curves for the cylinders No.4 and No.9 in a square array (No.9 in 3-rd row), $\bar{m}\delta_0 \approx 1.9 - 2.8$.

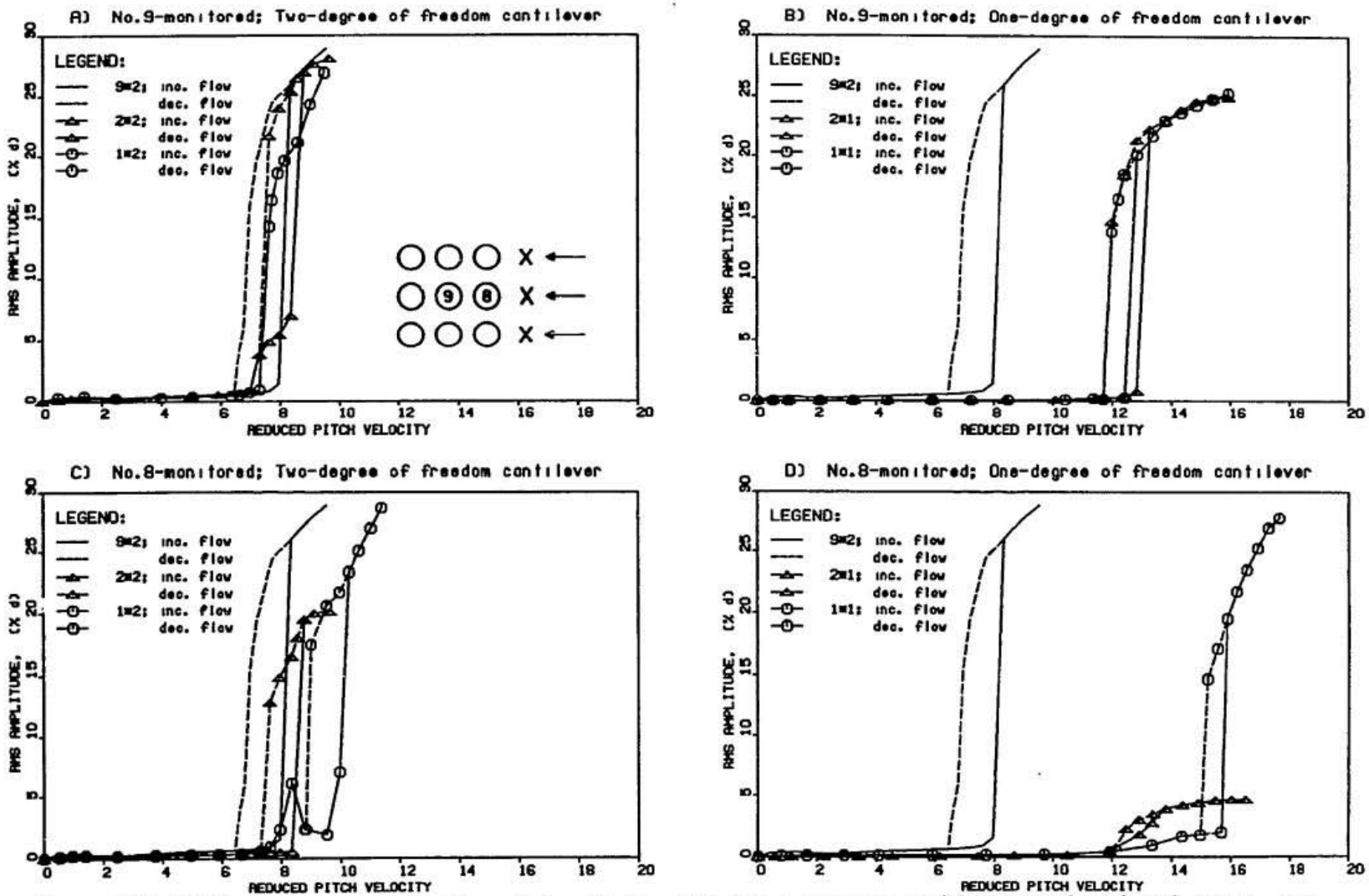

Figure A.23: RMS response curves for the cylinders No.8 and No.9 in a square array (No.9 in 3-rd row), $\bar{m}\delta_0 \approx 1.9 - 2.8$.

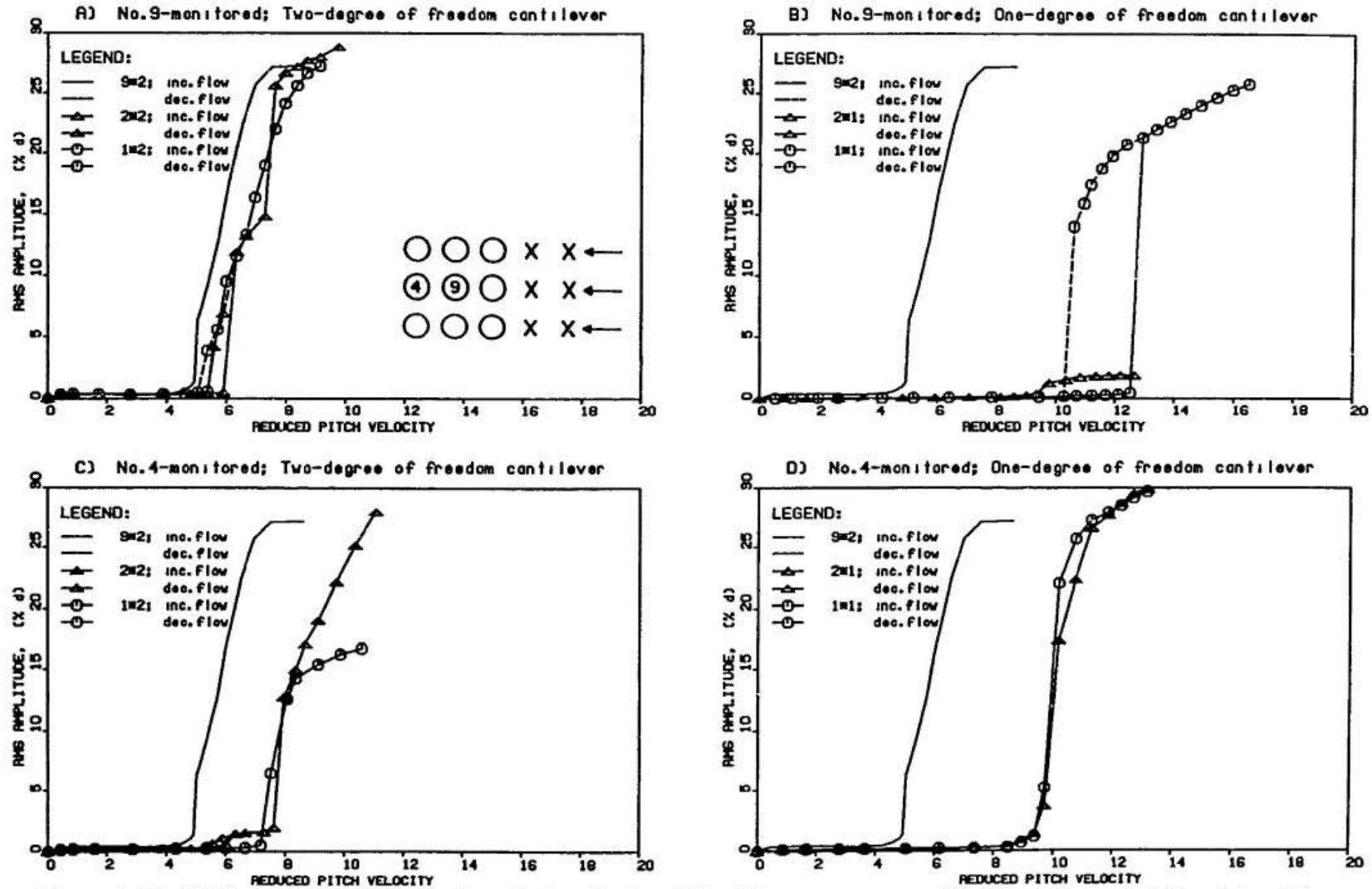

Figure A.24: RMS response curves for the cylinders No.4 and No.9 in a square array (No.9 in 4-th row), $\bar{m}\delta_0 \approx 1.9 - 2.8$.

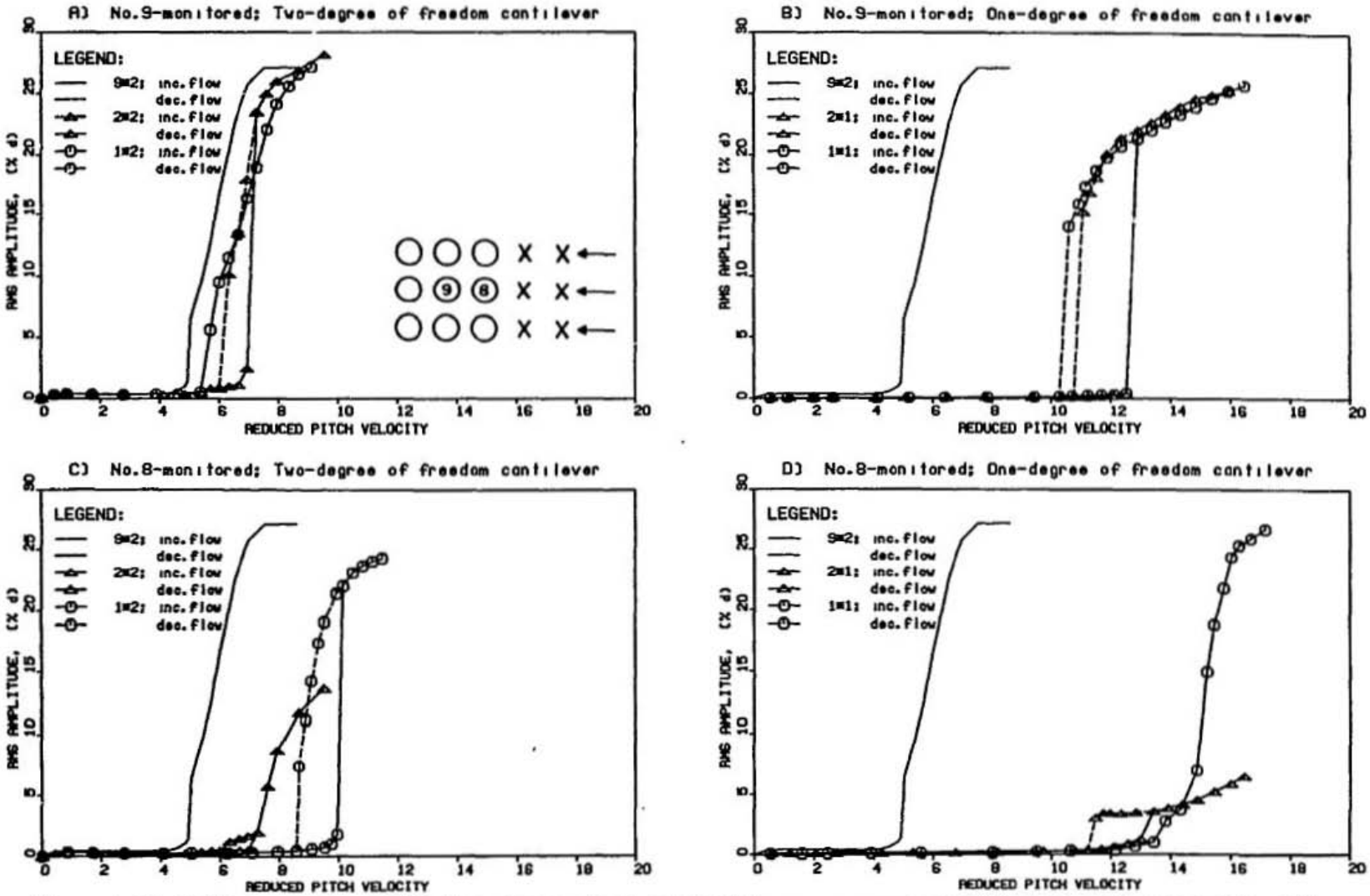

Figure A.25: RMS response curves for the cylinders No.8 and No.9 in a square array (No.9 in 4-th row), $\bar{m}\delta_0 \approx 1.9 - 2.8$.

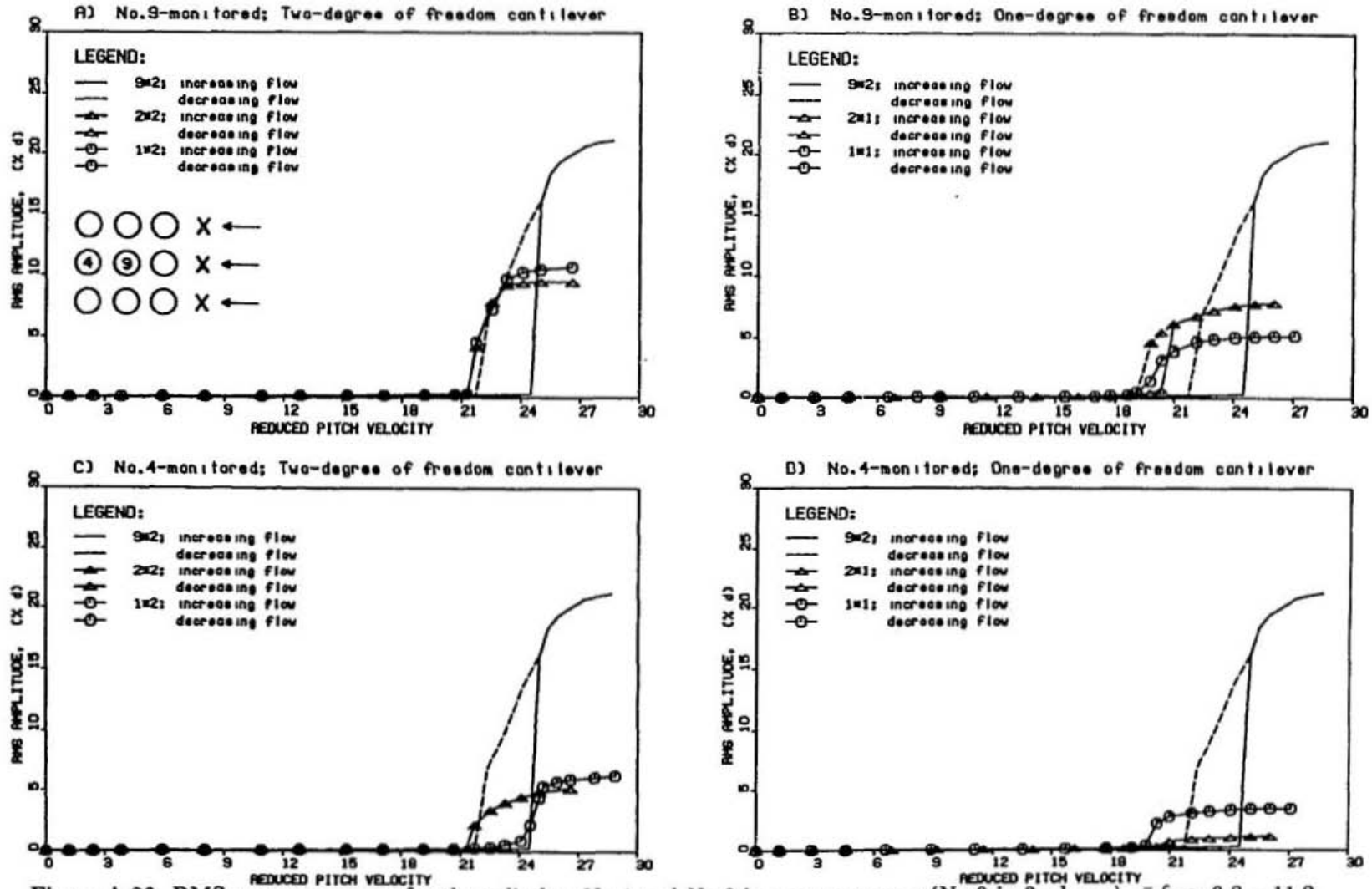

Figure A.26: RMS response curves for the cylinders No.4 and No.9 in a square array (No.9 in 3-rd row), $\bar{m}\delta_0 \approx 9.8 - 11.2$.

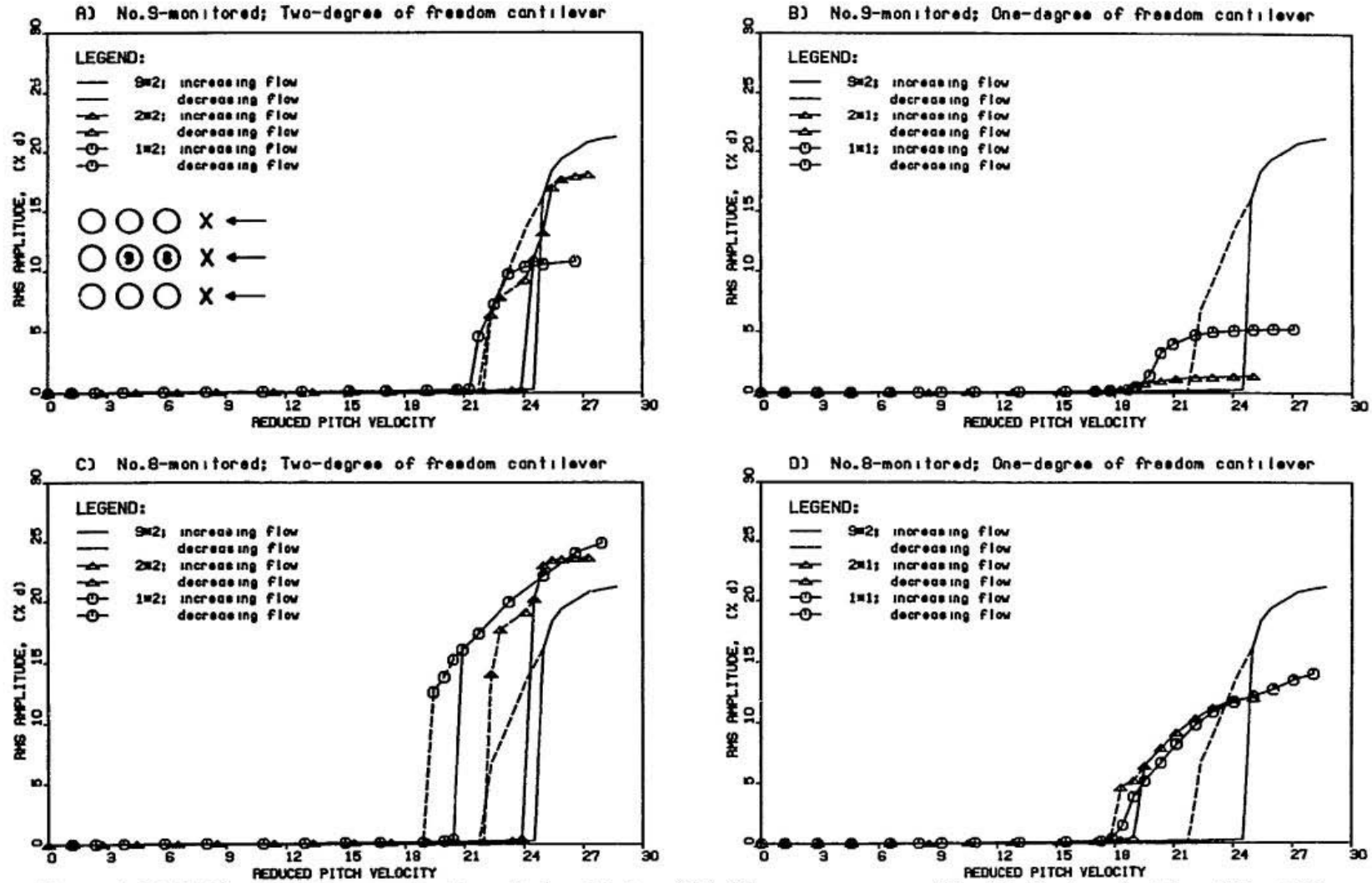

Figure A.27: RMS response curves for the cylinders No.8 and No.9 in a square array (No.9 in 3-rd row), $\bar{m}\delta_0 \approx 9.8 - 11.2$.

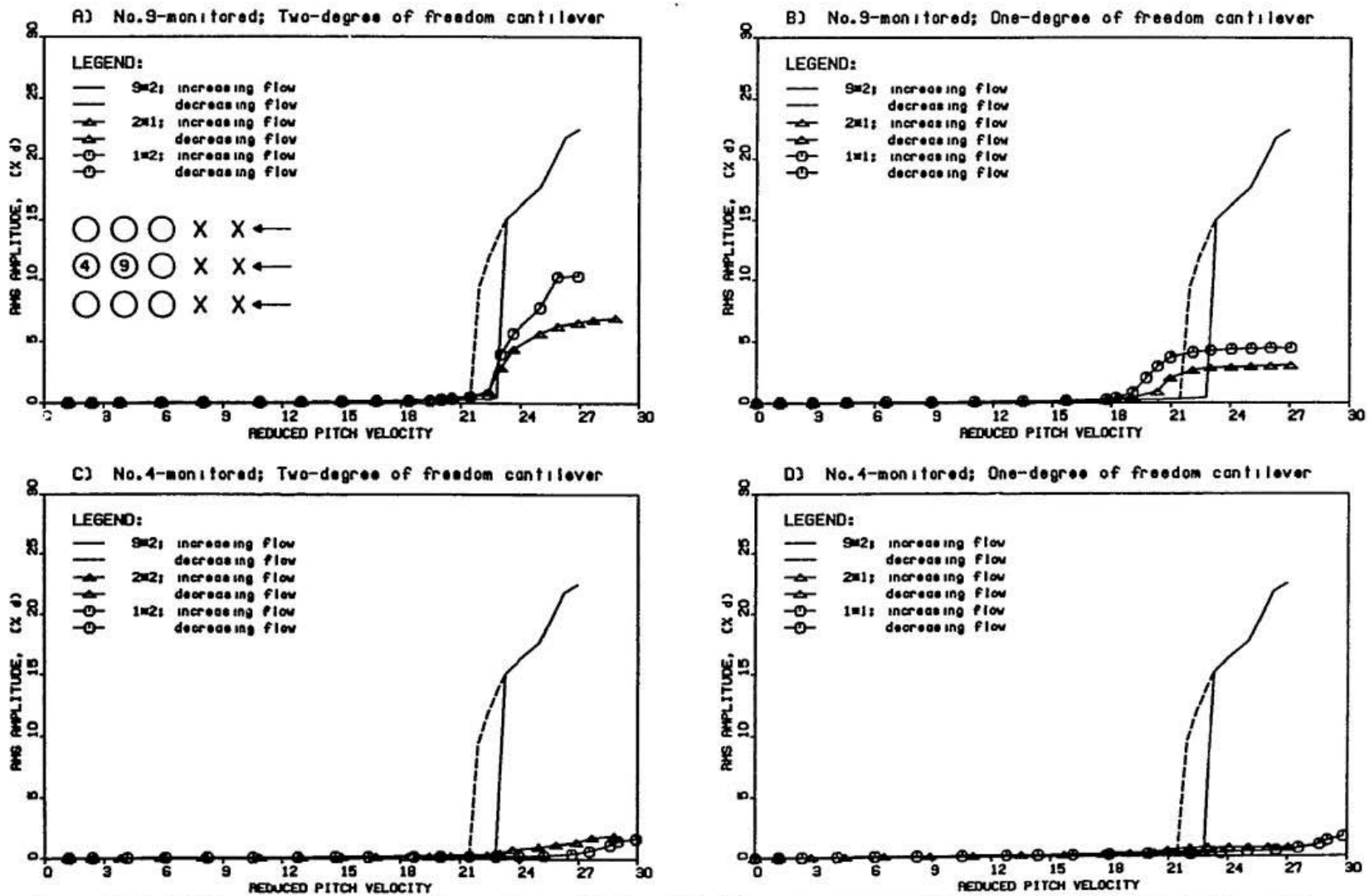

Figure A.28: RMS response curves for the cylinders No.4 and No.9 in a square array (No.9 in 4-th row), $\bar{m}\delta_0 \approx 9.8 - 11.2$.

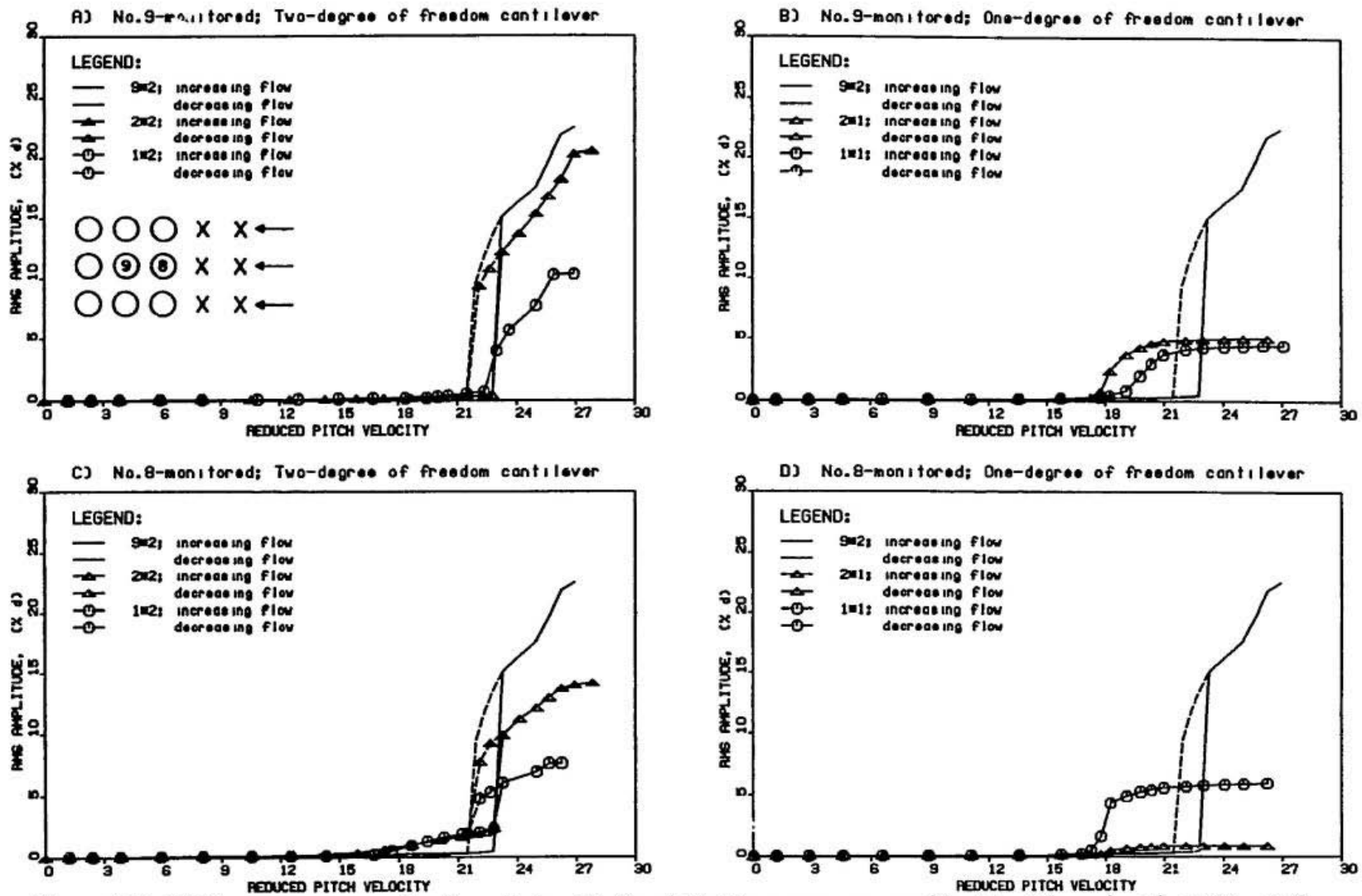

Figure A.29: RMS response curves for the cylinders No.8 and No.9 in a square array (No.9 in 4-th row), $\bar{m}\delta_0 \approx 9.8 - 11.2$.

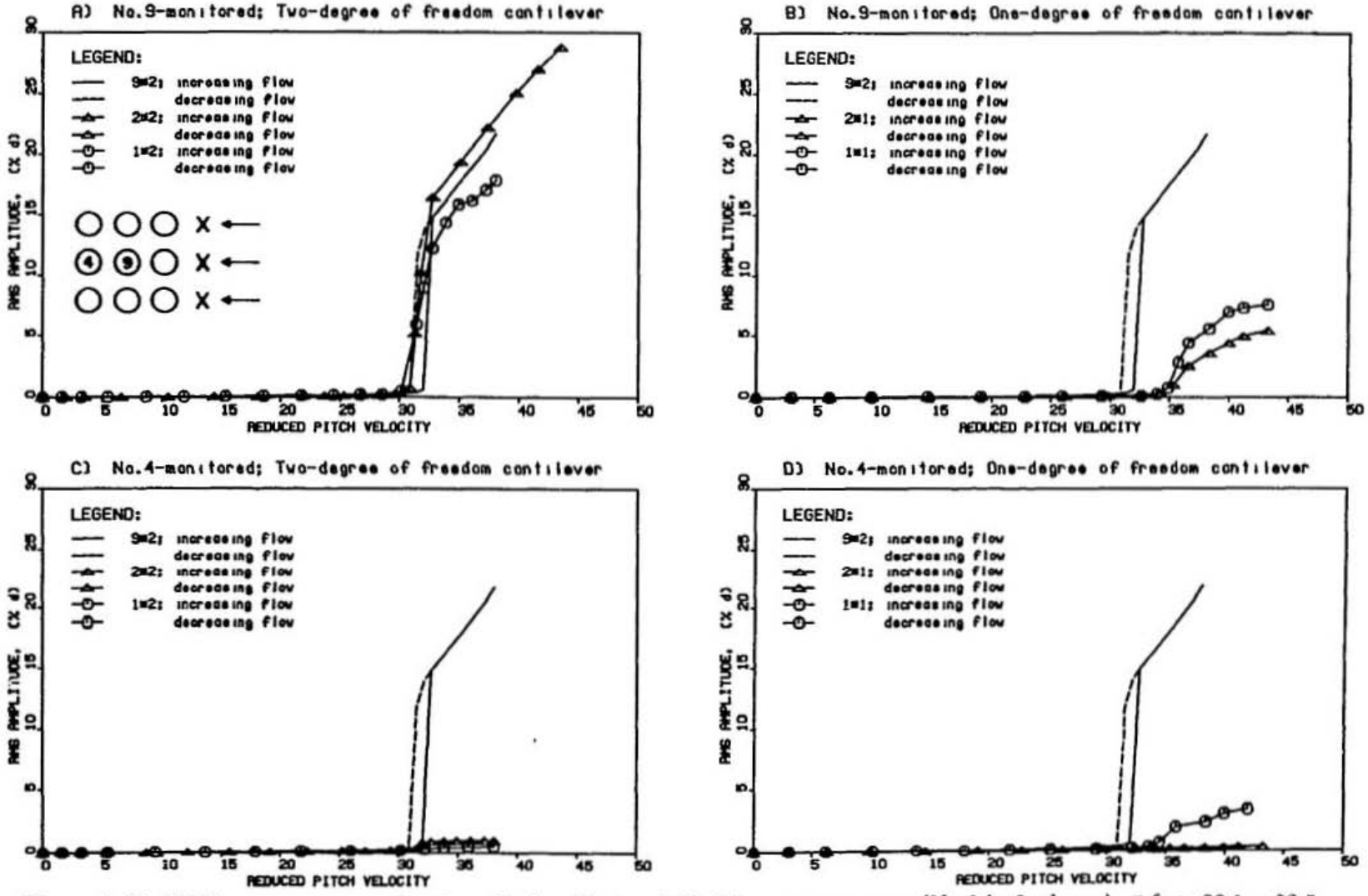

Figure A.30: RMS response curves for the cylinders No.4 and No.9 in a square array (No.9 in 3-rd row), $\bar{m}\delta_0 \approx 22.1 - 23.5$.

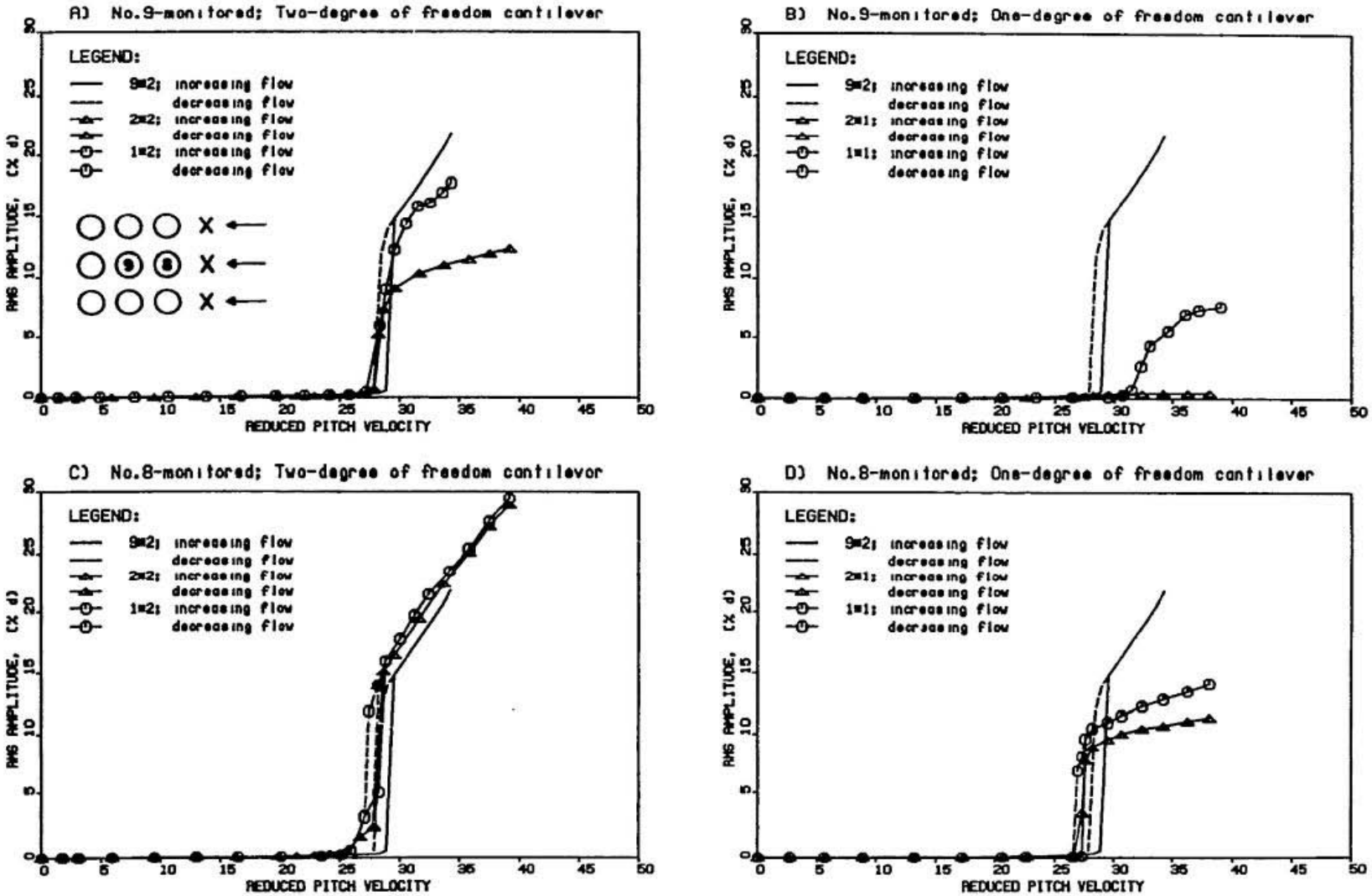

Figure A.31: RMS response curves for the cylinders No.8 and No.9 in a square array (No.9 in 3-rd row), $\bar{m}\delta_0 \approx 22.1 - 23.5$.

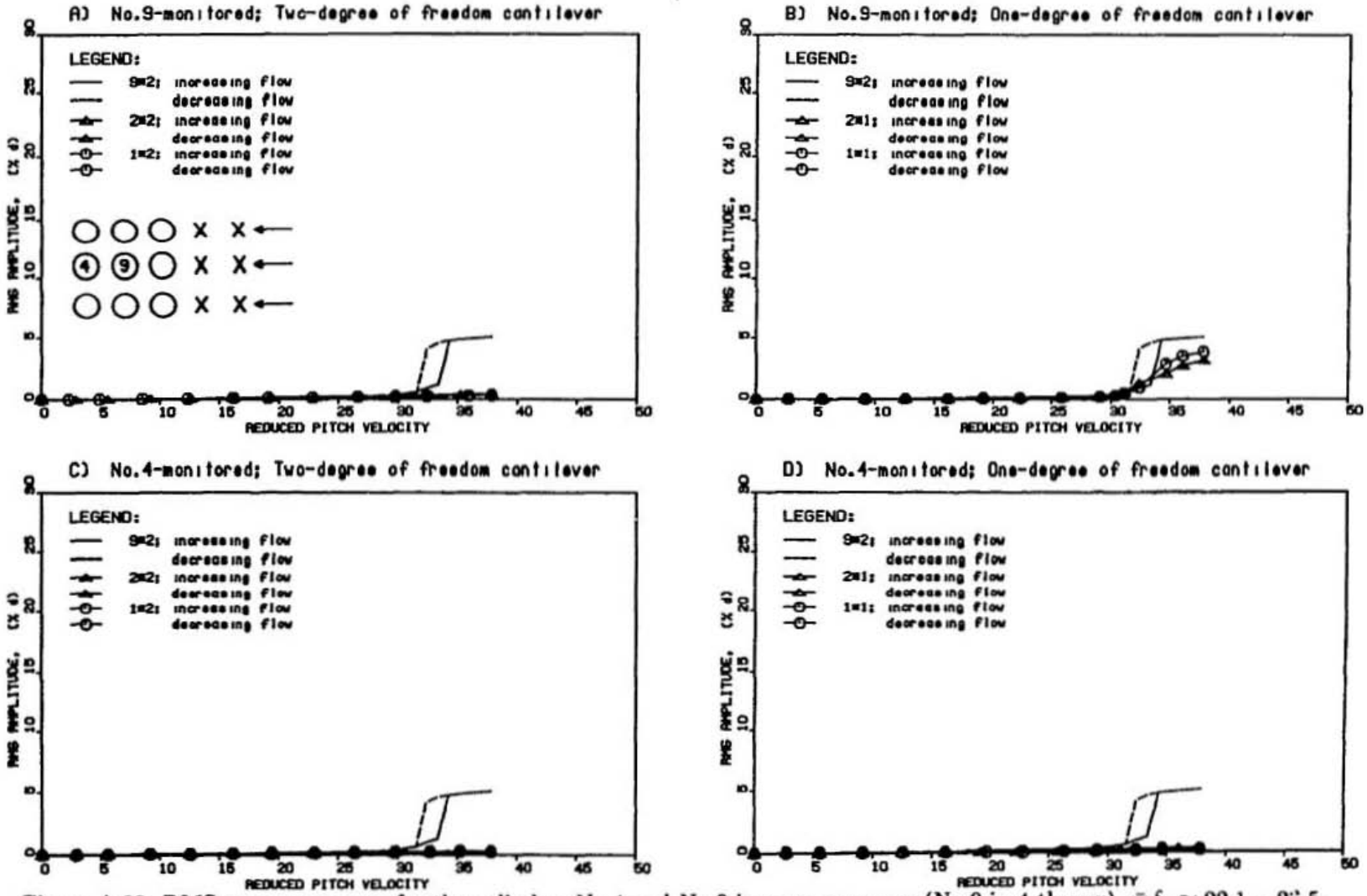

Figure A.32: RMS response curves for the cylinders No.4 and No.9 in a square array (No.9 in 4-th row), $\bar{m}\delta_0 \approx 22.1 - 23.5$.

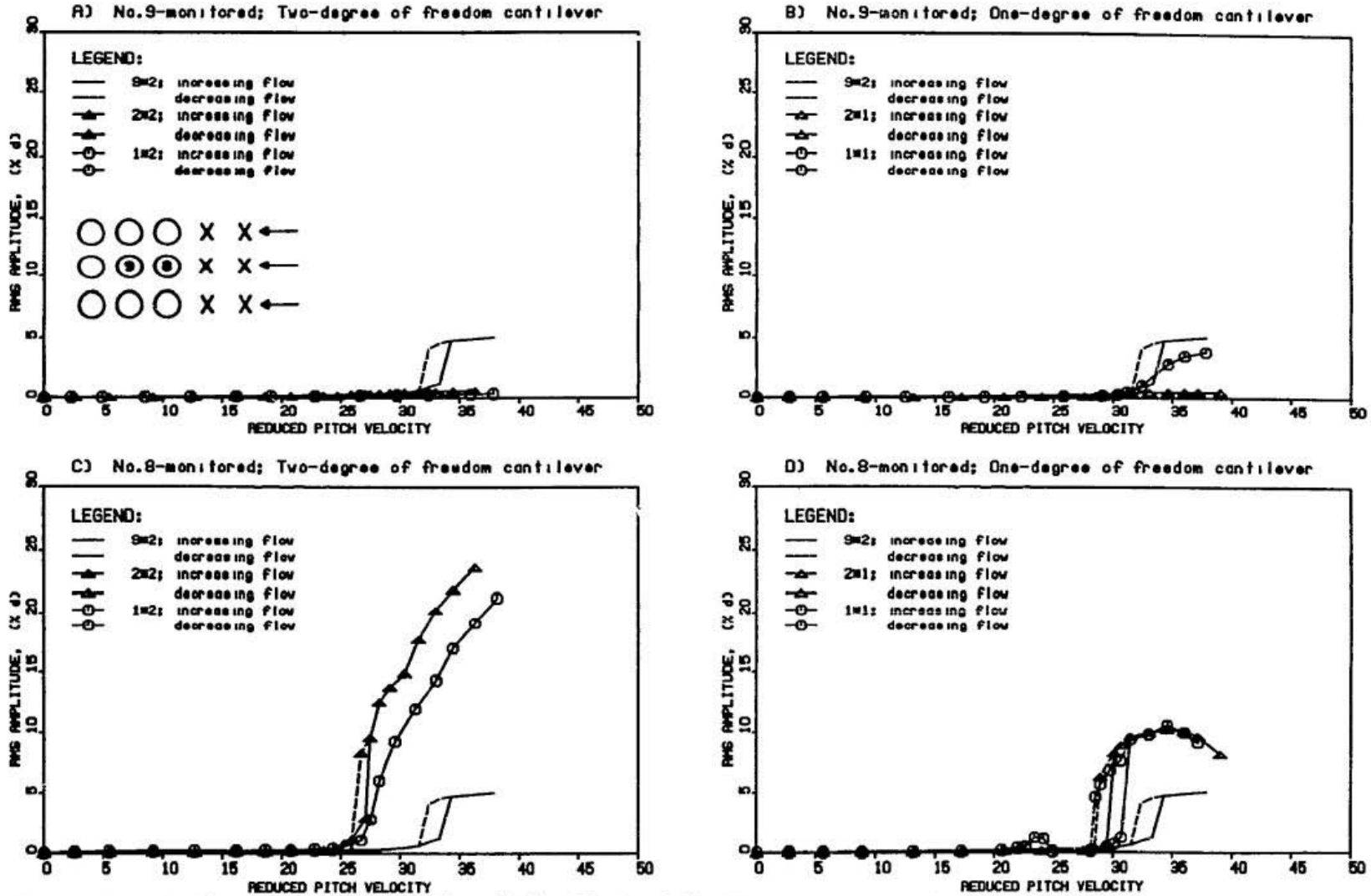

Figure A.33: RMS response curves for the cylinders No.8 and No.9 in a square array (No.9 in 4-th row), $\bar{m}\delta_0 \approx 22.1 - 23.5$.

Appendix B

Damping curves

This Appendix shows the fluidelastic component of damping, at various flow velocities below critical, as a function of amplitude. The results were obtained at $\bar{m}\delta_0 = 2.25$ for a parallel triangular array of pitch ratio 1.375 (Figures B1 and B2) and at $\bar{m}\delta_0 = 1.90$ for a square array of pitch ratio 1.433.

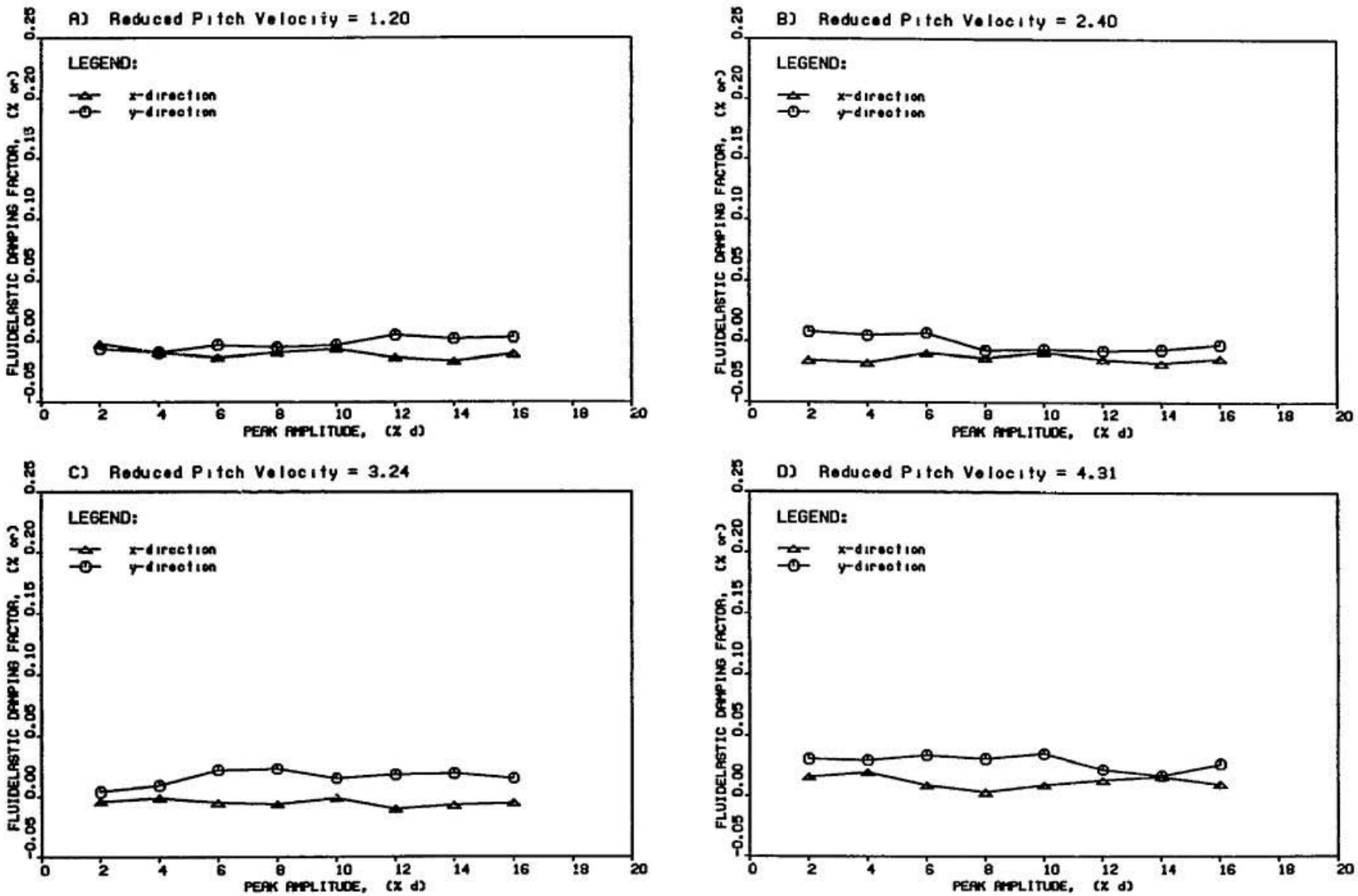

Figure B.1: Fluidelastic damping factor, $\zeta(A)$, for the 7 flexible cylinder parallel triangular array, $\bar{m}\delta_0 = 2.25$.

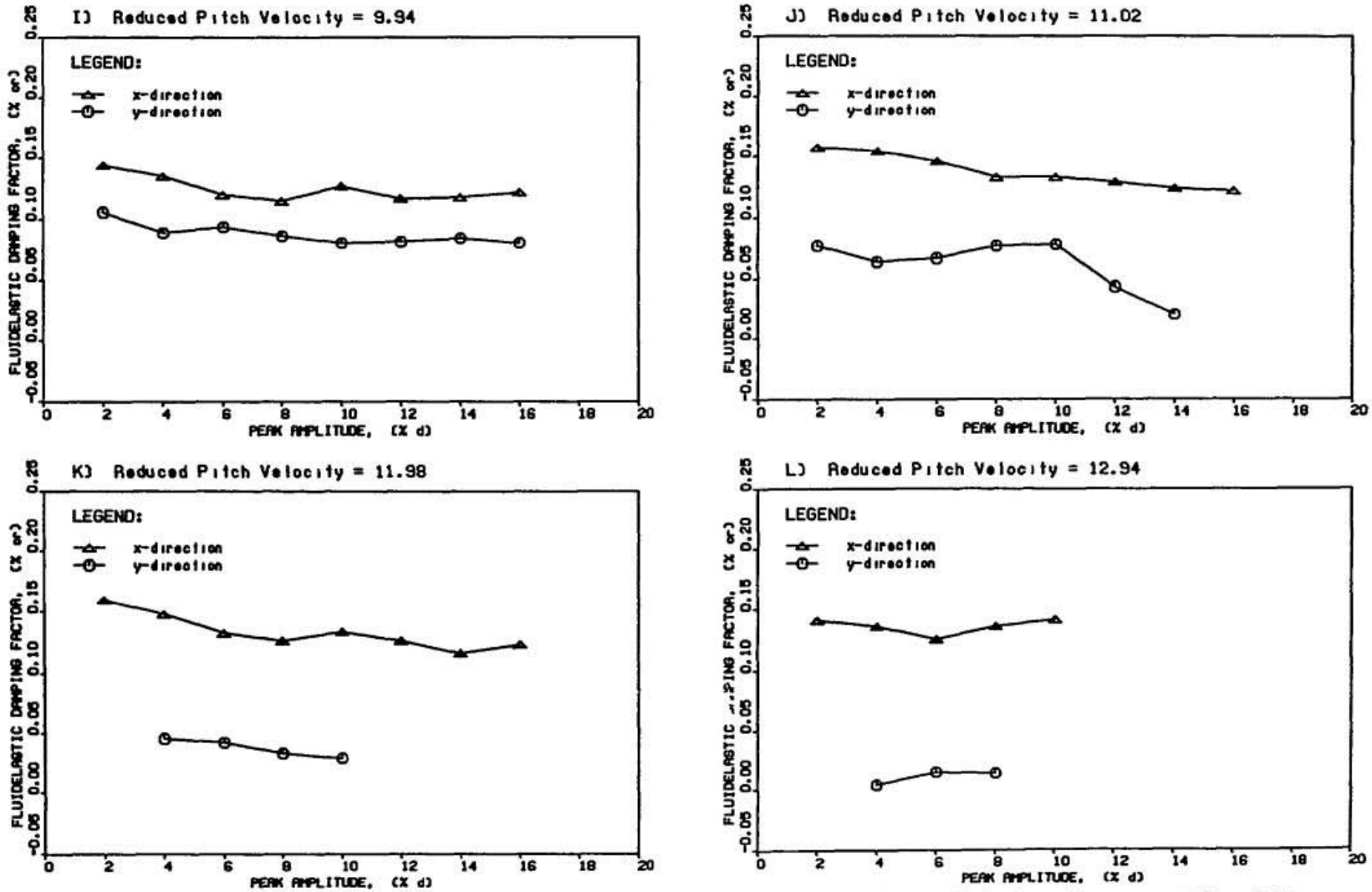

Figure B.1 (cont'd): Fluidelastic damping factor, $\zeta(A)$, for the 7 flexible cylinder parallel triangular array, $\bar{m}\delta_0 = 2.25$.

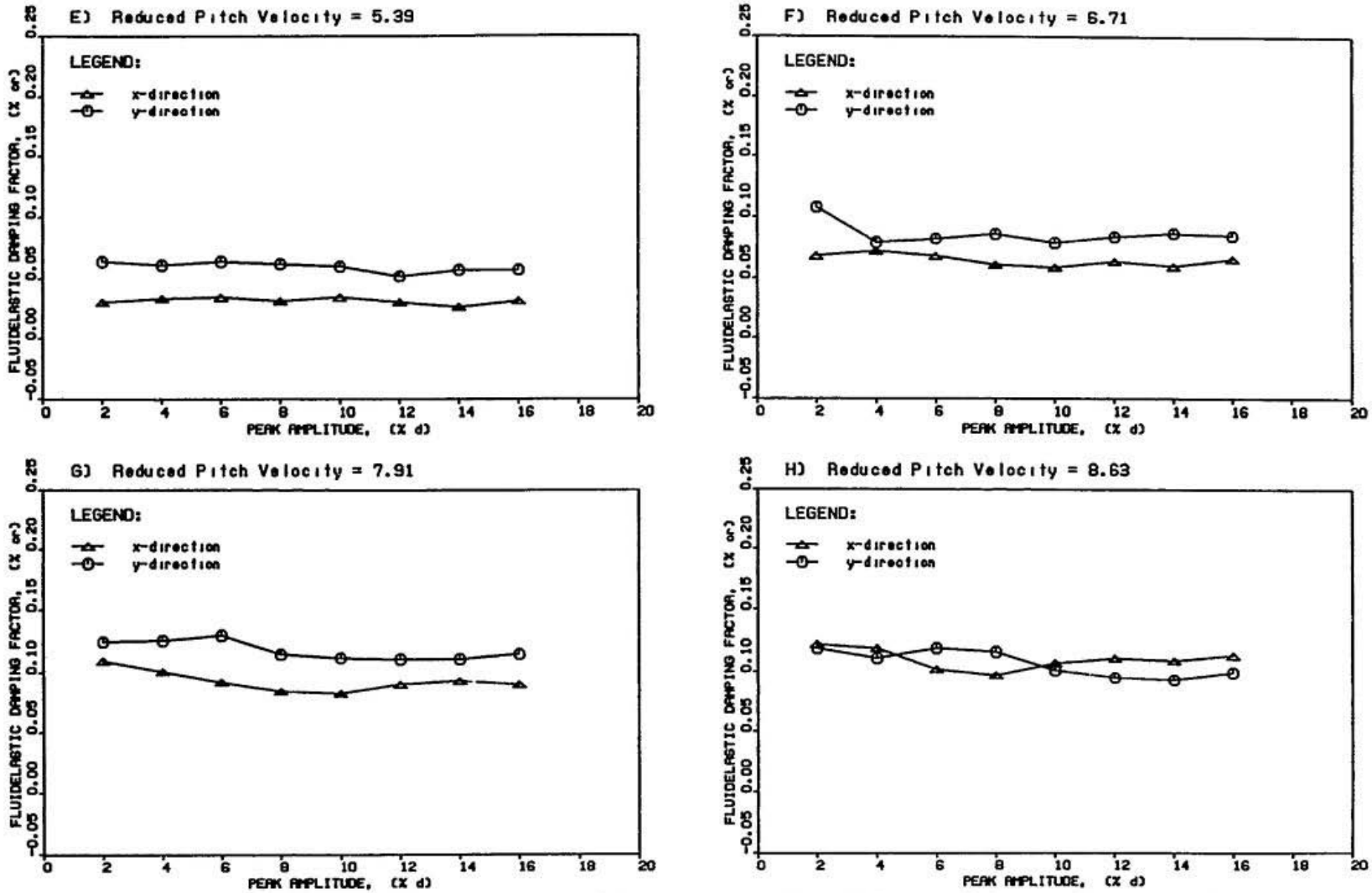

Figure B.1 (cont'd): Fluidelastic damping factor, $\zeta(A)$, for the 7 flexible cylinder parallel triangular array, $\bar{m}\delta_0 = 2.25$.

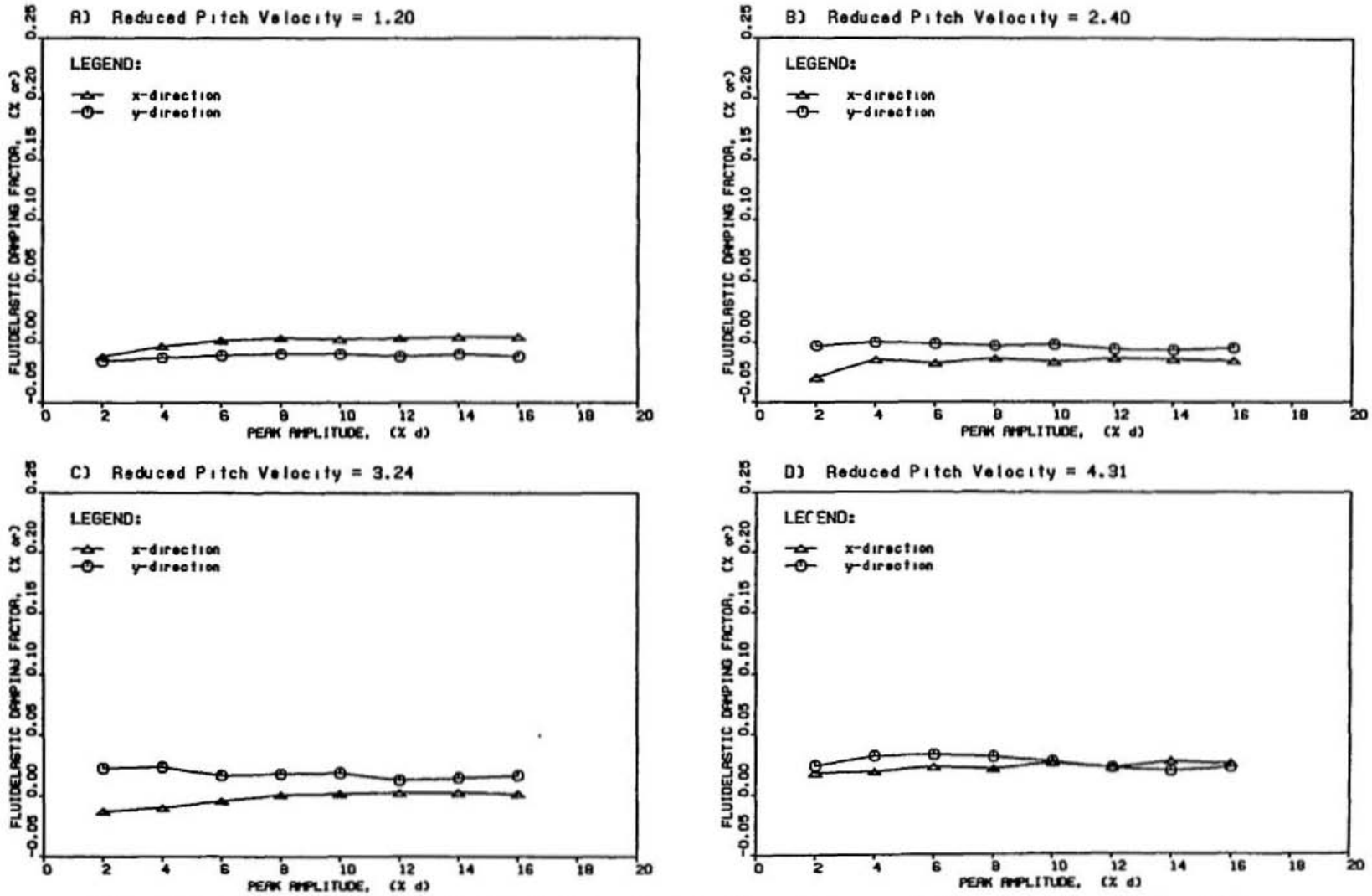

Figure B.2: Fluidelastic damping factor, $\zeta(A)$, for the 1 flexible cylinder parallel triangular array, $\bar{m}\delta_0 = 2.25$.

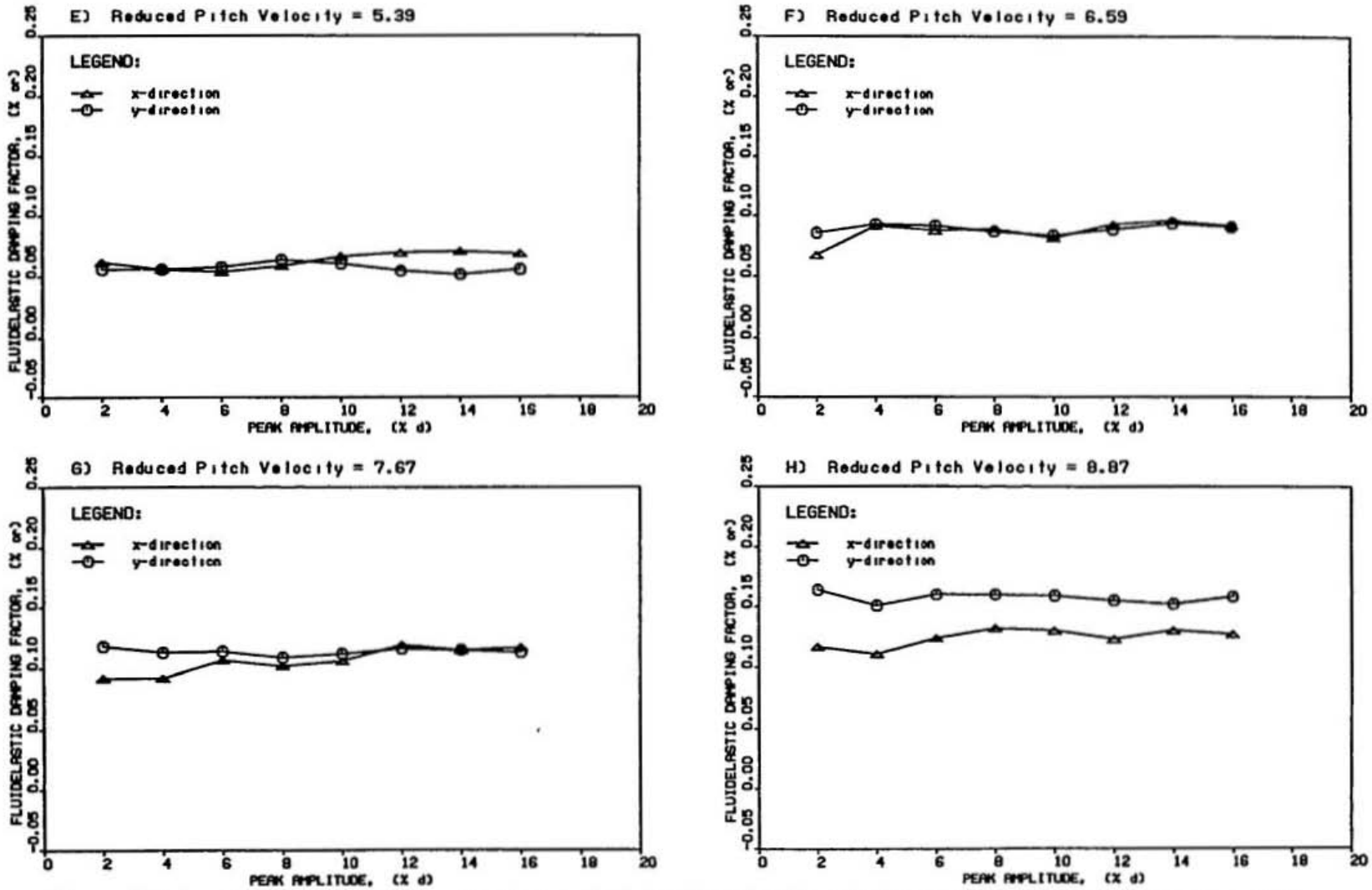

Figure B.2 (cont'd): Fluidelastic damping factor, $\zeta(A)$, for the 1 flexible cylinder parallel triangular array, $\bar{m}\delta_0 = 2.25$.

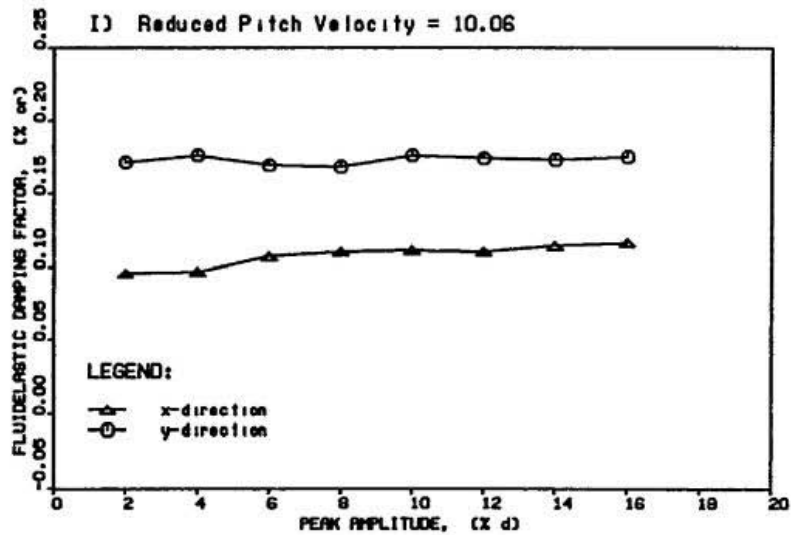

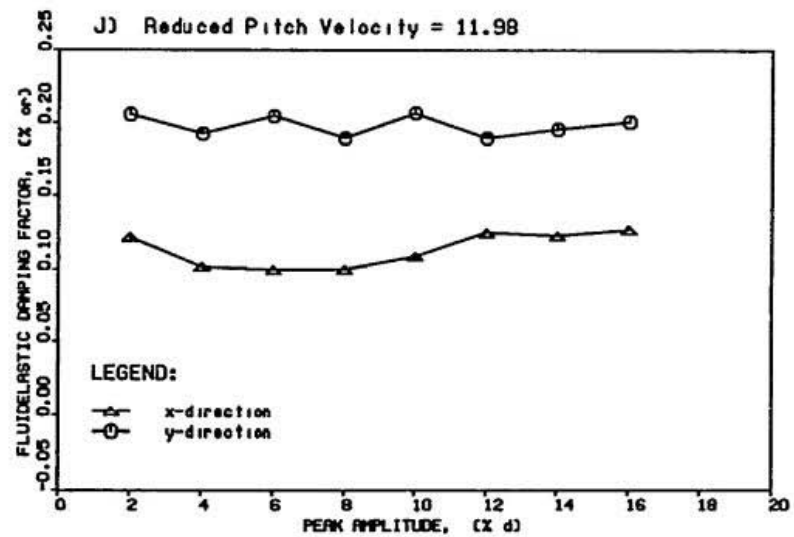

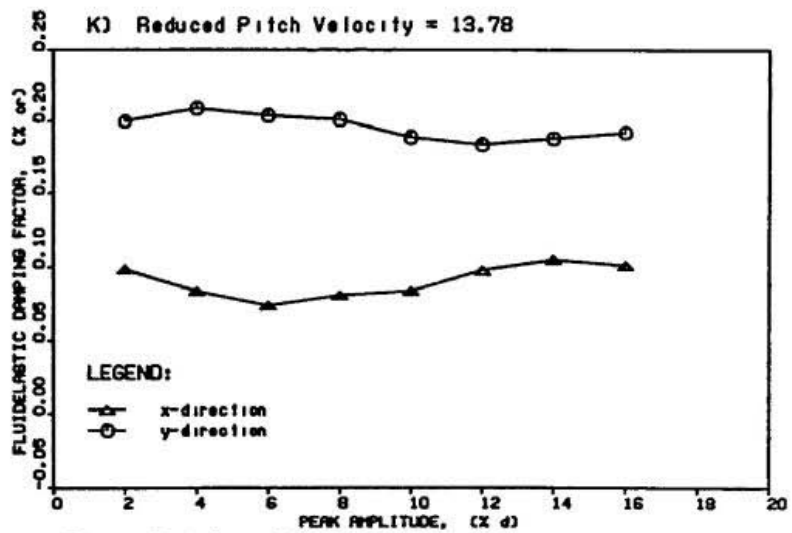

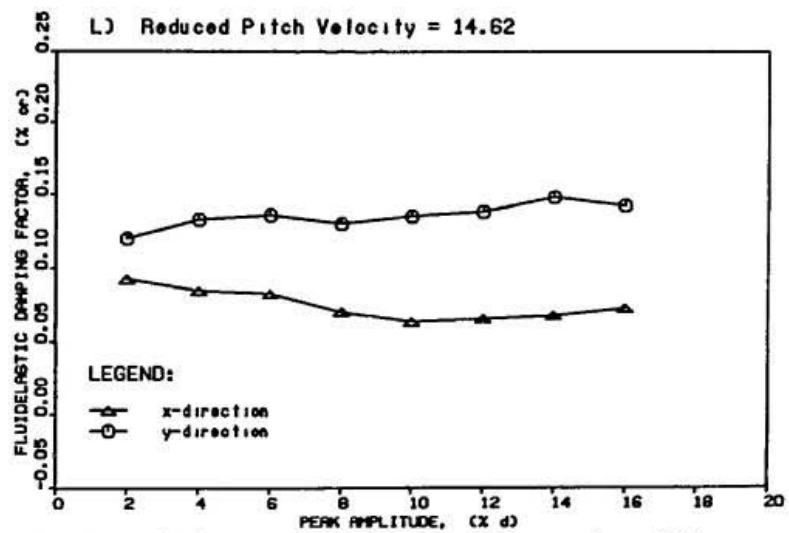

Figure B.2 (cont'd): Fluidelastic damping factor, $\zeta(A)$, for the 1 flexible cylinder parallel triangular array, $\bar{m}\delta_0 = 2.25$.

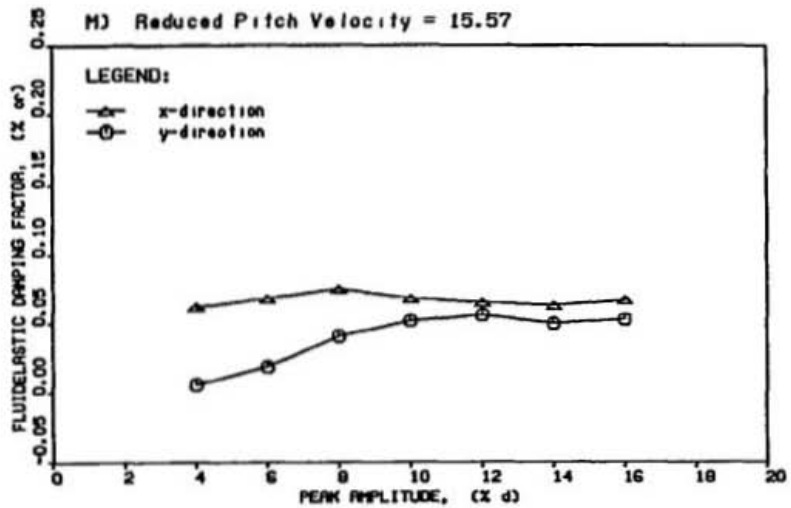

F' ure B.2 (cont'd): Fluidelastic damping factor, $\zeta(A)$, for the 1 flexible cylinder parallel triangular array, $\bar{m}\delta_0 = 2.25$.

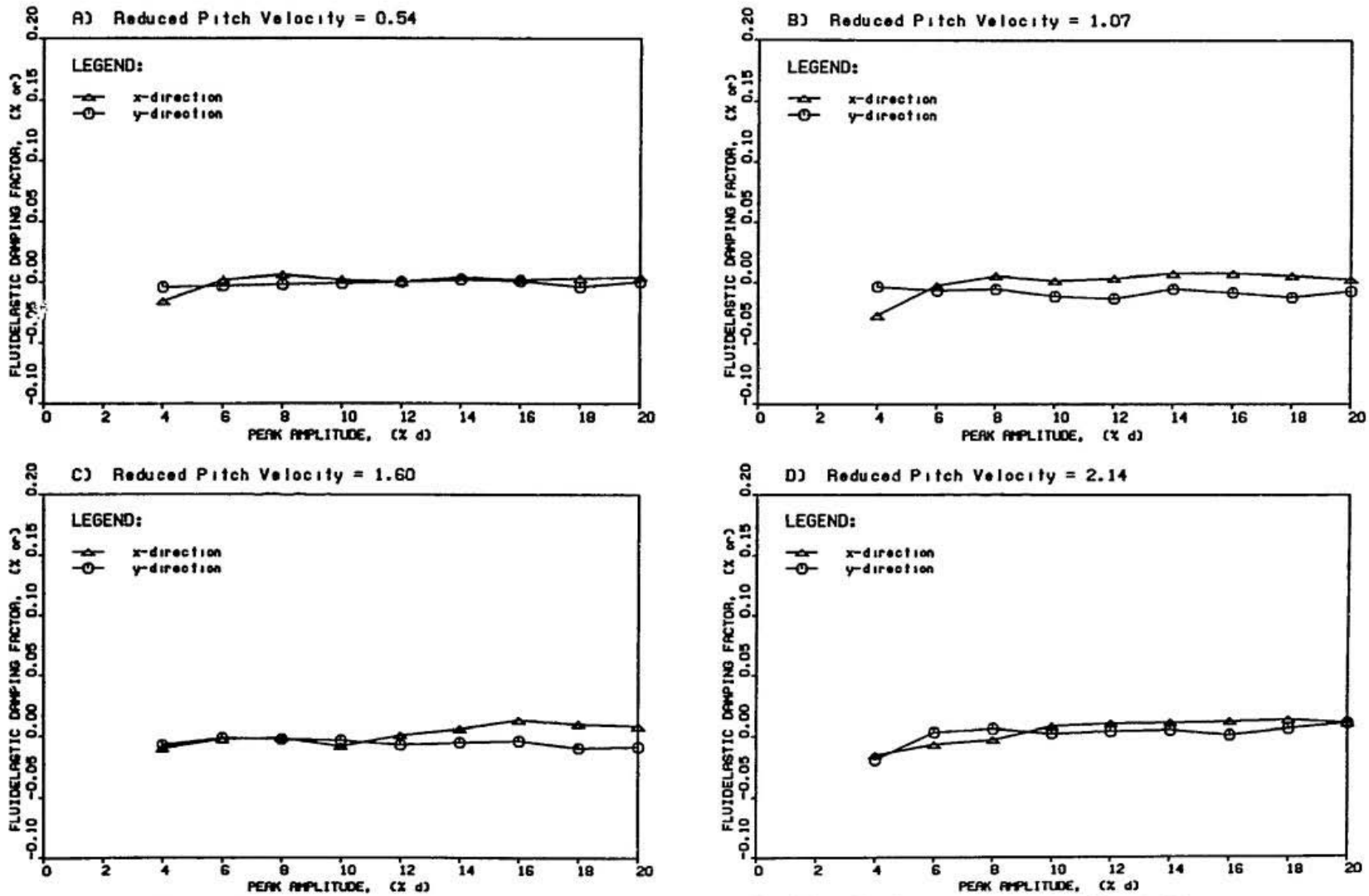

Figure B.3: Fluidelastic damping factor, $\zeta(A)$, for the 9 flexible cylinder square array, $\bar{m}\delta_0 = 1.90$.

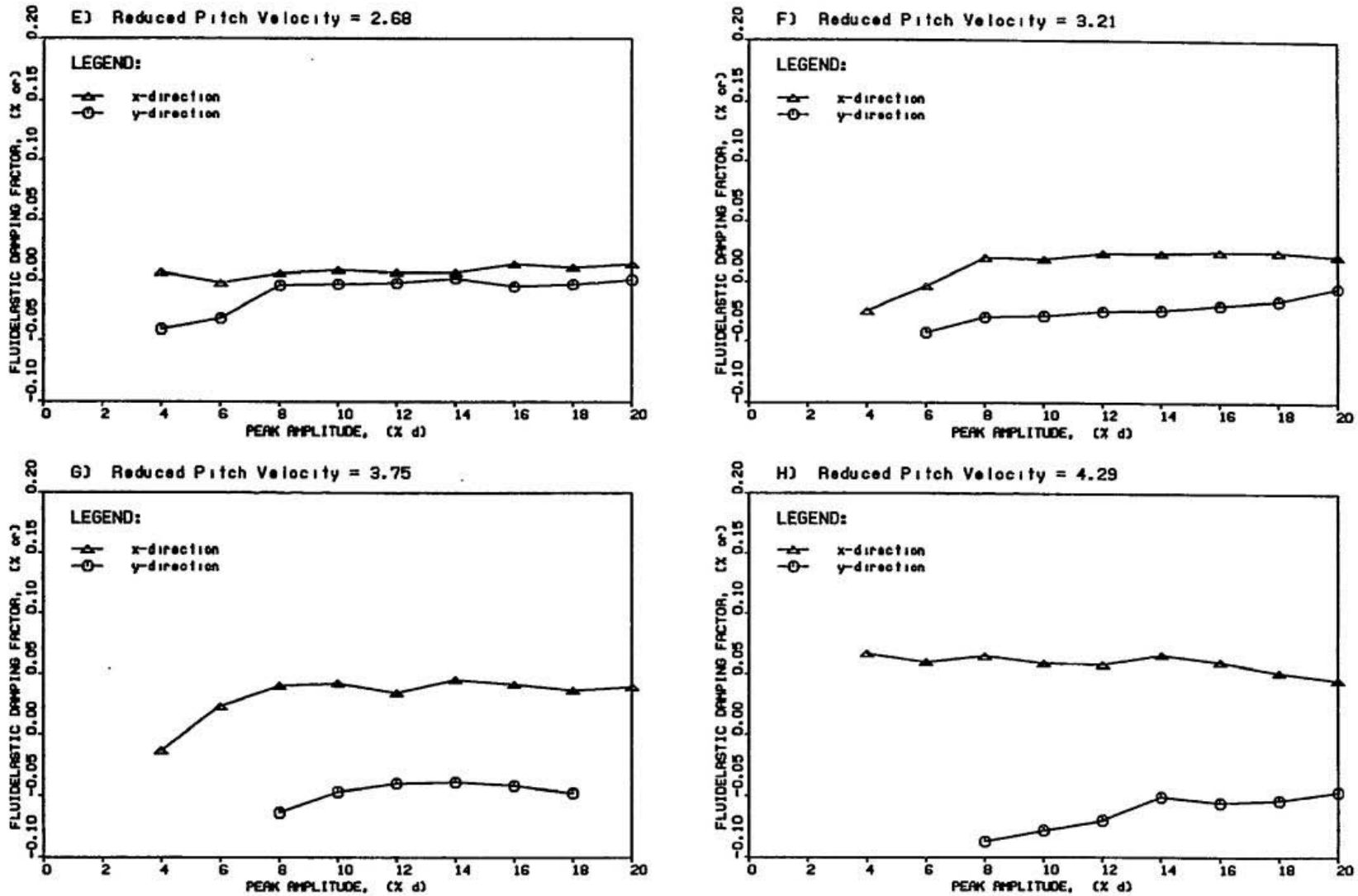

Figure B.3 (cont'd): Fluidelastic damping factor, $\zeta(A)$, for the 9 flexible cylinder square array, $\bar{m}\delta_0 = 1.90$.

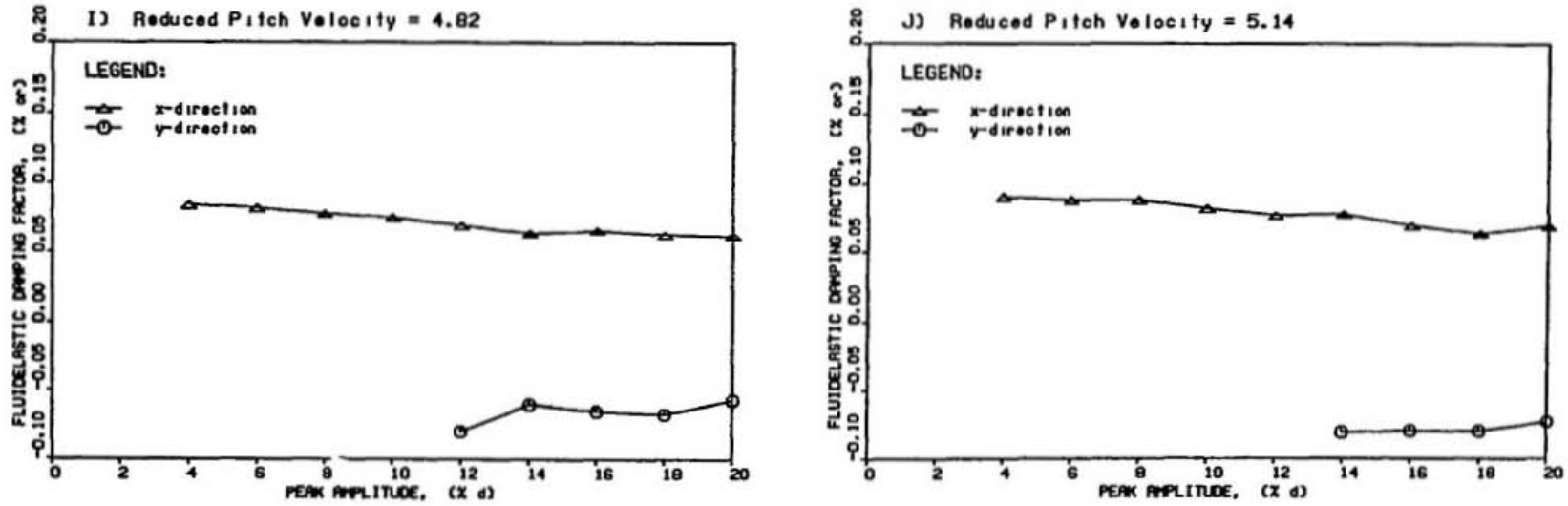

Figure B.3 (cont'd): Fluidelastic damping factor, $\zeta(A)$, for the 9 flexible cylinder square array, $\bar{m}\delta_0 = 1.90$.

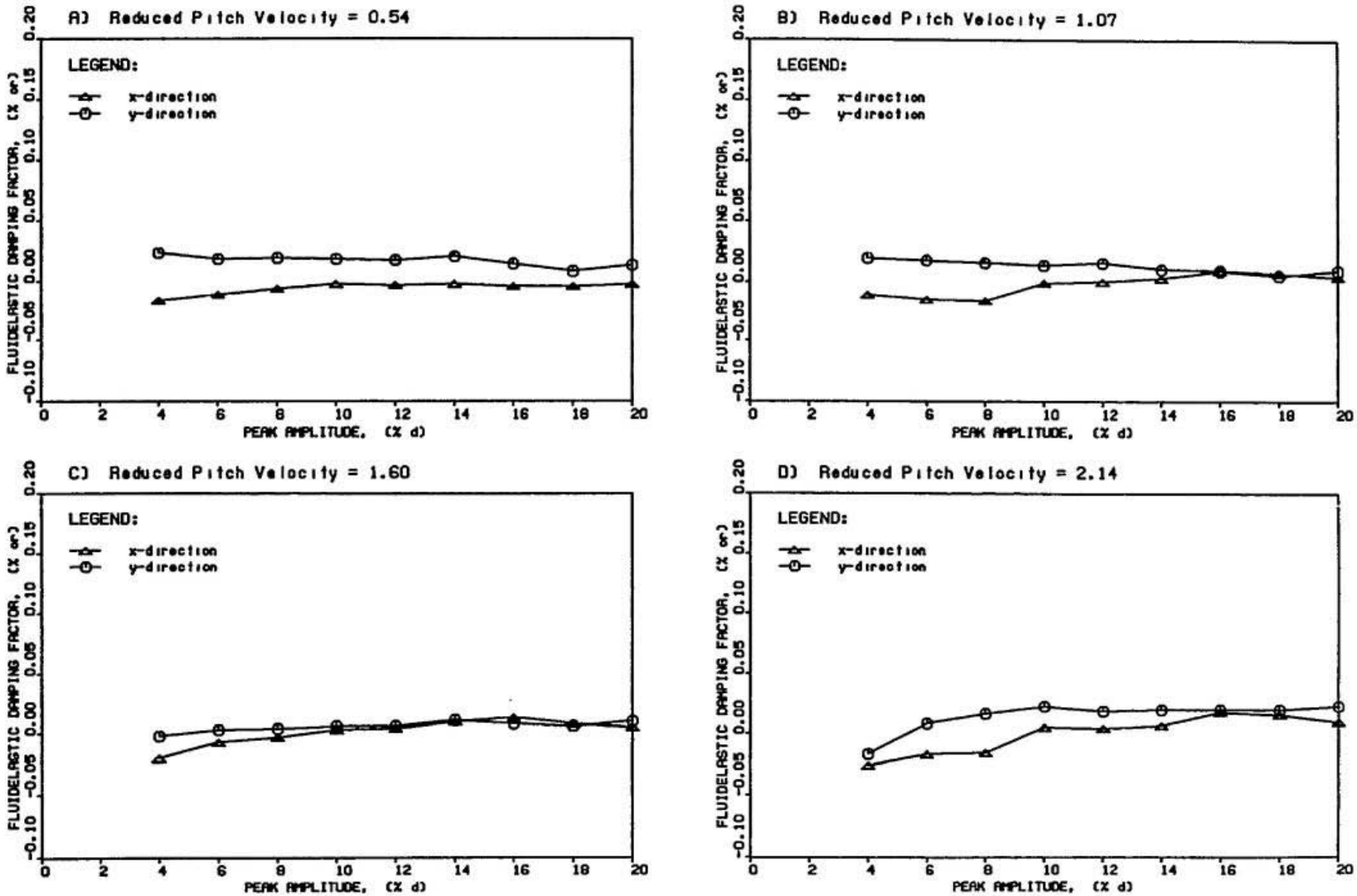

Figure B.4: Fluidelastic damping factor, $\zeta(A)$, for the 1 flexible cylinder square array, $\bar{m}\delta_0 = 1.90$.

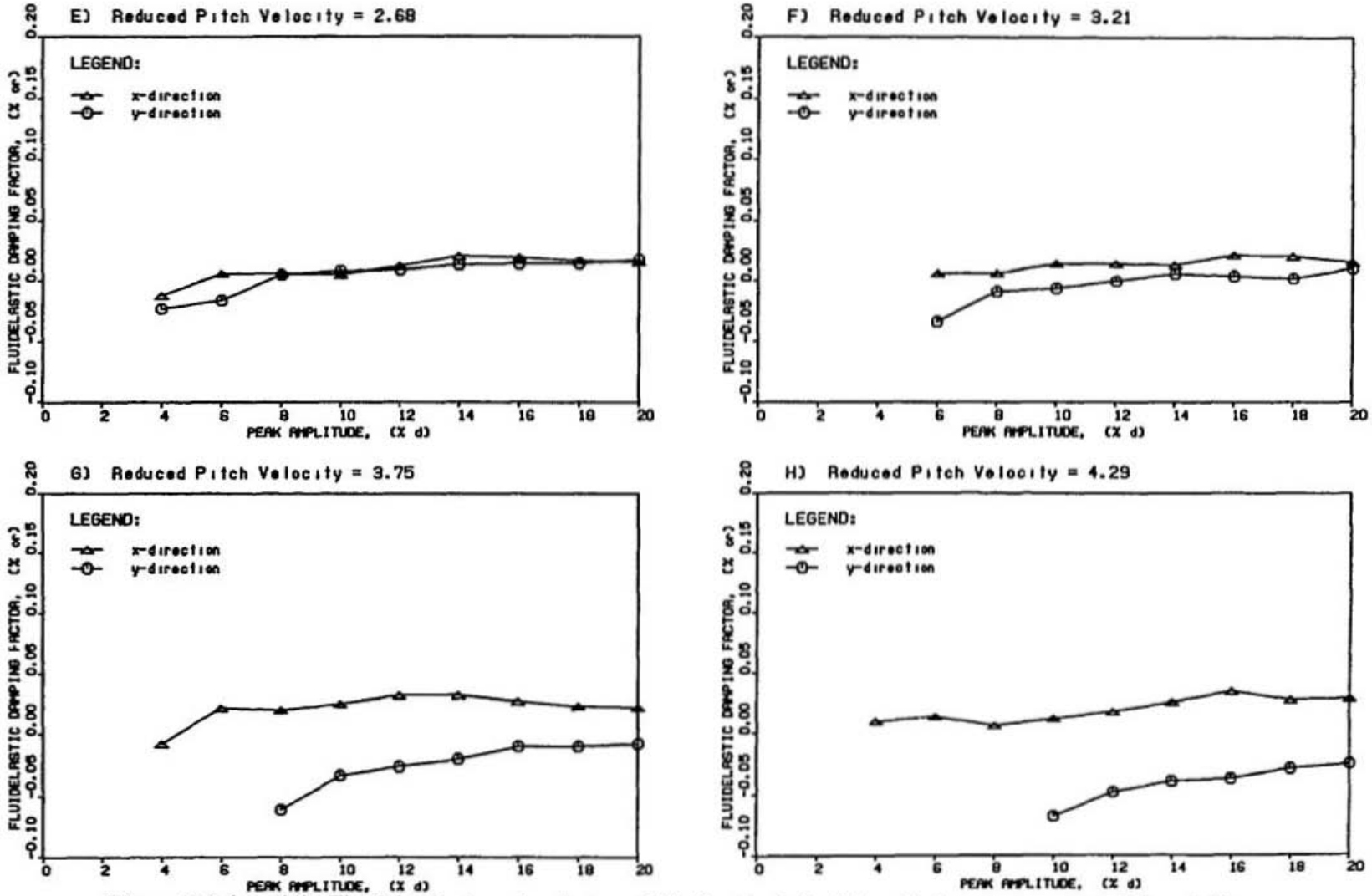

Figure B.4 (cont'd): Fluidelastic damping factor, $\zeta(A)$, for the 1 flexible cylinder square array, $\bar{m}\delta_0 = 1.90$.

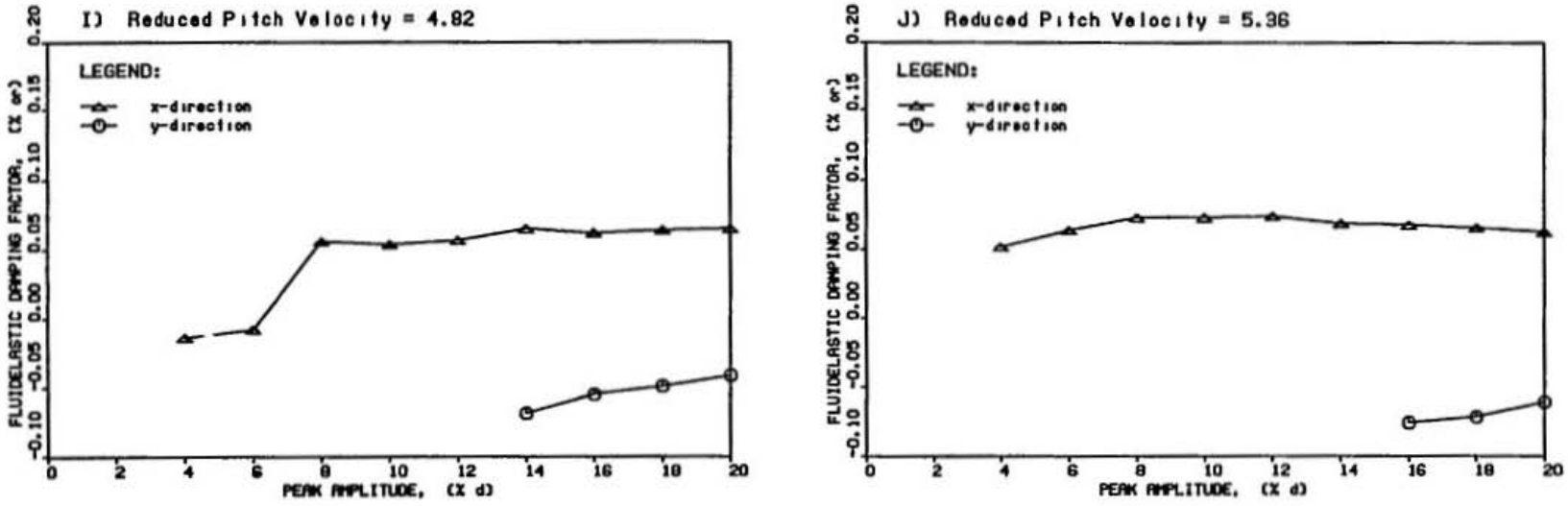

Figure B.4 (cont'd): Fluidelastic damping factor, $\zeta(A)$, for the 1 flexible cylinder square array, $\bar{m}\delta_0 = 1.90$.

Appendix C

Formulation of the first approximation method

An oscillating cylinder in a state of equilibrium (limit cycle) can be described in the form of the basic differential equation:

$$\ddot{y}(t) + \omega^2 y(t) + \mu f[y(t), \dot{y}(t)] = 0 \tag{C.1}$$

where $f[y(t), \dot{y}(t)]$ is a non-linear function of cylinder displacement and velocity, and μ is a small positive quantity.

Here, equation (C.1) is solved, using the first approximation method of Kryloff and Bogoliuboff [89], by writing the solution as:

$$y(t) = a(t)cos[\omega t + \Phi(t)] \tag{C.2}$$

and imposing the condition that $\dot{y}(t)$ takes the form:

$$\dot{y}(t) = -a\omega sin(\omega t + \Phi) \tag{C.3}$$

Evidently, equation (C.3) is correct only for $\mu = 0$. Physically, this implies that contribution of non-liner terms to the final solution of equation (C.1) is very small, $\mu \ll \omega^2$. Thus, the fluidelastic system under consideration is treated as nearly linear. From equations (C.2) and (C.3) it follows that:

$$\dot{a}(t)cos[\omega t + \Phi(t)] - \dot{\Phi}(t)a(t)sin[\omega t + \Phi(t)] = 0 \tag{C.4}$$

This means that the amplitude, $a(t)$, and the phase, $\Phi(t)$, are slowly varying functions of time, t, in the state of equilibrium. It can be shown that they satisfy the following formulas:

$$\dot{a}(t) = \frac{\mu}{\omega} f(a cos\Theta, -a\omega sin\Theta) sin\Theta \tag{C.5}$$

$$\dot{\Phi}(t) = \frac{\mu}{a\omega} f(a cos\Theta, -a\omega sin\Theta) cos\Theta \tag{C.6}$$

where $\Theta = \Theta(t)$ denotes the total phase. This set of two first order equation corresponds exactly to the initial second order differential equation (C.1). An important step to finding their solution is an application of the averaging principle. First, the right hand sides of equations (C.5) and (C.6) are expanded into Fourier series as periodic functions with the period $T = \frac{2\pi}{\omega}$. In this process, $a(t)$ and $\Phi(t)$ are considered to be made up of slowly varying components, $\bar{a}(t)$ and $\bar{\Phi}(t)$, and small rapidly oscillating terms. Then, by integrating these expressions over each period (assuming that $a(t) = \bar{a}(t)$ and $\Phi(t) = \bar{\Phi}(t)$ in the first approximation) all oscillating terms are "averaged out" since the slowly varying process is not influenced by small rapid oscillations. In other words, the instantaneous values of $a(t)$ and $\Phi(t)$ are replaced in this process by their averages which are calculated in the usual way. Thus, the equations of the first approximation, which satisfy equation (C.1) to within the order of μ^2, may be finally written as:

$$\dot{a}(t) = \frac{\mu}{2\pi\omega} \int_0^{2\pi} f(a cos\Theta, -a\omega sin\Theta) sin\Theta d\Theta \tag{C.7}$$

and

$$\dot{\Theta}(t) = \omega(a) \tag{C.8}$$

where the frequency of oscillation $\omega(a)$ depends on amplitude *via*:

$$\omega(a) = \omega + \frac{\mu}{2\pi\omega a} \int_0^{2\pi} f(a cos\Theta, -a\omega sin\Theta) cos\Theta d\Theta \tag{C.9}$$

Note that the function $f(a cos\Theta, -a\omega sin\Theta)$ may enter into equations (C.7) and (C.9) directly and not only through its non-linear part. Thus, after squaring both sides

of equation (C.9) and retaining only terms of the same order of smallness $0(\mu^2)$ as used in the formulation of the first approximation method, the expression for $\omega(a)$ takes the form:

$$\omega^2(a) = \omega_0^2 + \frac{\mu}{\pi a}\int_0^{2\pi} f(acos\Theta, -a\omega sin\Theta)cos\Theta d\Theta \qquad (C.10)$$

These equations yield the dynamic bifurcation formulae; a linear solution and a non-linear limit cycle. Since the limit cycle of constant amplitude is expected, its rate of change may be set equal to zero ($\dot{a}(t) = 0$ in equation (C.7)) and the linear solution becomes trivial ($a = 0$).

Further, it is interesting to note that, based on equation (C.9) or equation (C.10), the transition from an oscillatory to a static state can be defined. Physically, this implies that:

$$\lim_{\omega \to 0} \omega(a) = 0 \qquad (C.11)$$

Appendix D

Verification of numerical integration scheme

To verify the effectiveness of the numerical integration scheme and to specify certain parameters for its operation, a fourth order predictor-corrector method is applied to the Van der Pol's oscillator, which is expressed in the form of the basic differential equation:

$$m_0\ddot{y}(t) + [By^2(t) - B_0]\dot{y}(t) + k_0 y(t) = 0 \qquad \text{(D.1)}$$

where B and B_0 are positive constants. First, this equation is examined in the simplified version:

$$\ddot{y}(t) + C[y^2(t) - 1]\dot{y}(t) + y(t) = 0 \qquad \text{(D.2)}$$

for different values of the positive constant, C, which reflects the strength of non-linear and dissipative terms. This test showed, in particular, the importance of selecting the proper time step for accurate simulations. It was found that for small values of C ($C \leq 1$), the time step $\Delta t = \frac{T_n}{40}$ is sufficient, by three corrector iterations, to minimize the numerical error and the possibility of numerical instability. These simulation results, which in part are presented in Table D.1, were in excellent agreement with numerical data published by Urabe [91]. As can be seen, simulations with $C>1$ required finer time stepping than initially defined, due to the increasing steepness of response trajectories. The first approximation method yields a limit cycle of 2 for all C.

Table D.1: Prediction of limit cycle amplitude for Van der Pol's equation.

C	Time step				First approximation	Reference [91]
	$T_n/10$	$T_n/20$	$T_n/40$	$T_n/80$		
0.5	2.115	2.007	2.003	2.0030	2	—
1.0	unstable	2.028	2.009	2.0090	2	2.0090
3.0	unstable	unstable	unstable	2.0034	2	2.0035
5.0	unstable	unstable	unstable	2.0017	2	2.0016

Having specified the time step, equation (D.1) was examined for a large variety of system parameters. Table D.2 shows some numerical results, together with the solution of the first approximation which yields a limit cycle amplitude of $a = 2\sqrt{\frac{B_0}{B}}$.

Because equation (D.1) undergoes dynamic instability, one might expect its limit cycle to be sensitive to the periodic forcing conditions. Thus, it was decided to examine the Van der Pol's oscillator under harmonic excitation:

$$m_0\ddot{y}(t) + [By^2(t) - B_0]\dot{y}(t) + k_0y(t) = Esin\gamma t \tag{D.3}$$

where E and γ are the amplitude and the frequency of forcing term, respectively. First, numerical results were compared with the simplified solution of the first approximation ($m_0 = k_0 = 1$ and $B = B_0 = 1$) derived, for example, in Reference [89]. Next, equation (28) was solved, following Reference [89], and tested numerically for a variety of parameters. Table D.2 presents some examples of these validation tests.

Also, Rayleigh's oscillator was examined; another important equation with regards to non-linear systems. This equation is expressed in the form:

$$m_0\ddot{y}(t) + [B\dot{y}^2(t) - B_0]\dot{y}(t) + k_0y(t) = 0 \tag{D.4}$$

Its solution of the first approximation yields a limit cycle amplitude $a = \frac{1}{\omega_0}\sqrt{\frac{4B_0}{3B}}$ (for details, see Reference [89]). For completeness, some numerical and analytical exampies are included in Table D.2. It can be seen that, in nearly all examined cases, close agreement with the approximate solutions of equations (D.1),(D.2) and (D.3) was found.

Table D.2: Predictions of limit cycle amplitudes for equations (D.1,D.3,D.4).

Eq.	m_0	k_0	B	B_0	E	γ	Limit cycle amplitude, a	
							Numerical	First approximation
D.1	1	2	1	2			2.86	2.83
	2	1	4	3			1.75	1.73
	1	5	10	1			0.65	0.63
D.3	1	1	1	1	0.75	0.50	2.41	2.43
	1	1	1	0.25	0.75	0.50	1.00	1.02
D.4	1	1	1	1			1.25	1.16
	2	3	3	2			0.81	0.77
	5	1	5	1			1.18	1.16